Modeling and Control of Piezoelectric Actuators

A Thesis Submitted to the College of

Graduate Studies and Research

In Partial Fulfillment of the Requirements

For the Degree of Doctor of Philosophy

In the Department of Mechanical Engineering

University of Saskatchewan

Saskatoon

By

JINGYANG PENG

Permission to Use

In presenting this thesis in partial fulfillment of the requirements for a Postgraduate degree from the University of Saskatchewan, I agree that the Libraries of this University may make it freely available for inspection. I further agree that permission for copying of this thesis in any manner, in whole or in part, for scholarly purposes may be granted by the professor or professors who supervised my thesis work or, in their absence, by the Head of the Department or the Dean of the College in which my thesis work was done. It is understood that any copying or publication or use of this thesis or parts thereof for financial gain shall not be allowed without my written permission. It is also understood that due recognition shall be given to me and to the University of Saskatchewan in any scholarly use which may be made of any material in my thesis.

Requests for permission to copy or to make other use of material in this thesis in whole or part should be addressed to:

Head of the Department of Mechanical Engineering

University of Saskatchewan

Saskatoon, Saskatchewan S7N 5A9

Abstract

Piezoelectric actuators (PEAs) utilize the inverse piezoelectric effect to generate fine displacement with a resolution down to sub-nanometers and as such, they have been widely used in various micro- and nanopositioning applications. However, the modeling and control of PEAs have proven to be challenging tasks. The main difficulties lie in the existence of various nonlinear or difficult-to-model effects in PEAs, such as hysteresis, creep, and distributive vibration dynamics. Such effects can seriously degrade the PEA tracking control performances or even lead to instability. This raises a great need to model and control PEAs for improved performance. This research is aimed at developing novel models for PEAs and on this basis, developing model-based control schemes for the PEA tracking control taking into account the aforementioned nonlinear effects.

In the first part of this research, a model of a PEA for the effects of hysteresis, creep, and vibration dynamics was developed. Notably, the widely-used Preisach hysteresis model cannot represent the one-sided hysteresis of PEAs. To overcome this shortcoming, a rate-independent hysteresis model based on a novel hysteresis operator modified from the Preisach hysteresis operator was developed, which was then integrated with the models of creep and vibration dynamics to form a comprehensive model for PEAs. For its validation, experiments were carried out on a commercially-available PEA and the results obtained agreed with those from model simulations.

By taking into account the linear dynamics and hysteretic behavior of the PEA as well as the presliding friction between the moveable platform and the end-effector, a model of the piezoelectric-driven stick-slip (PDSS) actuator was also developed in the first part of the research. The effectiveness of the developed model was illustrated by the experiments on the PDSS actuator prototyped in the author's lab.

In the second part of the research, control schemes were developed based on the aforementioned PEA models for tracking control of PEAs. Firstly, a novel PID-based sliding mode (PIDSM) controller was developed. The rational behind the use of a sliding mode (SM) control is that the SM control can effectively suppress the effects of matched uncertainties, while the PEA hysteresis, creep, and external load can be represented by a lumped matched uncertainty based on the developed model. To solve the chattering and steady-state problems, associated with the ideal SM control and the SM control with boundary layer (SMCBL), the novel PIDSM control developed in the present study replaces the switching control term in the ideal SM control schemes with a PID regulator. Experiments were carried out on a commercially-available PEA and the results obtained illustrate the effectiveness of the PIDSM controller, and its superiorities over other schemes of PID control, ideal SM control, and the SMCBL in terms of steady state error elimination, chattering suppression, and tracking error suppression.

Secondly, a PIDSM observer was also developed based on the model of PEAs to provide the PIDSM controller with state estimates of the PEA. And the PIDSM controller and the PIDSM observer were combined to form an integrated control scheme (PIDSM observer-controller or PIDSMOC) for PEAs. The effectiveness of the PIDSM observer and the PIDSMOC were also validated experimentally. The superiority of the PIDSMOC over the PIDSM controller with σ-β filter control scheme was also analyzed and demonstrated experimentally.

The significance of this research lies in the development of novel models for PEAs and PDSS actuators, which can be of great help in the design and control of such actuators. Also, the development of the PIDSM controller, the PIDSM observer, and their integrated form, i.e., PIDSMOC, enables the improved performance of tracking control of PEAs with the presence of various nonlinear or difficult-to-model effects.

Acknowledgements

I am heartily thankful to my supervisor, Prof. Daniel Chen, whose encouragement, guidance and support through my study program enabled me continuously reach my research goals. His expertise and enthusiasm inspired me to explore every challenge in my research. I will be always grateful.

I also would like to extend my appreciation to the members of my Advisory Committee: Prof. Greg J. Schoenau, Prof. Ramakrishna Gokaraju and Prof. Richard Burton for their examination and advices in my research program.

My thanks also go to Mr. Doug Bitner in the Department of Mechanical Engineering for his technical assistance for my experiments and the engineering machine shop for their construction of the experiment rig.

Special thanks are due to my friends for their help and support during my research. They are Dong Kang, Jianwei Li, Jun Li, Lu Wang, Qingshu Zhang, and Yu Cao.

Finally, I gratefully acknowledge the financial support from the Department of Mechanical Engineering (through the Scholarship) and Natural Science and Engineering Research Council (NSERC).

Contents

1 Introduction and Objectives

1.1 Introduction

Piezoelectric actuators (PEAs) utilize the inverse piezoelectric effect of piezoelectric materials to generate forces and displacements. By applying electric charges to a piece of piezoelectric material (usually by means of an electric voltage), a stress can be generated, resulting in an actuating force. This actuating force combining with the external force exerted on the piezoelectric material will cause the piezoelectric material to deform, i.e. generating a displacement. PEAs are characterized by large actuating force (e.g. a few hundred N) and fine displacement resolution (sub-nanometer), hence they have been widely used in micro- and nanopositioning applications. A PEA typically includes a piezoelectric element, an end-effector, and flexible hinges that connect the end-effector to the base, as schematically shown in Fig. 1. The end-effector provides a platform for mounting any equipment that requires position manipulation. And the use of flexible hinges eliminates the involvement of friction in the structure.

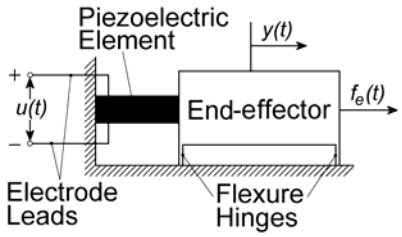

Fig. 1 Schematic of a PEA. *u(t)* is the input voltage, *y(t)* is the output displacement, and $f_e(t)$ is the external load.

Modeling and control of PEAs remain to be challenging tasks. This is mainly due to the fact

that the actuating force and the resulting displacement of PEAs are subject to several nonlinear or difficult-to-model effects including hysteresis, creep, distributive vibration dynamics, and external forces. Such effects may degrade the positioning performance of the PEA or even induce instability. Hysteresis is a kind of memory effect, which is nonlinear and modeled as either rate-independent or rate-dependent. The relationship between the input voltage to the PEA and the resulting actuating force are typically modeled as a rate-independent hysteresis. Creep is the phenomenon that the output displacement of the PEA changes (slowly increases or decreases) over a long time period as the input voltage to the PEA is kept constant. It is usually treated as a mechanical property rather than an electro-mechanical property of the piezoelectric material. The distributive vibration dynamics is due to the distributive nature of the piezoelectric material. The external force is the PEA load, which varies depending on applications and/or tasks. Since the performance of the classical non-model-based control schemes such as PID applied to such a system are shown to be unsatisfactory, as discussed in Chapter 5, it is of great desire to develop models that take into account the aforementioned effects to represent the PEA performance and on this basis, to develop model-based control schemes for its improved performance.

A number of modeling and control schemes for PEAs have been developed and reported in the literature, which are presented in Chapter 2 with details. In various models, the decoupled structure is quite common, in which the aforementioned effects of a PEA are modeled by individual sub-models and these sub-models are then combined together in a certain way to form one model for the PEA. The popularity of the decoupled structure models is due to their flexibility and accuracy. For the control of PEA, schemes based on sliding mode (SM) have

drawn considerable attention since they are highly robust against matched uncertainties in the plant while the aforementioned nonlinear or difficult-to-model effects of PEAs can be treated as matched uncertainties.

The issues associated with these models and control scheme are briefly discussed here, with more details presented in Chapter 2. Firstly, the widely used Preisach hysteresis model fails to represent the one-sided hysteresis behavior of PEAs if driven by non-negative input voltages (which is typical for PEA positioning application). Secondly, there are chattering problem and steady state error problem associated with the existing SM control schemes such as the ideal SM control and the sliding mode control with boundary layer (SMCBL), which is highly undesirable in positioning applications. Thirdly, the SM based control schemes for PEA controls usually involve the feedback of states, which are typically estimated by means of state observers. However, the existing state observers usually do not provide satisfactory performance in such applications or even not applicable since the PEA models do not satisfy the observer matching condition. This research addresses these issues by developing novel models and control schemes for PEAs. Also performed in this research is to develop a model for the PEA-driven stick-slip (PDSS) actuators. The PDSS actuator is one employing a PEA to drive a moveable platform, which in turn drives an end-effector placed on it in a stick-slip style through friction. As such, the end-effector can reach an extended range of displacement while the fine resolution of PEAs is preserved.

1.2 Objectives

The aim of this research work is to carry out a comprehensive study on the modeling and control of one-degree-of-freedom (1-DOF) PEAs. In particular, three specific objectives are set in this research.

The first objective is to develop a model to represent the PDSS actuator, specifically the displacement of its end-effector. Based on the developed model, the effects of different properties of the input voltage (e.g. magnitude and frequency) and the end-effector mass on the PDSS displacement are to be investigated.

The second objective is to develop a novel model for the PEA hysteresis based on the modified Preisach hysteresis operator and on this basis, to integrate the hysteresis model with the models of creep and vibration dynamics to form one model for the PEA performance.

The third objective is to develop novel control schemes based on the PEA model developed in the second objective for the tracking control of PEAs. Specifically, a novel PID-based sliding mode (PIDSM) controller and a novel PIDSM observer will be developed, in which the switching control term in SM control is replaced with a PID regulator; and then they will be integrated to form a new control scheme called PIDSM observer-controller (PIDSMOC) for PEA control.

The above models and control schemes developed in the present research will be experimentally validated on a commercially-available PEA (P-753, Physik Instrumente).

1.3 Organization of the Dissertation

This dissertation is comprised of eight chapters. Besides this chapter, it includes six manuscripts, followed by the conclusions drawn from this research.

Chapter 2 presents a literature review on the modeling and control techniques of PEAs with their advantages and disadvantages discussed.

Chapter 3 describes the modeling of PDSS actuators. In particular, the cascade of a Preisach hysteresis model and a linear second-order system is used to represent the dynamics of the moveable platform. A modified elastoplastic friction model is used to account for the end-effector-mass-dependent friction between the movable platform and the end-effector. Finally, the dynamics of the end-effector is modeled by Newton's second law and its effectiveness is verified experimentally.

Chapter 4 deals with the modeling of the one-sided hysteresis behavior of PEAs. Particularly, a novel hysteresis operator modified from the Preisach hysteresis by adding a second lower saturation value is proposed and on this basis, a rate-independent hysteresis model and a rate-dependent hysteresis model are developed. The effectiveness of the models is verified by comparing the experimental and simulation results. An algorithm for inverting the rate-independent hysteresis model is also developed and open/closed loop control experiments are performed on a PEA to show its effectiveness.

Chapter 5 presents a comprehensive model of PEAs that incorporates the rate-independent hysteresis model developed in Chapter 4 and the models of vibration dynamics and creep.

Comparisons between the experimental and simulation results show the effectiveness of the developed model.

Chapter 6 presents the development of a PIDSM controller for tracking control of PEAs. The PIDSM controller replaces the switching control term in the ideal SM controllers with a PID regulator, such that the chattering problem related to the ideal SM controllers and the steady-state error problem related to the SMCBL schemes can be solved. The stability analysis of the closed-loop system was presented. The effectiveness of the PIDSM controller developed and its superiority over the PID, ideal SM, and SMCBL schemes are verified experimentally.

Chapter 7 presents the development of a PIDSM observer for the PEA state estimation and the integration of the PIDSM controller with the PIDSM observer to form a PDSMOC for tracking control of PEAs. The PIDSM observer replaces the switching term in a conventional SM observer with a PID regulator, such that the resulting observer can be applied to the model of PEAs developed in Chapter 5, which does not satisfy the observer matching condition. The construction of the PDSMOC follows with the stability of the closed-loop system analyzed. The effectiveness of the PIDSM observer and the PIDSMOC, and the superiority of the PIDSMOC over the PIDSM controller with σ-β filter scheme developed in Chapter 6 are verified experimentally.

Chapter 8 presents the conclusions drawn from this research. This is followed by suggestions and recommendations for possible future work.

1.4 Contribution of the Primary Investigator

All papers are co-authored; however it is mutual understanding of the authors that Jingyang Peng, as the first author, is the primary investigator of the research work. The contributions of other authors are limited to an advisory and editorial capacity and they are acknowledged.

2 A Survey of Modeling and Control of Piezoelectric Actuators

2.1 Introduction and Objectives

This manuscript presents a review on the existing modeling and control techniques for PEAs. Particularly, the methods for modeling hysteresis, creep, and vibration dynamics in PEAs are discussed along with the model structures that integrate such models into comprehensive models of PEAs. Discussed are also various control schemes developed for PEAs. This is a critical step in understanding the current challenges in modeling and control of PEAs and establishing the objectives of this research work.

2.2 Justification of the Research

PEAs have been widely used in micro- and nano-positioning applications. In despite of its various advantages, the modeling and control of PEAs has proven to be a challenging task. The related issues concerned in this dissertation are discussed as follows.

There are two issues in the literatures regarding to the modeling of PDSS actuators. One issue is the influence of PEA nonlinearities such as hysteresis on the performance of the piezoelectric-driven stick-slip actuator, which has not been reported in the literature. The second issue is the effect of the end-effector mass on the performance of the stick-slip actuator. The first objective of this dissertation is to address these issues by presenting a comprehensive model representative of the dynamics of a PDSS actuator, especially, the dynamics of the displacement

of the end-effector.

Also, in the literature, the modeling and control methods utilizing the Preisach hysteresis model (one of the most widely used hysteresis model) were shown to be incapable of representing the one-sided hysteresis behavior of PEAs, i.e. the hysteresis behaviors of PEAs when they are subject to unipolar (usually nonnegative) input voltages. Such one-sided hysteresis behavior is characterized by the existence of an initial ascending curve in additional to the hysteresis loops. Such incapability of the Preisach hysteresis model is due to the fact that the Preisach hysteresis operator has only one lower saturation value, making the resultant Preisach hysteresis model incapable of representing the initial ascending curve and the hysteresis loops simultaneously. So, the second objective of this dissertation is to develop hysteresis models which are capable of representing the one-sided hysteresis behavior of PEAs based on the Preisach hysteresis model. And then based on the new hysteresis models, a comprehensive model of PEAs is to be developed. By doing so, the accuracy of the model of PEAs can be greatly improved as the hysteresis being the primary nonlinearity in PEAs. More importantly, based on the developed model of PEAs, one can further develop model-based control schemes for tracking control of PEAs.

Among various model-based tracking control schemes for PEAs, the use of SM-based techniques has shown to be very promising. However, there are two problems with the two most widely used SM-based control schemes, respectively, i.e. the chattering problem related to the ideal SM control and the steady state error related to the SMCBL method. Also, the conventional SM observers were found to be inapplicable to PEAs since the model of PEAs usually dose not

meet the observer matching condition. To address such problems, the third objective of this dissertation is to develop model-based control schemes for tracking control of PEAs, particularly, to develop a PIDSMOC which is composed of a PIDSM controller and a PIDSM observer for state estimation and control of PEAs.

A Survey of Modeling and Control of Piezoelectric Actuators

J. Y. Peng and X. B. Chen

Abstract

Piezoelectric actuators (PEAs) have been widely used in micro- and nanopositioning applications due to their fine resolution, fast responses, and large actuating forces. However, the existence of nonlinearities such as hysteresis makes modeling and control of PEAs challenging. This paper reviews the recent achievements in modeling and control of piezoelectric actuators. Specifically, various methods for modeling linear and nonlinear behaviors of PEAs, including vibration dynamics, hysteresis, and creep, are examined; and the issues involved are identified. In the control of PEAs as applied to positioning, a review of various control schemes of both model-based and non-model-based is presented along with their limitations. The challenges associated with the control problem are also discussed. This paper concludes with the unresolved issues identified in modeling and control of PEAs for future research.

Index Terms - Actuators, piezoelectric devices, servo control.

1 Introduction

Piezoelectric actuators (PEAs) and PEA-driven positioning systems have been widely used in the fields of micro- and nanopositioning such as atomic force microscopes [1-3], adaptive optics [4], computer components [5], machine tools [6], aviation [7], internal combustion engines [8], micromanipulators [9], and synchrotron-based imaging systems [10] due to their high displacement resolution (sub nanometer) and large actuating force (typically a few hundreds of N). PEA-driven positioning systems have also been developed with various configurations, for example, 1-degree-of-freedom (1-DOF) positioning systems with flexure hinge mechanisms [11,12], stick-slip actuators [13], multiple PEAs-driven inchworms [14], or walking actuators [15]; multi-DOF positioning systems with series mechanism [16], parallel mechanism [17], or stick-and-clamping actuators [18]. In all positioning control applications, the hysteresis and creep effects of PEAs have shown to be able to significantly degrade the system performance and even system stability [19]. For improvement, models are desirable to represent these effects and on this basis, tracking controllers can be designed and implemented to achieve desired positioning requirements.

This paper reviews the modeling and control methods of PEAs in micro- and nanopositioning applications and some remaining issues to be solved, and is arranged as follows. Firstly, the working principles and behaviors of PEAs are briefly introduced in Section 2. In Section 3 various models and modeling techniques for PEAs are examined, along with their limitation; and in Section 4 various control schemes for PEAs are reviewed with associated challenges. Section 5 concludes with emerging issues identified in modeling and control of PEAs for future research.

2 Piezoelectric actuators and their behaviors

2.1 Working principles of piezoelectric actuators

PEAs utilize the converse piezoelectric effect of piezoelectric materials to generate displacement and force, i.e. a piece of piezoelectric material will be mechanically strained if subject to an electric field (by placing it into the electric field or applying voltages to its surfaces) [20]. This property is resulted from the microscopic structure of piezoelectric materials as explained in the following. Most piezoelectric materials used in PEAs, e.g. lead zirconate titanate, undergo a structural phase transition as its temperature drops through the so-called Curie temperature, during which their structurally and electrically symmetric cubic unit cells deform into structurally and electrically asymmetric tetragonal unit cells, resulting in spontaneous strain and polarization [21]. Groups of adjoining unit cells with uniformly oriented spontaneous polarization are called Weiss [20] or ferroelectric [21] domains. The directions of spontaneous polarization of different domains thus developed are random, so in this state the piezoelectric materials exhibit no overall piezoelectric behavior. To fabricate PEAs from such piezoelectric materials, they are further exposed to a strong electric field (10^6 to 10^7 V/m) at a temperature just below the Curie temperature, forcing the directions of spontaneous polarization of the domains to align with the electric field. Such alignment can be approximately preserved after the removal of the electric field. This process is referred to as poling [21,20]. After poling, due to the approximate alignment of the spontaneous polarization of the domains, the deformations of the domains in the direction of their respective spontaneous polarization resulting form the application of an voltage to the piece of piezoelectric material (which generates an electric field that either enhance or suppress the spontaneous polarization of the domains, causing their dimension to change in the direction of the spontaneous polarization) can accumulate and causes an overall deformation or displacement. Thus the piece of piezoelectric material now possesses overall piezoelectric property including the converse piezoelectric effect and can be used as a PEA [20].

2.2 Behavior of piezoelectric actuators

In micro- and nanopositioning applications, typical behavior of PEA concerned include hysteresis, creep, and vibration dynamics.

Hysteresis is the nonlinear dependence of a system not only on its current input but also on its past input. In PEAs, hysteresis exists in both the electric field (voltage)-polarization relationship and the electric field (voltage)-strain (deformation or displacement) relationship, with the latter being mostly concerned in micro- and nanopositioning, and it is caused by the nonlinearities in the converse piezoelectric effect of the unit cells and the switching and movement of domain walls [21]. According to [22], the relationship between the actuating force exerted on the PEA and the resulting displacement of the PEA is linear, as such the electric field (voltage)-strain (displacement) hysteresis can also be treated as the result of the voltage-internal actuating force hysteresis.

The strain (deformation or displacement)-electric field (voltage) hysteresis, which is usually also the input-output hysteresis relationship, of a typical PEA is shown in Fig. 1(a). It can be seen in Fig. 1(a) that the hysteresis trajectory of a PEA can be treated as being composed of three types of components: (i) the major loop which is the hysteresis loop that spans the whole input (voltage) range, (ii) the minor loops which are the hysteresis loops that only span portions of the input range, and (iii) the initial ascending curve

which is the input-output trajectory traversed whenever the magnitude of the input applied to the PEA exceeds the maximum magnitude in the input history.

Hysteresis in PEAs occurs in both relatively static operating conditions (i.e. with constant or slow varying input) and dynamic operating conditions (i.e. with fast varying input). If the influence of the rate of change of the input on the hysteresis can be ignored, then the hysteresis is referred to as rate-independent, otherwise rate-dependent. The latter is usually can also be treated as a combined effect of the rate-independent hysteresis and the vibration dynamics (discussed below).

As hysteresis being the major nonlinearity of PEAs and possessing detrimental effects on the positioning accuracy and stability margins of feed-back control systems [23], compensation of hysteresis has always been a major concern in modeling and control of PEAs.

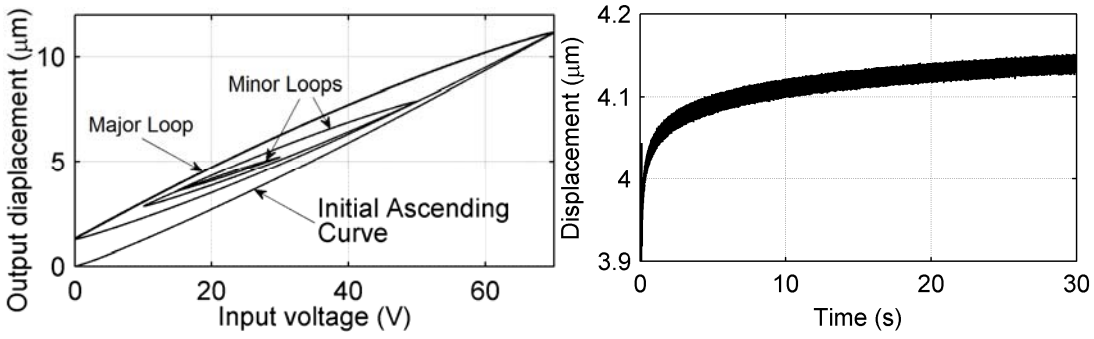

(a) (b)

Fig. 1 (a) Hysteresis of a PEA and (b) Creep of a PEA subject to a 30 V step input.

Creep is the slow variation in the PEA displacement that occurs without any accompanying change in the input voltage [24] as shown in Fig. 1(b). It is caused by the same piezoelectric material properties as PEA hysteresis [20]. Being a slow and a small effect (on the order of 1 % of the last displacement per time decade [20]), creep is sometimes neglected in closed loop and high frequency operations, e.g. in [25,26]. However, for slow and open-loop operations of PEAs, creep must be considered to avoid large positioning error [27].

Finally, PEAs also exhibit linear vibration dynamics, which is the dynamic relationship between the total force exerted on a PEA and the displacement of the PEA, and it resembles a distributed parameter system as the mass of the PEA is not concentrated at certain points [22]. However, if the positioning mechanism attached to the PEA, which is usually much more massive than the PEA, is also taken into account, the resulting overall vibration dynamics will approach that of a lumped parameter system [28].

3 Modeling of piezoelectric actuators

A large number of PEA models have been developed to mathematically represent the behaviors of PEAs mentioned in Section 2.2, and they can be generally classified into macroscopic models, which models a PEA as a whole, microscopic models, which models a PEA as a combination of a series of ferroelectric domains or discretized cells [21,29-39], and hybrid models, which combines the ideas behind these two categories has also been reported in [40]. Due to the requirement of using finite element methods, which is computationally expensive, to obtain the overall PEA behaviors, microscopic models and hybrid

models are not suitable for the use in micro- and nanopositioning applications. As such, the following discussion only concerns macroscopic models.

The linear electromechanical model reported in [41] is an early example of macroscopic PEA models. But it can represent neither the nonlinear behaviors (hysteresis and creep) nor the linear vibration dynamics in PEAs due to its linear and static nature. To solve this, various sub-models have been developed with each representing one or two of the linear/nonlinear behaviors of PEAs mentioned in Section 2.2, and then connected in appropriate manners to form (or used alone as) macroscopic PEA models. These sub-models, the methods of constructing macroscopic PEA models based on such sub-models, and the methods of inverting such sub-models for the use in model-based open-loop feedforward control of PEAs are reviewed as follows.

3.1 Hysteresis sub-models

3.1.1 Models for the major hysteresis loop

At the early stage, hysteresis models were developed only to represent the major loop in the hysteresis trajectories of PEAs (refer to Fig. 1). For example, in [42] polynomials were used to represent the major loop. The Jiles-Atherton hysteresis model, which was initially developed for representing ferromagnetic hysteresis [43] and afterwards adopted for the ferroelectric hysteresis in piezoelectric materials [44], is also limited to represent the major loop [45]. The inability of such models to represent minor loops in the hysteresis curves of PEAs limits their applications.

3.1.2 Rate-independent hysteresis models

To model both the major loops and the minor loops in the hysteresis of PEAs without concerning the influence of the rate of change of the input, in other words, to model the rate-independent hysteresis of PEAs, both existing and newly developed rate-independent hysteresis models have been adopted. Among which the Preisach hysteresis model [46] and its modifications [47-58], the Prandtl-Ishlinskii (PI) hysteresis model [25,59-63], and the Maxwell resistive capacitor (MRC) model [64-67] are among the most widely used. These rate-independent hysteresis models are reviewed as follows.

The Preisach hysteresis model represents the hysteresis by the combined effect of an infinite number of Preisach hysteresis operators $\delta_P(\alpha,\beta,u(t))$, as shown in Fig. 2. Two parameters are used to characterize a Preisach hysteresis operator: the up switching value α and the down switching value β, with $\alpha \geq \beta$. Each operator has two saturation values: 0 and 1, and its contribution to the model output is adjusted by $\mu(\alpha,\beta)$, referred to as the Preisach weighting function. As such, the resulting Preisach hysteresis model is expressed as

$$f(t)^{CPM} = \iint_{\alpha\geq\beta} \mu(\alpha,\beta)\delta_P(\alpha,\beta,u(t))\mathrm{d}\alpha\mathrm{d}\beta \tag{1}$$

where $u(t)$ is the input and $f(t)^{CPM}$ is the output of the hysteretic system [47]. To reduce the computational effort due to the involvement of the double integration, alternative expressions of the Preisach hysteresis model that only involves arithmetic operations have also been derived from Eq. (1) and the properties of the Preisach hysteresis operator [68,69].

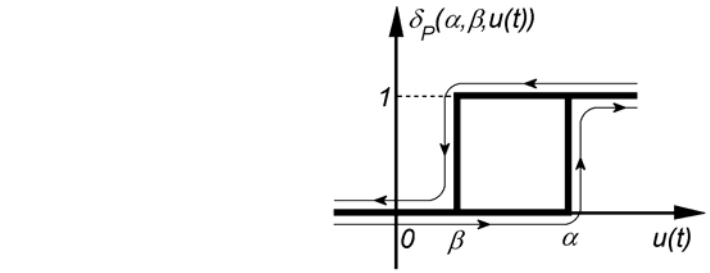

(a)

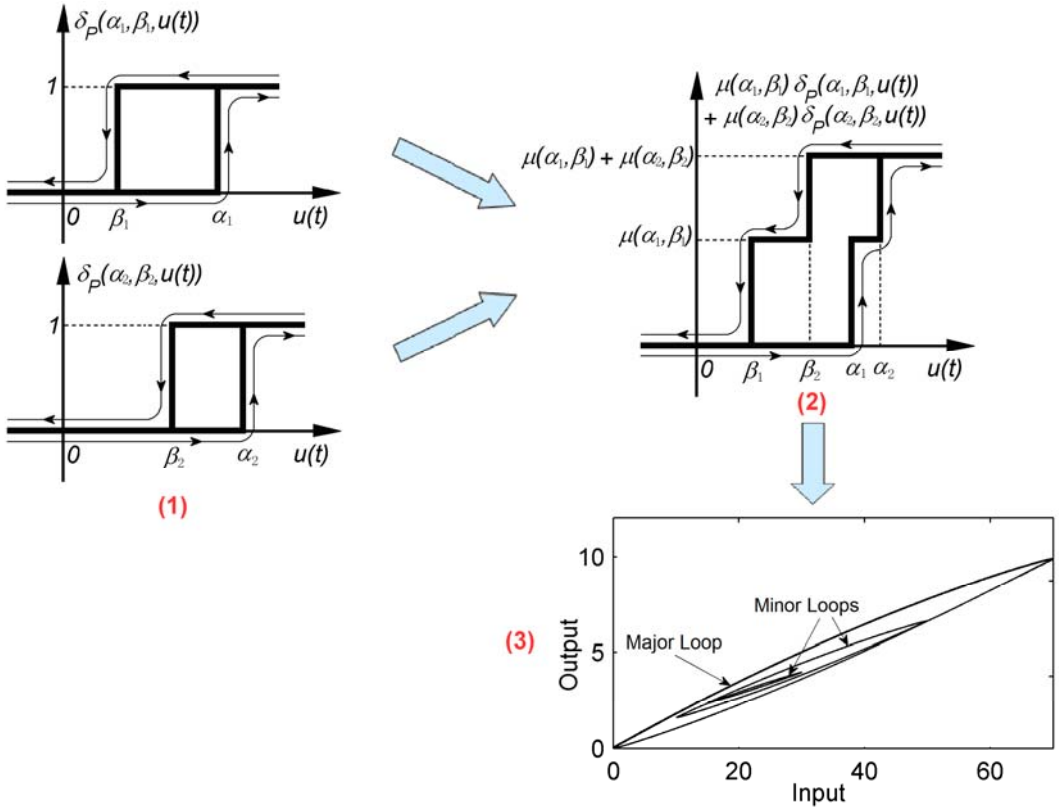

(b)

Fig. 2 (a) Preisach hysteresis operator and (b) working principle of the Preisach hysteresis model: the sum of two hysteresis operators of different switching values as shown in (1) can represent a simple but unsmooth hysteresis loop as shown in (2); by using the sum of an infinite number of hysteresis operators of different switching values, smooth hysteresis loops including both major and minor loops can then be represented as shown in (3).

In PI hysteresis models, hysteresis is represented by the combined effect of a finite number of play or backlash operators as shown in Fig. 3. Following this idea, the expression of a PI hysteresis model involving n play operators is given as

$$f(t)^{PI} = \sum_{i=1}^{n} \delta_{PI}(w_i, r_i, u(t)) \tag{2}$$

where $f(t)^{PI}$ is the model output; i denotes the index of the play operator; w_i and r_i are the weight parameter and the threshold parameter of the *i*-th play operator, respectively.

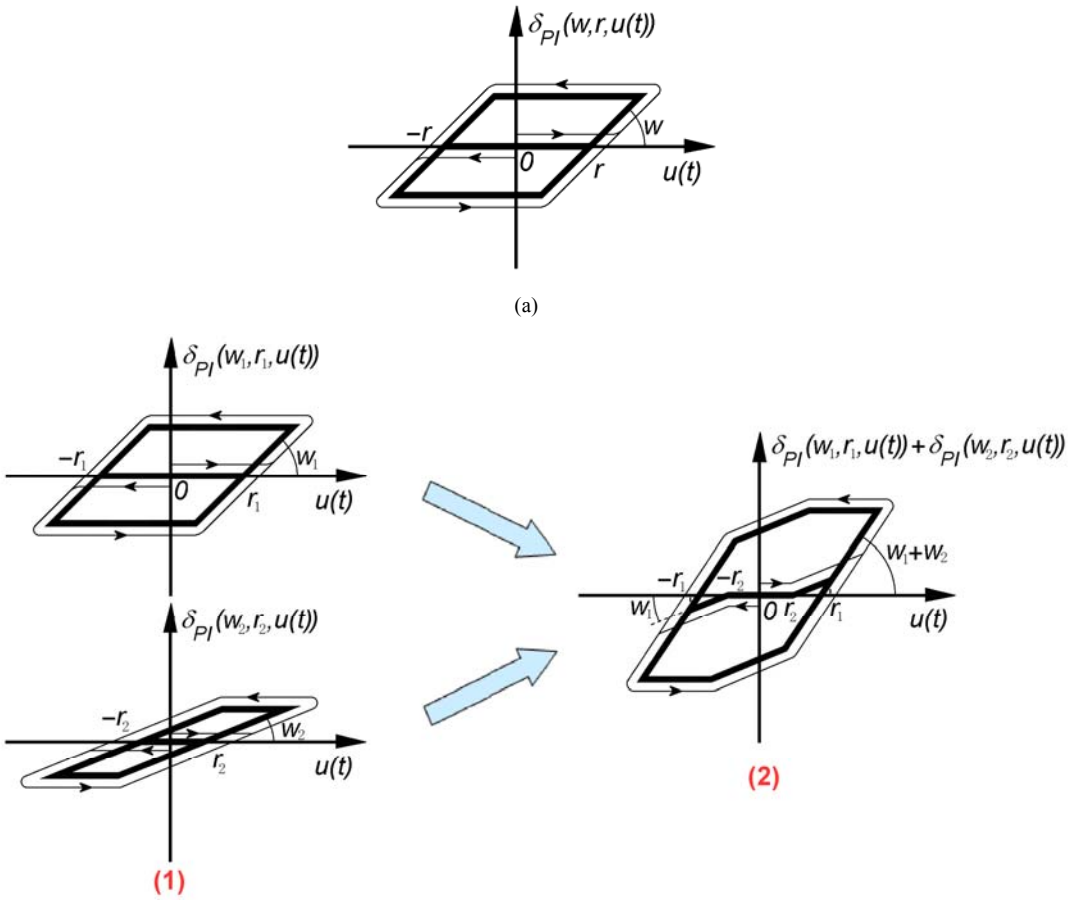

Fig. 3 (a) Play operator and (b) working principle of the PI hysteresis model: the sum of two play operators of different parameters as shown in (1) form a simple PI hysteresis model as shown in (2).

Similar to the PI hysteresis model, the MRC hysteresis model represents the hysteresis by the combined effect of a finite number of elasto-slide elements or operators as shown in Fig. 4 [64]. Each elasto-slide element or operator (Fig. 4(a)(1)) is composed of (i) a mass sliding on a surface with a Coulomb friction μN, where μ is the friction coefficient and N is the normal force between the mass and the surface, and (ii) a spring of stiffness k with one end connected to the mass whilst the displacement of the other end (the free end) $u(t)$ can be freely assigned and use as input to the elasto-slide element. As such, hysteresis relationship exists between the (input) displacement of the free end of the spring $u(t)$ and the resulting force in the spring $F(u(t))$, as can be seen in Fig. 4(a)(2). Connecting n elasto-slide elements as in Fig. 4(b), the resulting MRC hysteresis model or the relationship between the input displacement of the free ends of the springs $u(t)$ and the total force experienced at the free ends of the springs $f(t)^{MRC}$ can be expressed as

$$f(t)^{MRC} = \sum_{i=1}^{n} F_i(u(t)) \tag{3}$$

where $F_i(u(t))$ is the force in the spring of the *i*-th elasto-slide element induced by $u(t)$.

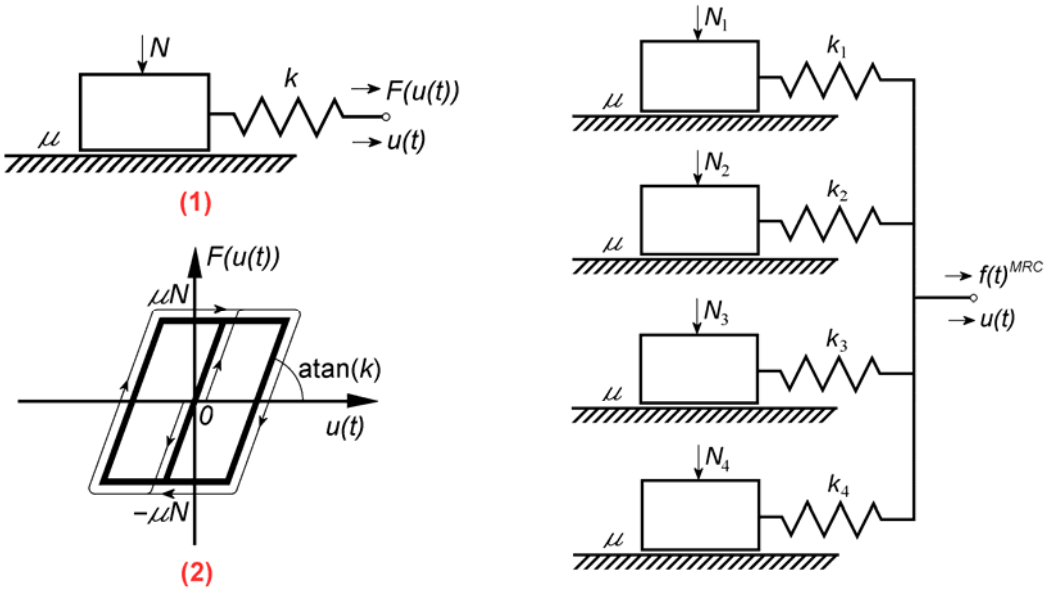

(a) (b)

Fig. 4 (a) An elasto-slide element and its input-output relationship; (b) the physical interpretation of the MRC hysteresis model [63].

3.1.3 Rate-dependent Preisach and PI hysteresis models

The rate-independent hysteresis models discussed in Section 3.1.2 are only capable of representing the hysteretic behavior of a PEA in narrow (a few Hz) frequencies bands. In wide band applications where both hysteresis and vibration dynamics are significant, the rate-independent hysteresis models need either to be combined with vibration dynamics models or to be modified into rate-dependent hysteresis models to represent the behaviors of the PEA. In the literature, both the Preisach hysteresis model and the PI hysteresis model have been modified into rate-dependent hysteresis models.

In the rate-dependent Preisach hysteresis models, the Preisach weighting function $\mu(\alpha,\beta)$ are adjusted to account for the input-rate dependency by using rate-dependent multiplicative modifying factors [70,71] or neural network approaches [69]. In [70], the rate-dependent multiplicative modifying factor for adjusting $\mu(\alpha,\beta)$ is a function of (a) the average voltage input rate between two input extrema and (b) the variation of the voltage between two input extrema. Even though this model can effectively represent the PEA hysteresis up to 800 Hz, it requires the *a priori* knowledge of the input voltage waveform (at least to the next extremum), and thus being not applicable to conventional situations in which the future input voltage is unknown. To avoid this problem, in [71] a multiplicative modifying factor which depends only on the input-rate or the first derivative of the input voltage is used instead. However, the small differences between the input-rate at the input extrema at different input frequencies limits the model accuracy at

higher input frequencies (the model is effective typically below 10 Hz). To achieve better accuracy (error of the model prediction being less than 5% of the maximum displacement of the PEA) in operations involving higher frequencies (~30 Hz), in [69] a neural network with rate-dependent output is used to account for the input-rate dependence of the Preisach weighting function. But the applicable frequency range remains low compared to the resonant frequencies of conventional PEAs (typically over 1 KHz).

Similarly, the rate-dependent PI hysteresis models, which are modified from the PI models by modeling the parameters as functions of the input rate, are also limited to represent low frequency (<30 Hz) PEA operations or the error becomes excessively high (over 10% of the peak-to-peak sinusoidal displacement of the PEA) [25,26].

So, in conventional applications where the *a priori* knowledge of the input voltage is not available, the rate-dependent Preisach and the rate-dependent PI hysteresis models are both limited to represent PEA operations over frequency bands only slightly wider than the applicable frequency bands of the rate-independent models.

3.1.4 Inverse Preisach and PI hysteresis models

Inverse hysteresis models are essential to the model-inversion-based feedforward hysteresis compensation technique for PEAs. The inverses of the two most widely used hysteresis models, i.e. the Preisach hysteresis model and the PI hysteresis model, have been established by employing different methods in the literature.

The Preisach hysteresis model cannot be inversed analytically; hence several methods of approximately inverting the Preisach hysteresis model have been developed instead [72]. Such approximate inverting methods can be classified into two categories.

The first category involves directly identifying the Preisach hysteresis model inversely (using the measured plant output as the input to the Preisach hysteresis model while using the plant input as the output to the Preisach hysteresis model) [1,73,74] or directly identifying the inverses of some intermediate functions that constitute the alternative expressions of the Preisach hysteresis model and then expressing the inverse Preisach hysteresis model based on them [56,72]. The advantage of this category of methods is that the computational effort of the inverse Preisach hysteresis model is the same as the Preisach hysteresis model, not more. However, in applications that also require the Preisach hysteresis model in additional to the inverse one, a different parameter identification procedure has to be performed (assume without using iterative methods) since the former can not be analytically derived from the latter, and the two resulting models are not necessarily accurate inversions of each other due to the different model errors introduced in their respective parameter identification procedures.

The second category involves iterative-algorithms-based methods [72], which find the input to an identified Preisach hysteresis model iteratively until the output of the hysteresis model converges to the desired value. Such methods are developed based on the contraction mapping principle, which are firstly proposed in [75] and [76], and they have been successfully applied to inverse the Preisach hysteresis modeled hysteresis in a magnetostrictive actuator [72] and a PEA [77]. The advantage of such methods is

that both the Preisach hysteresis model and the inverse one can be obtained via a single parameter identification procedure and the inversion can be highly accurate. However, the computational effort involved in the iterative-algorithms-based methods is generally much higher than that of calculating the Preisach hysteresis model output since the Preisach hysteresis model output needs to the calculated in each iteration.

The PI hysteresis model, in the contrary, can be inversed analytically, so good accuracy and low computational effort can be achieved simultaneously, making it much easier to implement than the inverse Preisach hysteresis models. The inversion algorithms for PI hysteresis models can be found, for example, in [63]. In [25,26] the inversion of the rate-dependent PI hysteresis model was also presented. In either case of rate-independent or rate-dependent, the PI hysteresis model inversion algorithms fail if the input frequency is so high that the rounding of the hysteresis loops due to phase lag introduced by other dynamics causes the hysteresis loading and unloading curves to be no longer monotonic. This problem was later solved in [78] by additional mappings to and back from a domain where the inversion of the rate-dependent PI hysteresis model always exists.

3.1.5 Other hysteresis models

Other hysteresis models, such as a first-order nonlinear differential equation model [79] and the Bouc-Wen hysteresis model [80-82] have also been used to model hysteresis in PEAs with promising results [22,83-85]. In [86], a non-linear auto-regressive moving average model with exogenous inputs (NARMAX) was employed to represent the hysteresis of a PEA. In [74] a hysteresis model was developed for PEAs by using a polynomial-based linear mapping strategy. In [87], a hysteresis model based on a new hysteresis operator, which in turn is based on two hyperbola functions, are developed for PEAs along with its inverse model. Such hysteresis models have not seen wide application mainly due to their high complexity but limited improvements on accuracy as compared to other widely used hysteresis models discussed before.

3.2 Creep sub-models

3.2.1 Frequently used creep models

The creep response in a PEA has a logarithmic shape over time, so it is sometimes referred to as the Log(t)-type creep, and the nonlinear creep model given by Eq. (4) has been used to represent such creep behavior [88,89].

$$y(t) = y_0\left[1+\gamma \log_{10}\left(\frac{t}{t_0}\right)\right] \tag{4}$$

where $y(t)$ is the creep model output, y_0 is the creep output at t_0 after the static input voltage is applied, and γ is a coefficient depending on the input voltage. The dependence of γ on the input voltage and the unboundness of such a nonlinear creep model as $t \to 0$ and $t \to +\infty$ pose difficulties in its implementation [19].

To avoid the problem of unboundness encountered in the nonlinear creep model Eq. (4) and to avoid the nonlinearity, a linear creep model was proposed as.

$$G_c(s) = 1 + \sum_{i-1}^{n_c} \frac{1}{c_i s + k_i} \tag{5}$$

where the creep transfer function $G_c(s)$ is represented by the combined effects of n_c spring (k_i) damper (c_i) systems [1,89]. Besides, an operator-based linear creep model was also reported in [60]. However, these linear creep models have linear and memory free equilibrium values, whist the actual equilibrium value of the creep effect of PEA exhibits hysteresis nonlinearity [90].

To further solve the problems encountered in both the nonlinear and linear creep model above, the PI hysteresis model design approach was adopted in [63] to develop an operator-based nonlinear creep model, whose output is a weighted sum of the values of a series of elementary creep operators.

3.2.2 Inverse creep models

Similar to the case of inverse hysteresis models, inverse creep models are essential in feedforward creep compensation.

While the analytic inversion of the nonlinear creep model was not mentioned in the literature, a method of feeding a voltage with an inverse Log(t)-type creep itself to a PEA to compensate for the creep in the output displacement was found to be effective [88].

On the other hand, the inversion of the linear creep model (Eq. (5), not operator-based) is usually carried out together with the inversion of the vibration dynamics model since they can be combined into a single linear dynamics model. An optimal inversion approach, which minimizes a quadratic cost function representing the weighted sum of the input voltage energy and the output displacement error energy [91], can be used to inverse the combined vibration dynamics and creep model in [1]. Linear creep models can also be combined with hysteresis models and then inverted, e.g. via iterative methods [89].

The inversion of the operator-based linear and nonlinear creep models together with other dynamics are reported in [60,63], respectively.

3.3 Vibration dynamics sub-models

3.3.1 Frequently used vibration dynamic models

According to Section 2.2, for the consideration of accuracy, the vibration dynamics of a PEA should be modeled as a distributed linear system for a stand-alone PEA [22]. But for the convenience of practical uses, the vibration dynamics of a PEA and the attached positioning mechanism is often modeled as a whole as a single second-order system, as in [64,28,92,93], whilst higher order linear dynamical systems are only used in applications requiring higher level of accuracy [1]. Such lumped linear vibration dynamics models of PEAs are usually identified through fitting the measured frequency response of the PEA to that of a specific model structure by using a dynamic signal analyzer [1,94]. On the other hand, the axiomatic design method has also been used to find a higher order linear system representation of the vibration dynamics of a PEA with an attached positioning mechanism [95,96].

3.3.2 Inverse vibration dynamic models

Inverse vibration dynamics are usually used in open-loop feedforward control of PEAs, especially in the case of controlling piezoelectric tube actuators as in [1]. Methods for inverting the vibration dynamics

have been reviewed in Section 3.2.2.

3.4 Model Structures

With different sub-models representing hysteresis, creep, and vibration dynamics of PEAs defined, macroscopic PEA models are constructed by connecting such sub-models according to certain model structures. There are two categories of model structures for macroscopic PEA models.

In the first category, the behavior of a PEA, when subject to a voltage input and an external loading force, is decoupled into several effects such as rate-independent hysteresis, vibration dynamics, and creep based on physical laws. Such effects are then represented by individual sub-models and such sub-models are connected in various manners to form a comprehensive model of the PEA.

The most well known model structure of PEAs belonging to this category is the electromechanical model proposed in [64], which is further refined in [22]. Fig. 5 shows the schematic representation of this model.

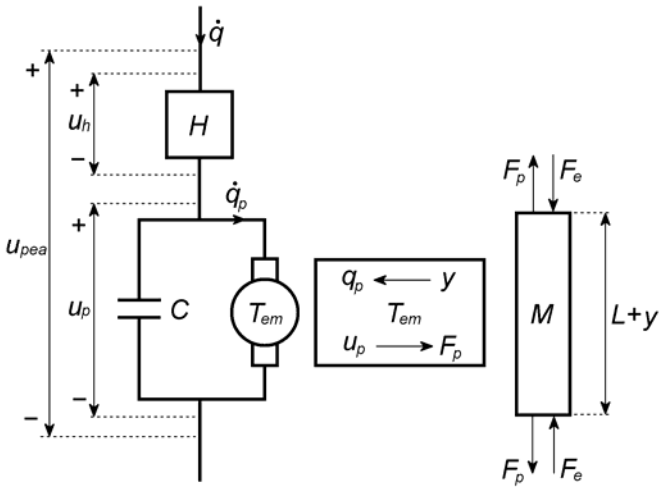

Fig. 5 Schematic representation of a electromechanical model of a PEA [22].

There are 3 effects in Fig.5, namely (i) the hysteresis, H, between the charge in the PEA, q, and the resulting voltage, u_h; (ii) the electromechanical transducer, T_{em}, converts the mechanical deformation of the PEA, y, into charge, q_p (inverse piezoelectric effect), and converts the voltage, u_p, into an actuating force, F_p (piezoelectric effect); and (iii) the vibration dynamics, M, relating the deformation of the PEA, y, to the internal actuating force, F_p, and the external load, F_e. Other symbols in Fig. 5 include u_{pea}, which is the voltage across the PEA, L, which is the original length of the PEA, and C, which is the capacitance of the PEA. The model can then be expressed as

$$u_{pea} = u_h + u_p \tag{6}$$

$$q = H(u_h) \tag{7}$$

$$q = Cu_p + q_p \tag{8}$$

$$q_p = T_{em} y \tag{9}$$

$$F_p = T_{em} u_p \tag{10}$$

$$y = M\left(F_p - F_e\right) \tag{11}$$

The hysteresis effect, H, and the vibration dynamics, M, can be modeled by different kinds of sub-models. Specifically, H is usually represented by rate-independent hysteresis models, e.g. the MRC model was used in [64] whist the first-order nonlinear differential equation model, which was firstly proposed in [79], was employed in [22]. The vibration dynamics, M, can be modeled by any models discussed in Section 2.1.3. It is noted that the use of this electromechanical model usually requires the measurements of the charge, q, in the PEA for model parameter estimation, which is difficult in practice. So this model is usually employed in applications that the relationship between u_{pea} and F_p, which is difficult to identify, can be approximated by a simple function (e.g. an affine function) with an error term as model uncertainties, such as in [92,93]. Also, creep is usually not considered in this electromechanical model [22,79] expect being treated as model uncertainties [92,93].

Another model structure proposed in [1] models the relationship between u_{pea} and F_p by a rate-independent hysteresis model directly, based on a conclusion drawn from the analysis in [64] that the rate-independent hysteresis of a PEA only exists between the input voltage and the resulting internal actuating force. This hysteresis sub-model is then cascaded to a vibration dynamic sub-model and a creep sub-model to form the complete model of a PEA, as shown in Fig. 6. Without the involvement of charge measurement for parameter estimation, this model structure is much easier to apply than the electromechanical model. Similar to the case of the electromechanical model, this model structure is highly flexible that each sub-model can be implemented in various ways, e.g. in [1], the Preisach hysteresis model was used for H and a fourth-order and a third-order linear dynamic systems are used to represent M and the creep effect, G_c, whist in [63], a modified PI hysteresis model is used for H and an operator based model of complex log(*t*)-type creep for G_c. Also, due to the cascading connection between the sub-models, this model structure is very suitable for implementing control schemes with inverse nonlinearity and/or vibration dynamics compensation as in [1,63,94,97,98]. A similar model structure constructed using a bond-graph representation was also presented in [67].

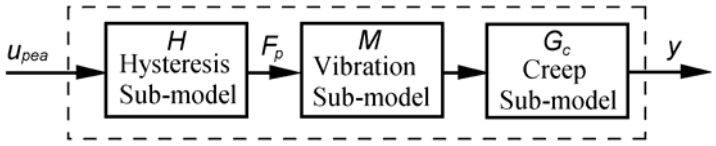

Fig. 6 Model structure of a PEA as in [1].

In the second category, the different behaviors of a PEA are not decoupled. In such cases, rate-dependent hysteresis models such as the rate-dependent Preisach hysteresis model, the rate-dependent PI hysteresis model (Section 3.1.3), and the rate-dependent neural-network-based hysteresis model [99] are used directly as models of the PEA. However, as mentioned in Section 3.1.3, such models are only accurate

over small frequency ranges. And, as can be seen above, creep is usually neglected. These disadvantages seriously limit their usage.

4 Control of PEAs

Over the years, a number of control schemes have been reported for positioning control of PEAs. Due to the detrimental effects of the nonlinearities (especially hysteresis) of PEAs on positioning control performances in terms of positioning error and stability [19], the compensation or rejection of such nonlinear effects has been a major consideration in all of these control schemes. In the following, the typical control schemes for PEAs are reviewed.

4.1 Open-loop control schemes

Open-loop control schemes are usually employed in applications in which position feedback are difficult to implement due to mechanical constraints, e.g. atomic force microscopes [1-3]. In such control schemes, inverse model of the PEA to be controlled is found and then cascaded to the PEA. The methods for finding such inverse models have been reviewed in Sections 3.1.4, 3.2.2, and 3.3.2. The inverse model generates an input voltage u_{pea} to the PEA according to the desired displacement y_d, such that the PEA subject to u_{pea} produces an output displacement of PEA y that follows y_d. Fig. 7 shows a typical open-loop control scheme for PEAs.

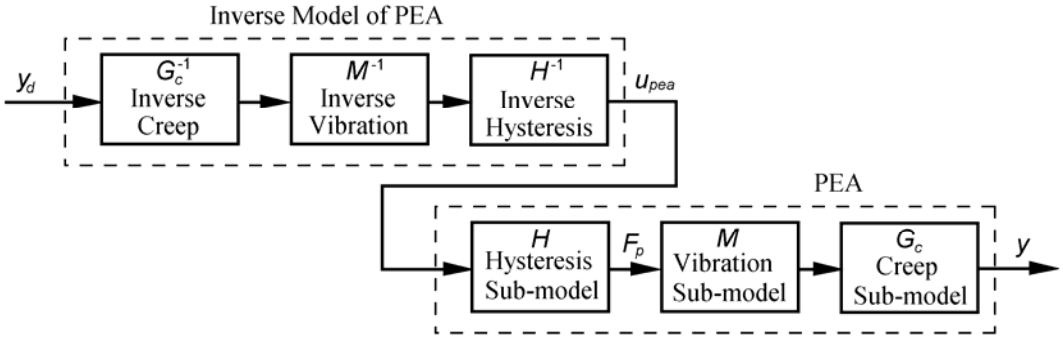

Fig. 7 Open-loop control scheme for PEAs [1].

In some of the open-loop control schemes, all three effects in the PEA shown in Fig. 6 are compensated by the inverse model of PEA to achieve best tracking accuracy (as the case in Fig. 7). For example, in [1,67], inverse models of PEA representing hysteresis, vibration dynamics, and creep are used to compensate these effects; whist in [94] a charge control technique was firstly employed to remove the hysteresis effect and then an inverse model was used to compensate for the linear dynamics.

Other open-loop control schemes only focus on compensating some of the three effects shown in Fig. 6. For example, in [73,74,87,100], only hysteresis was compensated by using the inverses of the Preisach hysteresis model, a hysteresis model developed by using a polynomial-based linear mapping strategy, a hysteresis model developed based on hyperbola-shaped hysteresis operators, and a hysteresis model developed in [101], respectively, since hysteresis is the most significant nonlinearity in PEAs. In [91,102], creep is also compensated in additional to hysteresis by using operator-based inverse creep models and

inverse PI hysteresis models to achieve better tracking performance. However, due to the negligence of the vibration dynamics in these schemes, their performances are only guaranteed in fixed frequency or narrow band operations unless inverse rate-dependent hysteresis models are employed, e.g. the use of inverse rate-dependent PI hysteresis models in [25,26,78]. Nonetheless, the applicable frequency ranges (with acceptable tracking error, e.g. <5% of the maximum displacement of the PEA) of the schemes using inverse rate-dependent hysteresis models are still relatively small (less than 50 Hz) compared with those also inverting the vibration dynamics (up to a few hundreds of Hz) [1,25,78].

In no load condition the open-loop control schemes have been shown to be highly effective in their applicable frequency ranges [1].

However, one major disadvantage of the open-loop control schemes is that their positioning performances are highly sensitive to unknown effects such as model errors, external loads, and changes in the dynamics of the PEA. To partially alleviate the problem, reference [65] proposed to use a disturbance-observer-based scheme in addition to the inverse MRC hysteresis model to compensate for the hysteresis and unknown effects simultaneously. Specifically, the estimated disturbance input to the PEA, which has the same effect as the aforementioned unknown effects on the PEA output, is subtracted from u_{pea}. However, the effectiveness of this scheme was not examined through experiments. In [103], the inverse hysteresis model is updated adaptively to account for the unknown effects. However, the influence of the unknown effects on the PEA output, though largely suppressed, can still be clearly observed in the experiment results. As such, the best solution to this problem remains introducing feedback into the control schemes, which is to be discussed in the following sections.

4.2 Feedback

Feedback control schemes as shown in Fig. 8 lead to strong suppression of the unknown effects including model errors, external loads, and changes in the dynamics of the PEA on the position control performances, hence they are widely used.

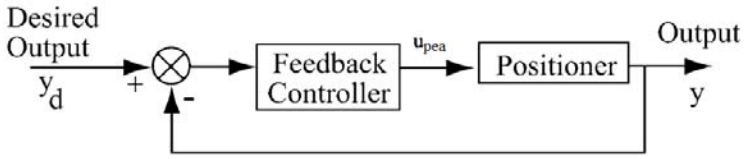

Fig. 8 A feedback control scheme for PEAs [19].

In static or low frequency operations, classical control techniques such as PID control or using multiple integrators for tracking desired displacement profiles are widely used because of their simplicity and capability of eliminating steady state errors in such applications [20,104,105]. Various PID tuning techniques has been reported in PEA positioning control applications, e.g. by trial and error [20], by grey relational analysis [106], using an optimal linear quadratic regulation method [107], by a semi-automatic tuning technique [108], and by an automatic tuning technique [109]. However, in broadband operations with large system uncertainties including modeling errors, nonlinearities, external loads, etc., advanced control techniques are required because PID control is limited in bandwidth while dealing with

uncertainties [110].

Among all of such advanced control techniques, sliding mode control has drawn a lot of attention in the recent years. This is due to the fact that sliding mode controllers can completely reject the effects of the so-call matched uncertainties or uncertainties in the input channel of the plant, resulting in strong robustness [111].

Specifically, in its basic form, the control signal generated by a sliding mode controller can be divided into two parts. The first part is discontinuous, referred to as the switching control, for compensating for the matched uncertainties while driving the plant trajectory to a prescribed geometric entity in the phase space (a space with each dimension corresponding to one state variable in the plant model), referred to as the sliding surface. The second part is continuous, referred to as the equivalent control, for keeping the plant trajectory on the sliding surface after the latter is reached. Since the sliding surface and hence the closed loop system dynamics after reaching the sliding surface can be freely designed, the closed-loop system becomes insensitive to the matched uncertainties after the sliding surface is reached [111]. The major problem of implementing the sliding mode control techniques on PEAs is chattering and the need of the knowledge about the bounds of the matched uncertainties for designing the discontinuous control signal [111], which is to be discussed in more detail in Section 5.2.

Based on the model structure shown in Fig. 6, hysteresis and creep in a PEA can be treated as (matched) uncertainties in the input channels of the vibration dynamics sub-model of the PEA (given that a linear creep model is used). As such, a sliding mode controller can be designed using the vibration dynamics sub-model as a nominal model of the PEA, and the effects of hysteresis and creep on the PEA output displacement can be strongly suppressed without knowing the exact expression of the hysteresis sub-model and the creep sub-model, thus largely reducing the efforts involved in hysteresis and creep modeling and compensation [96,112-115]. Various modifications of the basic sliding mode control technique have also been reported for controlling PEAs for improved performance. For instance, adaptive methods are combined with sliding mode control to remove the requirement of model parameter estimation or lead to better compensation for the nonlinearities as in [116-118]. And in [119] the nonlinearities of the positioning mechanism driven by a PEA in additional to those of the PEA itself were considered in sliding mode controller design.

Robust control techniques constitute another branch of widely used advanced control techniques for positioning control of PEAs. They try to find the control law via optimizing an objective function that incorporates the robustness objective, for example, minimizing the H_∞ norm (in H_∞ control [89,120-123]) or the H_2 norm (in H_2 control [77]) of the transfer functions relating the disturbances to the plant output, thus minimizing the effects of the disturbances on the plant output and enhancing robustness. Robust control techniques can be combined with sliding mode control to suppress unmatched uncertainties (which the sliding mode control techniques cannot compensate for), while sliding mode control are considered to be superior in dealing with matched uncertainties because robust control techniques can only minimize the effects of the matched uncertainties on the plant output whilst sliding mode control techniques can

completely reject such effects in theory [111].

Other advanced control techniques such as state feedback [124], optimal control [110,125], adaptive control [126-129], and neuron network methods [130-132] have also been applied to control PEAs.

Inverse sub-models of the nonlinearities of PEA are sometimes inserted between the feedback controller and the controller in Fig. 8 to linearize the PEA thus facilitating the use of linear feedback controllers. For example, an inverse Preisach hysteresis model is used to cancel out the hysteresis and then a linear H_2 controller is designed based on the remaining linear dynamics of a PEA in [77], while an inverse PI hysteresis model and a sliding mode controller are used in [114].

One problem with the feedback control schemes for PEAs is that the resulting closed-loop systems have low gain margins, which limit the use of high gain controllers. Such low gain margin is largely due to the quick phase loss near the first resonant peak in the frequency response of a PEA [23]. This problem can be alleviated by using a notch filter to reduce the gain around the first resonant peak [20,133,134].

4.3 Feedback with feedforward

Feedforward is sometimes used to augment feedback controllers for nonlinearity compensation. A typical control scheme of this type is shown in Fig. 9. An advantage of this scheme is that the low gain margin problem can be alleviated such that high frequency positioning performances can be improved over the feedback control schemes [125,135,136]. Recent researches adopting this scheme can be found, e.g. in [137] a hysteresis compensator based on the inverse Preisach hysteresis model was used as the feedforward controller to compensate for hysteresis whist a PID feedback controller was used to account for other effects, in [138] a inverse nonlinear differential equation hysteresis model was used as the feedforward controller and a PI controller was used as a feedback controller, and in [16] a inverse extended Coleman-Hodgdon model was used as the feedforward controller and a feedback controller designed via loop shaping techniques was employed.

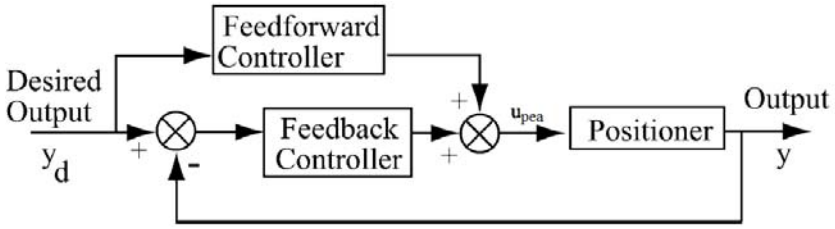

Fig. 9 A feedback augmented with feedforward control scheme for PEAs [19].

Another control scheme involving feedback and inverse model feedforward is shown in Fig. 10 [98,139]. In this scheme, the feedback controller is a high gain controller used for nonlinear effect suppression such that the closed loop system has linear dynamics. Then a feedforward controller, which is the inverse linear dynamics of the closed loop system, is applied to make the output y follow the desired output y_d. This control scheme can be seen as being evolved from the open-loop control scheme shown in Fig. 7. The rationale behind this scheme is that the accurate modeling and inversion of the nonlinear effects such as hysteresis are complicated whist the inversion of a linear plant is relatively easy to compute [140].

However the low gain margin problem with the feedback loop exists in this scheme [19]. Also, similar to the open-loop control schemes, this scheme is sensitive to the disturbances acting outside the closed-loop system.

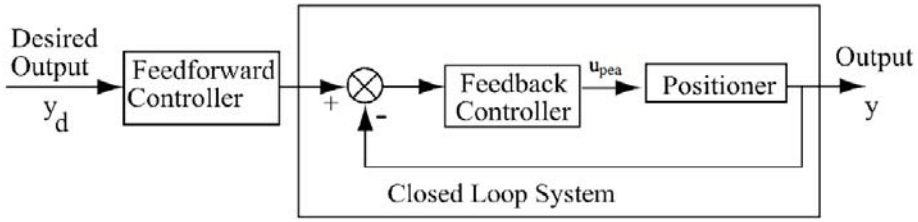

Fig. 10 A feedback controller is used for nonlinear suppression whist a feedforward controller is the inverse model of the closed loop system for canceling out the dynamics of the closed loop system, which can be treated as linear. [19].

4.4 Disturbance observer based schemes

Recently, a technique call disturbance observer is used for the compensation of hysteresis and other nonlinear/uncertain effects in PEAs. In this scheme, a PEA is modeled as a linear dynamic system $G(s)$, so when subject to the same input voltage u_{pea}, the output of the PEA y and that of the corresponding $G(s)$ are different due to hysteresis and other nonlinear/uncertain effects. The disturbance observer utilizes u_{pea} and y to estimate an additional input voltage u_d such that if $u_{pea}+u_d$ is applied to $G(s)$, the output of $G(s)$ is the same as y. u_d is referred to as an input disturbance to $G(s)$ that represents the hysteresis and other nonlinear/uncertain effects. As such, to compensate for hysteresis and other nonlinear/uncertain effects in the PEA, one only needs to subtract u_d from u_{pea} before u_{pea} being applied to the PEA. A control scheme with such a disturbance observer is shown in Fig. 11. This scheme has been shown to be effective in both step [141] and high frequency tracking (200 Hz sinusoidal) [142] operations.

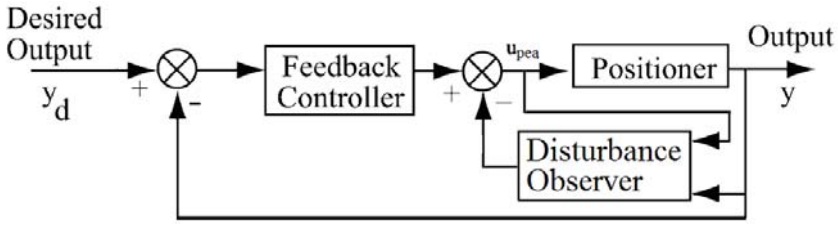

Fig. 11 Augmenting the feedback control loop with a disturbance observer.

5 Emerging issues in PEA modeling and control

Based on the reviews in the previous sections, some emerging issues regarding the modeling and control of PEAs and PEA-driven positioning stages are discussed in this section.

5.1 Modeling issues

5.1.1 Limitations of the existing hysteresis models of PEAs

While the modeling of creep and vibration dynamics of PEAs have been relatively well address, the existing models of hysteresis, especially the rate-independent hysteresis models reviewed in Section 3.1.2, still possess issues, as follows. Though being highly effective in representing both the major hysteresis loops and the minor hysteresis loops, it is noted in the literature [40,53-56,58] that the Preisach hysteresis model cannot at the same time represent the initial ascending curve when the PEA is subject to nonnegative voltage inputs. This is due to the fact that the Preisach hysteresis operator has only two saturation values and without a separate initial section that connects the origin to the hysteresis loop (Fig. 2(a)). The PI hysteresis models and the MRC hysteresis model do not suffer from this problem due to the existence of initial sections in their respective hysteresis operator besides the hysteresis loop (Figs. 3(a) and 4(a)(2)). However, to limit the computational effort, the number of hysteresis operators used in PI or MRC hysteresis models in practice is usually very small (typically around 10) compared to the Preisach hysteresis model (infinity). As a result, the PI and MRC models tend to be less accurate than the Preisach hysteresis model in representing the hysteresis loops, especially in the cases of the small minor loops. So, given a tractable amount of computational effort, there is a contradiction between the capability of representing all hysteresis phenomena, including one-sided hysteresis (the PI and MRC hysteresis models), and the accuracy (Preisach hysteresis models) in the existing rate-independent hysteresis models. This remains an issue to be solved in future research.

5.1.2 Applications of different structures

The applications of PEA-driven positioning systems with structures different from the conventional ones (those can be treated as a mass fixed to one end of the PEA) also pose modeling problems. A typical example is the PEA-driven stick-slip actuator shown in Fig. 12, in which an end-effector is supported and guided by a movable platform that is driven by a PEA, and it works as follows. During the course of slow expansion of the PEA, the end-effector moves along with the platform. If the PEA suddenly contracts, the end-effector slides on the platform because the force due to inertia becomes larger than the friction between the end-effector and the movable platform. As a result, the end-effector moves a step, ΔS, with respect to its original position. Such steps can be accumulated to achieve a theoretically unlimited displacement (actually limited by the size of the moveable platform). The modeling of the dynamics of the end-effector displacement has not been well addressed in the literature. Chang and Li [143] developed a model for the PEA-driven stick-slip actuator without considering the dynamics of the PEA while the friction involved was modeled as Coulomb friction, which is over simplified. By taking into account presliding friction, models were developed and reported in more recent studies on stick-slip actuators, e.g. [144]. However, issues including the influence of PEA nonlinearities and the end-effector mass on the performance of the PEA-driven stick-slip actuator remain to be addressed.

5.2 Control issues

5.2.1 Controller design

As can be seen from Section 4.2, sliding mode control has been one of the most promising techniques for PEA control applications due to their capability to largely suppress hysteresis and creep in practice.

However, there are two remaining problems. One problem of implementing the sliding mode control techniques on PEAs is chattering. This is a kind of high frequency vibration in the plant output displacement induced by the discontinuous control signal generated by a sliding mode controller, and it can induce wear, noises, and even resonance and instability in the plant. Chattering is especially severe in plants with fast responses, such as PEAs, because they cannot filter out the high frequency component in the switching control signal. Another problem is that the bounds of the matched uncertainties need to be known for designing the discontinuous control signal, but such bounds are usually difficult to determine in practice while conservatively setting the bounds to large values only leads to more severe chattering [111]. Existing research efforts have been focused on solving the chattering problem. For example, a method referred to as the sliding mode with boundary layer control was developed by approximating the discontinuous control signal with a continuous one, but with the cost of introducing nonzero steady state error, and chattering is still significant if the bounds of the matched uncertainties are large [111]. Higher order sliding surfaces are also used for chattering suppression, such as the integral sliding mode technique in [93,145] and the PID sliding surface in [116]. However, the second problem remains to be solved.

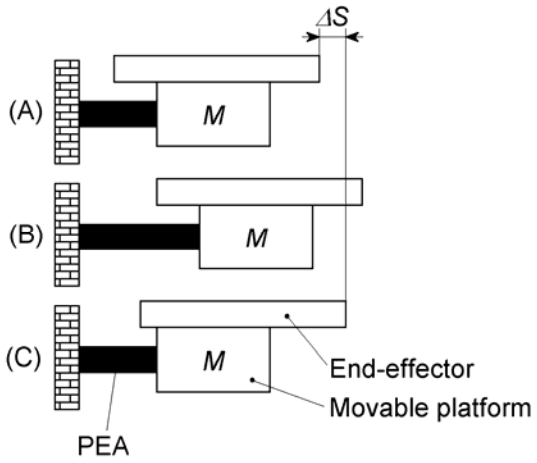

Fig. 12 Actuation sequence of a PEA-driven stick-slip actuator: (A) start, (B) slow expansion and (C) fast contraction.

5.2.2 State estimation

Many advanced control techniques reviewed in Section 4, such as sliding mode control [115], require state feedback. Since usually not all of the states of a PEA model are measurable in application, state observers must be used. However, the problem of estimating the states of PEA models has not been well addressed in the literature, as discussed below.

Currently, many kinds of state observers are applicable to PEA control and they can be classified into two categories: non-model-based and model-based. Non-model-based filters/differentiators, such as the low-pass filter plus ideal differentiator, the α-β filter [146], the high-gain differentiator [147], the integral-chain differentiator [147], and the sliding mode differentiator based on the super-twisting algorithm [148] (given that the states needed are the derivatives of the measured plant output), usually generate large

phase lags if the desired level of noise suppression is enforced (for the first four aforementioned methods) or excessive chattering in noisy systems (for the last method). Compared to non-model-based filters/differentiators, model-based observers, e.g., the extended Kalman filter [149], the unscented Kalman filter [150,151], and the high-gain observer [115], can generate more accurate estimations if the imperfection of the model can be ignored. However, with the presence of uncertainties such as the effects of hysteresis, creep, and external load on a PEA, however, the performances of the model-based observers degrade. For improvement, in the cases that the system uncertainties can be treated as a lumped unknown input to the system model, a kind of model-based observers should be used to estimate the system states even with the presence of the unknown input, which is referred to as unknown input observers (UIOs) in the literature. Many UIOs have been reported in the past three decades, including the full-order UIO [152], the reduced-order UIO [153], the UIO designed based on projection operator [154], and the sliding-mode-based observers (SMOs) [111,154-156].

Applications of these UIOs require that the observer matching condition be satisfied [157,158], which states that the rank of the product of the output matrix and the unknown input matrix in the state space model of the system must be equal to that of the unknown input matrix [111]. However, existing PEA models, such as the one in [93], do not meet this condition. Attempts to relax the observer matching condition have been reported [157,158], but the resultant UIOs were very complicated. As such, a UIO with a simpler structure and the capability of relaxing the observer matching condition still needs to be developed in future research for the use in PEA tracking control.

5.3 Modeling and control of multi-degree-of-freedom (multi-DOF) PEA-driven positioning systems

All of the above discussions have been focused on single-DOF PEA-driven positioning systems. However, there are modeling and control issues uniquely related to multi-DOF PEA-driven positioning systems and they are briefly discussed in this section.

The multi-DOF PEA-driven positioning systems reported in the literature can be divided in to two categories: series mechanisms and parallel mechanisms. Among which, multi-DOF PEA-driven series mechanisms [16] and the xyz-type parallel mechanisms (translations along x-, y- and z-axis) such as those in [16,159-161] can usually be treated as a series of individual 1-DOF PEA-driven mechanisms without significant coupling between the moving axes, as such their modeling and control can be well address with the techniques applied to the single-DOF systems.

The remaining multi-DOF PEA-driven parallel mechanisms whose moving axes are significantly coupled can be further divided into fully-actuated systems, i.e. the number of actuation is the same as the number of DOF [17,115,162-168], and over-actuated systems, i.e. the number of actuation is the more than the number of DOF [20,113].

For the fully-actuated systems, their models are usually established based on the geometric structure of the mechanism and mechanics. Since most of such mechanisms use flexure hinges instead of conventional hinges to avoid friction and backlash [17,115,159,160-167], the modeling of the flexure hinges becomes an important part in modeling such mechanisms [115,161,167]. Two kinds of workflows can be adopted for modeling the multi-DOF PEA-driven positioning systems. For the first kind of workflows, a kinematic model is firstly constructed based on the geometric structure of the mechanism, and then either a phenomenological [115] or physical [161] dynamic model can be established based on the kinematic model. The second kind of workflows involves direct identification of the dynamic model of the mechanism without establishing the kinematic model [16].

Many control schemes that have been applied to control single-DOF PEA-driven positioning systems can also be extended to control fully-actuated PEA-driven positioning systems, e.g. PID control [113,169], H_2 control [169], and sliding mode control [113] since such methods can be easily extended to fully-actuated multi-input-multi-output cases.

Compared to the fully-actuated systems, the over-actuated systems have certain advantages in the performance point of view, e.g. singularity elimination, dexterity improvement, and better load carrying ability [170]. However, the over-actuated structure poses difficulties in both modeling and control. Specifically, the PEAs in the mechanism need to cooperate well or excessive internal forces will occur and may damage the mechanism, whilst the involvement of PEA nonlinearities makes such cooperation difficult to model and control. As a result, very few researches on the modeling and control of over-actuated PEA-driven parallel mechanism have been reported compared to its popularity in macro parallel mechanisms. The only example is [113], in which the modeling and control of a $z\theta_x\theta_y$ 3-DOF positioning system driven by 4 PEAs are concerned. Specifically, in [113] each PEA in the mechanism is modeled and controlled individually and uses only the output displacements of the corresponding PEA as feedback, while the inverse kinematic model of the mechanism is used to generate the desired displacement for each PEA according to the desired position of the end-effector. The cross-axis couplings are considered as disturbances. As such, the control problem is transformed into several 1-DOF control problems, which are much simpler. However, in this scheme the actual position of the end-effector is not closed-loop-controlled,

and the requirement of being able to measure the displacement of each PEA in the mechanism limits the generality of this scheme. As such, more general schemes for modeling and controlling over-actuated multi-DOF PEA-driven positioning systems that can relax the aforementioned requirement are still to be developed in the future.

6 Conclusions

Though possessing fine resolution, high actuating forces, and fast responses, the nonlinear effects make modeling and control of PEAs for the use in micro- and nanopositioning challenging. Researches for solving such problems are abundant, and the resulting typical methods developed are reviewed in this paper, from which some major conclusions can be drawn: (a) the decoupled-structure PEA models have the advantages of being more accurate and flexible as compared to the undecoupled ones; (b) in the decoupled-structure PEA models, the sub-models concerning vibration dynamics and creep have been relatively well addressed in the literature; (c) however, among the existing hysteresis sub-models, for a tractable among of computation efforts, a contradiction between the capability of representing all hysteresis phenomena and maintaining model accuracy remains to be solved; (d) among the control schemes reviewed, the sliding mode control is among the most promising ones as applied to PEA positioning since when designed based on the decoupled-structure PEA models, it can completely reject the hysteresis and creep effects in theory; (e) however, there are still issues associated with sliding mode control (chattering) and the corresponding state estimators (the incompatibility between the observer matching condition and the existing PEA models); finally, (f) the modeling and control of some PEA-driven positioning systems with unconventional structures, e.g. PEA-driven stick-slip actuators and over-actuated multi-DOF PEA-driven positioning systems, are largely untouched in the literature, thus remain to be addressed in future research.

References

[1] D. Croft, G. Shed, and S. Devasia, “Creep, hysteresis, and vibration compensation for piezoactuators: Atomic force microscopy application,” *Journal of Dynamic Systems, Measurement, and Control*, vol. 123, no. 1, pp. 35-43, Mar. 2001.

[2] Q. Zou, K. K. Leang, E. Sadoun, M. J. Reed, and S. Devasia, “Control issues in high-speed AFM for biological applications: Collagen imaging example,” *Asian Journal of Control*, vol. 6, no. 2, pp. 164-178, Jun. 2004.

[3] R. Kassies, K. O.Van derWerf, A. Lenferink, C. N. Hunter, J. D. Olsen, V. Subramaniam, and C. Otto, “Combined AFM and confocal fluorescence microscope for applications in bio-nanotechnology,” *Journal of Microscopy*, vol. 217, pt. 1, pp. 109-116, Jan. 2005.

[4] H. Song, G. Vdovin, R. Fraanje, G. Schitter, and M. Verhaegen, “Extracting hysteresis from nonlinear measurement of wavefront-sensorless adaptive optics system,” *Optics Letters*, vol. 34, no. 1, pp. 61-63, Jan. 2009.

[5] W. Yang, S.-Y. Lee, and B.-J. You, “A piezoelectric actuator with a motion-decoupling amplifier for optical disk drives,” *Smart Materials and Structures*, vol. 19, no. 6, 065027, June 2010.

[6] G. Stöppler and S. Douglas, “Adaptronic gantry machine tool with piezoelectric actuator for active error compensation of structural oscillations at the tool centre point,” *Mechatronics*, vol. 18, no. 8, pp. 426-433, Oct. 2008.

[7] S. R. Viswamurthy, A. K. Rao and R. Ganguli,” Dynamic hysteresis of piezoceramic stack actuators used in helicopter vibration control: experiments and simulations,” *Smart Materials and Structures*, vol. 16, no. 4, pp. 1109-1119, Aug. 2007.

[8] M.S. Senousy, F.X. Li, D. Mumford, M. Gadala, and R.K.N.D. Rajapakse, “Thermo-electro-mechanical performance of piezoelectric stack actuators for fuel injector applications,” *Journal of Intelligent Material Systems and Structures*, vol. 20, no. 4, pp. 387-399, Mar. 2009.

[9] J.-J. Wei, Z.-C. Qiu, J.-D. Han, and Y.-C. Wang, “Experimental comparison research on active vibration control for flexible piezoelectric manipulator using fuzzy controller,” *Journal of Intelligent and Robotic Systems*, vol. 59, no. 1, pp. 31-56, July 2010.

[10] D. Shu, J. Maser, M. Holt, R. Winarski, C. Preissner, A. Smolyanitskiy, B. Lai, S. Vogt, and G. B. Stephenson, “Optomechanical Design of a Hard X-ray Nanoprobe Instrument with nanometer-Scale Active Vibration Control,” *AIP Conference Proceedings*, Vol. 879, pp. 1321-1324, Jan, 2007.

[11] H. Zhou and B. Henson, “Analysis of a diamond-shaped mechanical amplifier for a piezo actuator,” *The International Journal of Advanced Manufacturing Technology*, vol. 32, no. 1-2, pp. 1-7, Feb. 2007.

[12] M. Muraokaa and S. Sanada, “Displacement amplifier for piezoelectric actuator based on honeycomb link mechanism,” *Sensors and Actuators A: Physical*, vol. 157, no. 1, pp. 84-90, Jan. 2010.

[13] Y. Zhang, G. Liu, and J. Hesselbach, “On development of a rotary-linear actuator using piezoelectric translators,” *IEEE/ASME Transactions on Mechatronics*, vol. 11, no. 5, pp. 647-650, Apr. 2006.

[14] J. Li, R. Sedaghati, J. Dargahi and D. Waechter, “Design and development of a new piezoelectric linear Inchworm actuator,” *Mechatronics*, vol. 15, no. 6, pp. 651-681, July 2005.

[15] R. Merry, R. van de Molengraft, and M. Steinbuch, “Modeling of a walking piezo actuator,” *Sensors and Actuators A: Physical*, vol. 162, no. 1, pp. 51-60, July 2010.

[16] R. Merry, M. Uyanik, R. van de Molengraft, R. Koops, M. van Veghel, and M. Steinbuch, “Identification, control and hysteresis compensation of a 3 DOF metrological AFM,” *Asian Journal of Control*, vol. 11, no. 2, pp. 130-143, Mar. 2009.

[17] T.-F. Lu, D. C. Handley, Y. K. Yong, and C. Eales, “A three-DOF compliant micromotion stage with flexure hinges,” *Industrial Robot: An International Journal*, vol. 31 no. 4, pp.355-361, 2004.

[18] S. W. Lee, K.-G. Ahn, and J. Ni, "Development of a piezoelectric multi-axis stage based on stick-and-clamping actuation technology," *Smart Materials and Structures*, vol. 16, no. 6, pp. 2354-2367, Dec. 2007.

[19] S. Devasia, E. Eleftheriou, and S.O.R. Moheimani, "A survey of control issues in nanopositioning," *IEEE Transactions on Control Systems Technology*, vol. 15, no. 5, pp. 802-823, Sept. 2007.

[20] Physik Instrumente, *The World of Nanopositioning and Micropositioning 2005 / 2006*, 2005.

[21] I. Mayergoyz and G.Bertotti (Eds.), *The Science of Hysteresis*, vol. 3. St. Louis: Elsevier, 2005.

[22] H. J. M. T. S. Adriaens, W. L. De Koning, and R. Banning, "Modeling piezoelectric actuators," *IEEE/ASME Transactions on Mechatronics*, vol. 5, no. 4, pp. 331-341, Dec. 2000.

[23] J. A. Main and E. Garcia, "Piezoelectric stack actuators and control system design: Strategies and pitfalls," *Journal of Guidance, Control, and Dynamics*, vol. 20, no. 3, pp. 479-485, May/Jun. 1997.

[24] T. Fett and G. Thun, "Determination of room-temperature tensile creep of PZT," *Journal of Materials Science Letters*, vol. 17, no. 22, pp. 1929-1931, 1998.

[25] W. T. Ang, F. A. Garmón, P. Khosla, and C. N. Riviere, "Modeling rate-dependent hysteresis in piezoelectric actuator", In *Proceedings of the 2003 IEEE/RSJ International Conference on Intelligent Robots and Systems*, pp. 1975 – 1980, 2003.

[26] W. T. Ang, P. K. Khosla, and C. N. Riviere, "Feedforward controller with inverse rate-dependent model for piezoelectric actuators in trajectory-tracking applications," *IEEE/ASME Transactions on Mechatronics*, vol. 12, no. 2, pp. 134-142, Apr. 2007.

[27] R. S. Robinson, "Interactive computer correction of piezoelectric creep in scanning tunneling microscopy images," *Journal of Computer-Assisted Microscopy*, vol. 2, no. 1, pp. 53-58, 1996.

[28] X. B. Chen, Q. Zhang, D. Kang, and W. Zhang, "On the dynamics of piezoactuated positioning systems" *Review of Scientific Instruments*, vol. 79, pp. 116101-1 to 116101-3, 2008.

[29] W. Chen and C. S. Lynch, "A micro-electro-mechanical model for polarization switching of ferroelectric materials," *Acta Materialia*, vol. 46, no. 15, pp. 5305-5311, Sept. 1998.

[30] W. Seemann, A. Arockiarajan, and B. Delibas, "Modeling and simulation of piezoceramic materials using micromechanical approach," In: *European Congress on Computaional Methods in Applied Sciences and Engineering (ECCOMAS)*, Jyväskylä, Finland, 2004.

[31] A. Arockiarajan, B. Delibas, A. Menzel, and W. Seemann, "Studies on nonlinear electromechanical behavior of piezoelectric materials using finite element modeling," In: *IWPMA 2005, 2nd International Workshop on Piezoelectric Materials and Applications in Actuators, Heinz Nixdorf Institute*, Paderborn, Germany, 2005.

[32] B. Delibas, A. Arockiarajan, and W. Seemann, "Intergranular effects on domain switchings in polycrystalline piezoceramics," In: *IWPMA 2005, 2nd International Workshop on Piezoelectric*

Materials and Applications in Actuators, Heinz Nixdorf Institute, Paderborn, Germany, 2005.

[33] M. Kamlah and Q. Jiang, "A constitutive model for ferroelectric PZT ceramics under uniaxial loading," *Smart Materials and Structures*, vol. 8, no. 4, pp. 441-459, Aug. 1999.

[34] M. Kamlah and C. Tsakmakis, "Phenomenological modeling of the non-linear electro-mechanical coupling in ferroelectrics," *International Journal of Solids and Structures*, vol. 36, no. 5, pp. 669–695, Feb. 1999.

[35] M. Kamlah and U. Böhle, "Finite element analysis of piezoceramic components taking into account ferroelectric hysteresis behavior," *International Journal of Solids and Structures*, vol. 38, no. 4, pp. 605-633, Jan. 2001.

[36] C. M. Landis, J. Wang, and J. Sheng, "Microelectromechanical determination of the possible remanent strain and polarization states in polycrystalline ferroelectrics and the implications for phenomenological constitutive theories," *Journal of Intelligent Material Systems and Structures*, vol. 15, no. 7, pp. 513-525, July 2004.

[37] J. Schröder and H. Romanowski, "A simple coordinate invariant thermodynamic consistent model for nonlinear electro-mechanical coupled ferroelectrica," In: *European Congress on Computaional Methods in Applied Sciences and Engineering (ECCOMAS)*, Jyväskylä, Finland, 2004.

[38] J. Schröder and H. Romanowski, "A thermodynamically consistent mesoscopic model for transversely isotropic ferroelectric ceramics in a coordinate-invariant setting," *Achive of Applied Mechanics*, vol. 74, no. 11-12, pp. 863-877, Nov. 2005.

[39] S. Klinkel, "A thermodynamic consistent 1D model for ferroelastic and ferroelectric hysteresis effects in piezoceramics," *Communications in Numerical Methods in Engineering*, vol. 22, no. 7, pp. 727–739, July 2006.

[40] T. Hegewald, B. Kaltenbacher, M. Kaltenbacher, and R. Lerch, "Efficient modeling of ferroelectric behavior for the analysis of piezoceramic actuators," *Journal of Intelligent Material Systems and Structures*, vol. 19, no. 10, pp. 1117-1129, Oct. 2008.

[41] IEEE *Standard on Piezoelectricity*, ANSI/IEEE Std. 976-987, 1988

[42] P. G. Harper, "Kinematic theory of piezoelectric hysteresis," *Journal of Applied Physics*, vol. 52, no. 11, pp. 6851-6855, Nov. 1981.

[43] D. C. Jiles and D. L. Atherton, "Theory of the magnetisation process in ferromagnets and its application to the magnetomechanical effect," *Journal of Physics D: Applied Physics*, vol. 17, no. 6, pp. 1265-1281, June 1984.

[44] R.C. Smith, and C.L. Hom, " Domain wall model for ferroelectric hysteresis," *Technical Report CRSC-TR99-07*, Center for Research in Scientific Computation, 1999.

[45] T. Hegewald, M. Kaltenbacher, and R. Lerch, "Characterization and modeling of piezoelectric stack actuators," In: *IWPMA 2005, 2nd International Workshop on Piezoelectric Materials and*

Applications in Actuators, Proceedings, Heinz Nixdorf Institute, Paderborn, Germany, pp. 99-106, 2005.

[46] E. Preisach, "Über die magnetische Nachwirkung," *Zeitschrift für Physik A Hadrons and Nuclei*, vol. 94, no. 5-6, pp. 277-302, May 1935.

[47] I. D. Mayergoyz, "Mathematical models of hysteresis," *Physical Review Letters*, vol. 56, no. 15, pp. 1518-1521, Apr. 1986.

[48] I. D. Mayergoyz and G. Friedman, "Generalized Preisach model of hysteresis," *IEEE Transactions on Magnetics*, vol. 24, no. 1, pp. 212-217, Jan. 1988.

[49] P. Hejda, T. Zelinka, "Generalized Preisach model of hysteresis - theory and experiment," *Czechoslovak Journal of Physics*, vol. 40, no. 1, pp. 57-68, Jan. 1990.

[50] M.-J. Jang, C.-L. Chen, and J.-R. Lee, "Modeling and control of a piezoelectric actuator driven system with asymmetric hysteresis," *Journal of the Franklin Institute*, vol. 346, no. 1, pp. 17-32, Feb. 2009.

[51] P.N. Sreeram, G. Salvady, and N. G. Naganathan, "Hysteresis prediction for a piezoceramic material system," In: *The ASME Winter Annual Meeting*, vol. 35, ASME, New Orleans, Louisiana, 1993.

[52] D. C. Hughes, and J. T. Wen, "Preisach modeling and compensation for smart material hysteresis,'' In: *Proceedings of SPIE 2427*: pp. 50-64.1995.

[53] P. Ge, and M. Jouaneh, "Generalized Preisach model for hysteresis nonlinearity of piezoceramic actuators," *Precision Engineering*, vol. 20, no. 2, pp. 99-111, Mar. 1997.

[54] H. Hu, R. Ben Mrad, "On the classical Preisach model for hysteresis in piezoceramic actuators," *Mechatronics*, vol. 13, no. 2, pp. 85-94, Mar. 2002.

[55] G. Robert, D. Damjanovic, and N. Setter, "Preisach modeling of piezoelectric nonlinearity in ferroelectric ceramics," *Journal of Applied Physics*, vol. 89, no. 9, pp. 5067-5074, May 2001.

[56] G. Song, J. Zhao, X. Zhou, and J.A. De Abreu-Garcia, "Tracking control of a piezoceramic actuator with hysteresis compensation using inverse Preisach model," *IEEE/ASME Transactions on Mechatronics*, vol. 10, no. 2, pp. 198-209, Apr. 2005.

[57] X. Zhao and Y. Tan, "Neural network based identification of Preisach-type hysteresis in piezoelectric actuator using hysteretic operator," *Sensors and Actuators A: Physical*, vol. 126, no. 2, pp. 306-311, Feb. 2006.

[58] X. Zhao and Y. Tan, "Modeling hysteresis in piezo actuator based on neural networks," *Advances in Computation and Intelligence, Lecture Notes in Computer Science, 2008*, vol. 5370/2008, pp. 290-296, 2008.

[59] K. Kuhnen and H. Janocha, "Adaptive inverse control of piezoelectric actuators with hysteresis operators," In *Proceedings of European Control Conference (ECC)*, Karsruhe, Germany, paper F

0291, 1999.

[60] P. Krejci and K. Kuhnen, “Inverse control of systems with hysteresis and creep,” *IEE Proceedings - Control Theory and Applications*, vol. 148, no. 3, pp. 185-192, May 2001.

[61] K. Kuhnen and H. Janocha, “Complex hysteresis modeling of a broad class of hysteretic nonlinearities,” In *Proceedings of the 8th international conference on New Actuators*, Bremen, Germany, pp. 688-691, June 2002.

[62] K. Kuhnen and F. Previdi, “Modeling, identification and compensation of complex hysteretic nonlinearities: A modified Prandtl-Ishlinskii approach,” *European Journal of Control*, vol. 9, no. 4, pp. 407-421, 2003.

[63] K. Kuhnen, “Modeling, Identification and Compensation of complex hysteretic Nonlinearities and Log(*t*)-type Creep Dynamics,” *Control and Intelligent System*, vol. 33, no. 2, pp. 134-147, 2005.

[64] M. Goldfarb and N. Celanovic, “Modeling piezoelectric stack actuators for control of micromanipulation,” *IEEE Control Systems Magazine*, vol. 17, no. 3, pp. 69-79, June 1997.

[65] S.-H. Lee, T. J. Royston, and G. Friedman, “Modeling and compensation of hysteresis in piezoceramic transducers for vibration control,” *Journal of Intelligent Material Systems and Structures*, vol. 11, no. 10, pp. 781-790, Oct. 2000.

[66] T.-J. Yeh, S.-W. Lu, and T.-Y. Wu, “Modeling and identification of hysteresis in piezoelectric actuators,” *Journal of Dynamic Systems, Measurement, and Control*, vol. 128, no. 2, pp. 189-196, June 2006.

[67] T.-J. Yeh, R.-F. Hung, and S.-W. Lu, “An integrated physical model that characterizes creep and hysteresis in piezoelectric actuators,” *Simulation Modelling Practice and Theory*, vol. 16, no. 1, pp. 93-110, Jan. 2008.

[68] R. B. Mrad and H. Hu, “A model for voltage to displacement dynamics in piezoceramic actuators subject to dynamic voltage excitations,” *IEEE/ASME Transactions on Mechatronics*, vol. 7, no. 4, pp. 479-489, Dec. 2002.

[69] D. Song and C. J. Li, “Modeling of piezo actuator’s nonlinear and frequency dependent dynamics,” *Mechatronics*, vol. 9, no. 4, pp. 391-410, June 1999.

[70] R. Ben Mrad and H. Hu, “A model for voltage-to-displacement dynamics in piezoceramic actuators subject to dynamic-voltage excitations,” *IEEE/ASME Transactions on Mechatronics*, vol.7, no, 4, pp, 479-489, Dec. 2002.

[71] Y. Yu, Z. Xiaob, N. G. Naganathan, and R. V. Dukkipati, “Dynamic Preisach modeling of hysteresis for the piezoceramic actuator system,” *Mechanism and Machine Theory*, vol. 37, no. 1, pp. 75-89, Jan. 2002.

[72] X. Tan, R. Venkataraman, and P. S. Krishnaprasad, “Control of hysteresis: theory and experimental results,” *Pentagon Technical report A687934*, 2001.

[73] H. Hu and R. Ben Mrad, "A discrete-time compensation algorithm for hysteresis in piezoceramic actuators," *Mechanical Systems and Signal Processing*, vol. 18, no. 1, pp. 169-185, Jan. 2004.

[74] S. Bashash and N. Jalili, "A polynomial-based linear mapping strategy for feedforward compensation of hysteresis in piezoelectric actuators," *Journal of Dynamic Systems, Measurement, and Control*, vol. 130, no. 3, 031008, May 2008.

[75] R. Venkataraman and P. S. Krishnaprasad, "Novel algorithm for the inversion of the Preisach operator smart structures and materials," In *Mathematics and Control in Smart Structures*, Vasundara V. Varadan, Editors, pp. 404-414, June 2000.

[76] R. Venkataraman and P. S. Krishnaprasad, "Approximate inversion of hysteresis: theory and numerical results," In *IEEE Conference on Decision and Control (December 2000)*, pp. 4448-4454, Dec. 2000.

[77] J. Y. Peng and X. B. Chen, "H_2-optimal digital control of piezoelectric actuators," In *Proceedings of the 8th World Congress on Intelligent Control and Automation, WCICA-2010*, Jinan, China, pp. 3684-3690, July 2010.

[78] U-X. Tan, W. T. Latt, C. Y. Shee, C.N. Riviere, and W. T. Ang, "Feedforward controller of ill-conditioned hysteresis using singularity-free Prandtl–Ishlinskii model," *IEEE/ASME Transactions on Mechatronics*, vol. 14, no. 5, pp. 598-605, Oct. 2009.

[79] B. D. Coleman and M. L. Hodgdon, "A constitutive relation for rate-independent hysteresis in ferromagnetically soft materials," *International Journal of Engineering Science*, vol. 24, no. 6, pp. 897-919, 1986.

[80] R. Bouc, "Forced vibrations of a mechanical system with hysteresis," In *Proceedings of the Fourth Conference on Non-linear Oscillations*, Prague, 1967.

[81] Y.-K. Wen, "Method of random vibration of hysteretic systems," *Journal of the Engineering Mechanics Division*, vol. 102, no. 2, pp. 249-263, Mar./Apr. 1976.

[82] M. Ismail, F. Ikhouane, and J. Rodellar, "The hysteresis Bouc-Wen model, a survey," *Archives of Computational Methods in Engineering*, vol. 16, no. 2, pp. 161-188, 2009.

[83] O. Gomis-Bellmunt, F. Ikhouane, and D. Montesinos-Miracle, "Control of Bouc-Wen hysteretic systems: Application to a piezoelectric actuator 2008," In *the 13th Power Electronics and Motion Control Conference, 2008. EPE-PEMC 2008*, Poznan, Poland, Sept. 2008.

[84] M. Rakotondrabe, "Bouc–Wen modeling and inverse multiplicative structure to compensate hysteresis nonlinearity in piezoelectric actuators," *IEEE Transactions on Automation Science and Engineering*, accepted for publication, 2010.

[85] D. H. Wang, W. Zhu, Q. Yang, "Linearization of stack piezoelectric ceramic actuators based on Bouc-Wen model," *Journal of Intelligent Material Systems and Structures*, accepted for publication, 2010.

[86] L. Deng and Y. Tan, "Modeling hysteresis in piezoelectric actuators using NARMAX models," *Sensors and Actuators A: Physical*, vol. 149, no. 1, pp. 106-112, Jan. 2009.

[87] A. Badel, J. Qiu, T. Nakano, "A new simple asymmetric hysteresis operator and its application to inverse control of piezoelectric actuators," *IEEE Transactions on Ultrasonics, Ferroelectrics and Frequency Control*, vol. 55, no. 5, pp. 1086-1094, May. 2008.

[88] H. Jung, J. Y. Shim, and D. Gweon, "New open-loop actuating method of piezoelectric actuators for removing hysteresis and creep," *Review of Scientific Instruments*, vol. 71, no. 9, pp. 3436-3440, Sept. 2000.

[89] K. Kuhnen and H, Janocha, "Compensation of creep and hysteresis effects of piezoelectric actuators with inverse systems," In *6th International Conference on New actuators, Actuator'98*, Bremen Germany, pp. 309-312, 1998.

[90] H. Janocha and K. Kuhnen, "Real-time compensation of hysteresis and creep in piezoelectric actuators," *Sensors Actuators A*, vol. 79, pp. 83-89, 2000.

[91] J. S. Dewey, K. Leang, and S. Devasia, ''Experimental and theoretical results in output-trajectory redesign for flexible structures," *Journal of Dynamic Systems, Measurement, and Control*, vol. 120, no. 4, pp. 456-461, Dec. 1998.

[92] K. S. Abidi and A. Şabanoviç, "Sliding mode control for high-precision motion of a piezostage," *IEEE Transactions on Industrial Electronics*, vol. 54, no. 1, pp. 629-637, 2007.

[93] H. C. Liaw, B. Shirinzadeh, and J. Smith, "Enhanced sliding mode motion tracking control of piezoelectric actuators," *Sensors and Actuators A: Physical*, vol. 138, no. 1, pp. 194-202, July 2007.

[94] G.. M. Clayton, S. Tien, A. J. Fleming, S. O. R. Moheimani, and S. Devasia, "Inverse-feedforward of charge-controlled piezopositioners," *Mechatronics*, vol. 18, no. 5-6, pp. 273-281, June 2008.

[95] J. W. Li, X. B. Chen, and W. J. Zhang, "A new approach to modeling system dynamics - in the case of a piezoelectric actuator with a host system," *IEEE/ASME Transactions on Mechatronics*, vol. 15, no. 3, pp. 371-380, June 2010.

[96] J. W. Li, X. B. Chen, and W. J. Zhang, "Axiomatic-design-theory-based approach to modeling linear high order system dynamics," *IEEE/ASME Transactions on Mechatronics*, vol. 16, no. 2, pp. 341-350, Apr. 2011.

[97] K. Kuhnen, H. Janocha, D. Thull, and A. Kugi, "A new drive concept for high-speed positioning of piezoelectric actuators," In *Proceedings of the 10th International Conference on New Actuators*, pp. 82, 2006.

[98] K. K. Leang and S. Devasia, "Feedback-linearized inverse feedforward for creep, hysteresis, and vibration compensation in AFM piezoactuators," *IEEE Transactions on Control Systems Technology*, vol. 15, no. 5, pp. 927-935, Sept, 2007.

[99] X. Dang and Y. Tan, "An inner product-based dynamic neural network hysteresis model for

piezoceramic actuators," *Sensors and Actuators A: Physical*, vol. 121, no. 2, pp. 535-542, June 2005.

[100] C. Ru, L. Chen, B. Shao, W. Rong, and L. Sun, "A hysteresis compensation method of piezoelectric actuator: Model, identification and control," *Control Engineering Practice*, vol. 17, no. 9, pp. 1107-1114, Sept. 2009.

[101] L. Sun, C. Ru, W. Rong, L. Chen, and M. Kong, "Tracking control of piezoelectric actuator based on a new mathematical model," *Journal of Micromechanics and Microengineering*, vol. 14, no. 11, pp. 1439-1444, Nov. 2004.

[102] C. Ru and L. Sun, "Hysteresis and creep compensation for piezoelectric actuator in open-loop operation," *Sensors and Actuators A: Physical*, vol. 122, no. 1, pp. 124-130, July 2005.

[103] H. H. Najafabadi, S. M. Rezaei, S. S. Ghidary, M. Zareinejad, K. Razi, and R. Seifabadi, "Hysteresis compensation of piezoelectric actuators under dynamic load condition," In: *IEEE/RSJ International Conference on Intelligent Robots and Systems, 2007. IROS 2007*, San Diego, USA, pp. 1166-1171, Oct. 2007.

[104] E. Kouno, "A fast response piezoelectric actuator for servo correction of systematic errors in precision machining," *CIRP Annals-Manufacturing Technology* vol. 33, no. 1, pp. 369-372, 1982.

[105] J. F. Cuttino, A. C. Miller, and D. E. Schinstock, "Performance optimization of a fast tool servo for single-point diamond turning machines," *IEEE/ASME Transactions on Mechatronics*, vol. 4, no. 2, pp. 169–179, June 1991.

[106] J. Lin, H. Chiang, and C. C. Lin, "Tunnung PID control gains for micro piezo-stage in using grey relational analysis," in: *2008 International Conference on Machine Learning and Cybernetics*, Kunming, China. pp. 3863-3868, July 2008.

[107] H.-J. Shieh, Y.-J. Chiu, and Y.-T. Chen, "Optimal PID Control System of a Piezoelectric Microospitioner," In: 2008 *IEEE/SICE International Symposium on System Integration*, Nagoya, Japan. pp. 1-5, Dec. 2008.

[108] D. Y. Abramovitch, S. Hoen, and R. Workman, "Semi-automatic tuning of PID gains for atomic force microscopes," *Asian Journal of Control*, vol. 11, no. 2, pp. 188–195, Mar. 2009.

[109] K. K. Tan, T. H. Lee, and H. X. Zhou, "Micro-positioning of linear-piezoelectric motors based on a learning nonlinear PID controller," *IEEE/ASME Transactions on Mechatronics*, vol. 6, no. 4, pp. 428-436, Dec. 2001.

[110] W. S. Oates, and R. C. Smith, "Nonlinear Control Design for a Piezoelectric-Driven Nanopositioning Stage," *Pentagon Technical report A591444*, 2005.

[111] C. Edwards and S. K. Spurgeon, *Sliding mode control: theory and applications*, Taylor & Francis, Abingdon, UK, 1998.

[112] P.-K. Huang, P.-H. Shieh, F.-J. Lin, and H.-J. Shieh, "Sliding-mode control for a two-dimensional piezo-positioning stage," *Control Theory & Applications, IET*, vol. 1, no. 4, pp. 1104-1113, Juny,

2007.

[113] J.-C. Shen, W.-Y. Jywe1, C.-H. Liu, Y.-T. Jian, and J. Yang, “Sliding-mode control of a three-degrees-of-freedom nanopositioner,” *Asian Journal of Control*, vol. 10, no. 3, pp. 267-276, May 2008.

[114] J.-C. Shen, J.-C. Shen, H.-K. Chiang, and Y.-L. Shu, “Precision tracking control of a piezoelectric-actuated system,” *Precision Engineering*, vol. 32, no. 2, pp. 71-78, Apr. 2008.

[115] Q. Xu and Y. Li, “Dynamics modeling and sliding mode control of an XY micropositioning stage,” In: *the 9th International Symposium on Robot Control (SYROCO'09), The International Federation of Automatic Control*, Gifu, Japan, Sept. 2009.

[116] Y. Li, Q. Xu, “Adaptive Sliding Mode Control With Perturbation Estimation and PID Sliding Surface for Motion Tracking of a Piezo-Driven Micromanipulator,” *IEEE Transactions on Control Systems Technology*, vol. 18, no. 4, pp. 798-810, July 2010.

[117] H. C. Liaw, B. Shirinzadeh, and J. Smith, “Sliding-Mode Enhanced Adaptive Motion Tracking Control of Piezoelectric Actuation Systems for Micro/Nano Manipulation,” *IEEE Transactions on Control Systems Technology*, vol. 16, no. 4, pp. 826-833, July 2008.

[118] X. Chen and T. Hisayama, “Adaptive Sliding-Mode Position Control for Piezo-Actuated Stage,” *IEEE Transactions on Industrial Electronics*, vol. 55, no. 11, pp. 3927-3934, Nov. 2008.

[119] H. C. Liaw, B. Shirinzadeh, “Enhanced sliding-mode constrained motion tracking control of piezo-actuated flexure-based mechanisms,” In: *IEEE/ASME International Conference on Advanced Intelligent Mechatronics, 2009. AIM 2009*, Singapore. pp. 1879-1884, July 2009.

[120] G. Schitter, P. Menold, H. F. Knapp, F. Allgower, and A. Stemmer, “High performance feedback for fast scanning atomic force microscopes,” *Review of Scientific Instruments*, vol. 72, no. 8, pp. 3320-327, Aug. 2001.

[121] M. S. Tsai and J. S. Chen, “Robust tracking control of a piezoactuator using a new approximate hysteresis model,” *Journal of Dynamic Systems, Measurement, and Control*, vol. 125, pp. 96-102, Mar. 2003.

[122] G. Schitter, A. Stemmer, and F. Allgöwer, “Robust two-degree-of-freedom control of an atomic force microscope,” *Asian Journal of Control*, vol. 6, no. 2, pp. 156-163, June 2004.

[123] A. Sebastian and S. M. Salapaka, “Design methodologies for robust nano-positioning,” *IEEE Transactions on Control Systems Technology*, vol. 13, no. 6, pp. 868-876, Nov. 2005.

[124] Y. Okazaki, “A micro-positioning tool post using a piezoelectric actuator for diamond turning machines,” *Precision Engineering*, vol. 12, pp. 151-156, July 1990.

[125] D. Croft, S. Stilson, and S. Devasia, “Optimal tracking of piezo-based nanopositioners,” *Nanotechnology*, vol. 10, no. 2, pp. 201-208, June 1999.

[126] C. J. Li, H. S. M. Beigi, S. Li, and J. Liang, "Nonlinear piezo-actuator control by learning self tuning regulator," *Journal of Dynamic Systems, Measurement, and Control*, vol. 115, no. 4, pp. 720-723, Dec. 1993.

[127] H.-J. Shieh, F.-J. Lin, P.-K. Huang, and L.-T. Teng, "Adaptive tracking control solely using displacement feedback for a piezo-positioning mechanism." *IEE Proceedings - Control Theory and Applications*, vol. 151, no. 5, pp. 653-660, Sept. 2004.

[128] X. Tan and J. S. Baras, "Adaptive identification and control of hysteresis in smart materials," *IEEE Transactions on Automatic Control*, vol. 50, no. 6, pp. 827-839, June 2005.

[129] H. C. Liaw and B. Shirinzadeh, "Enhanced adaptive motion tracking control of piezo-actuated flexure-based four-bar mechanisms for micro/nano manipulation," *Sensors and Actuators A: Physical*, vol. 147, no. 1, pp. 254-262, Sept. 2008.

[130] J.-H. Xu, "Neural network control of a piezo tool positioner," In: *Canadian Conference on Electrical and Computer Engineering, 1993*. Vancouver, Canada. vol. 1, pp. 333-336, Sept. 1993.

[131] F.-J. Lin, H.-J. Shieh, and P.-K. Huang, "Adaptive wavelet neural network control with hysteresis estimation for piezo-positioning mechanism," *IEEE Transactions on Neural Networks*, vol. 17, no. 2, pp. 432-444, Mar. 2006.

[132] F.-J. Lin, H.-J. Shieh, P.-K. Huang, and L.-T. Teng, "Adaptive control with hysteresis estimation and compensation using RFNN for piezo-actuator," *IEEE Transactions on Ultrasonics, Ferroelectrics and Frequency Control*, vol. 53, no. 9, pp. 1649-1661, Sept. 2006.

[133] H. Numasato and M. Tomizuka, "Settling control and performance of a dual-actuator system for hard disk drives," IEEE/ASME Transactions on Mechatronics, vol. 8, no. 4, pp. 431-438, Dec. 2003.

[134] K. Leang and S. Devasia, "Hysteresis, creep, and vibration compensation for piezoactuators: Feedback and feedforward control," In: *Proceedings of the 2nd IFAC Conference on Mechatronic Systems,* pp. 283-289, 2002.

[135] L. Y. Pao, J. A. Butterworth, and D. Y. Abramovitch, "Combined feedforward/feedback control of atomic force microscopes," In: *Proceedings of the 2007 American Control Conference*, New York City, USA. July 2007.

[136] D. Croft and S. Devasia, "Vibration compensation for high speed scanning tunneling microscopy," *Review of Scientific Instruments*, vol. 70, no. 12, pp. 4600-4605, Dec. 1999.

[137] H. Hu, H.M.S. Georgiou, and R. Ben-Mrad, "Enhancement of tracking ability in piezoceramic actuators subject to dynamic excitation conditions," *IEEE/ASME Transactions on Mechatronics*, vol. 10, no. 2, pp. 230-239, Apr. 2005.

[138] C.-J. Lin and S.-R. Yang, "Modeling of a piezo-actuated positioning stage based on a hysteresis observer," *Asian Journal of Control*, vol. 7, no. 1, pp. 73-80, Mar. 2005.

[139] S. S. Aphale, S. Devasia, and S. O. Reza Moheimani, "High-bandwidth control of a piezoelectric

nanopositioning stage in the presence of plant uncertainties," *Nanotechnology*, vol. 19, no. 12, 125503, Mar. 2008.

[140] D. Croft and S. Devasia, "Vibration compensation for high speed scanning tunneling microscopy," *Review of Scientific Instruments*, vol. 70, no. 12, pp. 4600-4605, Dec. 1999.

[141] S. Khan, M. Elitas, E. D. Kunt, and A. Sabanovic, "Discrete Sliding Mode Control of Piezo Actuator in Nano-Scale Range," *IEEE International Conference on Industrial Technology, 2006. ICIT 2006*. Mumbai, India. pp. 1454-1459, Dec. 2006.

[142] S. Chang, J. Yi, and Y. Shen, "Disturbance-observer-based hysteresis compensation for piezoelectric actuators," In: *American Control Conference, 2009. ACC '09*. St. Louis, USA. pp. 4196-4201, June 2009.

[143] S. Chang and S. Li, "A high resolution long travel friction-drive micropositioner with programmable step size," *Review of Scientific Instruments*, vol. 70, pp. 2276-2782, 1999.

[144] A. Bergander, J. Breguet, "Performance improvements for stick-slip positioners," in *Proceedings of 2003 International Symposium on Micromechatronics and Human Science*, Nagoya, pp. 59-66, 2003.

[145] F. Castanos and L. Fridman, "Analysis and design of integral sliding manifolds for systems with unmatched perturbations," *IEEE Transactions on Automatic Control*, vol. 51, pp. 853-858, May 2006.

[146] J.H. Painter, D. Kerstetter, and S. Jowers, "Reconciling steady-state Kalman and alpha-beta filter design", *IEEE Transactions on Aerospace and Electronic Systems*, vol. 26, no. 6, pp. 986-991, Nov. 1990.

[147] X. Wang, "High-order integral-chain differentiator and application to acceleration feedback," submitted to *Computer Science* for possible publication, 2011.

[148] A. Levant, "Robust Exact Differentiation via Sliding Mode Technique," *Automatica*, vol. 34, no. 3, pp. 379-384, 1998.

[149] Q. Xu and Y. Li, "Sliding mode control of a piezo-driven micropositioning system using extended Kalman filter," In: *IEEE International Conference on Automation and Logistics (ICAL), 2010*, Hong Kong and Macau, China. pp. 427-432, Aug. 2010.

[150] J. L. Minase, T.-F. Lu, and F. Wornle, "State estimation of nonlinear piezoelectric stack actuator hysteresis model," *Proceedings of SPIE*, vol. 6414, pp. 641403.1-641403.10, Dec. 2006.

[151] J. Minase, T.-F. Lu, B. Cazzolato, and S. Grainger, "Adaptive identification of hysteresis and creep in piezoelectric stack actuators," *The International Journal of Advanced Manufacturing Technology*, vol. 46, no. 9-12, pp. 913-921, May 2009.

[152] F. Yang and R. W. Wilde, "Observers for linear systems with unknown inputs," *IEEE Transactions on Automatic Control*, vol. 33, pp. 667-681, July 1988.

[153] M. Hou and P. C. Muller, “Design of observers for linear systems with unknown inputs,” *IEEE Transactions on Automatic Control*, vol. 37, pp. 871-875, June 1992.

[154] S. Hui and S. Żak, “Observer design for systems with unknown inputs,” *International Journal of Applied Mathematics and Computer Science*, vol. 15, pp. 431-546, 2005.

[155] S. H. Zak and S. Hui, S. “Output feedback variable structure controllers and state estimators for uncertain/nonlinear dynamic systems,” *IEE Proceedings D: Control Theory and Applications*, vol. 140, pp. 41-50, Jan. 1993.

[156] J.-L. Chang and T.-C. Wu, “Robust disturbance attenuation with unknown input observer and sliding mode controller,” *Electrical Engineering*, vol. 90, pp. 493-502, 2008.

[157] T. Floquet, C. Edwards, and S. K. Spurgeon, “On sliding mode observers for systems with unknown inputs,” *International Journal of Adaptive Control and Signal Processing*, vol. 21, no. 8-9, pp. 638–656, Oct.-Nov. 2007.

[158] K. Kalsi, J. Lian, S. Hui, and S. H. Zak, “Sliding-mode observers for systems with unknown inputs: A high-gain approach,” *Automatica*, vol. 46, no. 2, pp. 347-353, Feb. 2010.

[159] X. Liu, J. Jeong, and J. Kim, “A three translational DoFs parallel cube-manipulator,” *Robotica*, vol. 21, pp. 645-653, Apr. 2003.

[160] Q. Xu, and Y. Li, “A novel design of a 3-PRC translational compliant parallel micromanipulator for nanomanipulation,” *Robotica*, vol. 24, pp. 527-528, July 2006.

[161] Y. Yue, F. Gao, X. Zhao, and Q. Jeffrey Ge, “Relationship among input-force, payload, stiffness and displacement of a 3-DOF perpendicular parallel micro-manipulator,” *Mechanism and Machine Theory*, vol. 45, pp. 756-771, May 2010.

[162] S. Awtar and A. Slocum, “Constraint-Based Design of Parallel Kinematic XY Flexure Mechanisms,” *Journal of Mechanical Design*, vol. 129, pp. 816-830, Aug. 2007.

[163] Q. Yao, J. Dong, and P. Ferreira, “A novel parallel-kinematics mechanisms for integrated, multi-axis nanopositioning: Part 1. Kinematics and design for fabrication,” *Precision Engineering*, vol. 32, pp. 7-19, Jan. 2008.

[164] J. Dong, Q. Yao, and P. Ferreira, “A novel parallel-kinematics mechanism for integrated, multi-axis nanopositioning: Part 2: Dynamics, control and performance analysis,” *Precision Engineering*, vol. 32, pp. 20-33, Jan. 2008.

[165] J. Dong, S. Salapaka, and P. Ferreira, “Robust Control of a Parallel-Kinematic Nanopositioner,” *Journal of Dynamic Systems, Measurement, and Control*, vol. 130, pp. 041007-1-041007-15, July 2008.

[166] Y. Tian, B. Shirinzadeh, and D. Zhang, “A flexure-based five-bar mechanism for micro/nano manipulation,” *Sensors and Actuators A: Physical*, vol. 153, pp. 96-104, June 2009.

[167] Y. Tian, B. Shirinzadeh, and D. Zhang, “Design and dynamics of a 3-DOF flexure-based parallel mechanism for micro/nano manipulation,” *Microelectronic Engineering*, vol. 87, pp. 230-241, Feb. 2010.

[168] K. Hu, J. Kim, J. Schmiedeler, and C. Menq, “Design, implementation, and control of a six-axis compliant stage,” *Review of scientific instruments*, vol. 79, pp. 025108-2-025105-11, Feb. 2008.

[169] T. W. Seo, D. S. Kang and J. Kim, “Synthesis and comparison of fine actuator controllers for a 3-DOF micro parallel positioning platform,” In: *Proceedings of the 10th International Conference on Control, Automation, Robotics and Vision*, Hanoi, Vietnam, Dec. 2008.

[170] M. Grotjahn, B. Heimann, and H. Abdellatif, “Identification of Friction and Rigid-Body Dynamics of Parallel Kinematic Structures for Model-Based Control,” *Multibody System Dynamics*, vol. 11, pp. 273-294, Apr. 2004.

3 Modeling of Piezoelectric-Driven Stick-Slip Actuators

Published as:
J. Y. Peng and X. B. Chen, "Modeling of Piezoelectric-Driven Stick-Slip Actuators,"
IEEE/ASME Transactions on Mechatronics, vol. 16, no. 2, pp. 394-399, April 2011.

3.1 Introduction and Objectives

A PDSS actuator utilizes the stick-slip motion between an end-effector and a piezoelectric-driven movable platform to generate displacement accumulatively with high resolution and long range.

As a result of employing piezoelectric actuators, the performances of such actuators are affected by hysteresis. Also, the change in the mass of the end-effector can greatly affects the stick-slip motion through affecting the friction between the end-effector and the movable and changing the inertia of the end-effector itself. Unfortunately, such effects are ignored in the models reported in the literature. As such, the objective of this paper is to develop a dynamic model of PDSS actuators, in which the piezoelectric hysteresis and the stick-slip motion affected by different end-effector masses are taken into account.

3.2 Methods

The model of a PDSS actuator is composed of two parts: the modeling of the displacement of the movable platform driven by the piezoelectric actuator and the modeling of the displacement of the end-effector. The displacement of movable platform is modeled by the cascade of a Preisach hysteresis model and a linear second-order system, with the former accounting for the

piezoelectric hysteresis and the latter accounting for the vibration dynamics. The dynamics of the end-effector is governed by Newton's second law, with the actuating force being the friction between the movable platform and the end-effector. This friction is modeled by a modified elastoplastic friction model such that the friction is end-effector mass-dependent.

3.3 Results

Experiment results showed that the PDSS actuator model developed can accurately represent the displacement of the end-effector when the PDSS actuator is subject to saw-tooth voltage inputs of different magnitudes. Also, the effects of the magnitude and frequency of the saw-tooth voltage inputs and the end-effector mass on the average speed of the end-effector are accurately represented by the model.

3.4 Contributions

The contribution of this paper rests on the development of such a comprehensive model representative of PDSS actuators, which can be of great help in the design and control of such actuators.

Modeling of Piezoelectric-Driven Stick-Slip Actuators

J. Y. Peng, and X. B. Chen, *Member, IEEE*

***Abstract*—Piezoelectric-driven stick-slip actuators have been drawing extensive attention in various applications of long-range and ultra-precision positioning. In such an actuator, the dynamics of the end-effector displacement is of importance for its design and control, yet challenging to be modeled due to the complexity involved. By taking into account the linear dynamics and hysteretic behavior of the piezoelectric actuator (PEA) as well as the presliding friction on the end-effector, a model representative of the end-effector displacement is presented in this paper. The effectiveness of the developed model is illustrated by the experiments on the piezoelectric-driven stick-slip actuator prototyped in the authors' lab.**

***Index Terms*—Dynamics, friction, modeling, piezoelectric devices.**

I. INTRODUCTION

PIEZOELECTRIC-DRIVEN stick-slip actuators have been drawing extensive attention for micro-/nanopositioning applications due to their simple configuration, minute step size and theoretically-unlimited displacement [1]. The working principle behind such an actuator is illustrated in Fig. 1, in which an end-effector is supported and guided by a movable platform that is driven by a piezoelectric actuator (PEA). During the course of slow expansion of the PEA, the end-effector moves along with the platform. If the PEA suddenly contracts, the end-effector slides on the platform because the force due to inertia becomes larger than the friction between the end-effector and the movable platform. As a result, the end-effector moves a step, ΔS, with respect to its original position. Such steps can be accumulated to achieve a theoretically unlimited displacement (actually limited by the size of the moveable platform). One challenging task in controlling such a stick-slip actuator is modeling the dynamics of the end-effector displacement, which has not been well documented in the literature. Chang and Li [2] developed a model for the piezoelectric-driven stick-slip actuator without considering the dynamics of the PEA while the friction involved was modeled as Coulomb friction. By taking into account presliding friction, models were developed and reported in recent studies on stick-slip actuators, e.g. [3]. However, several issues remain to be addressed.

One issue is the influence of PEA nonlinearities such as

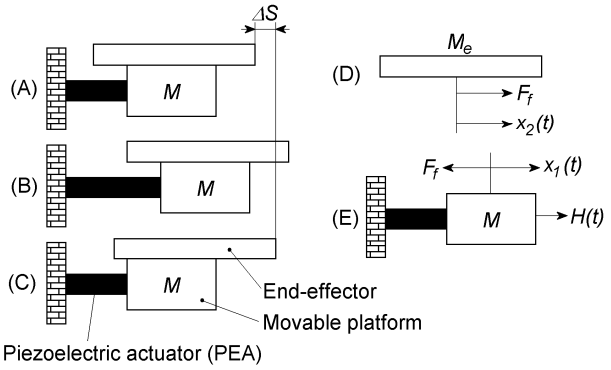

Fig. 1 (A) to (C) actuation sequence of a piezoelectric-driven stick-slip actuator: (A) start, (B) slow expansion and (C) fast contraction; (D) forces on the end-effector and its displacement; and (E) forces on the movable platform and its displacement.

hysteresis on the performance of the piezoelectric-driven stick-slip actuator, which has not been reported yet to the best of our knowledge. The second issue is the effect of the end-effector mass on the performance of the stick-slip actuator. The end-effector mass determines the inertia of the end-effector and also affects the friction between the movable platform and the end-effector. Notably, this friction is dominated by the presliding displacement, i.e., the motion prior to fully developed slip, and the nature of presliding friction is inherently different from the Coulomb friction [4]-[7]. Although friction models capable of describing presliding friction such as the Dahl model [5], the LuGre model [6], and the elastoplastic model [7] are readily available, the applications of these models to uncover the influence of the end-effector mass on the actuator performance is still lacking in the literature. By addressing these issues, this paper is to present a comprehensive model representative of the dynamics of end-effector displacement. Modeling of the end-effector mass dependent friction is given in Section II, and the development of the model for the end-effector dynamics is presented in Section III. The effectiveness of this model is validated experimentally in Section IV.

II. MODELING OF THE FRICTION IN PRESLIDING

Manuscript received November 25, 2009. This work was supported by the President's NSERC research fund of the University of Saskatchewan.

J. Y. Peng is with the Department of Mechanical Engineering, University of Saskatchewan, Saskatoon, SK S7N5A9 Canada (e-mail: jip747@mail.usask.ca).

X. B. Chen is with the Department of Mechanical Engineering, University of Saskatchewan, Saskatoon, SK S7N5A9 Canada (corresponding author, phone: (306)966-1267; fax: (306)966-5427; e-mail: xbc719@mail.usask.ca).

The friction between the end-effector and the movable platform is presliding-dominated and normal force dependent. To model this friction, the elastoplastic friction model was adapted in the present study due to its demonstrated ability to substantially reduce drift while preserving the favorable properties of other existing models [7]. Furthermore, in this study a modified form of the elastoplastic friction model was developed in order to explicitly include the effect of the end-effector mass.

In the elastoplastic friction model, the relative motion of the frictional surfaces x is decomposed into two components: elastic (reversible) and plastic (irreversible), denoted by z and w respectively, i.e.,

$$x = z + w \tag{1}$$

And the friction F_f takes the following form

$$F_f = \sigma_0 z + \sigma_1 \dot{z} + \sigma_2 \dot{x} \tag{2}$$

where σ_0 is the contact stiffness, σ_1 is the damping of the tangential compliance, σ_2 is the coefficient of viscous friction, and z is governed by

$$\dot{z} = \dot{x}\left(1 - \alpha(z) z / z_s\right) \tag{3}$$

where z_s is the steady-state value of z for a given speed $\dot{x}$; and $\alpha(z)$ takes the function given in [7]. Specifically, if $\mathrm{sgn}(\dot{x}) = \mathrm{sgn}(z)$,

$$\alpha(z) = \begin{cases} 0, & |z| \le z_b \\ \dfrac{1}{2}\sin\left(\dfrac{z - (z_s + z_b)/2}{z_s - z_b}\pi\right) + \dfrac{1}{2}, & z_b < |z| < z_s(\dot{x}) \\ 1, & |z| \ge z_s(\dot{x}) \end{cases} \tag{4}$$

and if $\mathrm{sgn}(\dot{x}) \neq \mathrm{sgn}(z)$, then $\alpha(z) = 0$. In Eq. (4), z_b denotes the breakaway displacement, which is introduced by assuming that the elastic displacement occurs only if $z < z_b$.

As noted in [8], the contribution of viscous friction to the dry friction can be negligible given that the relative motion of the frictional surfaces is presliding-dominant and its speed is really small. This leads to $\sigma_2 \dot{x} \approx 0$. It is known that the friction between the end-effector and the platform varies with the normal force in contact, which is in turn proportional to the end-effector mass. Thus, in this study the parameters in the elastoplastic model are considered as functions of the end-effector mass. Furthermore, it is assumed that

(a) the variation of friction due to the change in the end-effector mass is captured by σ_0 in Eq. (2) based on the reported studies [9], [10] on the relationship between σ_0, σ_1 and the normal force. Although σ_1 is also normal force dependent, this dependence is very limited if the dry friction normal force exceeds 0.2 to 0.4 N [9,10]. Given that the normal force encountered in the present study is mostly greater than this threshold, σ_1 is modeled as a constant.

(b) z_s is dependent on the end-effector mass given by $z_s = F_c/\sigma_0$, in which F_c is the Coulomb friction proportional to the normal load, i.e., $F_c = \beta M_e$.

(c) the breakaway displacement (z_b) is also dependent on the end-effector mass and z_b/z_s is a constant regardless of the change in the end-effector mass.

Under the above assumptions, a modified elastoplastic friction model is then obtained from Eqs. (2) and (3), i.e.,

$$F_f = \sigma_0(M_e) z + \sigma_1 \dot{z} \tag{5}$$

$$\dot{z} = \dot{x}\left[1 - \alpha(z) z / \left(\beta M_e / \sigma_0\right)\right] \tag{6}$$

where $\sigma_0(M_e)$ denotes that σ_0 is a function of the end-effector mass (M_e). The function of $\sigma_0(M_e)$ and the values of β are to be estimated experimentally (see Section IV).

III. MODELING OF THE END-EFFECTOR DISPLACEMENT

A. Dynamics of the Combination of the Piezoelectric Actuator and the Movable Platform

In practice, a PEA is always used to drive a positioning mechanism (a mass). As shown in Fig. 1(E), if taking into account the movable platform, the dynamics of the combination of a PEA and the movable platform can be approximated as that of a second-order system given that the mass of the movable platform is much larger than that of the PEA [11]. The linear dynamics is described by

$$M\ddot{x}_1(t) + C\dot{x}_1(t) + Kx_1(t) = Du(t) \tag{7}$$

where $x_1(t)$ and M are the displacement and mass of the movable platform, C and K are the damping coefficient and stiffness of the system, $u(t)$ is the voltage applied to the PEA, and D is the electromechanical transformer ratio.

Besides linear vibrational dynamics, a PEA also presents nonlinearities such as hysteresis and creep [12], [13]. Since creep is very slow compared to the displacement dynamics concerned in this study, the influence of creep is neglected and only the influence of hysteresis is considered. Based on the fact that in a PEA, hysteresis presents between the input voltage and the induced strain in a PEA whereas the relationship between the input external force and the output strain are linear if the leads of the PEA are open [14], it is speculated that the input voltage induced actuating force (the $Du(t)$ term in Eq. (7)) generated in the PEA exhibits a hysteretic dependency on the applied voltage, while the induced displacement of the PEA is proportional to this voltage induced force. Specifically, the linear actuating force $Du(t)$ in Eq. (7) is replaced by the input voltage induced hysteretic actuating force generated in the PEA. This force, denoted by $H(t)$ in the following, is represented by means of the classical Preisach hysteresis model [15], i.e.,

$$H(t) = \iint_{\alpha \ge \beta} \mu(\alpha, \beta) \gamma_{\alpha\beta}[u(t)] \, \mathrm{d}\alpha \mathrm{d}\beta \tag{8}$$

where $\mu(\alpha, \beta)$ is a weighting function that needs to be determined experimentally for a given PEA; and $\gamma_{\alpha\beta}[u(t)]$ are a collection of simple bistable units, each of which has an up

switching value α and a down switching value β, and their values are either 1 or 0, depending on the input voltage $u(t)$. If the input voltage is monotonically increased ($\dot{u}(t) > 0$), Eq.(8) can be reduced [16] to

$$H(t) = \sum_{k=1}^{n-1} \left[F(M_k, m_{k-1}) - F(M_k, m_k) \right] + F\left[u(t), m_{n-1}\right] \tag{9}$$

and if the input voltage is monotonically decreased ($\dot{u}(t) < 0$),

$$H(t) = \sum_{k=1}^{n-1} \left[F(M_k, m_{k-1}) - F(M_k, m_k) \right] + \left\{ F(M_n, m_{n-1}) - F\left[M_n, u(t)\right] \right\} \tag{10}$$

where $(n-1)$ is the number of input local maximum/minimum stored, the pairs $\{(M_k, m_k)\}$ represent the sequence of local maximum and minimum values of the input signal, and

$$F(\alpha, \beta) = H_\alpha - H_{\alpha\beta} \tag{11}$$

where H_α is the hysteretic system output once the input $u(t)$ is increased from 0 to α; and $H_{\alpha\beta}$ is the system output once the input $u(t)$ is decreased from α to β. To use Eqs. (9) and (10), the values of Eq. (11) for every combinations of $\{(M_k, m_k)\}$ need to be determined, which is presented in Section IV. It should be noted that classical Preisach hysteresis model is input-rate independent. In the cases where the input-rate range is large, models such as the dynamic Preisach hysteresis model are suggested for use instead [16].

B. Dynamics of the End-effector Displacement

Fig. 1(D) and (E) shows the piezoelectric stick-slip actuator with the displacements of interest. Taking into account the friction between the moveable platform and the end-effector, F_f, one has the following equation governing the moveable platform displacement $x_1(t)$

$$M\ddot{x}_1(t) + C\dot{x}_1(t) + Kx_1(t) = H(t) - F_f \tag{12}$$

Under the friction, F_f, the motion of the end-effector, denoted by $x_2(t)$ in Fig. 1(D), is governed by

$$M_e\ddot{x}_2(t) = F_f \tag{13}$$

F_f is given in the original or modified elastoplastic models outlined previously (i.e., Eqs. (1) to (6)), in which the relative motion between the platform and the end-effector is used, i.e.

$$x(t) = x_2(t) - x_1(t) \tag{14}$$

in which $x_2(t)$ can then be established by

$$x_2(t) = \int_0^t \dot{x}_2(\tau) d\tau \tag{15}$$

Based on the above, the block diagram for simulating the dynamics of the end-effector displacement is shown in Fig. 2.

IV. EXPERIMENT AND SIMULATION RESULTS

A. Prototype of a Piezoelectric-driven Stick-slip Actuator

In order to validate the model developed in this study, a piezoelectric-driven stick-slip actuator was prototyped, which is shown in Fig. 3. A piezoelectric actuator (P-753, Physik Instrumente) with a motion range of 15 μm and a resolution of 0.5 nm was chosen. For displacement measurements, an inductive sensor (SMU 9000, Kaman) with a resolution of 0.01 μm is used. Both the actuator and the sensor are interfaced to a host computer via an I/O board (PCI-DAS1602/16, Measurement Computing Corporation). The movable platform is driven by the actuator; and on the platform is the end-effector, which can slide horizontally on the platform via a pair of V grooves machined on them. Polished silicon wafers are attached to the V grooves as frictional surfaces to ensure the uniformity of the frictional characteristics throughout the traveling range of the end-effector. Care was taken in assembly of the system to ensure even contact between the frictional surfaces of the movable platform and the end-effector. All the displacements presented in this study were measured by the inductive sensor with a sampling interval of 0.05 ms.

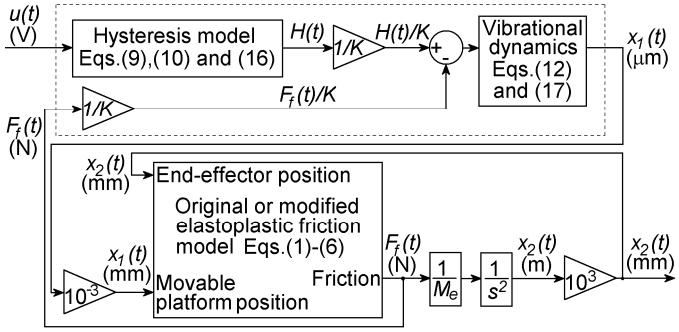

Fig. 2 Block diagram for simulating the dynamics of the piezoelectric-driven stick-slip actuator. Included in the dashed line is the model of the PEA-driven movable platform.

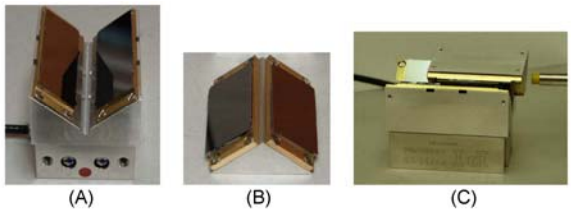

Fig. 3 Prototype of a piezoelectric-driven stick-slip actuator: (A) the movable platform affixed on the piezoelectric actuator, (B) the end-effector; and (C) the assembly of the system, along with the displacement sensor shown on the right.

B. Experimental Determination of Model Parameters

In order to estimate the parameters involved in the model presented previously, three experiments were designed and conducted on the prototyped actuator. The first experiment was conducted for the estimation of the parameters of the classical Preisach hysteresis model. In this experiment, the end-effector was removed from the moveable platform so $F_f = 0$ in Eq. (12), and the displacements of the moveable platform $x_1(t)$ were measured for the evaluation of the function of $F(\alpha, \beta)$ in Eq. (11). During the experiments, the

minimum and maximum values of the voltage applied to the PEA were set as 0 V and 100 V; and α and β were taken values from 0 V to 100 V with a steps of 5 V, respectively. For the evaluation of $F(\alpha,\beta)$ at each pair of (α,β), the voltage was slowly increased from 0 to α and the displacement was measured; and then, slowly decreasing the voltage from α to β, the displacement was measured again. During this process, it is reasonable to ignore the vibrational dynamics of the PEA, so the force generated in the PEA can be considered as proportional to the measured displacement. Multiplying the measured displacements by a gain (K) of 45 N/μm (which is the stiffness of the PEA- moveable platform assembly and its value is provided by the supplier), one has the values of both H_α and $H_{\alpha\beta}$. From Eq. (11) the values of $F(\alpha,\beta)$ were calculated. Based on the maximum likelihood method, $F(\alpha,\beta)$ was correlated to α and β by using the following 3rd-order trend surface.

$$\begin{aligned} F(\alpha,\beta) = {} & 0.938 - 3.89\,\beta + 3.72\,\alpha + 0.0418\,\beta^2 \\ & - 0.0855\,\beta\alpha + 0.0492\,\alpha^2 + 0.000163\,\beta^3 \\ & - 0.000414\,\beta^2\alpha + 0.000445\,\beta\alpha^2 - 0.000240\,\alpha^3 \end{aligned} \tag{16}$$

The second experiment was implemented for the estimation of the parameters of the second order system, representative of the linear dynamics of the combination of PEA and the moveable platform. In this experiment, the PEA was driven by step voltages; and the end-effector was removed from the moveable platform. During the experiment, the moveable platform displacements $x_1(t)$ were measured as the step voltages of 50 V and 100 V were applied to the PEA, respectively. The measured displacements were then used to estimate the parameters of the second order system with the following transfer function, which is derived from Eq. (12) with $F_f = 0$.

$$G(s) = \frac{X_1(s)}{H(s)/K} = \frac{K/M}{s^2 + Cs/M + K/M} = \frac{\omega^2}{s^2 + 2\xi\omega s + \omega^2} \tag{17}$$

where $X_1(s)$ is the Laplace transforms of the moveable platform displacement and $H(s)$ is the Laplace transforms of the input voltage induced actuating force. ω, ξ are the natural frequency and damping ratio, respectively. The values of ω, ξ were found to be 1526 rad/s, and 0.7696 based on the measured step responses.

In the third experiment for the estimation of the parameters of the original elastoplastic friction model (Eqs. (2) and (3)), the PEA was driven by a sawtooth voltage with a magnitude of 50 V and a frequency of 60 Hz; and the end-effector is placed on the moveable platform, able to slide freely on it. During the experiment, the displacements of the end-effector were measured and shown with a solid line in Fig. 4 (the 50 V curve). The measured displacements were used to determine the parameters of the friction model by using the function of nonlinear least-squares regression in Matlab. This function estimates the parameters by starting with a set of initial values and then altering the values until the error or the difference between the measured displacements and the model predictions is minimal. By doing so, the estimated values of the original elastoplastic friction model parameters are listed in TABLE 1.

TABLE I
ESTIMATED FRICTION MODEL PARAMETERS

Parameter	Estimated Values
F_c (N)	0.0362
σ_0 (N/mm)	482
σ_1 (N/(mm/s))	0.273
$z_{b/}z_s$ (mm/mm)	0.801

C. Model Validation

Two experiments were carried out to illustrate the effectiveness of the application of the classical Preisach hysteresis model to represent the PEA hysteresis. In the first experiment, the end-effector was removed from the moveable platform, and the moveable platform displacements were measured with the PEA driven by a 50 V 10 Hz sawtooth inputs. The measured displacements are given in Fig. 5(A). Based on Eq. (12) with $F_f = 0$ and its parameters estimated previously, simulations were performed to predict the moveable platform displacements with and without considering PEA hysteresis, respectively. In the case where the PEA hysteresis was considered, the classical Preisach hysteresis model (Eqs. (9) and (10)) with the estimated function $F(\alpha,\beta)$ in Eq. (16) was used to evaluate the hysteretic $H(t)$. Both simulation results are shown in Fig. 5(A), along with the experimental results, for comparison. In the second experiment, the displacements of the end-effector were measured and simulated with and without considering hysteresis under 50 V 20 Hz sawtooth inputs, both shown in Fig. 5(B). It can be seen that, by considering the effect of PEA hysteresis, the model can generate more accurate predictions of the PEA-driven moveable platform displacements and end-effector displacements, indicating the significance of the effect of the PEA hysteresis.

In order to validate the model as a whole for the piezoelectric-driven stick-slip actuator developed in this study, the end-effector was placed on the movable platform and sawtooth voltages with magnitudes U = 30 V and 60 V were applied to the PEA, respectively. The displacements of the end-effector were measured and presented in solid lines in Fig. 4, along with the measured displacement for the model parameter estimation (i.e., the 50 V curve). Simulations were performed to predict the end-effector displacement $x_2(t)$. The results obtained are shown in dash lines in Fig. 4. The root mean squared (RMS) error is used to measure the difference between the measured displacements and the model predictions:

$$E_{RMS} = \sqrt{\left[\sum_{i=1}^{n}(MD_i - SD_i)^2\right]/n} \tag{18}$$

where MD_i is the measured displacements, SD_i is the model predictions, and n is the number of samplings. The values of E_{RMS} between the measured displacements and

model predicted displacements shown in Fig. 4 were calculated to be 0.658 μm. The agreement between the measured displacements and model predictions indicates that the model developed in this study is promising for representing the end-effector displacement in the piezoelectric-driven stick-slip actuator.

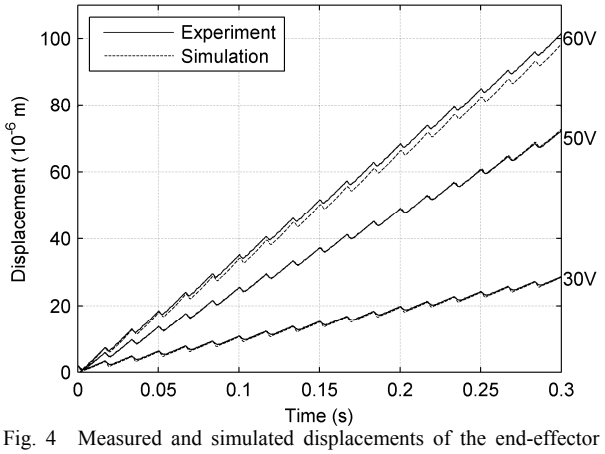

Fig. 4 Measured and simulated displacements of the end-effector for different applied voltages with a frequency of 60 Hz.

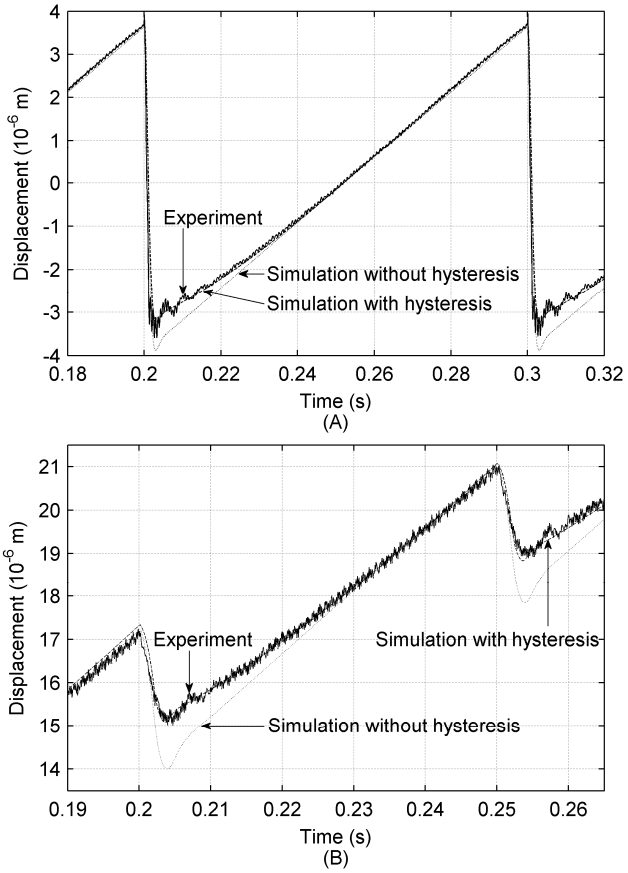

Fig.5 Comparison of the measured displacements and model predictions of (A) the moveable platform and (B) the end-effector.

D. Investigation into the End-effector Speed

The speed of the end-effect of a stick-slip actuator is measured in terms of its average value, i.e., the displacement of the end-effector produced in a certain time period. The average speed is critical to many applications and needs to be controlled precisely. This section presents an investigation into the end-effector speed and another illustration of the effectiveness of the developed model as well.

To illustrate the influence of the applied voltage on the end-effector speed, sawtooth signals with different magnitudes and frequencies were applied to the PEA. The measured and predicted average speeds are shown in Fig. 6 against the input signal magnitudes at frequencies of 20 Hz, 40 Hz, 60 Hz, and 80 Hz, respectively, and in Fig. 7 against the input signal frequencies at magnitudes of 30 V, 50 V, and 70 V. It is seen that the end-effector speed increases with both magnitude and frequency of the applied sawtooth signal and both experimental and simulation results agree with each other. This suggests that the model is capable of capturing the influence of the magnitude and frequency of the applied voltage on the end-effector speed and that the model can be applied to determine both of the magnitude and frequency of the applied sawtooth voltage in order to achieve the desired speed of the end-effector.

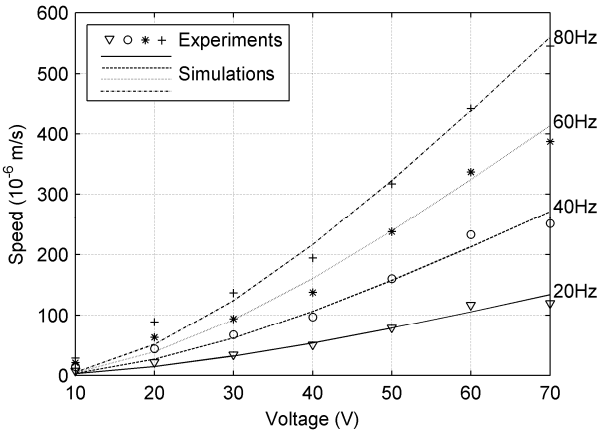

Fig. 6 Measured and simulated average end-effector speed vs. the magnitude of the input sawtooth signal with frequencies of 20Hz, 40Hz, 60Hz, and 80 Hz.

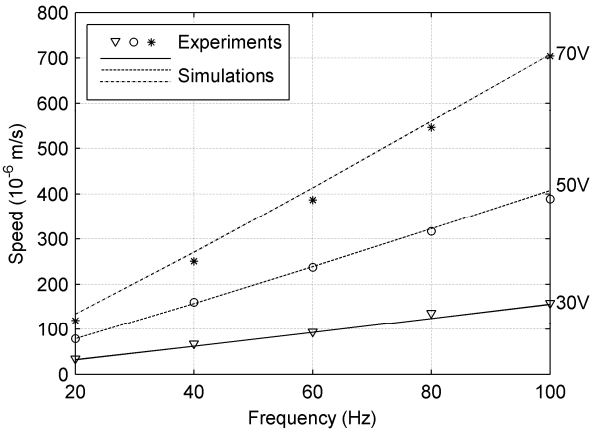

Fig. 7 Measured and simulated average end–effector speed vs. the frequency of the input sawtooth signal with magnitudes of 30 V, 50V and 70V.

To investigate into the influence of the mass of the end-effector on the end-effector speed, blocks with different masses were affixed to the end-effector, moving together. Fig. 8 shows the measured speed of the end-effector for the voltage of 50 V with a frequency of 60 Hz applied to the PEA. From

the measured results marked with triangles in Fig. 8, the corresponding σ_0 values are estimated. And the function $\sigma_0(M_e)$ (in N/mm) in the modified elastoplastic model given by Eqs. (5) and (6) is approximated by a cubic spline of M_e (in Kg) as follow: when $M_e \le 0.157$,

$$\sigma_0(M_e) = -5.07\times10^5 M_e^3 + 1.25\times10^5 M_e^2 + 287 M_e + 90.8 \quad (19)$$

when $0.157 < M_e \le 0.253$,

$$\sigma_0(M_e) = 4.71\times10^5 M_e^3 - 3.35\times10^5 M_e^2 + 7.22\times10^4 M_e - 3.66\times10^3 \quad (20)$$

and when $M_e > 0.253$,

$$\sigma_0(M_e) = -2.29\times10^4 M_e^3 + 4.06\times10^4 M_e^2 - 2.29\times10^4 M_e + 4.36\times10^3 \quad (21)$$

The value of β was calculated according to $M_e = 63.5g$ and the value of F_c in Table 1 and given by 0.571 N/Kg.

The modified elastoplastic model (Eqs. (5) and (6)) with the above estimated parameter values were then can be used to evaluate the friction between the end-effector and the movable platform. On this basis, the end-effector speeds were simulated based on the developed model. The results obtained are also presented in Fig. 8 (solid curve), along with the extra measured speeds for validation (marked with circles). The agreement between the two results suggests that the model developed is capable of capturing the influence of the mass of the end-effector on the end-effector speed and the modified elastoplastic model is promising to represent the friction involved in the piezoelectric-driven stick-slip actuator. Also of note, the end-effector speed increases with the end-effector mass initially and then begins to decrease once the mass reaches a certain value. This suggests that the end-effector can be properly designed using the model developed with an optimum mass in order to achieve the highest speed, which would greatly facilitate its control for improve performance.

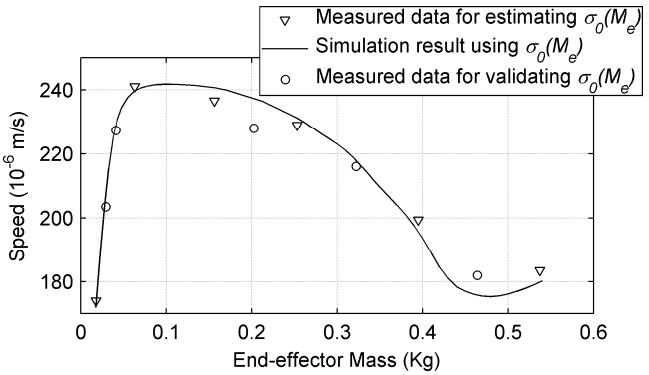

Fig. 8 Measured and simulated average end-effector speed vs. the end-effector mass, under the sawtooth voltage input of 50 V, 60 Hz. Since the data points marked with triangles are obtained by calculating the average speeds of the measured data whereas the solid curve is obtained by simulation, they contain different sources of errors and hence deviate from each other, though they are obtained from the same set of measured

V. CONCLUSIONS

Modeling of the end-effector displacement for piezoelectric-driven stick-slip actuators has been proven to be a challenging task. This is mainly due to the involvement of the linear dynamics and nonlinear hysteresis of the PEA as well as the complexity of the friction between the end-effector and the platform. By taking these into account, a comprehensive model representation of the end-effector displacement was developed in the present study. The developed model was verified by the experiments on the piezoelectric-driven stick-slip actuator prototyped in the authors' lab. It is concluded that the developed model has the capability to represent the dynamics of the end-effector, as well as the influence of applied voltage and end-effector mass on the actuator performance. Thus this model can be of great help in the design and control of such actuators. As of note, the model developed in the present study is applicable to the actuators in which the end-effector moves horizontally. Otherwise, motions with directional bias will occur and the effect of the gravity should be taken into account in the model development.

ACKNOWLEDGEMENT

The authors also thank Q.S. Zhang and D. Kang for their initial work on this project.

REFERENCES

[1] M. Rakotondrabe, Y. Haddab, and P. Lutz, "Development, modeling, and control of a micro-/nanopositioning 2-DOF stick–slip device," *IEEE/ASME Transactions on Mechatronics*, vol. 14, pp. 733-745, Dec. 2009.

[2] S. Chang and S. Li, "A high resolution long travel friction-drive micropositioner with programmable step size," *Review of Scientific Instruments*, vol. 70, pp. 2276-2782, 1999.

[3] A. Bergander, J. Breguet, "Performance improvements for stick-slip positioners," in *Proceedings of 2003 International Symposium on Micromechatronics and Human Science*, Nagoya, 2003, pp. 59-66.

[4] J. Swevers, F. Al-Bender, C. G. Ganseman, and T. Projogo, "An integrated friction model structure with improved presliding behavior for accurate friction compensation," *IEEE Transactions on Automatic Control*, vol. 45, pp. 675-686, Apr. 2000.

[5] P. Dahl, "A solid friction model," The Aerospace Corporation, EI-Se-gundo, CA, Tech. Rep., TOR-158, pp. 3107-3118, 1968.

[6] C. de Wit, H. Slsson, and K.astrom, "A new model for control of systems with friction," *IEEE Transactions on Automatic Control*, vol. 40, pp. 419-425, Mar. 1995.

[7] P. Dupont, V. Hayward, B. Armstrong, and F. Altpeter, "Single state elastoplastic friction models," *IEEE Transactions on Automatic Control*, vol. 47, pp. 787-792, May. 2002.

[8] F. Landolsi, F. Ghorbel, Jun Lou, Hao Lu and Yuekai Sun "Nanoscale friction dynamic modeling," *Journal of Dynamic Systems, Measurement, and Control*, vol. 131, pp. 061102-1-7, Nov. 2009.

[9] X. Shi and A. Polycarpou, "Measurement and modeling of normal contact stiffness and contact damping at the meso scale," *Journal of Vibration and Acoustics*, vol. 127, pp. 52-60, Feb. 2005.

[10] X. Shi and A. Polycarpou, "Investigation of contact stiffness and contact damping for magnetic storage head-disk interfaces," *Journal of Tribology*, vol. 130, pp. 021901-1-9, Apr. 2008.

[11] X. B. Chen, Q. Zhang, D. Kang, and W. Zhang, "On the dynamics of piezoactuated positioning systems" *Review of Scientific Instruments*, vol. 79, pp. 116-101, 2008.

[12] S. Devasia, E. Eleftheriou, and S. O. Reza Moheimani, "A survey of control issues in nanopositioning," *IEEE Transactions on Control Systems Technology*, vol. 15, pp. 802-823, Sep. 2007.

[13] S. Bashash, and N. Jalili, "Robust adaptive control of coupled parallel piezo-flexural nanopositioning stages," *IEEE/ASME Transactions on Mechatronics*, vol. 14, pp. 11-20, Feb. 2009.

[14] D. Croft, G. Shed, and S. Devasia, "Creep, hysteresis, and vibration compensation for piezoactuators: atomic force microscopy application", *Journal of Dynamic Systems, Measurement, and Control*, vol. 123, pp. 35-43, Mar. 2001.

[15] I. Mayergoyz, "Mathematical Models of Hysteresis," *Physical Review Letters*, vol. 56, pp. 1518-1521, 1986.

[16] R. Ben Mrad, and H. Hu, "A model for voltage to displacement dynamics in piezoceramic actuators subject to dynamic voltage excitations," *IEEE/ASME Transactions on Mechatronics*, vol. 7, pp. 479-489, Dec. 2002.

4 Novel Models for One-Sided Hysteresis of Piezoelectric Actuators

Published as:
J. Y. Peng and X. B. Chen, "Novel Models for One-Sided Hysteresis of Piezoelectric Actuators," *Mechatronics*, 2012, in press, DOI: 10.1016/j.mechatronics.2012.03.006.

4.1 Introduction and Objectives

The Preisach hysteresis model, which is one of the most widely used, represents hysteresis behaviors by the combined (superpositioned) effect of an infinite number of Preisach hysteresis operators. However, it is noticed that it is incapable of representing the one-sided hysteresis behavior of PEAs, i.e. incapable of representing the initial ascending curve and the hysteresis loops simultaneously. This is due to the fact that the Preisach hysteresis operator has only one lower saturation value.

To solve this problem, the objectives of this paper are to propose a novel hysteresis operator and then develop a rate-independent and a rate-dependent hysteresis model based on this hysteresis operator, such that the resulting new hysteresis models can simultaneously represent the initial ascending curve and the hysteresis loops in one-sided hysteresis behaviors such as that of a PEA. An inversion algorithm of the rate-independent hysteresis model is also developed for hysteresis compensation.

4.2 Methods

A novel hysteresis operator was constructed by introducing a second lower saturation value to the Preisach hysteresis operator to allow the representation of the initial ascending curve of the one-sided hysteresis behavior.

A rate-independent hysteresis model was developed based on the novel hysteresis operator following a similar procedure used in the derivation of the Preisach hysteresis model. However, due to the introduction of the additional saturation value in the novel hysteresis operator, the geometric representation of the rate-independent hysteresis model developed and hence the model expressions and properties are different from those of the Preisach hysteresis model.

A rate-dependent hysteresis model, whose output depends on both the input and the change rate of the input, was obtained by making the parameters of the rate-independent hysteresis model depend on the change rate of the input.

An inversion algorithm of the rate-independent hysteresis model, which iteratively calculates the model input using the model output, was developed and used as a feedforward hysteresis compensator.

4.3 Results

Experimental and simulation results showed that in operations that the PEA is subject to an voltage input of a fixed absolute rate of change the rate-independent hysteresis model developed can represent both the initial ascending curve and the hysteresis loop in one-sided hysteresis

accurately whilst the classical Preisach hysteresis model cannot. Also, in operations with inputs of varying change rates, the rate-dependent hysteresis model yields a maximum 3% error in the 0 to 50 Hz frequency band.

It is also found in the experiments that, when used as an open-loop feedforward controller for hysteresis compensation of a PEA, the inversion algorithm of the rate-independent hysteresis model developed can largely compensate for the rate-independent hysteresis of the PEA, thus verifying its effectiveness. When the inversion algorithm of the rate-independent hysteresis model is combined with a proportional-integral (PI) controller to form a feedback-augmented feedforward control scheme, good tracking control performance over a large frequency band was obtained since the rate-dependent effects were also effectively suppressed.

4.4 Contributions

The contribution of this work is the development of the novel hysteresis operator and the corresponding hysteresis models, which can effectively represent the one-sided hysteresis behavior, along with the corresponding methods for parameter estimation and inversion algorithm. It should be noticed that the rate-dependent hysteresis model developed is actually a lumped-structure model of the PEA. For broadband input signals, the rate-dependent hysteresis model may not be satisfactory and the decoupled-structure models can be used instead.

Novel Models for One-Sided Hysteresis of Piezoelectric Actuators

J. Y. Peng* and X. B. Chen

Department of Mechanical Engineering, University of Saskatchewan, Saskatoon, SK S7N5A9 Canada

*Corresponding author. Tel.: +1 306 241 5471. E-mail address: jip747@mail.usask.ca (J. Y. Peng)

Abstract

The hysteretic behavior of a plant with a non-negative input, referred to as one-sided hysteresis, is characterized by an initial ascending curve and hysteresis loops. It is observed that the widely-used classical Preisach hysteresis model and its modifications cannot represent such one-sided hysteresis due to the limitation of the Preisach hysteresis operator. To address this issue, a novel hysteresis operator modified from the Preisach hysteresis operator is proposed in this study and on this basis, a rate-independent hysteresis model and a rate-dependent hysteresis model are developed with methods to estimate their parameters. An algorithm to invert the rate-independent hysteresis model and its application to tracking control are also presented. The models and control schemes developed were verified experimentally on a commercially-available piezoelectric actuator. The results obtained show that the models developed are promising to represent the one-sided hysteresis of the piezoelectric actuator and that the inverting algorithm of the rate-independent hysteresis model is effective as applied to the tracking control of piezoelectric actuators.

Keywords: Hysteresis, Nonlinear systems, Piezoelectric devices.

1. Introduction

Hysteresis behavior can be found in piezoelectric actuators (PEAs), causing the actuator output displacement to depend not only on the input or applied voltage at the present time but also on the input history [1]. Currently, most commercially-available stack PEAs are configured to generate expansion displacement only as they have much higher mechanical strength or loading capacity in compression than in tensile [2]. As such, the voltages to drive PEAs are non-negative [3]. The hysteresis of PEAs under such non-negative voltage inputs is referred to as one-sided hysteresis. As shown in Fig. 1, the one-sided hysteresis is characterized by an initial ascending curve and hysteresis loops [4]-[6]. The initial ascending curve starts from the origin upon the application of voltage to the PEA; whereas the hysteresis loops exhibit

input-voltage-history dependency and the loops do not go back to the origin even if the applied voltage is back to zero. It is noted that the polarization and elongation of some piezoelectric domains that occurs in the piezoelectric material under a positive voltage cannot be completely recovered even if the applied voltage returns to zero [1]. As such, the initial ascending curve differs from the hysteresis loops.

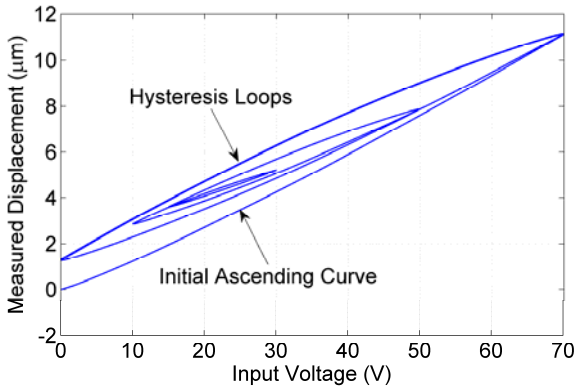

Fig. 1. Hysteresis loops and the initial ascending curve of a piezoelectric actuator under non-negative voltage inputs.

As one of the most widely-used categories of hysteresis models, the classical Preisach (CP) hysteresis model and its modifications [7]-[9] based on the Preisach operator (Fig. 2) have been shown to be promising to represent the hysteresis loops. In these models, the hysteresis is expressed as an addition of an infinite number of Preisach hysteresis operators. However, given the fact that the Preisach operator has only one lower saturation value (i.e., 0), the Preisach-operator-based models cannot simultaneously describe both the initial ascending curve and the hysteresis loops in plants. Unfortunately, this problem associated with the Preisach operator is ignored in the literature [10]-[15]. As such, it is desired to improve the Preisach-operator-based hysteresis models so as to represent the one-sided hysteresis, including both the initial ascending curve and the hysteresis loops.

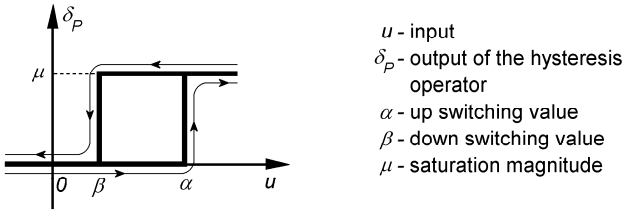

Fig. 2. Preisach hysteresis operator.

This paper presents a novel hysteresis operator and the development of a rate-independent (RI) hysteresis model and a rate-dependent (RD) hysteresis model for the PEA one-sided hysteresis. An algorithm to invert the RI hysteresis model and its application to the PEA tracking control are also presented. Specifically, the novel hysteresis operator is described in Section 2 and based on this operator, the development of the RI hysteresis model and the RD hysteresis model are presented in Section 3 and Section 4, respectively; an algorithm to invert the RI hysteresis model is then presented in Section 5 along with its applications to the PEA tracking control. This is followed by the experimental verifications on a commercially-available PEA in Section 6.

2. The Proposed Hysteresis Operator

To overcome the limitation of the Preisach operator, i.e., it has only one lower saturation value (Fig. 2), a novel hysteresis operator is proposed as shown in Fig. 3, in which the operator takes two different lower saturation values, i.e. 0 and μ_2, for the representation of the initial ascending curve and the hysteresis loops, respectively. Mathematically, the operator is expressed as

$$\delta(\alpha,\beta,u(t)) = \begin{cases} 0 & \max(u(\tau)) < \alpha \text{ where } \tau \in [0,t] \\ \mu_1(\alpha,\beta) & (u(t) \geq \alpha) \text{OR } [(u(t) > \beta) \text{ AND } (\delta(\alpha,\beta,u(t-dt)) = \mu_1(\alpha,\beta))] \\ \mu_2(\alpha,\beta) & [(u(t) \leq \beta) \text{ AND } \max(u(\tau)) \geq \alpha \text{ }] \\ & \text{OR } [(u(t) < \alpha) \text{ AND } (\delta(\alpha,\beta,u(t-dt)) = \mu_2(\alpha,\beta))] \text{ where } \tau \in [0,t] \end{cases} \quad (1)$$

where $u(t)$ is the non-negative input, α the up switching value, β the down switching value, and μ_1 the upper saturation magnitude. It is noted that α and β are within the range of $u(t)$, i.e., $0 \leq u_{\min} \leq \beta \leq \alpha \leq u_{\max}$ and that both μ_1 and μ_2 are either constants (in the rate-independent case) or functions of input rate, $\dot{u}(t)$ (in the rate-dependent case). In either case, μ_1 and μ_2 are to be estimated experimentally.

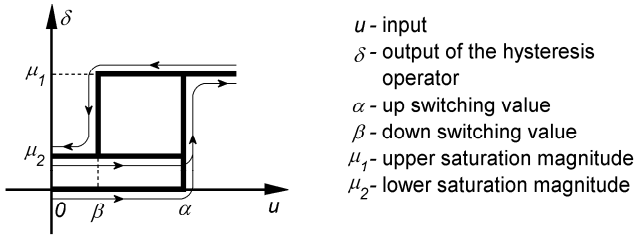

Fig. 3. Novel hysteresis operator.

3. Rate-Independent (RI) Hysteresis Model

3.1 Model Development and Its Geometric Interpretation

Based on the novel hysteresis operator (Fig. 3), the proposed RI hysteresis model is to describe the relationship between the input and output regardless of the change in the input rate. Specifically, the output of the proposed RI hysteresis model, $f(t)$, is expressed as the sum of an infinite number of hysteresis operators given in (1), i.e.,

$$f(t) = \sum_{i=1}^{\infty} \delta_i \quad (2)$$

The idea behind the above equation is similar to the one used in the CP model [7][16].

Consider a plane with coordinates α and β and on this plane, each point (α,β) is mapped through (1) to a specific hysteresis operator. Thus, the sum given in (2) can also be expressed by a double integration over the region defined by $0 \leq u_{\min} \leq \beta \leq \alpha \leq u_{\max}$, which is referred to as the limiting triangle

and denoted by T_0 shown in Fig. 4, i.e.,

$$f(t)=\iint_{u_{\min}\le\beta\le\alpha\le u_{\max}}\delta \,\mathrm{d}\alpha\mathrm{d}\beta \tag{3}$$

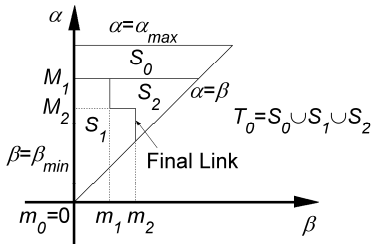

Fig. 4. Geometric interpretation of the RI hysteresis model.

Due to the introduction of a second lower saturation value in the new hysteresis operator, the geometric interpretation of the RI model is different from that of the CP hysteresis model, which is discussed as follows. Different from two regions in the CP hysteresis model, the limiting triangle in Fig. 4 has three regions, i.e. S_0, S_1, and S_2, in which $\delta=0$, $\delta=\mu_1$, and $\delta=\mu_2$, respectively. Thus, one has $\iint_{S_0}\delta\mathrm{d}\alpha\mathrm{d}\beta=0$ and (3) can be reduced to

$$f(t)=\iint_{S_1}\mu_1(\alpha,\beta)\mathrm{d}\alpha\mathrm{d}\beta+\iint_{S_2}\mu_2(\alpha,\beta)\mathrm{d}\alpha\mathrm{d}\beta \tag{4}$$

And consequently, instead of one in the case of the CP hysteresis model, there are two interfaces between the regions in the limiting triangle, i.e. the interface between S_0 and the other two regions (the S_0 - S_1 / S_2 interface) and the interface between S_1 and S_2 (the S_1 - S_2 interface).

The S_0 - S_1 / S_2 interface is horizontal, as shown in Fig. 4, and characterized by $\alpha=\max\{u(\tau)|0\le\tau\le t\}=M_1=M_{\max}$, where $M_{\max}$ is the maximum vale of the input $u(t)$ in history. If $u(t)$ exceeds $M_{\max}$, this interface moves up meanwhile $M_{\max}$ is updated with the value of $u(t)$. The S_1 - S_2 interface is a staircase line composed of horizontal and vertical line sections (referred to as links). The vertex coordinates of this staircase line are (m_i,M_j), where $i=0,1,\cdots,m$, $j=1,2,\cdots,n$, and M_j and m_i are the local maximum and minimum of $u(t)$, respectively. The link in the S_1 - S_2 interface connecting to the line $\alpha=\beta$ is referred to as the final link. The final link is either horizontal and moves up at a speed of $|\dot{u}(t)|$ if $\dot{u}(t)>0$ or vertical and moves left at a speed of $|\dot{u}(t)|$ if $\dot{u}(t)<0$.

It can be seen from the movements of the interfaces that the final link may wipe out certain vertexes and links, or (m_i,M_j) pairs whenever $u(t)<m_m$ or $u(t)>M_n$. This wipe-out motion is governed by a modified version of the wipe-out property of the CP hysteresis model. The modification is that in the RI hysteresis model, the first (minimum) local minimum $m_0\equiv 0$ and the maximum local maximum $M_{\max}$ are never wiped out (though $M_{\max}$ may change). Besides, it should be noted that the congruency property of the CP hysteresis model is only applicable to the hysteresis loops but not to the initial ascending curve in

the RI hysteresis model developed here. This is because the initial ascending curve is not part of any hysteresis loops and no first order reversal curve will drop back to intercept the initial ascending curve.

A simple example demonstrating the movements of the regional interfaces in T_0 and the corresponding changes of the integrating regions in (4) is given in Fig. 5. Initially, $t = t_0$, $u(t_0) = 0$, $f(t_0) = 0$, and $\delta(\alpha, \beta, u(t_0)) = 0$ in the whole area of T_0, so S_0 is the same as T_0, as shown in Fig. 5 (A). If the input $u(t)$ increases monotonically from $u(t_0) = 0$ to $u(t_1) = M_1 \le u_{\max}$, the operator value of $\delta(\alpha, \beta, u(t_1))$ corresponding to any point (α, β) in T_0 with $\alpha < u(t_1)$ switches from zero to $\mu_1(\alpha, \beta)$ whilst the others in T_0 remain zero. Thus, T_0 is divided into two regions, i.e., S_0 and S_1, as shown in Fig. 5 (B). During this increase of $u(t)$, the S_0 - S_1 / S_2 interface is defined by a horizontal line $\alpha = u(t)$ and this line moves up until $\alpha = M_1$. Once reaching $u(t) = M_1$, $u(t)$ decreases monotonically to $u(t_2) = m_1 \ge u_{\min}$. The value of $\delta(\alpha, \beta, u(t_2))$ corresponding to any point (α, β) in S_1 with $\beta > u(t_2)$ switches from $\mu_1(\alpha, \beta)$ to $\mu_2(\alpha, \beta)$. As a result, the third region, S_2, emerges in T_0 as shown in Fig. 5 (C) and the operator values in the rest part of S_0 and S_1 remain the same. During this decrease of $u(t)$, the S_1 - S_2 interface is defined by a vertical line $\beta = u(t)$ and moves left along the $-\beta$ direction until $\beta = m_1$ whilst the S_0 - S_1 / S_2 interface remains at $\alpha = M_1$. If $u(t)$ is subsequently increased to M_2 ($M_2 < M_1$), a horizontal new link in the S_1 - S_2 interface that attaches to the line of $\alpha = \beta$ (i.e. this new link is the final link) will emerge and move up to $\alpha = M_2$, as shown in Fig. 5 (D).

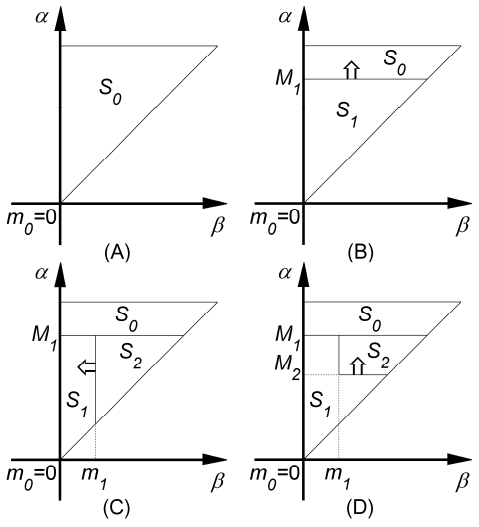

Fig. 5. An example to demonstrate the movements of the regional interfaces in T_0

3.2 Alternative Model Expression for Implementation

The double integration in (3) and (4) poses difficulties in applying the RI hysteresis model in practice. Therefore, a simpler model expression is desirable. From the previous discussion about the movements of

the regional interfaces in T_0, the integrating regions S_1 and S_2 in (4) can be seen as a result of the unification and subtraction of a series of triangular regions $\Delta S_1(u(t_i),u(t_{i+1}))$ and $\Delta S_2(u(t_i),u(t_{i+1}))$. Each of such triangular regions represents the shape change in S_1 or S_2 as the input changes monotonically between two adjacent extrema $u(t_i)$ and $u(t_{i+1})$ (which are not wiped-out) in the input history, as shown in Fig. 5. Two functions (instead of one in the case of the CP hysteresis model) are defined to represent the model output changes in term of the integration over $\Delta S_1(u(t_i),u(t_{i+1}))$ and $\Delta S_2(u(t_i),u(t_{i+1}))$, which are given by, respectively,

$$F_1(u(t_i),u(t_{i+1})) = \iint_{\Delta S_1(u(t_i),u(t_{i+1}))} \mu_1(\alpha,\beta)\,\mathrm{d}\alpha\mathrm{d}\beta \tag{5}$$

$$F_2(u(t_i),u(t_{i+1})) = \iint_{\Delta S_1(u(t_i),u(t_{i+1}))} \mu_2(\alpha,\beta)\,\mathrm{d}\alpha\mathrm{d}\beta \tag{6}$$

Thus, the RI hysteresis model output can be expressed as a linear combination of $F_1(u(t_i),u(t_{i+1}))$ and $F_2(u(t_i),u(t_{i+1}))$.

Based on the congruency property and the property of the initial ascending curve, $F_j(u(t_i),u(t_{i+1}))$ defined in (5) and (6) for all $u(t_i)$ and $u(t_{i+1})$ (or m and M), can be expressed as

$$\begin{aligned} F_1(M,m) &= F_1(m,M) = \iint_{\Delta S_1(M,m)} \mu_1(\alpha,\beta)\,\mathrm{d}\alpha\mathrm{d}\beta = f_{1M} - f_{1Mm} \\ F_2(M,m) &= \iint_{\Delta S_2(M,m)} \mu_2(\alpha,\beta)\,\mathrm{d}\alpha\mathrm{d}\beta = f_{2Mm} - f_{2M} = f_{2Mm} - 0 = f_{2Mm} \\ F_2(m,M) &= \begin{cases} F_2(M,m) & \text{(the initial ascending curve is not traversed)} \\ 0 & \text{(the initial ascending curve is traversed)} \end{cases} \end{aligned} \tag{7}$$

In (7), f_{jM} (with $j=1,2$) represents the part in $f(t)$ contributed by the S_j region at the moment when $u(t)$ is initially increased form 0 to M; and f_{jMm} (with $j=1,2$) the part in $f(t)$ contributed by the S_j region at the moment when $u(t)$ is subsequent decreased to m from M. It is noted that $F_2(m,M)$ is not always equal to $F_2(M,m)$ because the initial ascending curve in the proposed RI hysteresis model is not constrained by the congruency property as discussed previously.

Let the past local minima and maxima of $u(t)$ be denoted by $\beta_{\min} \equiv m_0 \equiv 0 < m_1 < \cdots < m_n < M_n < \cdots < M_1 \le \alpha_{\max}$ for $\dot{u}(t) > 0$, and $\beta_{\min} = m_0 = 0 < m_1 < \cdots < m_{n-1} < M_n < \cdots < M_1 \le \alpha_{\max}$ for $\dot{u}(t) < 0$. If the input monotonically increases, i.e., $\dot{u}(t) > 0$, one has

$$\begin{aligned} f(t) = &\sum_{k=0}^{n-1}\left[F_1(M_{k+1},m_k) - F_1(M_{k+1},m_{k+1})\right] + F_1(u(t),m_n) \\ &+ \sum_{k=1}^{n-1}\left[F_2(M_k,m_k) - F_2(M_{k+1},m_k)\right] + F_2(M_n,m_n) - F_2(u(t),m_n) \end{aligned} \tag{8}$$

and if the input monotonically decreases, i.e., $\dot{u}(t) < 0$

$$f(t)=\sum_{k=0}^{n-2}\left[F_1(M_{k+1},m_k)-F_1(M_{k+1},m_{k+1})\right]+F_1(M_n,m_{n-1})-F_1(M_n,u(t))$$
$$+\sum_{k=1}^{n-1}\left[F_2(M_k,m_k)-F_2(M_{k+1},m_k)\right]+F_2(M_n,u(t)) \tag{9}$$

Once $F_j(M,m)$ for any combination of (M,m) are known, the RI hysteresis model output $f(t)$ can be evaluated by using (8) and (9). In practice, the expressions of $F_j(M,m)$ used for calculating their values need to be identified by experiments. However, during the identification process it is difficult, in certain circumstances, to distinguish $F_1(M,m)$ from $F_2(M,n)$ in the experimental measurements. In other words, $F_1(M,m)$ and $F_2(M,n)$ cannot be identified by simply using (7), (8), and (9). To solve this problem, two new functions are introduced and defined by

$$F(M_{\max})=F_1(M_{\max},0) \tag{10}$$

$$G(M,m)=F_1(M,m)-F_2(M,m) \tag{11}$$

where $F(M_{\max})$ is the model output increment as $u(t)$ is increased from 0 to $M_{\max}$ along the initial ascending curve, and $G(M,m)$ is the model output decrement once $u(t)$ is subsequently decreased to m. Their values of the above two functions, given in (10) and (11), can be readily identified based on the measured inputs and outputs of a plant (to be discussed below). Substituting (10) and (11) into (8) and (9) yields the expressions of the RI hysteresis model, for $\dot{u}(t)>0$:

$$f(t)=F(M_{\max})-\sum_{k=1}^{n-1}\left[G(M_k,m_k)-G(M_{k+1},m_k)\right]-\left[G(M_n,m_n)-G(u(t),m_n)\right] \tag{12}$$

For $\dot{u}(t)<0$:

$$f(t)=F(M_{\max})-\sum_{k=1}^{n-1}\left[G(M_k,m_k)-G(M_{k+1},m_k)\right]-G(M_n,u(t)) \tag{13}$$

3.3 RI Hysteresis Model Parameter Estimation

To apply the RI hysteresis model given in (12) and (13), one needs to calculate the values of $F(M_{\max})$ and $G(M,m)$ or $G(\alpha,\beta)$. Generally speaking, $F(M_{\max})$ is a curve in the f - u plane, which goes through the origin; and $G(\alpha,\beta)$ takes the form of a surface function whose projection on the α - β plane is the limiting triangle T_0. $G(\alpha,\beta)$ intercepts the α - β plane along the line $\alpha=\beta$. In the present study, a 4th-order polynomial is used for $F(M_{\max})$ and a 4th-order trend surface model for $G(\alpha,\beta)$, i.e.,

$$F(M_{\max})=b_0+b_1M_{\max}+b_2M_{\max}^2+b_3M_{\max}^3+b_4M_{\max}^4 \tag{14}$$

$$G(\alpha,\beta)=p_1+p_2\beta+p_3\alpha+p_4\beta^2+p_5\alpha\beta+p_6\alpha^2+p_7\beta^3+p_8\alpha\beta^2+p_9\alpha^2\beta$$
$$+p_{10}\alpha^3+p_{11}\beta^4+p_{12}\alpha\beta^3+p_{13}\alpha^2\beta^2+p_{14}\alpha^3\beta+p_{15}\alpha^4 \tag{15}$$

where $b_0=0$. It should be noted that polynomials and/or trend surfaces of different orders can also be used, depending on the requirements of the application (e.g. model accuracy vs. model simplicity). To

estimate b_1 to b_4 in (14) and p_1 to p_{15} in (15), the parameter estimation techniques for linear-in-parameter models such as the linear least square method and the maximum likelihood method can be used based on the measured values of $F(M_{\max})$ and $G(M,m)$ or $G(\alpha,\beta)$.

4. Rate-Dependent (RD) Hysteresis Model

It is observed that the hysteresis loops change with the input-rate $\dot{u}(t)$. To represent such rate-dependent hysteresis, an RD hysteresis model is presented in this section. The basic idea behind the model development is that the values of μ_1 and μ_2 in the hysteresis operator (Fig. 3) are not constants, but functions of the input-rate. Correspondingly, both $F(M_{\max})$ and $G(\alpha,\beta)$ discussed previously become rate dependent, which are denoted by $F(M_{\max},\dot{u}(t))$ and $G(\alpha,\beta,\dot{u}(t))$. To express $F(M_{\max},\dot{u}(t))$ and $G(\alpha,\beta,\dot{u}(t))$, the parameters b_0 to b_4 in (14) and p_1 to p_{15} in (15) are assumed rate-dependent [14] and in present study, they are approximated by a series of polynomial curves as

$$b_k(\dot{u}(t)) = \begin{bmatrix} 1 & |\dot{u}(t)| & \cdots & |\dot{u}(t)|^m \end{bmatrix} \begin{bmatrix} b_{k0} & b_{k1} & \cdots & b_{km} \end{bmatrix}^T = \dot{\mathbf{U}}\mathbf{B}_k \qquad k = 0,\cdots,4 \qquad (16)$$

$$p_k(\dot{u}(t)) = \begin{bmatrix} 1 & |\dot{u}(t)| & \cdots & |\dot{u}(t)|^n \end{bmatrix} \begin{bmatrix} p_{k0} & p_{k1} & \cdots & p_{kn} \end{bmatrix}^T = \dot{\mathbf{U}}\mathbf{P}_k \qquad k = 1,\cdots,15 \qquad (17)$$

To estimate the parameters of the RD hysteresis model, the following steps can be followed.

(a) Estimate the parameters in the expressions of $F(M_{\max},\dot{u}(t))$ and $G(M,m,\dot{u}(t))$ at different $\dot{u}(t)$ by following the process presented in Section 3.3

(b) Select appropriate orders for (16) and (17) and then use parameter estimation techniques such as the least square method and the maximum likelihood method to estimate $\mathbf{B}_k$ and $\mathbf{P}_k$ in (16) and (17) based on the values of $b_k(\dot{u}(t))$ and $p_k(\dot{u}(t))$ that are estimated in Step (a).

To evaluate the output of the RD hysteresis model, one only needs to calculate $b_k(\dot{u}(t))$ and $p_k(\dot{u}(t))$ from given $\dot{u}(t)$ based on (16) and (17); and then to find the values of $F(M_{\max},\dot{u}(t))$ and $G(\alpha,\beta,\dot{u}(t))$ by using (14) and (15); finally to calculate $f(t)$ from (12) or (13).

5. Inversion of the RI Hysteresis Model and Its Applications to PEA Control

5.1 Inversion Algorithm of the RI Hysteresis Model

The purpose of the inversion algorithm of the RI hysteresis model is to find the input (u) to the RI hysteresis model such that the RI hysteresis model yields a prescribed or desired output. In the algorithm described below, the input (u) is calculated iteratively based on the RI hysteresis model. Specifically, in each iteration the input value is generated and updated to reduce the difference between the model output (f) and the desired output (y_d) until this difference is lower than a prescribed value. Then the input value obtained in the last iteration is taken as the input to the RI hysteresis model. Since the RI hysteresis model is time-independent, y_d, u, and f are all treated as time-independent number sequences when

implemented on a computer. Assuming zero initial condition, i.e. $y_d(0)=0$, $u(0)=0$, $f(0)=0$, the algorithm to find the present input $u(k)$ is summarized as follows.

while $y_d(k)$ *exists (*$k=1,2,3\cdots$*)*

if $y_d(k)=y_d(k-1)$ *then return* $u(k)=u(k-1)$.

else

if $y_d(k)>y_d(k-1)$

Let $u_{temp0}=u(k-1)+\Delta u$*, where* Δu *is a prescribed value. Obtain the RI hysteresis model output,* $f(k)$*, via simulation (*u_{temp0} *as input).*

while $f(k)<y_d(k)$

$u_{temp0}=u_{temp0}+\Delta u$ *and then Obtain the RI hysteresis model output,* $f(k)$*, via simulation (*u_{temp0} *as input).*

end

If $u_{temp0}>\Delta u$ *then* $u_{temp1}=u_{temp0}-\Delta u$, ***else*** $u_{temp1}=0$.

else

If $u(k-1)>\Delta u$ *then* $u_{temp1}=u(k-1)-\Delta u$, ***else*** $u_{temp1}=0$.

Obtain the RI hysteresis model output, $f(k)$*, via simulation (*u_{temp1} *as input).*

while $f(k)>y_d(k)$

If $u(k-1)>\Delta u$ *then* $u_{temp1}=u_{temp1}-\Delta u$, ***else*** $u_{temp1}=0$.

Obtain the RI hysteresis model output, $f(k)$*, via simulation (*u_{temp1} *as input).*

end

$u_{temp0}=u_{temp1}+\Delta u$

end

end

Obtain the RI hysteresis model output, $f(k)$*, via simulation (*$(u_{temp1}+u_{temp0})/2$ *as input).*

while $|f(k)-y_d(k)|\geq e_{\max}$ *(*$e_{\max}$ *is a positive number representing the maximum allowable error between* $f(k)$ *and* $y_d(k)$*)*

if $f(k)-y_d(k)\geq e_{\max}$ *then* $u_{temp0}=(u_{temp1}+u_{temp0})/2$

else $u_{temp1}=(u_{temp1}+u_{temp0})/2$

Obtain the RI hysteresis model output, $f(k)$*, via simulation (*$(u_{temp1}+u_{temp0})/2$ *as input).*

end

$u(k)=(u_{temp1}+u_{temp0})/2$

end

■

The convergence of the algorithm requires that the initial ascending curve and the ascending curves in the hysteresis loops determined by the RI hysteresis model are monotonically increasing and the descending curves in the hysteresis loops determined by the RI hysteresis model are monotonically decreasing. This requirement is met for the case of a RI hysteresis model of PEA.

5.2 Applications to the PEA Control

If a PEA is subject to an input with constant or nearly constant input-rate, the inversion algorithm of the RI hysteresis model can be employed as an open-loop feedforward controller to compensate the

influence of hysteresis, as shown in Fig. 6 (a). It is noted that in such an open-loop control scheme, the effects of vibration dynamics, creep, and exogenous disturbances cannot be compensated. In applications where such effects need to be accounted for and/or where the input-rate varies significantly with time, it is rational to augment the feedforward controller with a feedback controller, forming a so-called feedback-augmented feedforward control scheme, as shown in Fig. 6 (b). The effectiveness of these control schemes as applied to PEAs are examined and presented in Section 6.

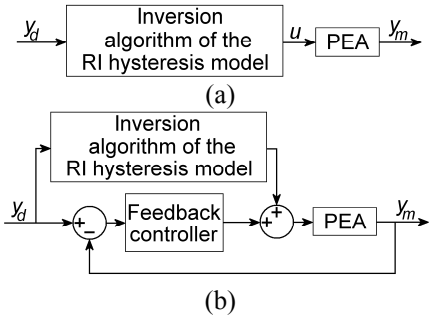

Fig. 6. Two PEA control schemes employing the inversion algorithm of the RI hysteresis model: (a) open-loop feedforward; and (b) feedback-augmented feedforward.

6. Simulation and Experimental and Validation

6.1 Experiment Setup

Experimental validations of the RI and RD hysteresis models were carried out on a PEA (P-753, Physik Instrumente). Driven by a power amplifier (E-625.CR, Physik Instrumente), the actuator can generate motion in a range of 15 μm with a resolution of 0.00005 μm. For displacement measurements, the built-in capacitive displacement sensor of the P-753 PEA with a resolution of 0.00005 μm was used. Both the actuator and the sensor were interfaced to a host computer via an I/O board (PCI-DAS1602/16, Measurement Computing Corporation) and controlled via SIMULINK programs. All measured displacements presented in this study were measured with a sampling interval of 0.05 ms.

6.2 Parameter Estimation and Verification of the RI Hysteresis Model

The parameters of the RI hysteresis model or $F(M_{\max})$ and $G(M,m)$ in (14) and (15) were estimated following the discussion in Section 3.3. The input $u(t)$ used was a voltage of triangular wave with slopes of ±200 V/s and a minimum (maximum) magnitude of 0 V ($\{V_{pp} : V_{pp} \le 70 \text{ V}\}$). V_{pp}, $M_{\max}$, α, and β were then taken values from 0 V to 70 V with a step of 5 V, respectively. By applying such $u(t)$ with different values of $M_{\max}$ to the PEA, the displacements of the PEA were measured. Particularly, once $u(t)$ was increased to reach a given $M_{\max}$ from 0, the displacement was measured and taken as a value of $F(M_{\max})$; and then the voltage was decreased from $\alpha = M = M_{\max}$ to a specific β, the displacement was measured again. The difference between these two measured displacements was the value of $G(\alpha,\beta)$ associated with this specific pair of (α,β). The values of the parameters in (14) and (15) were then estimated by using the maximum likelihood method based on the aforementioned measurements of

$F(M_{\max})$ and $G(\alpha,\beta)$. To reduce the influence of the system error, the PEA output over a time period of 1 second was measured when the PEA was subject to a zero voltage and its mean was taken as the system error. This mean was then subtracted from all subsequent measurements. Besides, the variance of the measurement noise, which is a measure of the random error, was found to be 7.29×10^{-4} μm^2, corresponding to a standard deviation of 0.0270 μm. The estimated values of the parameters, along with their standard deviations, which were calculated according to the variance of the measurement noise and the property of the maximum likelihood method, are listed in Table 1. The least significant digit of the estimated value of each parameter given in Table 1 is of the same order of magnitude as the most significant digit of the standard deviation of the estimated value of that parameter. The standard deviations of the parameters also indicate the sensitivity of the parameters. Specifically, the larger the standard deviation of the parameter is, the less sensitive it is to the model output. With these parameters, the RI hysteresis of the PEA can be evaluated by using (12), (13), (14) and (15).

Table 1. Estimated values and standard deviations of the parameters in (13) and (14)

Par.	Est. Value	Std. Dev.	Par.	Est. Value	Std. Dev.	Par.	Est. Value	Std. Dev.
b_0	0	N/A	p_3	8.99×10^{-2}	9.8×10^{-4}	p_{10}	-1.1×10^{-5}	1.0×10^{-6}
b_1	0.000	1.5×10^{-3}	p_4	1.15×10^{-3}	4.4×10^{-5}	p_{11}	5.4×10^{-8}	6.3×10^{-9}
b_2	1.37×10^{-3}	7.9×10^{-5}	p_5	-2.45×10^{-3}	8.5×10^{-5}	p_{12}	-2.4×10^{-7}	1.8×10^{-8}
b_3	1.12950×10^{-1}	1.6×10^{-6}	p_6	1.27×10^{-3}	5.0×10^{-5}	p_{13}	3.2×10^{-7}	2.7×10^{-8}
b_4	-1.460805×10^{-2}	1.1×10^{-8}	p_7	1.14×10^{-5}	7.5×10^{-7}	p_{14}	-1.9×10^{-7}	2.0×10^{-8}
p_1	-7×10^{-3}	7.2×10^{-3}	p_8	-2.9×10^{-5}	2.1×10^{-6}	p_{15}	4.9×10^{-8}	7.0×10^{-9}
p_2	-9.0×10^{-2}	1.0×10^{-3}	p_9	2.9×10^{-5}	2.3×10^{-6}			

To verify the RI hysteresis model, the input voltage shown in Fig. 7 was used. The slopes of the input were ±200 V/s, same as those used for the parameter estimation. The variations of the magnitudes of the maxima and the minima were used for verifying the capability of the RI model to represent the initial ascending curve and the arbitrary hysteresis loops.

The measured PEA displacements against the input and time are shown in Fig. 8 (a) and (b), respectively, along with the RI model simulation results. The modeling errors or the differences between the measured and simulated displacements are shown in Fig. 8 (c). It can be found that the maximum error is 0.090 μm and that the root-mean-square (RMS) error is 0.028 μm, showing a good agreement between the RI model simulations and the measured displacements. This suggests that the RI hysteresis model is effective to represent the one-sided hysteresis of the PEA subject to a fixed-rate nonnegative (one-sided) voltage input. For the purpose of comparison, the simulations by means of the CP hysteresis model subject to the same $u(t)$ were also carried out, in which the parameters of the CP model were estimated by using the same measured data for estimating the RI hysteresis model parameters. The simulation results of the CP model are shown in Fig. 8 (d) (e) (f). It is seen that the simulated hysteresis loops are negatively biased and the error in this case is much bigger than that in the case by using the RI hysteresis model due to the negligence of the initial ascending curve. Thus, it is reasonable to conclude that the RI hysteresis model

developed is superior to the CP model to represent the one-sided hysteresis behavior.

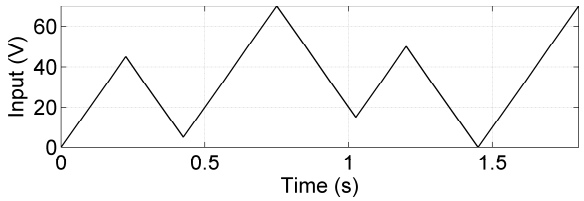

Fig. 7. Input for RI hysteresis model verification.

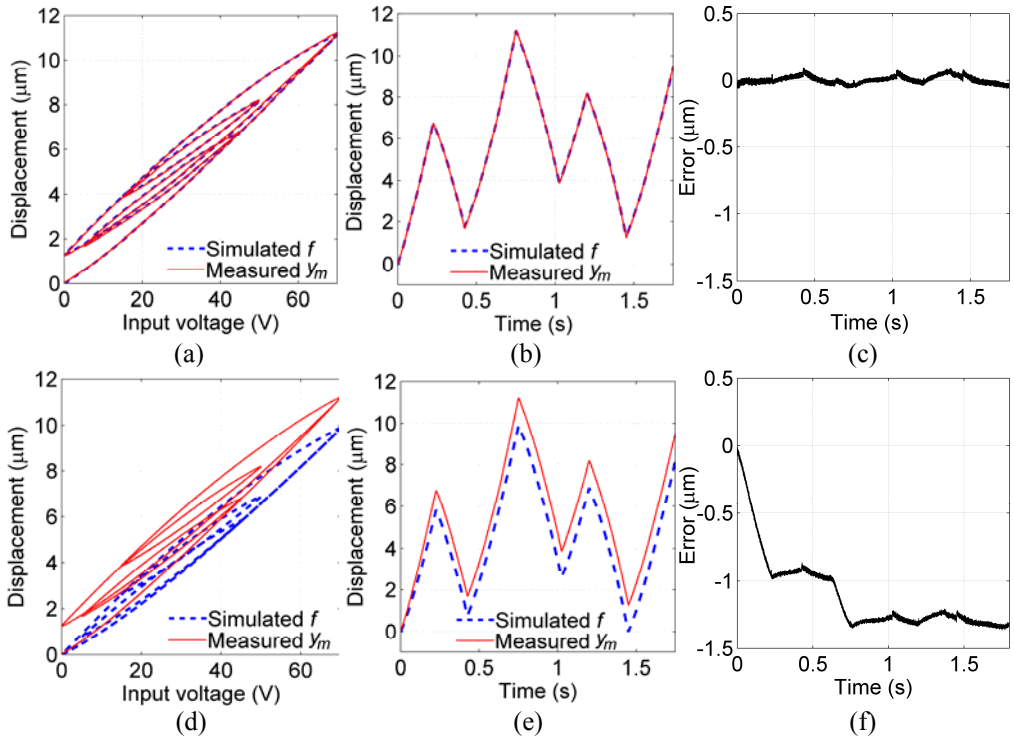

Fig. 8. Comparison of the new RI hysteresis model simulations ((a) (b) (c)) and the CP hysteresis model simulations ((d) (e) (f)) to the measured displacements. (a) and (d): displacement versus input; (b) and (e): displacement versus time; and (c) and (f): error versus time.

6.3 Parameter Estimation and Verification of the RD Hysteresis Model

For the RD hysteresis model, the parameters of $F(M_{\max}, \dot{u}(t))$ and $G(\alpha, \beta, \dot{u}(t))$, or $\mathbf{B}_k$ and $\mathbf{P}_k$ in (16) and (17) were estimated by following the procedure discussed in Section 4. For a specific $\dot{u}(t)$, the procedure is similar to the one used for RI hysteresis model parameter estimation. However, $u(t)$ with a different shape shown in Fig. 9 was used. It resembles a triangular wave with slopes of $\pm K$ where K represents the nominal input rate. Around the point where the slope changes from $+K$ to $-K$, the wave is rounded by using a portion of a sine function to prevent excessive excitation of the vibration dynamics. The magnitude of the sine function is given by AV_{pp} where $A < 1$ is a constant.

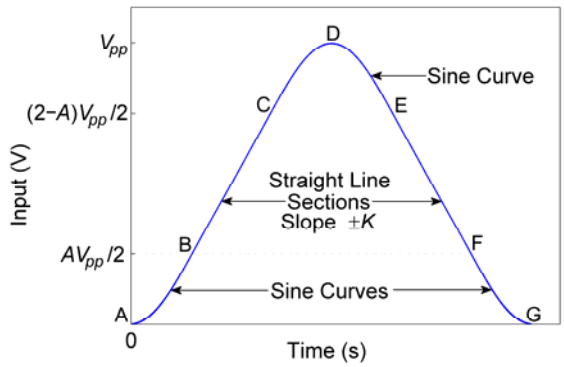

Fig. 9. Input for RD hysteresis model parameter estimation (only one period of the input is shown here).

In the experiments, the minimum and maximum of the voltage applied to the PEA was set as 0 V and 70 V, respectively. Also, it was selected that $A = 0.5$ and $K = 100$, 1000, 5000, 10000, 15000, 20000, 25000, 30000, and 35000 V/s, respectively. V_{pp}, $M_{\max}$, α and β were taken values from 0 V to 70 V with a step of 5 V, respectively. By applying such $u(t)$ with different values of $M_{\max}$ and K to the PEA, the displacements of the actuator were measured. Particularly, for a specific nominal $|\dot{u}(t)|$ or K, once the voltage was increased to a specific $M_{\max}$ from 0 (i.e., along the section ABCD in Fig. 9), the displacement was measured and taken as a value of $F(M_{\max}, \dot{u}(t))$ and then the voltage was decreased from $\alpha = M = M_{\max}$ to a specific β (i.e., along the section DEFG in Fig. 9 to a specific non-negative voltage), the displacement was measured again. The difference between these two measured displacements was evaluated and taken as a value of $G(\alpha, \beta, \dot{u}(t))$ at this specific point of (α, β). Equation (14) with rate-dependant coefficients was used to fit $F(M_{\max}, \dot{u}(t))$, whilst a 6th-order trend surface was used for $G(\alpha, \beta, \dot{u}(t))$, i.e.

$$\begin{aligned} G(M_k, m_k, \dot{u}(t)) = G(\alpha, \beta, \dot{u}(t)) &= p_1(\dot{u}(t)) + p_2(\dot{u}(t))\beta + p_3(\dot{u}(t))\alpha \\ &+ p_4(\dot{u}(t))\beta^2 + p_5(\dot{u}(t))\alpha\beta + p_6(\dot{u}(t))\alpha^2 + p_7(\dot{u}(t))\beta^3 \\ &+ p_8(\dot{u}(t))\alpha\beta^2 + p_9(\dot{u}(t))\alpha^2\beta + p_{10}(\dot{u}(t))\alpha^3 \\ &+ p_{11}(\dot{u}(t))\beta^4 + p_{12}(\dot{u}(t))\alpha\beta^3 + p_{13}(\dot{u}(t))\alpha^2\beta^2 \\ &+ p_{14}(\dot{u}(t))\alpha^3\beta + p_{15}(\dot{u}(t))\alpha^4 + p_{16}(\dot{u}(t))\beta^5 \\ &+ p_{17}(\dot{u}(t))\alpha\beta^4 + p_{18}(\dot{u}(t))\alpha^2\beta^3 + p_{19}(\dot{u}(t))\alpha^3\beta^2 \\ &+ p_{20}(\dot{u}(t))\alpha^4\beta + p_{21}(\dot{u}(t))\alpha^5 + p_{22}(\dot{u}(t))\beta^6 \\ &+ p_{23}(\dot{u}(t))\alpha\beta^5 + p_{24}(\dot{u}(t))\alpha^2\beta^4 + p_{25}(\dot{u}(t))\alpha^3\beta^3 \\ &+ p_{26}(\dot{u}(t))\alpha^4\beta^2 + p_{27}(\dot{u}(t))\alpha^5\beta + p_{28}(\dot{u}(t))\alpha^6 \end{aligned} \tag{18}$$

The values of the parameters in (14) and (18) were then estimated by using the maximum likelihood method based on the aforementioned measurements of $F(M_{\max}, \dot{u}(t))$ and $G(\alpha, \beta, \dot{u}(t))$. The estimated values of the parameters in (14) and (18) for $K = 1000$ V/s are shown in Table 2 along with their standard deviations.

Table 2. Estimated values and standard deviations of the parameters in (14) and (18) for K=1000 V/s

Par.	Est. Value	Std. Dev.	Par.	Est. Value	Std. Dev.	Par.	Est. Value	Std. Dev.
b_0	0	N/A	p_7	6.7×10^{-4}	3.4×10^{-5}	p_{18}	3.3×10^{-6}	6.8×10^{-8}
b_1	1.03197×10^{-1}	1.2×10^{-6}	p_8	-2.55×10^{-3}	7.7×10^{-5}	p_{19}	-3.0×10^{-6}	7.0×10^{-8}
b_2	1.92×10^{-3}	5.9×10^{-5}	p_9	2.34×10^{-3}	7.9×10^{-5}	p_{20}	1.2×10^{-6}	4.0×10^{-8}
b_3	0.000	1.0×10^{-3}	p_{10}	-4.6×10^{-4}	3.8×10^{-5}	p_{21}	-1.0×10^{-7}	1.2×10^{-8}
b_4	0.000	5.4×10^{-3}	p_{11}	4.49×10^{-5}	7.9×10^{-7}	p_{22}	2.85×10^{-9}	4.1×10^{-11}
p_1	-2×10^{-2}	2.5×10^{-2}	p_{12}	-1.23×10^{-4}	2.5×10^{-6}	p_{23}	-9.9×10^{-9}	1.7×10^{-10}
p_2	-8.17×10^{-1}	5.0×10^{-3}	p_{13}	1.45×10^{-4}	3.6×10^{-6}	p_{24}	2.23×10^{-8}	4.1×10^{-10}
p_3	8.20×10^{-1}	7.2×10^{-3}	p_{14}	-7.6×10^{-5}	2.7×10^{-6}	p_{25}	-2.96×10^{-8}	5.9×10^{-10}
p_4	3.23×10^{-2}	6.4×10^{-4}	p_{15}	8.8×10^{-6}	9.7×10^{-7}	p_{26}	2.06×10^{-8}	4.8×10^{-10}
p_5	-5.3×10^{-2}	1.1×10^{-3}	p_{16}	9.6×10^{-8}	8.6×10^{-9}	p_{27}	-6.7×10^{-9}	2.2×10^{-10}
p_6	2.02×10^{-2}	7.7×10^{-4}	p_{17}	-1.50×10^{-6}	3.5×10^{-8}	p_{28}	4.3×10^{-10}	5.5×10^{-11}

The relationships between the input-rate K and the corresponding estimated values of the $F(M_{\max},\dot{u}(t))$ and $G(M_k,m_k,\dot{u}(t))$ parameters $b_k(\dot{u}(t))$ and $p_k(\dot{u}(t))$ were represented by a series of 3rd-order polynomials. By using the least square method, $\mathbf{B}_k$ and $\mathbf{P}_k$ for all k were estimated. With these estimated parameters, Equations (12), (13), (14), (16), (17), and (18) can be used to predict the actuator hysteresis.

To verify the RD hysteresis model, the $u(t)$ shown in Fig. 10 was used and it was set that T_v = 1/5 s, 1/10 s, 1/20 s, 1/30 s, 1/40 s and 1/50 s. The corresponding displacements of the PEA $y_m(t)$ were measured. The comparison of the measured displacements to the model predictions for the cases where T_v = 1/10 s and 1/40 s are shown in Fig. 11, along with the modeling errors or the differences between these two displacements. The RMS errors and the maximum errors calculated over one period of the $u(t)$ are listed in Table 3. The maximum RMS error and the maximum of the maximum errors were found about 1% and 3 % of the maximum displacement of the PEA, respectively. The main sources for the errors may include (a) the rounding effects at the maxima/minima sections of the hysteresis loops due to the phase lag introduced by other linear/nonlinear dynamics, which becomes more profound as the input-rate increases; (b) the difference between the input rate used in estimating the model parameters and the one of the input waveform caused by the rounding up of the input triangular wave for parameter estimation; and (c) the PEA creep effect. However, the agreement between the simulation results and the measured displacements shown in Fig. 11 and the relatively small errors shown in Table 3 still suggest that the RD hysteresis model developed is promising to represent the one-sided hysteretic behavior of the PEA subjected to input profiles with a small range of input-rates.

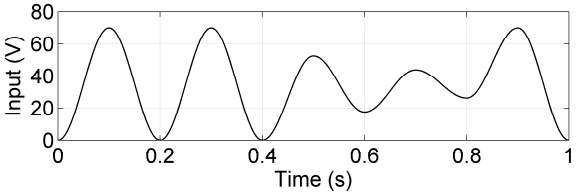

Fig. 10. $u(t)$ used for RD hysteresis model validation.

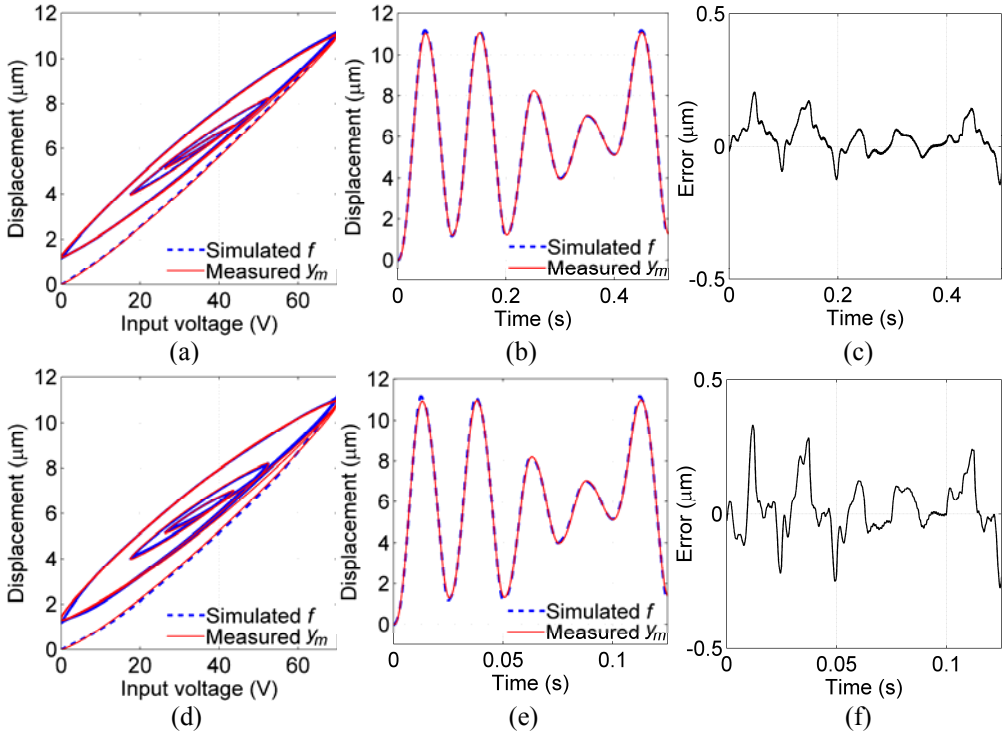

Fig. 11. Results of the RD hysteresis model verification with $1/T_v = 10\,\text{Hz}$ in (a) (b) (c) and $1/T_v = 40\,\text{Hz}$ in (d) (e) (f). (a) and (d): the displacements versus the input; (b) and (e): the displacements versus time; and (c) and (f): the error versus time.

Table 3. Errors in the RD model validation experiments

$1/T_v$ (Hz)	RMS Error (μm)	Maximum Error (μm)
5	0.06	0.17
10	0.07	0.27
20	0.08	0.25
30	0.09	0.30
40	0.11	0.34
50	0.12	0.35

6.4 Case studies – Applications to the PEA Tracking Control

The open-loop control scheme presented in Section 5.2 was examined experimentally on the PEA. The

desired trajectory y_d used is shown in Fig. 12 (b). The slopes of the line sections in y_d were chosen such that the slopes of u calculated by using the inversion algorithm of the RI hysteresis model were around ±200 V/s, close to those used for RI hysteresis model parameter estimation above. The input u calculated by using the inversion algorithm of the RI hysteresis model is shown in Fig. 13 and it was then applied to the PEA. The comparison of the measured and simulated displacements is shown in Fig. 12 (b), along with their differences or the errors in Fig. 12 (c). It is noted that the PEA displacement followed the desired trajectory closely, with a maximum error of 0.13 μm. There was no noticeable hysteresis between them, as seen in Fig. 12 (a). Besides, it is also observed from Fig. 12 (c) that the error increased with time. This is considered being caused by the creep effect of the PEA, which is not included in the RI hysteresis model.

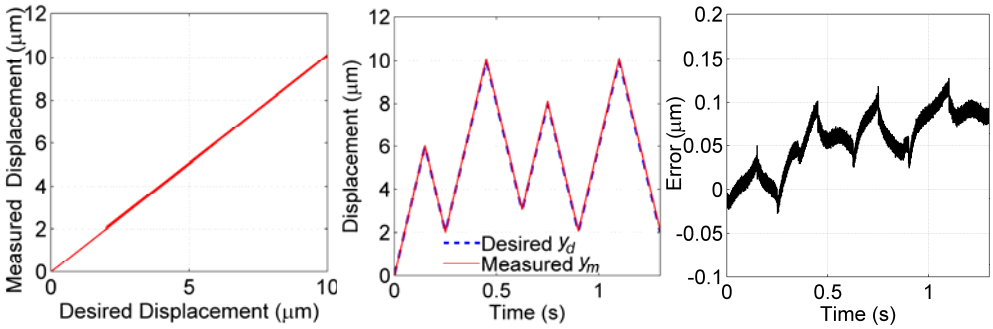

(a) (b) (c)

Fig. 12. Open-loop control experiment results: (a) the measured displacement versus the measured displacement, (b) the displacements versus time, and (c) the error versus time.

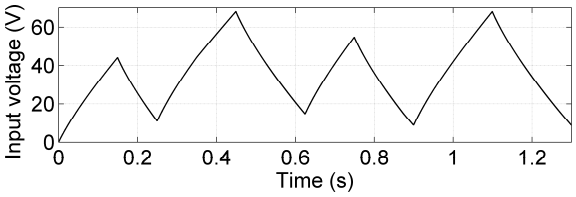

Fig. 13. Input to the PEA as calculated by using the inversion algorithm of the RI hysteresis model.

The feedback-augmented feedforward control scheme shown in Fig. 6 (b) was also examined. A proportional-integral (PI) controller was used for feedback control with the gains $K_p = 3$ and $K_I = 50000$. The desired displacement y_d used is shown in Fig. 14 (b), which is a chirp signal with frequencies varying from 5 Hz to 50 Hz such that the rate-dependent hysteresis can be excited. The experiment results are shown in Fig. 14. It can be seen that the PEA can track y_d closely. An average RMS error of 0.01 μm was obtained after repeating the same experiment 5 times, indicating that the feedback-augmented feedforward control scheme is highly effective for tracking control of the PEA even though the rate-dependent hysteresis is present. Also, the creep effect is eliminated, as shown in Fig. 14 (c), which is due to the use of feedback control.

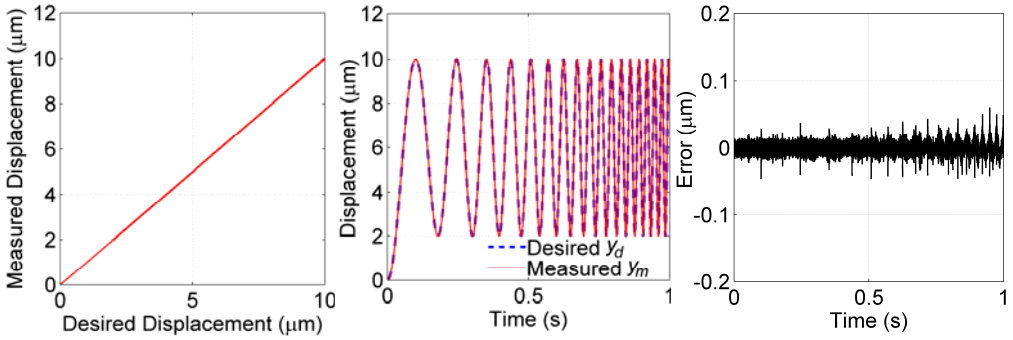

(a) (b) (c)

Fig. 14. Feedback-augmented feedforward control experiment results: (a) the measured displacement versus the measured displacement, (b) the displacement versus time, and (c) the error versus time.

7. Conclusions

In this study, a novel hysteresis operator was proposed by modifying the existing Preisach hysteresis operator. Based on this novel operator, an RI hysteresis model and an RD hysteresis model were developed to describe the one-sided hysteretic behaviors of a system, which would not be represented by means of the CP hysteresis model. An inversion algorithm of the RI hysteresis model was also presented for the hysteresis compensation. As case studies, an open-loop control scheme and a feedback-augmented feedforward control scheme employing the inversion algorithm were also examined for PEA tracking control.

Experiments on a commercially-available PEA with a non-negative input were performed to illustrate the effectiveness of the hysteresis models, the inversion algorithm and its applications to PEA control. The results showed that the RI hysteresis model developed can effectively describe the one-sided hysteretic behavior of the PEA under a fixed-rate voltage input waveform; whereas the RD hysteresis model can be used to effectively describe the one-sided hysteretic behavior of the PEA driven by input voltages with various input-rates. The inversion algorithm of the RI hysteresis model was also illustrated effective as applied to the open-loop feedforward and feedback-augmented feedforward controls of the PEA.

Acknowledgement

The authors would acknowledge the financial support from the Natural Sciences and Engineering Research Council (NSERC) of Canada to the present study. The authors also wish to thank Mr. Jun Li for his help on experiments.

References

[1] D. Damjanovic, Hysteresis in piezoelectric and ferroelectric materials, in: I. Mayergoyz and G.Bertotti (Eds.), The Science of Hysteresis, vol. 3, Elsevier, St. Louis, 2005, pp. 337-465.

[2] Physik Instrumente, The World of Nanopositioning and Micropositioning 2005 / 2006, 2005.

[3] T. Hegewald, B. Kaltenbacher, M. Kaltenbacher, and R. Lerch, Efficient modeling of ferroelectric behavior for the analysis of piezoceramic actuators, J. Intel. Mat. Syst. Str. 19(2008) 1117-1129.

[4] U-X. Tan, W. T. Latt, C. Y. Shee, C. N. Riviere, and W. T. Ang, Feedforward controller of ill-conditioned hysteresis using singularity-free Prandtl–Ishlinskii model, IEEE/ASME T. Mech. 14(2009) 598-605.

[5] S. Bashash and N. Jalili, Robust adaptive control of coupled parallel piezo-flexural nanopositioning stages, IEEE/ASME T. Mech. 14(2009) 11-20.

[6] C.-J. Lin and S.-Y. Chen, Evolutionary algorithm based feedforward control for contouring of a biaxial piezo-actuated stage, Mechatronics, 19(2009) 829-839.

[7] I. Mayergoyz, Mathematical models of hysteresis, Phys. Rev. Lett. 56(1986) 1518-1521.

[8] I. Mayergoyz, Generalized Preisach model of hysteresis, IEEE T. Magn., 24(1988) 212-217.

[9] A.-F. Boukari, J.-C. Carmona, G. Moraru, F. Malburet, A. Chaaba, and M. Douimi, Piezo-actuators modeling for smart applications, Mechatronics, 21(2011) 339-349.

[10] H. Hu and R. Ben Mrad, On the classical Preisach model for hysteresis in piezoceramic actuators, Mechatronics, 13(2003) 85-94.

[11] X. Yang, W. Li, Y. Wang, and G. Ye, Modeling hysteresis in piezo actuator based on neural networks, Lecture Notes in Computer Science, 5370(2008) 290-296.

[12] D. Croft, G. Shed, and S. Devasia, Creep, hysteresis, and vibration compensation for piezoactuators: atomic force microscopy application, J. Dyn. Sys., Meas., Control, 123(2001) 35-43.

[13] X. Zhao, and Y. Tan, Neural network based identification of Preisach-type hysteresis in piezoelectric actuator using hysteretic operator, Sensor Actuat. A: Phys. 126(2006) 306-311.

[14] W. T. Ang, P. K. Khosla, and C. N. Riviere, Feedforward controller with inverse rate-dependent model for piezoelectric actuators in trajectory-tracking applications, IEEE/ASME T. Mech. 12(2007) 134-142.

[15] J. Y. Peng and X. B. Chen, Modeling of piezoelectric-driven stick-slip actuators, IEEE/ASME T. Mech. 16(2011) 394-399.

[16] B. K. Nguyen and K. Ahn, Feedforward control of shape memory alloy actuators using fuzzy-based inverse Preisach model, IEEE T. Contr. Syst. T. 17(2009) 434-441.

5 Modeling of Piezoelectric Actuators based on a New Rate-Independent Hysteresis Model

Published as:
J. Y. Peng and X. B. Chen, "Modeling of Piezoelectric Actuators based on a New Rate-Independent Hysteresis Model," *Modern Mechanical Engineering*（http://www.scirp.org/journal/mme/）, vol. 1, no. 2, pp. 25-30, 2011.

5.1 Introduction and Objectives

As mentioned before, the rate-dependent hysteresis model of PEA developed in Chapter 4 is actually a lumped-structure model of a PEA. However, it is found in experiment that its accuracy degrades rapidly as the input frequency grows beyond 10 Hz with possible explanations given in the paper in Chapter 4. Therefore, for broadband input signals, the decoupled-structure models, which are more flexible for accuracy improvement, are preferred.

Based on the hysteresis models developed in Chapter 4, the objective of this paper is to develop a comprehensive model of a PEA which can represent the over all behaviors of the PEA being subject to broadband voltage inputs.

5.2 Methods

The structure of the model of PEA was a cascade of a rate-independent (RI) hysteresis sub-model, a vibration dynamics sub-model, and a creep sub-model. The RI hysteresis model developed in Chapter 4 was utilized. The vibration dynamics sub-model was represented by a

second order linear system. The creep sub-model was represented by a high-order linear system.

To identify the parameters of the second order linear vibration sub-model, the creep effect was neglected at the moment. The steady state gain of the vibration sub-model was set to 1. The damping ratio and the natural frequency were identified by fitting the phase-frequency response of the second order linear vibration sub-model to the measured phase-frequency response of the PEA by using the least squares method.

To identify the parameters of the rate-independent hysteresis model, the creep effect was again neglected at this moment. The parameter identification method developed in Chapter 4 was employed. The voltage inputs to the hysteresis sub-model were known. Whist the outputs of the rate-independent hysteresis model, which were the inputs to the second order linear vibration sub-model, were calculated by substituting the measured displacements of the PEA and their derivatives (estimated through an observer) into the vibration sub-model.

To identify the creep sub-model parameters, a step input of 30 V was applied to the PEA over 30 s. By using the System Identification Toolbox in MATLAB, the output of an ARX (Auto Regressive with eXogenous input) model, whose input was the simulated output of the vibration sub-model, was fitted to the measured displacement of the PEA by using the least squares method. The ARX model was then converted into a continuous-time fourth-order system, which was used as the creep sub-model.

5.3 Results

Comparing the simulated and measured displacements of the PEA subject to sine waves with

varying magnitudes and frequencies between 50 Hz and 500 Hz, it was found that the model developed can represent the broadband behavior of the PEA with good accuracy (RMS error less than 1% of the maximum PEA displacement) up to 400 Hz.

5.4 Contributions

The contribution of this paper is the integration of the newly developed RI hysteresis model into a comprehensive model of PEA to represent the one-sided hysteresis behavior, including the initial ascending curve, of a PEA subject to broadband voltage inputs. This comprehensive model of PEA can be of great use in controller and state observer design for such actuators.

Modeling of Piezoelectric Actuators based on a New Rate-Independent Hysteresis Model

J. Y. Peng* and X. B. Chen
Department of Mechanical Engineering, University of Saskatchewan, Saskatoon, SK S7N5A9 Canada
*Corresponding author. Tel.: +1 306 241 5471. E-mail address: jip747@mail.usask.ca (J. Y. Peng)

Abstract
Accurate model representatives of piezoelectric actuators (PEAs) are important for both understanding the dynamic behaviors of PEAs and control scheme development. However, among the existing models, the most widely used classical Preisach hysteresis model are incapable of representing the commonly-encountered one-sided (non-negative voltage input range) hysteresis behaviors of PEAs. To solve this problem, a new rate-independent hysteresis model was developed for the one-sided hysteresis and then integrated with the models representative of creep and dynamics to form a single model for the PEAs. Experiments were carried out to validate the developed models.

Keywords: Piezoelectric actuator, Hysteresis.

1. Introduction

Piezoelectric actuators (PEAs) have been widely used in micro-/nano-positioning systems due to their fine displacement resolution and large actuation force [1]. In such applications, accurate models of PEAs are usually required for both understanding of their dynamic behaviors and controller design. A widely-used category of PEA models takes the form of a cascade of three sub-models, each of which representing the effect of hysteresis, creep, and vibration dynamics, respectively, e.g. [2]. While the modeling of the vibration dynamics and creep has been well addressed in the literature, there are still problems with the modeling of hysteresis. Most commercially available PEAs have a non-negative input voltage range and their corresponding hysteresis behaviors subject to such one-sided input range are referred to as one-sided hysteresis, as shown in Fig. 1, which contains an initial ascending curve in addition to the hysteresis loops. It is observed in the authors' earlier study [3] that the classical Preisach (CP) hysteresis model [4] cannot represent such one-sided hysteresis since it can not represent the initial ascending curve. This deficiency of the CP hysteresis model has been neglected in the literature, e.g. [5]-[8]. This problem of modeling the one-sided hysteresis was solved in [3] by developing a new rate-independent (RI) hysteresis model based on a novel hysteresis operator.

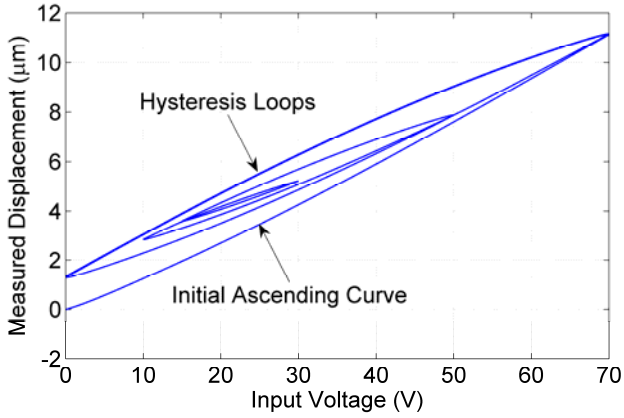

Fig. 1. One-sided hysteresis behavior measured from a PEA subjected to non-negative voltage input.

On this basis, in this paper, this new RI hysteresis model is integrated with a vibration sub-model and a creep sub-model to form an integrated model for PEAs. The parameter estimation scheme for such a model of PEAs is also developed. Experiments were conducted and the results obtained were compared with simulation results to validate the model developed.

2. Outline of the Rate-Independent (RI) Hysteresis Model

The RI hysteresis model developed in [3] represents one-sided hysteresis behaviors as the combined effects of an infinite number of hysteresis operators, one of which is shown in Fig. 2. Compared to the Preisach hysteresis operator, the hysteresis operator in Fig. 2 has one more lower saturation value to account for the initial ascending curve in one-sided hysteresis. The two switching values satisfy $\alpha \geq \beta$. The hysteresis is then expressed mathematically as

$$f(t) = \iint_{u_{\max} \geq \alpha \geq \beta \geq u_{\min} \geq 0} \delta(\alpha, \beta, u(t)) \mathrm{d}\alpha \mathrm{d}\beta \tag{1}$$

where $f(t)$ is the hysteresis, i.e. the model output, $u_{\max}$ and $u_{\min}$ are the maximum and minimum input $u(t)$ in history, respectively [3].

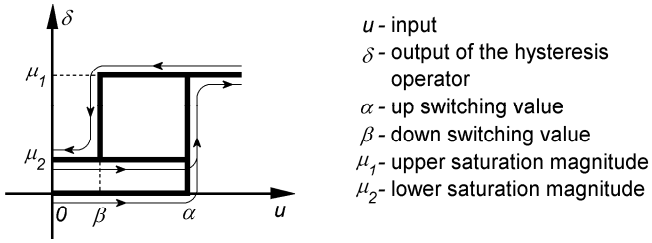

Fig. 2. The novel hysteresis operator $\delta(\alpha, \beta, u(t))$ [3].

The double integration suggests that the hysteresis model output is the combined effect of an infinite number of hysteresis operators with bounded values of α and β, which can be explained via the geometric interpretation shown in Fig. 3. Each hysteresis operator $\delta(\alpha, \beta, u(t))$ is assigned to a point (α, β) on the α-β plane. All such (α, β) points are in a region satisfying $u_{\max} \geq \alpha \geq \beta \geq u_{\min} \geq 0$, which is referred to as the limiting triangle T_0. According to the values of $\delta(\alpha, \beta, u(t))$, T_0 is divided into three regions denoted by S_0, S_1, and S_2, where $\delta = 0$, $\delta = \mu_1$, and $\delta = \mu_2$, respectively. The interface between S_0 and the other two regions is a horizontal line characterized by $\alpha = \max\{u(\tau) | 0 \leq \tau \leq t\} = M_1 = M_{\max}$ in which $M_{\max}$ is the maximum local maximum. The interface between S_1 and S_2 is a staircase line with vertex coordinates (m_i, M_j), where $i = 0,1,\cdots,m$ and $j = 1,2,\cdots,n$, M_j and m_i are the historical local maxima and minima of $u(t)$, respectively. The link in the S_1-S_2 interface that attaches to the line $\alpha = \beta$ is referred to as the final link and it represents the influence of the changes in input $u(t)$ to the shapes of S_0, S_1, and S_2. This link is horizontal and goes up at a speed of $|\dot{u}(t)|$ when $\dot{u}(t) > 0$, and is vertical and goes left at a speed of $|\dot{u}(t)|$ when $\dot{u}(t) < 0$. Noting that $\iint_{S_0(u(t))} 0 \mathrm{d}\alpha \mathrm{d}\beta = 0$, so Eq. (1) can be reduced to

$$f(t) = \iint_{S_1} \mu_1(\alpha, \beta) \mathrm{d}\alpha \mathrm{d}\beta + \iint_{S_2} \mu_2(\alpha, \beta) \mathrm{d}\alpha \mathrm{d}\beta \tag{2}$$

The motion of the final link will wipe out certain vertexes and links, or (m_i, M_j) pairs whenever $u(t) < m_m$ or $u(t) > M_n$. A modified version of the wipe-out property [4] of the CP hysteresis model governs such wipe-out processes. The modification is that in the RI hysteresis model, the first local minimum $m_0 \equiv 0$ and the maximum local maximum $M_{\max}$ are never wiped out. Besides, the congruency property [4] of the CP hysteresis model still applies to the hysteresis loops but not to the initial ascending curve in the RI hysteresis model as the initial ascending curve is not part of any hysteresis loops.

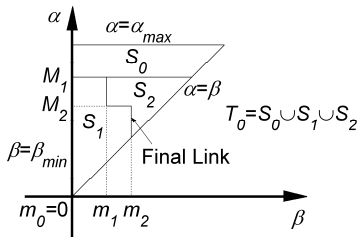

Fig. 3. Geometric interpretation of the RI hysteresis model.

Eqs. (1) and (2) involve double integration which is difficult to implement in practice, so an alternative model expression without calculus is desirable and is given in [3]. The rationale behind this alternative model expression is that the S_1 and S_2 regions in Eq. (2) can be treated as a result of the unification and subtraction of a series of triangular regions $\Delta S_1(u(t_i),u(t_{i+1}))$ and $\Delta S_2(u(t_i),u(t_{i+1}))$. Then the integration of $\delta(\alpha,\beta,u(t))$ over each of such triangular regions can be pre-identified and used to calculate $f(t)$ through a series of adding and subtracting operations.

Specifically, each of such triangular regions represents the shape change in S_1 or S_2 as the input changes monotonically between two adjacent extrema $u(t_i)$ and $u(t_{i+1})$ in the input history which are not wiped-out. The changes in the model output due to $\Delta S_1(u(t_i),u(t_{i+1}))$ and $\Delta S_2(u(t_i),u(t_{i+1}))$ are represented by the following two functions.

$$F_1(u(t_i),u(t_{i+1})) = \iint_{\Delta S_1(u(t_i),u(t_{i+1}))} \mu_1(\alpha,\beta)\,\mathrm{d}\alpha\mathrm{d}\beta \tag{3}$$

$$F_2(u(t_i),u(t_{i+1})) = \iint_{\Delta S_1(u(t_i),u(t_{i+1}))} \mu_2(\alpha,\beta)\,\mathrm{d}\alpha\mathrm{d}\beta \tag{4}$$

Thus, the RI hysteresis model output can be expressed as a linear combination of $F_1(u(t_i),u(t_{i+1}))$ and $F_2(u(t_i),u(t_{i+1}))$, as follows. Denoting two adjacent local minimum and local maximum by m and M, respectively, the following relationships related to Eqs. (3) and (4) are obtain by using the congruency property and the property of the initial ascending curve.

$$\begin{aligned} F_1(M,m) &= F_1(m,M) = \iint_{\Delta S_1(M,m)} \mu_1(\alpha,\beta)\,\mathrm{d}\alpha\mathrm{d}\beta = f_{1M} - f_{1Mm} \\ F_2(M,m) &= \iint_{\Delta S_2(M,m)} \mu_2(\alpha,\beta)\,\mathrm{d}\alpha\mathrm{d}\beta = f_{2Mm} - f_{2M} = f_{2Mm} - 0 = f_{2Mm} \\ F_2(m,M) &= \begin{cases} F_2(M,m) & \text{(the initial ascending curve is not traversed)} \\ 0 & \text{(the initial ascending curve is traversed)} \end{cases} \end{aligned} \tag{5}$$

where f_{jM} ($j=1,2$) represents the part in $f(t)$ contributed by the S_j region at the moment when $u(t)$ is initially increased form 0 to M; and f_{jMm} ($j=1,2$) the part in $f(t)$ contributed by the S_j region at the moment when $u(t)$ is subsequent decreased to m from M. Assume that the historical local minima and maxima of $u(t)$ that are not wiped out are $\beta_{\min} \equiv m_0 \equiv 0 < m_1 < \cdots < m_n < M_n < \cdots < M_1 \le \alpha_{\max}$ during $\dot{u}(t) > 0$, and $\beta_{\min} = m_0 = 0 < m_1 < \cdots < m_{n-1} < M_n < \cdots < M_1 \le \alpha_{\max}$ during $\dot{u}(t) < 0$. Then, if the input monotonically increases, i.e., $\dot{u}(t) > 0$, one has

$$\begin{aligned} f(t) = &\sum_{k=0}^{n-1}\left[F_1(M_{k+1},m_k) - F_1(M_{k+1},m_{k+1})\right] + F_1(u(t),m_n) \\ &+ \sum_{k=1}^{n-1}\left[F_2(M_k,m_k) - F_2(M_{k+1},m_k)\right] + F_2(M_n,m_n) - F_2(u(t),m_n) \end{aligned} \tag{6}$$

and if the input monotonically decreases, i.e., $\dot{u}(t) < 0$

$$f(t)=\sum_{k=0}^{n-2}\left[F_1(M_{k+1},m_k)-F_1(M_{k+1},m_{k+1})\right]+F_1(M_n,m_{n-1})-F_1(M_n,u(t))$$
$$+\sum_{k=1}^{n-1}\left[F_2(M_k,m_k)-F_2(M_{k+1},m_k)\right]+F_2(M_n,u(t)) \tag{7}$$

For the ease of parameter identification, define two new functions as

$$F(M_{\max})=F_1(M_{\max},0) \tag{8}$$

$$G(M,m)=F_1(M,m)-F_2(M,m) \tag{9}$$

where $F(M_{\max})$ is the model output increment when $u(t)$ is increased from 0 to $M_{\max}$ along the initial ascending curve, and $G(M,m)$ is the model output decrement when $u(t)$ is subsequently decreased to m. The values of $F(M_{\max})$ and $G(M,m)$ under different m, M, and $M_{\max}$ are readily measurable from a hysterical plant, so suitable expressions of $F(M_{\max})$ and $G(M,m)$ can be found. This is to be described in Section 4.

Finally, Substituting Eqs. (8) and (9) into Eqs. (6) and (7) yields the alternative expression of the RI hysteresis model for practical uses. For $\dot{u}(t)>0$

$$f(t)=F(M_{\max})-\sum_{k=1}^{n-1}\left[G(M_k,m_k)-G(M_{k+1},m_k)\right]-\left[G(M_n,m_n)-G(u(t),m_n)\right] \tag{10}$$

and for $\dot{u}(t)<0$

$$f(t)=F(M_{\max})-\sum_{k=1}^{n-1}\left[G(M_k,m_k)-G(M_{k+1},m_k)\right]-G(M_n,u(t)) \tag{11}$$

3. A Model of Piezoelectric Actuators

The model of PEA is developed by cascading a vibration sub-model and a creep sub-model to the above RI hysteresis model, as shown in Fig. 4. $u(t)$ represents the voltage input, and $x(t)$ represents the displacement of the PEA or the model output.

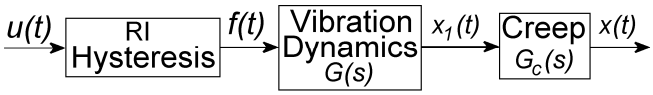

Fig. 4. Integrated model of a PEA.

The vibration sub-model is represented by means of a second order system under the assumption that the mass driven by the PEA is much larger than the mass of the PEA itself [9], i.e.,

$$\ddot{x}_1(t)+2\zeta\omega_n\dot{x}_1(t)+\omega_n^2x_1(t)=f(t) \tag{12}$$

where ζ and ω_n are the damping ratio and the natural frequency, respectively; and $f(t)$ is the hysteresis being represented by using the RI hysteresis model discussed in the previous section. Since the RI hysteresis $f(t)$ does not introduce phase lag, the phase lag between $x(t)$ and $u(t)$ is resulted from the vibration sub-model (Given the fact that the magnitude of creep is very small, its phase lag can be neglected). Thus, the values of ζ and ω_n can be estimated by fitting the frequency-phase response of Eq. (12) to the measured frequency-phase response of a PEA.

The parameter identification of the RI hysteresis model involves the identification of the functions $F(M_{\max})$ and $G(M,m)$. To do this, some input-output data or the values of $f(t)$ corresponding to certain inputs $u(t)$ need to be found. However $f(t)$ is difficult to measure in practice, so in this study such $f(t)$ values is calculated from Eq. (12) by using $x_1(t)$ and its derivatives when the PEA is subject to $u(t)$. It should be noted that in this process, creep is again neglected due to its small magnitude and $x(t)$ is taken as $x_1(t)$, which is measurable. The derivatives of $x_1(t)$ can be approximately found either by firstly passing through the measured $x(t)$ through a low pass filter to suppress the noise and then differentiating the low pass filter output or by a state estimator such as an α-β-γ filter. Once such $u(t)$ and

$f(t)$ data are obtained, a suitable expressions of $F(M_{\max})$ and $G(M,m)$ can then be found with their parameters estimated (to be discussed in Section 4).

The creep in Fig. 4 is represented by means of a linear dynamic system model $G_2(s)$ taking $x_1(t)$ as input and generating a creep displacement $x_2(t)$. $x_2(t)$ is then added to $x_1(t)$ to obtain the total displacement output of the PEA, $x(t)$, as shown in Fig. 5. The form and the parameters of $G_2(s)$ can be determined by system identification methods.

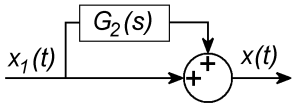

Fig. 5. The creep sub-model, i.e., $G_c(s)$ in Fig. 4.

Eventually, with a voltage input $u(t)$, a displacement output $x(t)$ in Fig. 4 can be derived from Eqs. (10), (11), (12), and

$$G_c(s) = X(s)/X_1(s) = [X_1(s) + X_2(s)]/X_1(s) = 1 + G_2(s) \tag{13}$$

where $X_1(s)$, $X_2(s)$, and $X(s)$ are the Laplace transforms of $x_1(t)$, $x_2(t)$, and $x(t)$ respectively.

4. Experiments and Results

A. Experiment Setup

Experimental validations of the PEA model are carried out on a PEA (P-753, Physik Instrumente). The actuator can generate motion in a range of 15 μm with a resolution of 0.5 nm. For displacement measurements, a built-in capacitive displacement sensor of the P-753 PEA with a resolution of 1nm was used. Both the actuator and the sensor are interfaced to a host computer via an I/O board (PCI-DAS1602/16, Measurement Computing Corporation) and controlled by SIMULINK programs. All measured displacements presented in this study were measured with a sampling interval of 0.05 ms.

B. Vibration Sub-model Parameter Estimation

As mentioned in the previous section, ζ and ω_n in Eq. (12) were estimated by fitting the phase frequency response of Eq. (12) to the measured response of the PEA based on the method of least squares. The phase frequency response curve of the PEA displacements was measured by feeding sinusoidal voltages between 0 and 1000 Hz to the PEA and then calculating the phase differences between the input voltages and the measured output displacements. The fitted results are shown in Fig. 6, from which ζ and ω_n were estimated as 0.788 and 5352 rad/s, respectively.

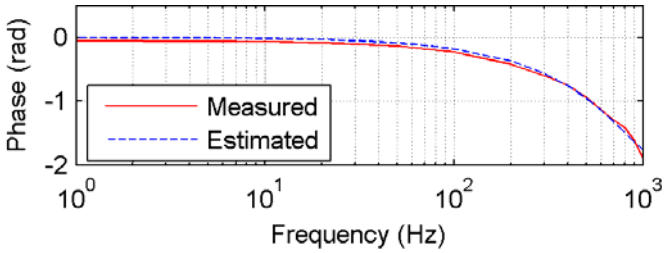

Fig. 6. Measured and estimated phase frequency responses.

C. RI Hysteresis Sub-model Parameter Estimation

To identify $F(M_{\max})$ and $G(M,m)$ in Eqs. (8) and (9), the displacements of the PEA were measured under the voltage inputs determined by

$$u(t) = V_{pp}/2 + (V_{pp}/2)\sin(200\pi t + 1.5\pi) \tag{14}$$

where V_{pp} is the peak-to-peak magnitudes. Since the frequency of voltage input, i.e., 100 Hz, was high, creep was insignificant over a few periods of the waveforms and thus neglected. The minimum and maximum of the voltage applied to the PEA were set to 0 V and 70 V, respectively. V_{pp} (or $M_{\max}$), M and m were then taken values from 0 V to 70 V with a step of 5 V, respectively and thus the series of

$u(t)$ were determined. By applying $u(t)$ of different V_{pp} or $M_{\max}$ to the PEA, the displacements of the actuator were measured. Each measured displacement waveform was the $x_1(t)$ in Eq. (12) corresponding to a given $u(t)$. $\dot{x}_1(t)$ and $\ddot{x}_1(t)$ were estimated by an α-β-γ filter ($\alpha = 8.7\times10^{-2}$, $\beta = 3.9\times10^{-3}$, $\gamma = 2.4\times10^{-3}$) from the measured $x_1(t)$. $x_1(t)$, $\dot{x}_1(t)$, and $\ddot{x}_1(t)$ were then substituted into Eq. (12) to calculate the "measured" $f(t)$ corresponding to the given $u(t)$. In the following, the values of $f(t)$ and the corresponding $u(t)$ from the initial conditions of $t = 0$, $u(t) = 0$, and $f(t) = 0$ were examined. Once $u(t)$ was increased to reach a given $M_{\max}$ from $u(t=0) = 0$, the corresponding $f(t)$ value was found and taken as a value of $F(M_{\max})$. Similarly, once the voltage was subsequently decreased from $M = M_{\max}$ to a specific value of m, the $f(t)$ value was found and taken again. This $f(t)$ value was subtracted from the $F(M_{\max})$ value just measured and the result was taken as a value of $G(M,m)$ at this specific (M,m) point. It was found that the measured points $(M_{\max}, F(M_{\max}))$ resemble a smooth curve, and the measured points $(M,m,G(M,m))$ resemble a smooth surface. Hence $F(M_{\max})$ was represented by a polynomial

$$F(M_{\max}) = b_0 + b_1 M_{\max} + b_2 M_{\max}^2 + b_3 M_{\max}^3 + b_4 M_{\max}^4 \tag{15}$$

And $G(M,m)$ was represented by a trend surface

$$\begin{aligned} G(M,m) = {} & p_1 + p_2 m + p_3 M + p_4 m^2 + p_5 Mm + p_6 M^2 \\ & + p_7 m^3 + p_8 Mm^2 + p_9 M^2 m + p_{10} M^3 + p_{11} m^4 \\ & + p_{12} Mm^3 + p_{13} M^2 m^2 + p_{14} M^3 m + p_{15} M^4 \end{aligned} \tag{16}$$

Then the values of the parameters in Eqs. (15) and (16) were estimated by using the maximum likelihood method based on the measurements of $F(M_{\max})$ and $G(M,m)$. The estimated parameter values are shown in Table 1. With these parameters, the RI hysteresis of the actuators can be evaluated for any given input $u(t)$ by using Eqs. (10) and (11).

D. Creep Sub-model Parameter Estimation

Creep is a slow effect. To identify the parameters involved in the creep sub-model, a step voltage input of 30V was applied to the PEA for an extended period of time (30 s). The output displacement $x(t)$ of the PEA was measured. And the corresponding $x_1(t)$ was obtained by simulation using the identified hysteresis and vibration sub-models. Then $x_2(t)$, which is the measured output of $G_2(s)$ in Fig. 5 induced by the input $x_1(t)$, was obtained by $x_2(t) = x(t) - x_1(t)$. By using the System Identification Toolbox in MATLAB, an ARX (Auto Regressive with eXogenous input) model with a sampling period of 0.1 s and having 4 poles, 1 zero, and 1 sampling period of delay between output and input was identified by the least squares method to model creep. This ARX model was then converted into a continuous-time model as

$$G_2(s) = \frac{0.1804s^3 + 4.181s^2 + 47.84s + 9.404}{s^4 + 14.10s^3 + 610.1s^2 + 1018s + 125.0} \tag{17}$$

The simulated (by using Eq. (17)) and the measured creep displacements of the PEA are compared in Fig. 7.

TABLE 1
ESTIMATED VALUES OF THE PARAMETERS IN EQS. (15) AND (16)

Par.	Value	Par.	Value	Par.	Value
b_0	4.84	p_3	2.85×10^{6}	p_{10}	362
b_1	−745	p_4	2.26×10^{4}	p_{11}	4.58
b_2	5.05×10^{4}	p_5	-3.35×10^{4}	p_{12}	−9.67
b_3	2.85×10^{6}	p_6	3.01×10^{3}	p_{13}	5.17
b_4	5.75×10^{4}	p_7	46.7	p_{14}	1.66
p_1	9.10×10^{5}	p_8	−49.0	p_{15}	−3.03
p_2	-2.77×10^{6}	p_9	−178		

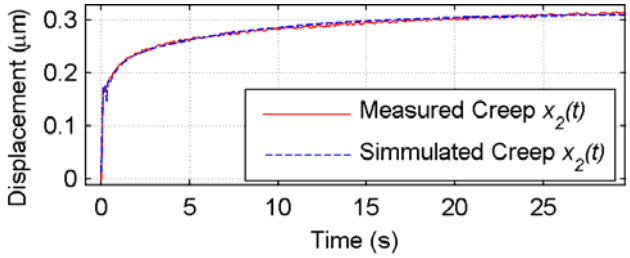

Fig. 7. Measured and simulated PEA creep displacements.

E. Validation of the Model of PEA

The input voltage $u(t)$ used for validating the integrated model of PEA is shown in Fig. 8. In the experiments, $1/T_v$ was set to 50, 100, 200, 300, 400, and 500 Hz. Two of the measured results are shown in Fig. 9; along with the simulation results obtained form the developed model, for the purpose of comparison. The root-mean-square (RMS) errors and the maximum errors calculated over two periods of the $u(t)$ waveform are given in Table 2.

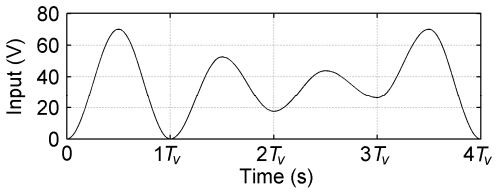

Fig. 8. $u(t)$ used for PEA model validation.

It can be seen from Fig. 9 and Table 2 that the PEA model integrating the RI hysteresis model with the vibration and creep sub-models can represent the dynamics of the PEA with good accuracy (the RMS error is less than 1% of the maximum displacement of the PEA) when the PEA is subject to voltage input signals with a frequency up to 400 Hz. The increase in the RMS error as the input frequency increases is considered as a result of the unmodeled high-frequency dynamics of the PEA. The higher RMS errors in the low frequency compared with those at medium are thought to be caused by the 2nd-order approximation of the vibration dynamics that leads to a smaller phase lag then reality.

TABLE 2
ERRORS IN THE PEA MODEL VALIDATION EXPERIMENTS

$1/T_v$ (Hz)	RMS Error (μm)	Maximum Error (μm)
50	0.093	0.212
100	0.066	0.157
200	0.055	0.127
300	0.059	0.136
400	0.095	0.252
500	0.188	0.593

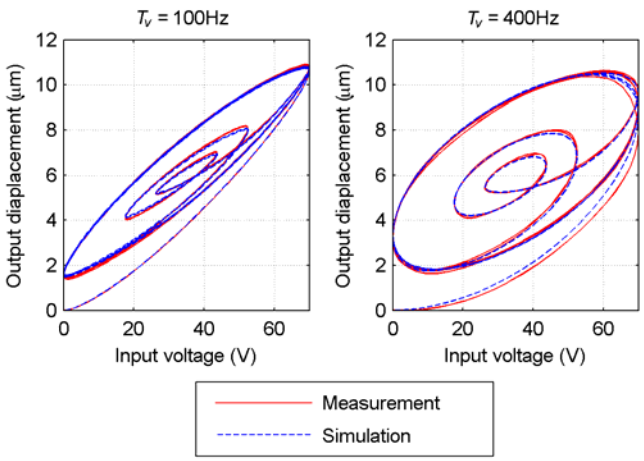

Fig. 9. PEA model validation

5. Conclusions

Accurate models of PEAs are highly desirable for both better understanding the behavior of such actuators and controller design. Such models can usually be constructed by cascading three sub-models together, each representing the RI hysteresis, the vibration dynamics, and the creep effect, respectively. While the vibration dynamics and the creep effect have been accurately modeled in the literature, there are still problems concerning the modeling of RI hysteresis. Traditionally, the CP hysteresis model has been widely used to represent the RI hysteresis in PEAs. However, it is found that the CP hysteresis model is incapable of representing the one-sided hysteresis behavior in PEAs since it cannot represent the initial ascending curve, inducing significant inaccuracy. To solve this problem, in this paper, an integrated model of PEAs was developed based on a new RI hysteresis model which is specifically designed to enable the representation of the one-sided hysteresis behavior. The resultant model of PEAs was validated through experiments. And it is concluded that the resultant model developed is capable of representing the dynamic behaviors of PEAs, including one-sided hysteresis, creep, and vibration dynamics accurately, with an RMS error less than 1% of the maximum PEA displacement and in operations with frequencies up to 400 Hz.

Acknowledgements

Financial support from the Natural Science and Engineering Research Council (NSERC) of Canada to the present study is acknowledged.

References

[1] Devasia, S., Eleftheriou, E., and Moheimani, S.O.R., "A survey of control issues in nanopositioning," *IEEE Transactions on Control Systems Technology*, Vol. 15, No. 5, 2007, pp. 802-823.

[2] Croft, D., Shed, G., and Devasia, S., "Creep, hysteresis, and vibration compensation for piezoactuators: atomic force microscopy application," Journal of Dynamic Systems, Measurement, and Control, Vol. 123, No. 1, 2001, pp. 35-43.

[3] Peng, J. Y. and Chen, X. B., "Hysteresis Models Based on a Novel Hysteresis Unit," Mechatronics, first revision submitted for possible publication, July 2011.

[4] Mayergoyz, I., "Mathematical models of hysteresis," Physical Review Letters, Vol. 56, No. 15, 1986, pp. 1518-1521.

[5] P. Ge, and M. Jouaneh, "Generalized preisach model for hysteresis nonlinearity of piezoceramic actuators," Precision engineering, Vol. 20, No. 2, 1997, pp. 99-111.

[6] H. Hu, R. Ben Mrad, "On the classical Preisach model for hysteresis in piezoceramic actuators," Mechatronics, Vol. 13, No. 2, 2002, pp. 85-94.

[7] G. Song, J. Zhao, X. Zhou, and J. Alexis De Abreu-García, "Tracking control of a piezoceramic actuator with hysteresis compensation using inverse Preisach model," IEEE/ASME Transactions on Mechatronics, Vol. 10, No. 2, 2005, pp. 198-209.

[8] X. Yang, W. Li, Y. Wang, and G. Ye, "Modeling hysteresis in piezo actuator based on neural networks," Lecture Notes in Computer Science, Vol. 5370, 2008, pp. 290-296.

[9] Chen, X. B., Zhang, Q., Kang, D., and Zhang, W., "On the dynamics of piezoactuated positioning systems" Review of Scientific Instruments, Vol. 79, No. 11, 2008, pp. 116101-1 to 116101-3.

6 PID-Based Sliding Mode Control for Piezoelectric Actuators

Submitted to *Mechatronics* for possible publication as:
J. Y. Peng and X. B. Chen, "PID-Based Sliding Mode Control for Piezoelectric Actuators," *Mechatronics*, 2012, under review, manuscript number: MECH-D-11-00116R3.

6.1 Introduction and Objectives

The main difficulty in tracking control of a PEA is to compensate for the nonlinear/difficult-to-model effects, such as hysteresis, creep, and external load. However, according to the model developed in Chapter 5, it is found that such effects can be lumped together and treated as the result of a matched unknown input applied to the vibration dynamics sub-model. As such, sliding mode control, which can compensate for the effects of matched unknown inputs, is very suitable for the task. But there is a chattering problem related to the ideal sliding mode control due to the use of a switching control term. The usual solution to this problem is to use the SMBL method instead, in which the switching control in the ideal sliding mode controller is replaced with a continuous one, e.g. a saturation function. However, such replacement introduces steady error since the continuous control, e.g. the saturation function, is equivalent to a proportional control in the non-saturated interval.

Based on the above discussion, the objective of this paper was to develop a PIDSM control scheme for PEAs based on the comprehensive model of PEAs developed in Chapter 5, in which the switching control in the ideal sliding mode controller is replaced with a PID regulator, as such the chattering problem related to the switching control term in ideal sliding mode control

and the steady state error problem related to the SMBL method is solved.

6.2 Methods

(1) The comprehensive model of PEA developed in Chapter 5 was used with slight modification (incorporating an external loading force to the model).

(2) Since the creep was modeled as a linear system, the vibration dynamics sub-model and the creep sub-model were swapped without affecting the output of the PEA model.

(3) The vibration dynamics sub-model was taken as a nominal model of the PEA. The effects induced by the rate-independent hysteresis, the creep, and the external loading force were treated as the result of a matched unknown input applied to the vibration dynamics sub-model.

(4) Construct an error system whose states are the differences between the desired states and the states of the model of PEA with uncertain inputs.

(5) Design the sliding function and the sliding mode. Since it was found that error system developed in the last step was a second-order system with one input (because the nominal model or the vibration dynamics sub-model of the PEA was a second-order system with one input), the sliding mode was a first order system.

(6) Find the equivalent control.

(7) Instead of using a switching control as in ideal SM control, a PID regulator was employed to compensate for the matched uncertainties and drive the states of the error system to the sliding mode,

(8) The reachability of the sliding mode, hence the stability of the PIDSM control scheme,

was proven. The steady state error (final value of the switching function) was also found to be zero.

(9) Experimental validation of the PIDSM control scheme (a continuous α-β filter was used for state estimation) and comparative studies between PIDSM control, ideal SM control, SMBL control, and PID control were performed.

6.3 Results

Experimental results showed that good tracking control performances with low tracking error (maximum error less than 4% and RMS error less than 3% of the maximum displacement of the PEA when tracking sine waves of up to 150 Hz), low chattering, and no steady state error were achieved by the used of the PIDSM control scheme developed. Also, experimental comparative study showed that the PIDSM controller is superior to the ideal SM controller and the SMBL controller in the aforementioned terms while the performance of the PIDSM controller is comparable to that of the PID controller in low frequency tracking operations (<100 Hz) but the former becomes superior than the latter in high frequency tracking operation.

6.4 Contributions

The contributions of this paper are the implementation of the PIDSM control scheme on a physical plant, especially, on PEAs, and the stability analysis of such a control scheme.

PID-Based Sliding Mode Control for Piezoelectric Actuators

J. Y. Peng* and X. B. Chen

Department of Mechanical Engineering, University of Saskatchewan, Saskatoon, SK S7N5A9 Canada

*Corresponding author. Tel.: +1 306 241 5471. E-mail address: jip747@mail.usask.ca (J. Y. Peng)

Abstract

Nonlinear effects of piezoelectric actuators (PEAs) due to hysteresis and creep can greatly degrade the system performance; and their compensation is a challenging task in the tracking control of PEAs. Nonlinearities of a PEA can be treated as matched unknown inputs to a linear nominal model representative of the PEA dynamics. As such, the sliding mode (SM) control is promising for PEA tracking control due to its ability of rejecting the effects of such unknown inputs. However, the chattering and steady state error associated with SM-based control methods remain to be addressed. This paper presents a study on a proportional-integral-derivative based sliding mode (PIDSM) control for PEAs, in which the discontinuous switching control action in SM control is replaced with a continuous one determined from the PID algorithm. Specifically, based on the model developed for the PEA, the development of a PIDSM controller, along with its stability analysis, is presented. The PIDSM controller was implemented on a typical commercially-available PEA (in combination with a continuous α-β filter for state estimation) and experiments were carried out to examine its tracking control performance. As compared to PID, ideal SM, and SM control with boundary layer (SMCBL), the PIDSM control showed its improved performance in terms of steady state error elimination, chattering suppression, and tracking error suppression.

Keywords: Sliding mode control, PID control, Piezoelectric devices.

1. Introduction

Piezoelectric actuators (PEAs) have been widely used in the fields of micro- and nano-positioning such as atomic force microscopes [1], adaptive optics [2], and micromanipulators [3] due to their high displacement resolution (sub nanometer) and large actuating force (typically a few hundreds of N) [4]. In these applications, the nonlinear effects of PEAs due to hysteresis and creep [1][4], and the distributed nature of their vibration dynamics [5] have shown to be able to significantly degrade the system performance and even lead to system unstable [4]. For improvement, the development of models representative of the PEA nonlinear effects and the development of model-based controllers for compensation have drawn considerable attention.

A number of models for the PEA have been reported in the literature, and they can be generally classified into two categories: phenomenon-based models and physics-based models. The phenomenon-based models of PEA are typically developed based on the experimental results alone, in

which both nonlinear and linear effects are lumped together. In [6]-[10], for example, the hysteresis and the vibration dynamics are combined to form a dynamic or rate-dependent hysteresis model for PEAs. In contrast, in the physics-based models of PEA the linear and nonlinear effects are decoupled by means of individual sub-models of PEAs. In [11]-[14], the PEA was modeled as a cascade of a nonlinear sub-model for the rate-independent hysteresis and a linear sub-model for the vibration dynamics. In [1],[15]-[17], sub-models for the creep effect, either linear or nonlinear, were included in addition to the ones for vibration dynamics and hysteresis.

Based on the models developed for PEAs, various control schemes have been developed and reported in the literature to improve the PEA performance. A significant number of such control schemes are open-loop inversion based or feedforward [1],[10],[18]-[24], in which the control action is generated based on the inverse of the PEA model. For instance, feedforward controllers were developed to compensate for rate-independent hysteresis [18]-[21],[25]. Such feedforward controllers works well in the cases with low operating frequencies, where hysteresis is the dominant effect. In addition to rate-independent hysteresis, the inversion-based compensation for rate-dependent hysteresis [10],[23],[24] as well as creep and vibration dynamics [1],[22] were also pursued, especially for the applications where the operation frequency is high. There are two problems associated with the feedforward schemes, which are the need of *a priori* accurate model for PEA and the computational effort to invert the model. To cope with the these problems, it is rational to use feedback in conjunction with feedforward [11],[24],[26]. Besides, the use of feedback control without the inverse-based feedforward component can also avoid the aforementioned problems; and the controllers are usually developed based on the linear nominal model of the PEA dynamics, while the nonlinearity and uncertainty due to hysteresis and external-loading changes are treated as disturbances to be suppressed. For performance improvement at both low- and high- frequencies, a high-gain feedback is always desirable, but this may not be feasible due to the system stability. With the increase in the operating frequency, there will be a fast phase loss in the frequency response of the closed-loop system due to the high-frequency PEA dynamics, which tends to destabilize the system. This, as a result, limits high gains for use at high frequencies [4][27]. One method for improvement is the use of a notch filter to lower the first resonant peak of the system, thus increasing the gain margin [28]. Adaptive/iterative methods [4],[20],[29],[30] and neuron network methods [31] can also be employed, but limited to in the applications with repetitive reference trajectories. The other method is the use of disturbance observers [32] to estimate and then provide the PEA with a portion of the control input required for disturbance compensation, which allows for the use of low-gain feedback. Since there are additional low pass filtering components in the disturbance observer to make it realizable [32], the capability of disturbance compensation degrades at high operating frequencies. Other advanced feedback controllers were also developed for PEA tracking control based on the idea of minimizing or rejecting the effect of the disturbances on the PEA output displacement. For example, robust controllers [33] were designed to minimize the effects of the disturbances based on a cost function.

If the disturbances can be treated as an unknown input applied to the PEA through the same channel as

the known input, referred to as matched uncertainty/unknown input in the literature, the effect of the disturbances on the PEA performance can be theoretically completely rejected by the use of sliding-mode-based (SM-based) controllers [34]. In its original form (simply referred to as SM control) is a type of variable structure control (VSC) technique, in which the control law is established fully or partially based on a sign function to drive the system states to approach a prescribed sliding surface, thus rejecting the effects of disturbances on the system states. Based on SM control [35]-[38], various modified control techniques have also been reported for tracking control of PEAs. For instance, the integral sliding mode technique was used in [39] to keep the system states on the sliding surface from the beginning (i.e. eliminating the reaching phase); adaptive methods were combined with sliding mode control for the nonlinearity compensation [40]-[42]; and linear matrix inequalities (LIMs) were employed to solve optimization problems involved in the SM control and sliding surface design [43][44]. It is noted that the control actions generated by SM control and most of its modified forms as well are discontinuous due to the use of the sign function. Such discontinuity of the control action induces the so-called chattering problem, which is highly undesirable in practice [34]. This is particularly true in the control of a PEA due to the relatively-high frequency of its first vibration mode. To alleviate the chattering problem, a modified SM control with boundary layer (SMCBL) were developed [34],[45], in which the discontinuous control action was replaced with a continuous approximation of the switching function with a boundary layer. Within the boundary layer, the control scheme is equivalent to a proportional controller. As such, the system states cannot converge to the sliding surface, thus causing a steady state error [34]. This phenomenon was also observed in the PEA control experiments presented later in Section 4. To overcome the steady-state error, meanwhile maintaining the advantage of continuous control action, one promising solution is to replace the discontinuous control action in the SM control with a continuous one that is determined by a proportional-integral-derivative (PID) regulator. This results in the so-called PID-based SM (PIDSM) control [45]. In addition to reducing chattering, the integral component in the PIDSM control can eliminate the steady state error. Another advantage of the PIDSM control is that the bounds on the matched uncertainties, as required by other control schemes (such as SM control and SMCBL) are not required. This is due to the fact that the PID regulator can generate theoretically infinite control signal to force the switching function to zero. Although the effectiveness of the PIDSM has been illustrated by computer simulations in the context of chemical engineering [45]-[47], its applications to physical plants, including PEAs, have not been reported to the best knowledge of authors, and the stability analysis of PIDSM control is also void in the literature. Furthermore, since the PEA nonlinearities and other disturbances can be treated as matched uncertainties for compensation, this eliminates the need of accurate models for the PEA nonlinearities in the PIDSM control, which is highly desirable. As motivated, this paper presents the development of the PIDSM control scheme for the PEA tracking control and its stability analysis in Sections 2 and 3. Experiments were also performed to illustrate the effectiveness of the PIDSM control scheme (in combination with a continuous α-β filter for state estimation), as compared to other SM-based control schemes and PID control, in Section 4.

2. Model of Piezoelectric Actuators

Fig. 1(a) shows the schematic of a PEA, in which the end-effector affixed to the base through flexure hinges is driven by a piezoelectric element. A physics-based model is used to represent the PEA in this study, i.e. the nonlinear and linear effects of the PEA are decoupled by means of individual sub-models that are connected in cascade. The block diagram of this model is shown in Fig. 1(b), in which the blocks of H, V, and F_c represents the PEA hysteresis, dynamics, and creep, respectively.

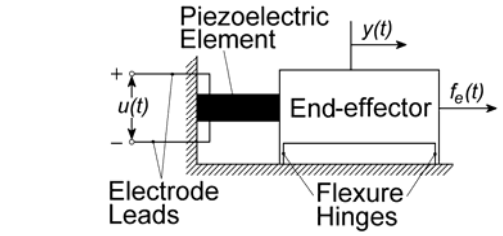

(a)

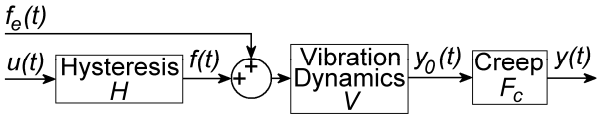

(b)

Fig. 1 (a) Schematic of a PEA and (b) its physics-based model.

In particular, the block H represents the nonlinear hysteretic relationship between the input voltage, $u(t)$, and the internal actuating force, $f(t)$. Such hysteresis is the dominant form of PEA nonlinearity [4] and typically represented by means of either rate-independent hysteresis models, such as the classical Preisach hysteresis model [1][11], or the differential-equation-based model [5]. In the development of a SM-based controller for PEAs as presented later, the effect of hysteresis is treated as a matched unknown input to the block V, so the accurate representation of hysteresis is not needed. The block V represents the vibration dynamics relating the internal actuating force, $f(t)$, and the external force, $f_e(t)$, to the end-effector displacement without the consideration of creep. Although the vibration dynamics of a PEA is distributed in nature, it can be approximated by a linear combination of several second-order systems [48], or one second-order system if the mass of the end-effector driven by the piezoelectric element is much larger than that of the piezoelectric element itself [49]. The error of such an approximation, along with the effect of $f_e(t)$, can also be lumped as a matched unknown input to the block V. The block F_c in Fig. 1(b) represents the creep, which can be either linear [1] or nonlinear [17]. In the present study, a linear sub-model is assumed to be used for F_c and then the blocks of F_c and V are swapped without effecting the output displacement, $y(t)$. As such, the creep effect F_c can also be treated as a part of the matched uncertain input to the block V.

If the second-order system approximation is used for the block V and the approximation error, along

with the effects of $f_e(t)$, H, and F_c, are lumped together as the matched unknown input to the block V, one has

$$\ddot{y}(t)+2\xi\omega_n\dot{y}(t)+\omega_n^2 y(t)=\omega_n^2 K_1\left[f(t)+f_e(t)+\varepsilon_0(t)\right] \tag{1}$$

where ξ, ω_n, and K_1 are the damping ratio, the natural frequency, and the steady state gain of the second-order system, respectively. $\varepsilon_0(t)$ is the matched input uncertainties to the block V, accounting for F_c and the approximation error due to the use of a second-order system. Notably, $f_e(t)$, and $\varepsilon_0(t)$ are unknown, but bounded. Recall that $f(t)$ is the internal actuating force upon the application of $u(t)$, which is dominated by the PEA hysteresis [50]. As such, $f(t)$ can be considered as the combination of a linear component proportional to $u(t)$ and a non-linear component associated with hysteresis [36][39][51], as shown in Fig. 2. Mathematically, this is given by

$$f(t)=K_2u(t)+\varepsilon_1(t) \tag{2}$$

where K_2 is the nominal gain from $u(t)$ to $f(t)$; and $\varepsilon_1(t)$ is the non-linear component associated with hysteresis and bounded in practice.

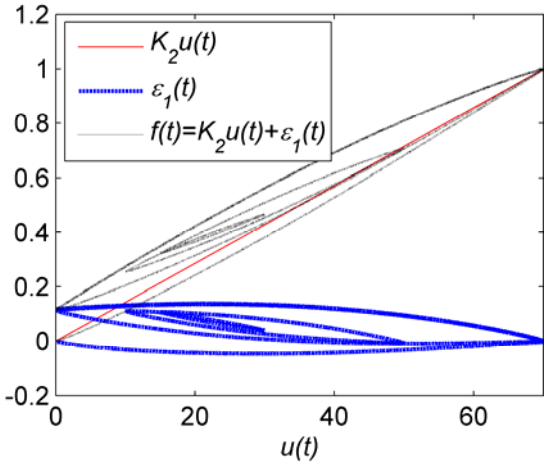

Fig. 2 Illustration of the decomposition of $f(t)$ in Eq. (2).

For the convenience of following discussion, the unknown terms of $f_e(t), \varepsilon_0(t)$, and $\varepsilon_1(t)$ in Eq. (1) and Eq. (2) are lumped together into a single term, i.e., $\varepsilon(t)=K_2^{-1}\left[f_e(t)+\varepsilon_0(t)+\varepsilon_1(t)\right]$, which is considered as the matched unknown input to the second-order system. Denoting $x_1=y$, $x_2=\dot{y}$, and let $K=K_1K_2$, one has the following state space representation for the PEA, as derived from Eq. (1) and Eq. (2)

$$\begin{aligned}\begin{bmatrix}\dot{x}_1\\ \dot{x}_2\end{bmatrix}&=\begin{bmatrix}0 & 1\\ -\omega_n^2 & -2\xi\omega_n\end{bmatrix}\begin{bmatrix}x_1\\ x_2\end{bmatrix}+\begin{bmatrix}0\\ K\omega_n^2\end{bmatrix}(u+\varepsilon)=\dot{X}=AX+Bu+B\varepsilon\\ y&=\begin{bmatrix}1 & 0\end{bmatrix}\begin{bmatrix}x_1\\ x_2\end{bmatrix}=CX\end{aligned} \tag{3}$$

Eq. (3) is referred to as the nominal model of the PEA if $\varepsilon(t)\equiv 0$.

3. PID-Based Sliding Mode Control and Its Stability

3.1 PID-Based Sliding Model (PIDSM) Control

As discussed in Section 1, the PIDSM controller is modified from a SM controller by replacing the switching control action with a continuous one generated by a PID regulator, such that the chattering associated with SM control can be suppressed and the steady state error associated with SMCBL can be eliminated. In this study, the PIDSM tracking controller developed for the PEA takes the structure of state tracking controller, which forces the state vector (consisting of the output displacement and velocity) of the PEA to track the desired or reference state vector. The development of such a controller is introduced as follows.

Let w be the desired output displacement with the second-order derivative existing and W be the desired or reference state vector, i.e., $W = \begin{bmatrix} w_1 & w_2 \end{bmatrix}^T = \begin{bmatrix} w & \dot{w} \end{bmatrix}^T$. The state tracking error vector or the difference between the state vector of the PEA, X, and the desired state vector, W, is

$$e = X - W \tag{4}$$

where $e = \begin{bmatrix} e_1 & e_2 \end{bmatrix}^T = \begin{bmatrix} x_1 - w_1 & x_2 - w_2 \end{bmatrix}^T = \begin{bmatrix} x_1 - w & x_2 - \dot{w} \end{bmatrix}^T$. From Eqs. (3) and (4), the error system is described by

$$\dot{e} = \dot{X} - \dot{W} = Ae + AW + Bu + B\varepsilon - \dot{W} \tag{5}$$

The objective of control is to find the control action $u(t)$ such that the state vector e of the error system Eq. (5) can be brought to the origin, i.e., $e_1 = 0$ and $e_2 = 0$.

Notice that the terms of AW and $-\dot{W}$ in Eq. (5) are known, hence their effects on $\dot{e}$ can be compensated by a part of u, which is given by the first term on the right hand side in the following equation:

$$u = \left(B^T B\right)^{-1} B^T \left(\dot{W} - AW\right) + u_{SM} \tag{6}$$

The other part of u, i.e. u_{SM}, is the control action generated by a PIDSM regulator.

Substituting Eq. (6) into Eq. (5) and making use of Eq. (3) yields

$$\dot{e} = Ae + Bu_{SM} + B\varepsilon = \begin{bmatrix} e_2 \\ A_{21}e_1 + A_{22}e_2 + B_2 u_{SM} + B_2\varepsilon \end{bmatrix} \tag{7}$$

where $A_{21} = -\omega_n^2$, $A_{22} = -2\xi\omega_n$, and $B_2 = K\omega_n^2$. To determine u_{SM}, the sliding surface needs to be defined. In the present study, it is defined by letting the switching function be zero. The switching function is a linear combination of the states of the error system Eq. (5), i.e.

$$q = \Lambda e = \begin{bmatrix} m & 1 \end{bmatrix} \begin{bmatrix} e_1 & e_2 \end{bmatrix}^T \tag{8}$$

where m is the parameter to characterize the sliding surface which meets the following equation

$$\Lambda e = me_1 + e_2 = me_1 + \dot{e}_1 = 0 \tag{9}$$

The motion of the system Eq. (7) on the sliding surface Eq. (9) is referred to as the sliding motion.

According to Eq. (9), it is governed by the first-order autonomous system

$$\dot{e}_1 = -me_1 \tag{10}$$

It can be seen from Eq. (10) that $m > 0$ is required to ensure the stability of the sliding motion. Eq. (10) also indicates that the magnitude of m should be chosen, depending on the desired rate of convergence of e_1 to 0. From Eqs. (7) and (9), during sliding motion one has

$$\begin{aligned} \dot{q} &= \Lambda\dot{e} = m\dot{e}_1 + \dot{e}_2 = me_2 + \dot{e}_2 \\ &= me_2 + A_{21}e_1 + A_{22}e_2 + B_2u_{SM} + B_2\varepsilon = 0 \end{aligned} \tag{11}$$

In the above equation, $B_2\varepsilon$ is associated with the lumped uncertainty, and the other terms of me_2, $A_{21}e_1$, and $A_{22}e_2$ can be estimated by means of a state estimator and referred to as measurable terms afterwards. As such, one can divide u_{SM} into two parts, i.e.

$$u_{SM} = -B_2^{-1}\left(me_2 + A_{21}e_1 + A_{22}e_2\right) + u_3 \tag{12}$$

where $-B_2^{-1}\left(me_2 + A_{21}e_1 + A_{22}e_2\right)$ is the equivalent control that compensates for the measurable terms and maintains the states of the system Eq. (7) on the sliding surface Eq. (9) given that $\varepsilon = 0$; and u_3 is the control action for compensating for the lumped uncertainty, i.e., $B_2\varepsilon$. In SM control, u_3 takes the form of

$$u_3 = -\eta\,\mathrm{sgn}(q) \tag{13}$$

where η is a positive number larger or equal to the bound of ε. Due to the discontinuity of u_3, chattering is present in the control of PEAs. In SMCBL, in order to reduce chattering, a continuous function such as the saturation function may be used to replace the sign function in Eq. (13). However, the limited feedback gain of u_3 would introduce a steady state error in the PEA displacement. To solve this problem, one solution is to use the PIDSM control, in which $u_3(q)$ takes the form of a PID component as

$$u_3 = -\left(P_c q + I_c\int_0^t q\,\mathrm{d}t + D_c\dot{q}\right) \tag{14}$$

where $P_c \geq 0$, $I_c \geq 0$, and $D_c \geq 0$ are the PID parameters. Thus, the control action u can be determined from Eqs. (6), (12), and (14).

3.2 PIDSM Stability

The PID parameters must satisfy certain requirements to ensure the reachability of the sliding surface such that if combined with the stability condition of the sliding motion ($m > 0$), the PIDSMC is stable. Such requirements are discussed as follows. Substituting Eqs. (12) and (14) into Eq. (11) without equating q or $\dot{q}$ to zero yields

$$\dot{q} = -B_2\left(P_c q + I_c\int_0^t q\,\mathrm{d}t + D_c\dot{q}\right) + B_2\varepsilon \tag{15}$$

The reachability condition of the sliding surface is given by the following theorem.

Theorem: *If both the initial value of switching function and the uncertainty in the system defined by Eq.*

(15) *are bounded, i.e.,* $|q(0)| \le q_{0\max} < \infty$ *and* $|\varepsilon| \le \varepsilon_{\max} < \infty$, *then*

(a) *the system defined by Eq.* (15) *is asymptotically stable if and only if the roots of* $(B_2 D_c + 1)s^2 + B_2 P_c s + B_2 I_c = 0$ *have negative real parts;*

(b) *the sliding surface* $q = 0$ *is asymptotically reachable if Eq.* (15) *is asymptotically stable.*

Proof:

(a) Divide q into two parts, i.e.

$$q(t) = q_1(t) + q_0(t) \tag{16}$$

where $q_0(t) \equiv q(0)$ is the initial value of q and $q_1(0) = 0$. Then Eq. (15) can be rewritten as

$$\dot{q} = \dot{q}_1 = -B_2 P_c q_1 - B_2 P_c q_0 - B_2 I_c \int_0^t q_1 \mathrm{d}t - B_2 I_c \int_0^t q_0 \mathrm{d}t - B_2 D_c \dot{q}_1 + B_2 \varepsilon \tag{17}$$

q_0 and ε can be treated as two inputs to the system Eq. (17). Since the system Eq. (17) is linear, it can be treated as the sum of two subsystems with q_0 and ε as their inputs, respectively. The output of these subsystems are q_{11} and q_{12}, respectively, i.e.

$$\begin{aligned} q_1(t) &= q_{11}(t) + q_{12}(t) \\ \dot{q}_1(t) &= \dot{q}_{11}(t) + \dot{q}_{12}(t) \\ q_1(0) &= q_{11}(0) = q_{12}(0) = 0 \end{aligned} \tag{18}$$

The combined system Eq. (17), thus the system Eq. (15), is asymptotically stable if and only if these two subsystems are asymptotically stable.

For the first system

$$\dot{q}_{11} = -B_2 P_c q_{11} - B_2 P_c q_0 - B_2 I_c \int_0^t q_{11} \mathrm{d}t - B_2 I_c \int_0^t q_0 \mathrm{d}t - B_2 D_c \dot{q}_{11} \tag{19}$$

Recall that $q_{11}(0) = 0$, the transfer function of the above system is

$$\frac{Q_{11}(s)}{Q_0(s)} = \frac{-B_2 P_c s - B_2 I_c}{(B_2 D_c + 1)s^2 + B_2 P_c s + B_2 I_c} \tag{20}$$

where $Q_{11}(s)$ and $Q_0(s)$ are the Laplace transforms of $q_{11}(t)$ and $q_0(t)$, respectively.

For the second system

$$\dot{q}_{12} = -B_2 P q_{12} - B_2 I \int_0^t q_{12} \mathrm{d}t - B_2 D \dot{q}_{12} + B_2 \varepsilon \tag{21}$$

Recall that $q_{12}(0) = 0$, the transfer function of this system is

$$\frac{Q_{12}(s)}{\Sigma(s)} = \frac{B_2 s}{(B_2 D_c + 1)s^2 + B_2 P_c s + B_2 I_c} \tag{22}$$

where $Q_{12}(s)$ and $\Sigma(s)$ are the Laplace transforms of $q_{12}(t)$ and $\varepsilon(t)$, respectively.

Eqs. (15) and (17) are asymptotically stable if and only if Eqs. (20) and (22) are asymptotically stable or the poles of Eqs. (20) and (22) are located in the left-half s-plane. This requires the roots of $(B_2 D_c + 1)s^2 + B_2 P_c s + B_2 I_c = 0$ have negative real parts.

(b) If Eq. (15) (hence Eq. (17)) is asymptotically stable, the application of the final value theorem of the Laplace transform to $Q_{11}(s)$ yields

$$q_{11}(\infty)=\lim_{s\to 0} sQ_{11}(s)=\lim_{s\to 0}\frac{s(-B_2P_cs-B_2I_c)Q_0(s)}{(B_2D_c+1)s^2+B_2P_cs+B_2I_c} \tag{23}$$

Recall that $q_0(t)\equiv q(0)$ and $|q(0)|\le q_{0\max}<\infty$, one has $Q_0(s)=q(0)/s$. Eq. (23) can be reduced to

$$q_{11}(\infty)=\lim_{s\to 0}\frac{s(-B_2P_cs-B_2I_c)\dfrac{q(0)}{s}}{(B_2D_c+1)s^2+B_2P_cs+B_2I_c}=-q(0) \tag{24}$$

Applying the final value theorem of the Laplace transform to $Q_{12}(s)$ yields

$$q_{12}(\infty)=\lim_{s\to 0} sQ_{12}(s)=\lim_{s\to 0}\frac{s^2B_2\Sigma(s)}{(B_2D_c+1)s^2+B_2P_cs+B_2I_c} \tag{25}$$

Denote $\mathrm{Re}(s)=s_r$ and $\mathrm{Im}(s)=s_i$. Notice that $|\varepsilon|\le\varepsilon_{\max}<\infty$, the Laplace transform of $\varepsilon(t)$, i.e. $\Sigma(s)$, is

$$\begin{aligned}|\Sigma(s)|&=\left|\int_0^{+\infty}e^{-st}\varepsilon(t)\mathrm{d}t\right|\le\int_0^{+\infty}\left|e^{-st}\varepsilon(t)\right|\mathrm{d}t\le\varepsilon_{\max}\int_0^{+\infty}\left|e^{-st}\right|\mathrm{d}t=\varepsilon_{\max}\int_0^{+\infty}\left|e^{-(s_r+is_i)t}\right|\mathrm{d}t\\&\le\varepsilon_{\max}\int_0^{+\infty}\left|e^{-s_rt}\right|\left|e^{-is_it}\right|\mathrm{d}t=\varepsilon_{\max}\int_0^{+\infty}\left|e^{-s_rt}\right|\left|\cos(-s_it)+i\sin(-s_it)\right|\mathrm{d}t\\&=\varepsilon_{\max}\int_0^{+\infty}e^{-s_rt}\mathrm{d}t=\frac{\varepsilon_{\max}}{-s_r}e^{-s_rt}\Big|_0^{+\infty}=\frac{\varepsilon_{\max}}{s_r}\end{aligned} \tag{26}$$

The region of convergence of $\Sigma(s)$ in the worst case scenario (i.e. $|\varepsilon(t)|$ is exponentially bounded only by $e^{-0t}\varepsilon_{\max}$, but not by any $e^{-\sigma t}\varepsilon_{\max}$ where $\sigma>0$) is the region of $\mathrm{Re}(s)=s_r>0$ on the s-plane. This implies that in the worst case scenario, $\Sigma(s)$ and hence $s^2B_2\Sigma(s)$ are analytic in the region of $\mathrm{Re}(s)=s_r>0$. So $|s^2B_2\Sigma(s)|$ is continuous in this region, leading to

$$\begin{aligned}\lim_{s\to 0}\left(\left|s^2B_2\Sigma(s)\right|\right)&=\lim_{|s|\to 0,\,s_r\to 0^+}\left(\left|s^2B_2\Sigma(s)\right|\right)\\&=\lim_{s_r\to 0^+,\,s_i\to 0}\left(\left|(s_r+is_i)(s_r+is_i)B_2\Sigma(s_r+is_i)\right|\right)\\&\le\lim_{s_r\to 0^+,\,s_i\to 0}\left(\left|s_r+is_i\right|\left|s_r+is_i\right|\left|B_2\right|\frac{\varepsilon_{\max}}{s_r}\right)\\&=\lim_{s_r\to 0^+}\left(s_r^2\left|B_2\right|\frac{\varepsilon_{\max}}{s_r}\right)=0\end{aligned} \tag{27}$$

In cases other than the above worst case scenario, $\Sigma(s)$ still converges on $\mathrm{Re}(s)=s_r>0$ since $|\varepsilon(t)|$ is still exponentially bounded by $e^{-0t}\varepsilon_{\max}$, so Eq. (27) is also applicable. Also, there must be

$$\left|s^2B_2\Sigma(s)\right|\ge 0 \tag{28}$$

Then it can be concluded from Eqs. (27) and (28) that

$$\lim_{s\to 0}s^2B_2\Sigma(s)=0 \tag{29}$$

Hence

$$q_{12}(\infty)=\lim_{s\to 0}\frac{s^2B_2\Sigma(s)}{(B_2D_c+1)s^2+B_2P_cs+B_2I_c}=\frac{0}{B_2I_c} \tag{30}$$

Since there must be $I_c\neq 0$ for Eq. (15) to be asymptotically stable and $B_2\neq 0$, one has

$$q_{12}(\infty)=0 \tag{31}$$

Substituting Eqs. (18), (24), and (31) into Eq. (16) yields

$$q(\infty)=q_1(\infty)+q_0(\infty)=q_{11}(\infty)+q_{12}(\infty)+q(0)=-q(0)+0+q(0)=0 \tag{32}$$

Therefore, the sliding surface $q=0$ is reachable and sliding motion occurs afterwards.

■

Remark: It can be seen from the above discussion that the sliding surface is reachable if and only if the PID parameters are chosen such that the roots of $(B_2D_c+1)s^2+B_2P_cs+B_2I_c=0$ have negative real parts. Furthermore, if the reachability condition of the sliding surface and the stability condition of the sliding motion ($m>0$) are met simultaneously, the convergence of e_1 to 0 during the sliding motion govern by Eq. (10) ensures the zero steady state error.

3.3 State Estimation

To implement the control law Eqs. (6), (12), and (14), the state vector of the plant must be known. For the case of PEA concerned in this paper, only the output displacement of the PEA is measured and a state observer is required to estimate the displacement velocity of the PEA. Given that the model of the lumped uncertainties in Eq. (3) is unknown, the observers used should not be model based. For this purpose, the α-β filter was adopted for use in the present study, which takes the following form for the PEA state estimation

$$\hat{x}_1(kT)=\hat{x}_1(kT-T)+T\hat{x}_2(kT-T)+\alpha[y(kT)-\hat{x}_1(kT)] \tag{33}$$

$$\hat{x}_2(kT)=\hat{x}_2(kT-T)+\beta[y(kT)-\hat{x}_1(kT)]/T \tag{34}$$

where $k=0,1,2,\cdots$; T is the sampling interval; and $\hat{x}_1$ and $\hat{x}_2$ are the estimated displacement and velocities, respectively. It can be seen that the α-β filter is a discrete-time estimator. However, the PIDSM controller developed in this study is in the continuous-time domain. As such, a continuous-time version of the α-β filter [52], which was obtain by taking the inverse impulse invariant transform of (33) and (34), was employed. The transfer functions of the continuous-time α-β filter are

$$G_1(s)=\frac{\hat{X}_1(s)}{Y(s)}=\frac{\omega_{fn}^2+\omega_{fn}(2\xi_f-\omega_{fn}T)s}{s^2+2\xi_f\omega_{fn}s+\omega_{fn}^2} \tag{35}$$

$$G_2(s)=\frac{\hat{X}_2(s)}{Y(s)}=\frac{s\omega_{fn}^2}{s^2+2\xi_f\omega_{fn}s+\omega_{fn}^2} \tag{36}$$

where $\hat{X}_1(s)$, $\hat{X}_2(s)$, and $Y(s)$ are the Laplace transform of $\hat{x}_1$, $\hat{x}_2$, and y, respectively; and ξ_f

and ω_{fn} are the damping ratio and the natural frequency of the continuous-time α-β filter, respectively. ξ_f, ω_{fn}, and T are related to α and β by

$$\alpha = \omega_{fn} T\left(2\xi_f - \omega_{fn} T/2\right) \tag{37}$$

$$\beta = \left(\omega_{fn} T\right)^2 \tag{38}$$

Eqs. (35) and (36) indicate that the continuous-time α-β filter is stable if the roots of $s^2 + 2\xi_f \omega_{fn} s + \omega_{fn}^2 = 0$ have negative real parts. The block diagram of the closed-loop system with the continuous-time α-β filter is shown in Fig. 3. The control scheme in Fig. 3 is referred to as the PIDSM Controller + α-β filter scheme or the PIDSMC + α-β filter scheme in the following discussion.

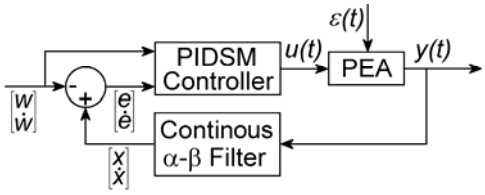

Fig. 3 Block diagram of the closed-loop system.

3.4 Stability of the Closed-loop System

The closed-loop system shown in Fig. 3 is actually a linear system with a known input $w(t)$ and an unknown input $\varepsilon(t)$ and its stability condition can be examined through its transfer function. In terms of the responses to the inputs of $w(t)$ and $\varepsilon(t)$, the output displacement $y(t)$ can be expressed as

$$y(t) = y_1(t) + y_2(t) \tag{39}$$

where $y_1(t)$ is the response to $w(t)$ and $y_2(t)$ is the response to $\varepsilon(t)$. Then, by using Eqs. (3), (4) (replace X with $\hat{X} = [\hat{x}_1 \quad \hat{x}_2]^T$), (8), (6), (12), (14), (35), and (36), the transfer functions of the aforementioned two responses can be derived and given by

$$\begin{aligned} G_3 &= \frac{Y_1(s)}{W(s)} \\ &= (s+m)\left(s^2 + 2\xi_f \omega_{fn} s + \omega_{fn}^2\right)\left(s^2 + B_2 D_c s^2 + B_2 P_c s + B_2 I_c\right) \\ &\quad /[s^5 + \left(2\xi_f \omega_{fn} - A_{22}\right)s^4 \\ &\quad + \left(\omega_{fn}^2 - A_{21} - 2A_{22}\xi_f \omega_{fn} + B_2 D_c \omega_{fn}^2 + 2B_2 D_c \xi_f \omega_{fn} m - B_2 D_c T m \omega_{fn}^2\right)s^3 \\ &\quad + \left(m\omega_{fn}^2 + B_2 P_c \omega_{fn}^2 - A_{21} T \omega_{fn}^2 + B_2 D_c m \omega_{fn}^2 + 2B_2 P_c \xi_f \omega_{fn} m - B_2 P_c T m \omega_{fn}^2\right)s^2 \\ &\quad + \left(B_2 I_c \omega_{fn}^2 + B_2 P_c m \omega_{fn}^2 + 2B_2 I_c \xi_f \omega_{fn} m - B_2 I_c T m \omega_{fn}^2\right)s \\ &\quad + B_2 I_c m \omega_{fn}^2] \end{aligned} \tag{40}$$

$$
\begin{aligned}
G_4 &= \frac{Y_2(s)}{\Sigma(s)} \\
&= \left(B_2 s^3 + 2B_2\xi_f\omega_{fn}s^2 + B_2\omega_{fn}^2 s\right)/[s^5 + \left(2\xi_f\omega_{fn} - A_{22}\right)s^4 \\
&+ \left(\omega_{fn}^2 - A_{21} - 2A_{22}\xi_f\omega_{fn} + B_2D_c\omega_{fn}^2 + 2B_2D_c\xi_f\omega_{fn}m - B_2D_cTm\omega_{fn}^2\right)s^3 \\
&+ \left(m\omega_{fn}^2 + B_2P_c\omega_{fn}^2 - A_{21}T\omega_{fn}^2 + B_2D_cm\omega_{fn}^2 + 2B_2P_c\xi_f\omega_{fn}m - B_2P_cTm\omega_{fn}^2\right)s^2 \\
&+ \left(B_2I_c\omega_{fn}^2 + B_2P_cm\omega_{fn}^2 + 2B_2I_c\xi_f\omega_{fn}m - B_2I_cTm\omega_{fn}^2\right)s \\
&+ B_2I_cm\omega_{fn}^2]
\end{aligned}
\tag{41}
$$

where $Y_1(s)$, $Y_2(s)$, $W(s)$, and $\Sigma(s)$ are the Laplace transform of $y_1(t)$, $y_2(t)$, $w(t)$, and $\varepsilon(t)$, respectively. The closed loop system is stable if and only if the poles of the transfer functions given in Eqs. (40) and (41) have negative real parts. This condition has to be satisfied in the design of the PIDSMC + α-β filter scheme.

4. Experiments and Simulations

4.1 Experiment Setup and PEA Model Parameter Identification

Experimental verifications of the PIDSMC + α-β filter scheme as compared to other control schemes were carried out on a typical commercially-available PEA (P-753, Physik Instrumente). The actuator can generate motion in a range of 15 μm with a resolution of 0.5 nm. For displacement measurements, the built-in capacitive displacement sensor of the actuator with a resolution of 1 nm was used. Both the actuator and the sensor were interfaced to a host computer via an I/O board (PCI-DAS1602/16, Measurement Computing Corporation) and MATLAB SIMULINK was used for all programming. The displacements presented in this study were measured with a sampling interval $\Delta T = 0.00005\,\text{s}$ and in a time period of 8 seconds.

The parameters in the PEA model given in Eq. (3) were identified experimentally. In the experiments, sinusoidal voltages of 70V magnitude with varying frequencies (0 Hz, 1 Hz, 5 Hz, 10 Hz, 20 Hz, 50 Hz, 100 Hz, 200 Hz, 300 Hz, 400 Hz, 500 Hz, 600 Hz, 700 Hz, 800 Hz, 900 Hz, and 1000 Hz) were applied the PEA and its displacement was measured. The phase differences between the measured PEA displacements and the sinusoidal input voltages were then evaluated and given in Fig. 4 as a function of frequency. The damping ratio ξ and the natural frequency ω_n were identified by fitting the phase-frequency response of the nominal model of the PEA (Eq. (3) with $\varepsilon(t) \equiv 0$), given by

$$
\varphi(\omega) = 0° - \angle\left(\omega_n^2 - \omega^2 + 2\xi\omega_n\omega j\right) = -\tan^{-1}\left(\frac{2\xi\omega_n\omega}{\omega_n^2 - \omega^2}\right) \tag{42}
$$

to the measured phase-frequency response of the PEA. By using the Levenberg-Marquardt algorithm to solve the nonlinear least square fitting problem, the parameters were found to be $\xi = 0.7876$ and $\omega_n = 5352\,\text{rad}/s$, with the fitting result shown in Fig. 4. Eventually, the nominal gain K in Eq. (3) was calculated by using $K = y_{\max}/u_{\max}$, where $y_{\max}$ is the measured PEA displacement upon the application

of the voltage with a maximum allowable amplitude $u_{\max}$. This leads to $K = 0.1347\mu\text{m/V}$. To illustrate the effectiveness of the identified PEA model, the frequency responses of the measurements and model predictions are shown in Fig. 4 for comparison.

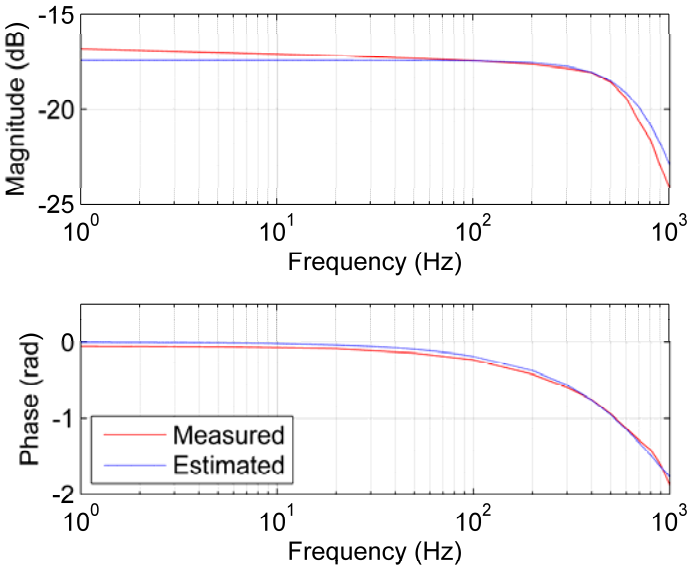

Fig. 4 Comparison of the PEA frequency responses between the measurements and model

4.2 Effectiveness of the PIDSMC + α-β Filter Scheme

4.2.1 Verification of the Sliding Mode Behavior

Since the discontinuous control term in the ideal SM control is replaced with a control signal generated by a continuous PID regulator in the PIDSM controller, it is desirable to verify whether the sliding mode behavior still occurs as predicted by the theory given in Sections 3.1 and 3.2. In this section, the sliding mode behaviors of the PIDSM controller and the PIDSMC + α-β filter scheme are examined by both simulation and experiment.

Firstly, a simulation was performed using the block diagram shown in Fig. 5 (a). The purpose of this simulation is to examine the sliding mode behavior of the PIDSM controller without the presence of state estimator. The nominal model, i.e., Eq. (3) with $\varepsilon(t) \equiv 0$, was used for the PEA model in Fig. 5 (a) with the parameters identified in Section 4.1 and initial conditions of $X_0 = [x_{10} \quad x_{20}]^T = [5 \quad 0]^T$. The desired displacement was set as $w(t) \equiv 0$; while the PIDSM controller parameters were $m = 2200$, $P_c = 0.004$, $I_c = 0.06$, and $D_c = 1 \times 10^{-8}$ such that the closed-loop system shown in Fig. 5 (a) was stable and that the sliding motion was clearly observed. The simulation was performed for a period of 1 second. The resulting phase portrait of e_1 vs. e_2 is shown in Fig. 5 (b), along with the theoretical sliding surface determined by Eq. (9). It can be observed that the sliding motion does occur and the sliding surface is in accord with that given by Eq. (9).

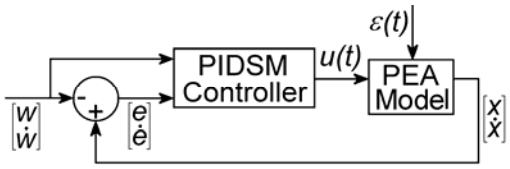

(a)

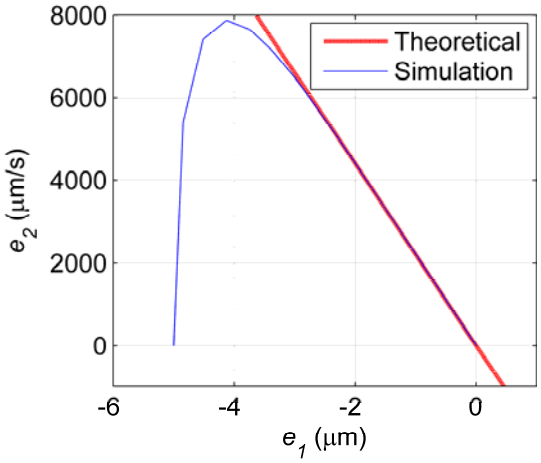

(b)

Fig. 5 Verification of the sliding mode behavior of the PIDSM controller through simulation: (a) the block diagram of the system used in simulation and (b) the simulated phase portrait and the theoretical sliding surface determined by Eq. (9).

Secondly, an experiment was performed on the system shown in Fig. 3. The purpose of this experiment is to examine the sliding mode behavior of the PIDSMC + α-β filter scheme. The initial condition of the PEA was $X_0 = \begin{bmatrix} x_{10} & x_{20} \end{bmatrix}^T = \begin{bmatrix} 0 & 0 \end{bmatrix}^T$ and the desired displacement was $w(t) \equiv 5$. The parameters of the continuous-time α-β filter were set as $\xi_f = 1/\sqrt{2}$ and $\omega_{fn} = 1000\pi$ rad/s such that there was no peaking in its frequency response and that the cutoff frequency was 500 Hz. The parameters of the PIDSM controller had the same values as those used in the simulation above. With the aforementioned parameters, the closed-loop system in Fig. 3 is stable since the poles of the transfer functions Eqs. (40) and (41) are -7606.5, -1919.2+5237.8*i*, -1919.2-5237.8*i*, -1413.5, and -15, all with negative real parts. The experiment was performed for a period of 1 second. The measured phase portrait of $e_1 = \hat{x}_1 - w_1$ vs. $e_2 = \hat{x}_2 - w_2$ is shown in Fig. 6 along with the theoretical sliding surface determined by Eq. (9). It can be observed that the measured trajectory of e_1 and e_2 oscillates around and eventually converges to the theoretically-predicted sliding surface. The oscillation of the measure phase portrait in Fig. 6 might be mainly caused by the unmatched uncertainty introduced by the continuous-time α-β filter in the channel of e_1.

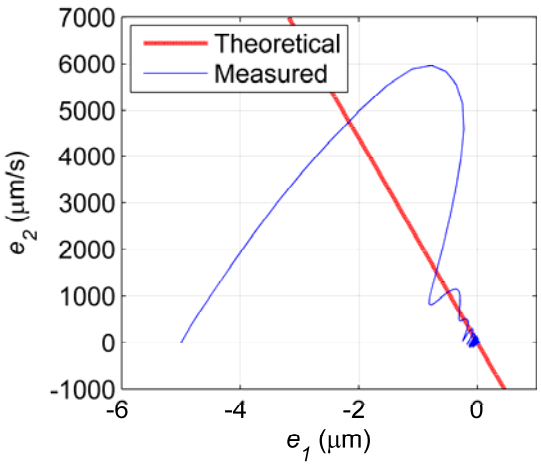

Fig. 6 Measured phase portrait of e_1 vs. e_2, showing the sliding mode behavior of the PIDSMC + α-β filter scheme, as compared to the theoretical sliding surface determined by Eq. (9).

4.2.2 Hysteresis Compensation

Experiments were performed to illustrate the effectiveness of the PIDSMC + α-β filter scheme as applied to the compensation for the PEA hysteresis.

The parameters of the continuous-time α-β filter remain the same as those used in the previous experiment. The parameters of the PIDSM controller were chosen as follows. The value of m was set to $m = 22000$ such that the sliding motion governed by Eq. (10) is stable. Also, a high rate of convergence of e_1 to 0 during the sliding motion was achieved as indicated by the resultant small rise time of the system Eq. (10), which is given by $T_r = -m^{-1}(\ln 0.1 - \ln 0.9) \approx 10^{-4}$s. The PID parameters in Eq. (14) were selected such that the reachability condition of the sliding surface given in Section 3.2 was satisfied and that the closed-loop system was stable according to Section 3.4. On this basis, their values were tuned for the best performance when tracking $w(t) = 5\sin(2\pi \cdot 10t) + 5$, leading to $P_c = 0.0004$, $I_c = 1$, and $D_c = 10^{-8}$. With these parameters, the poles of the transfer functions Eqs. (40) and (41) are given by -7779.3, -1435.4+5296.7i, -1435.4-5296.7i, -1111.6+1529.8i, and -1111.6-1529.8i, suggesting that the system is stable.

With the parameters of the control scheme set, a tracking control experiment with $w(t) = 5\sin(2\pi \cdot 10t) + 5$ was performed. The plot of the desired displacement versus the measured displacement was compared with the one obtained without the use of control scheme (or the open-loop experiment), as shown in Fig. 7. The open-loop experiment was conducted by applying an input voltage of $u(t) = 6.86w(t)$ to the PEA and the scaling factor was chosen as 6.86 such that the input voltage in the open-loop experiment produced the same amplitude of displacement as the previous experiment. From Fig. 7, it can be seen that the hysteresis of PEA has been successfully compensated with the introduction of the PIDSMC + α-β filter scheme.

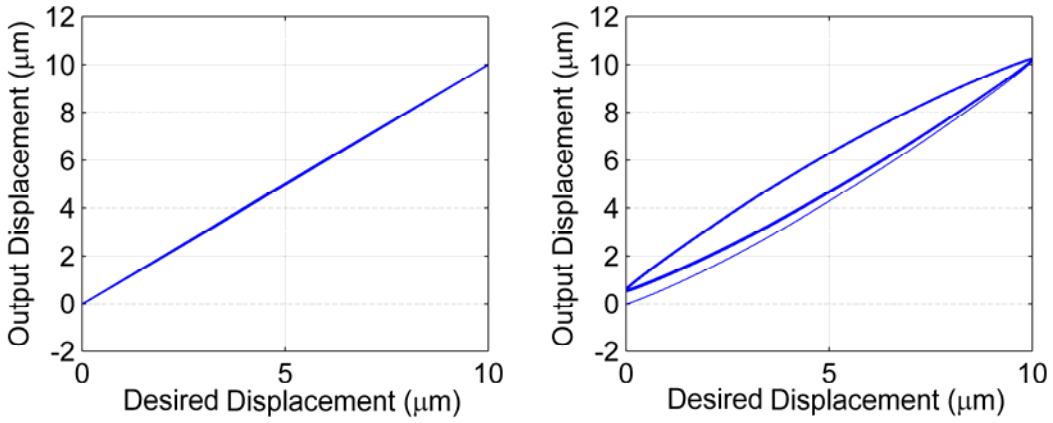

(a) (b)

Fig. 7 Desired displacement vs. measured displacement in (a) PIDSMC + α-β filter tracking control experiment and (b) open-loop experiment.

4.2.3 Tracking Control Performance of the PIDSMC + α-β Filter Scheme

In this section, the tracking control performance of the PIDSMC + α-β filter scheme with the same parameters as determined previously was examined by experiments. The first experiment was implemented to track a series of sine waves in the form of

$$w(t) = 5\sin(2\pi \cdot f_w t - 0.5\pi) + 5 \tag{43}$$

where f_w is the frequency of sine wave, with a value set as 10 Hz, 50 Hz, 100 Hz, and 150 Hz, respectively. Due to the limited space, only is the result of the experiment with $f_w = 10\,\text{Hz}$ shown in Fig. 8. It can be seen that the measured displacement followed the desired one tightly. To quantify their difference, the RMS errors and the maximum errors between the measured displacements and the desired ones over the examination time period (i.e., 8 s) in all four experiments were calculated with the results listed in Table I. Notably, the errors increased as f_w increased, but the maximum error remained below 4% of the maximum desired displacement in the worst scenario with $f_w = 150\,\text{Hz}$. From Fig. 8, it is also noted that there is no noticeable chattering in the measured PEA displacements.

The second experiment was to track a quasi-step so as to examine the steady state error of the developed control scheme. As discussed in Section 3 that the second-order derivative of the desired displacement must exist, a quasi-step was used, instead of a pure step, as the desired displacement in this experiment. Particularly the quasi-step, $w(t)$, was given by

$$\begin{aligned} &w(t) = 0 \quad \text{for} \quad t \le 0.1\,\text{s} \\ &w(t) = 9.60\times10^{7}t^{5} - 6.00\times10^{7}t^{4} + 1.48\times10^{7}t^{3} - 1.80\times10^{6}t^{2} + 1.08\times10^{5}t - 2.56\times10^{3} \\ &\qquad \text{for} \quad 0.1\,\text{s} < t \le 0.15\,\text{s} \\ &w(t) = 5 \quad \text{for} \quad t > 0.15\,\text{s} \end{aligned} \tag{44}$$

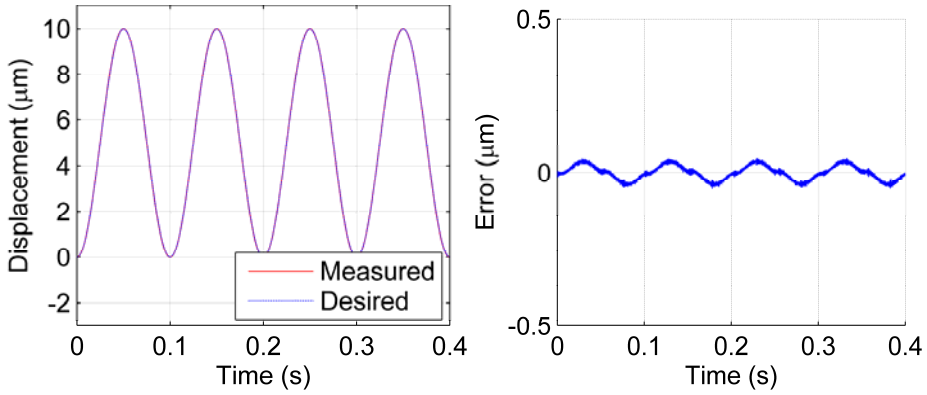

(a) (b)

Fig. 8 Results of the PIDSMC + α-β filter tracking control experiment with $f_w = 10$ Hz : (a) the desired and the measured displacements and (b) the tracking error.

The experimental results with the developed control scheme are shown in Fig. 9 and the RMS error and the maximum error are listed in Table I. From Fig. 9 (b), it can be seen that there is no steady state error, suggesting that the developed control scheme is capable to eliminate the steady-state error in the quasi-step tracking.

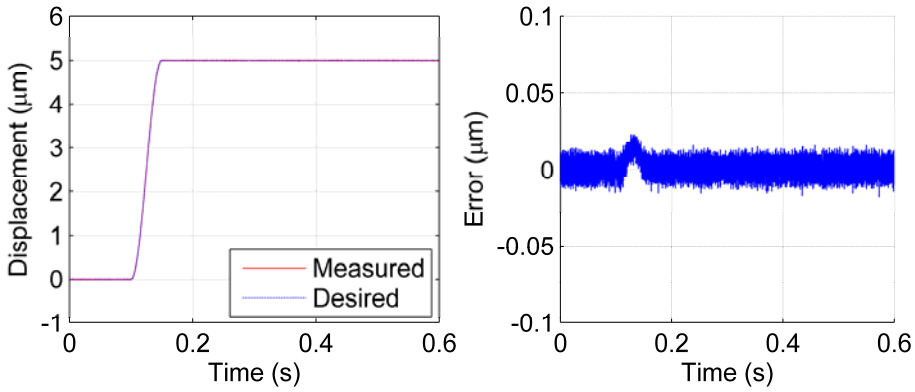

(a) (b)

Fig. 9 Results of the quasi-step tracking experiment with the PIDSMC + α-β filter scheme: (a) the desired and measured displacements and (b) the tracking error.

4.3 Comparative Study on PIDSMC + α-β Filter Scheme and Other Control Schemes.

For comparison, the experiments to track the same sine waves and quasi-step, as defined in the previous section, were performed by employing the traditional PID and other SM-based control schemes (i.e., SM + α-β filter and SMCBL + α-β filter), respectively. In the PID control scheme, the PID parameters were tuned by trial and error to ensure the RMS error as small as possible in low frequency operations, which gave $P = 4$, $I = 55100$, and $D = 10^{-8}$. The results of the PID tracking control experiments are shown in Fig. 10 for tracking a sine wave with $f_w = 10$ Hz and in Fig. 11 for tracking a quasi-step. From the measured displacement, the RMS error and the maximum error were evaluated. The results obtained are

listed in Table I along with the results of other control schemes. It can be seen that in the low frequency range ($f_w < 100\,\text{Hz}$), the tracking errors of the PID control scheme are in the same level as those of the PIDSMC + α-β filter scheme, but in the high frequency range ($f_w \geq 100\,\text{Hz}$), the PID control scheme becomes inferior to the PIDSMC + α-β filter scheme in terms of the RMS error and the maximum errors.

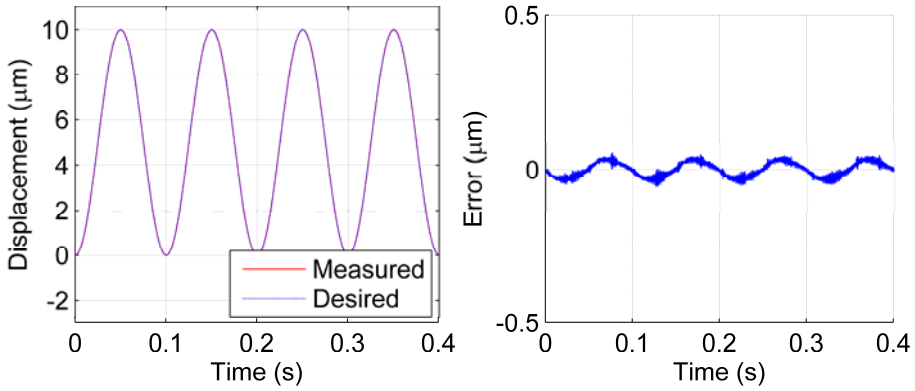

(a) (b)

Fig. 10 Results of the PID tracking control experiment with $f_w = 10\,\text{Hz}$: (a) the desired and the measured displacements and (b) the tracking error.

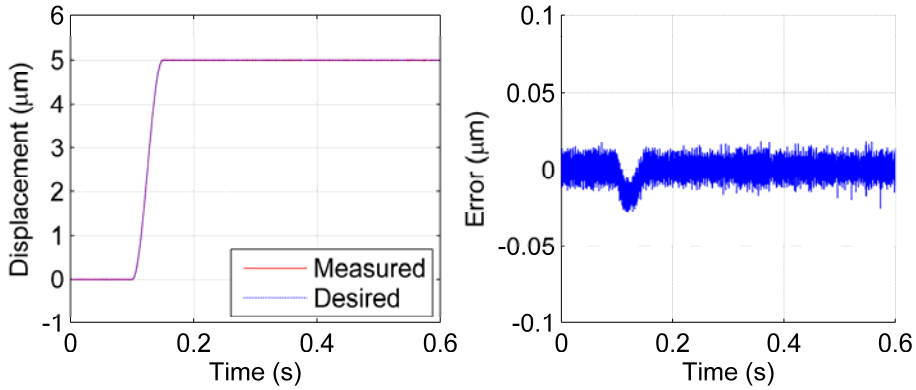

(a) (b)

Fig. 11 Results of the PID quasi-step tracking experiment: (a) the desired and measured displacements, and (b) the tracking error.

In the SM + α-β filter scheme, the continuous-time α-β filter with the parameters set previously was used to provide state estimates, and the parameter of η in Eq. (13) was tuned by trail and error. Specifically, η was initially set with a relatively-large positive number to ensure both the capability of matched-uncertainty rejection and the reachability of the sliding surface, and its values was then reduced to suppress chattering until the reachability of the sliding surface is almost lost. By this process, η was selected with a value of 7.0. The results of tracking a sine wave with $f_w = 10\,\text{Hz}$ are shown in Fig. 12, in which chattering is clearly observed. Since the chattering may cause damage to the PEA, no tracking experiments of higher frequencies were performed with the SM + α-β filter scheme.

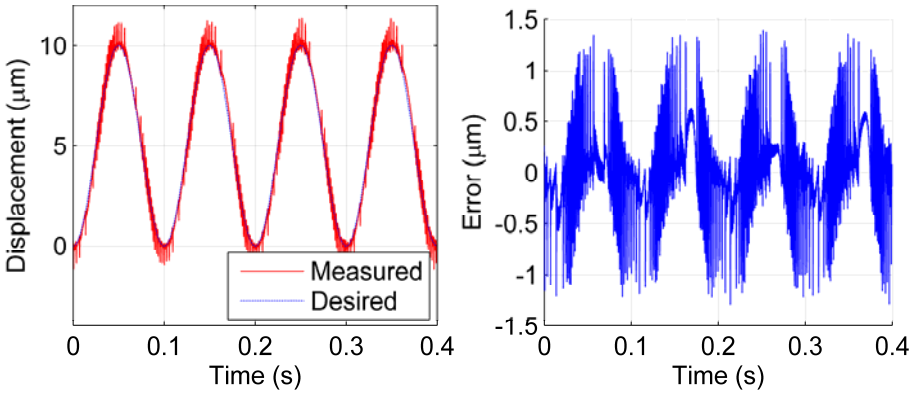

(a) (b)

Fig. 12 Results of the SM + α-β filter scheme tracking experiment with $f_w = 10\,\text{Hz}$: (a) the desired and the measured displacements and (b) the tracking error.

The results of the quasi-step tracking experiments on the PEA are shown in Fig. 13, and again chattering is obviously seen in the measured displacement. Besides, the drifting due to the PEA creep is also seen, which cannot be compensated by the SM control due to the limited switching frequency of u_3 in Eq. (13). The RMS error and the maximum error of all measurements were also evaluated, which are listed in Table I for comparison. Based on the above analysis, it can be concluded that the SM + α-β filter scheme is inferior to the PIDSM + α-β filter scheme in terms of uncertainty (e.g. creep) rejection, chattering suppression, and the RMS error and the maximum errors as well.

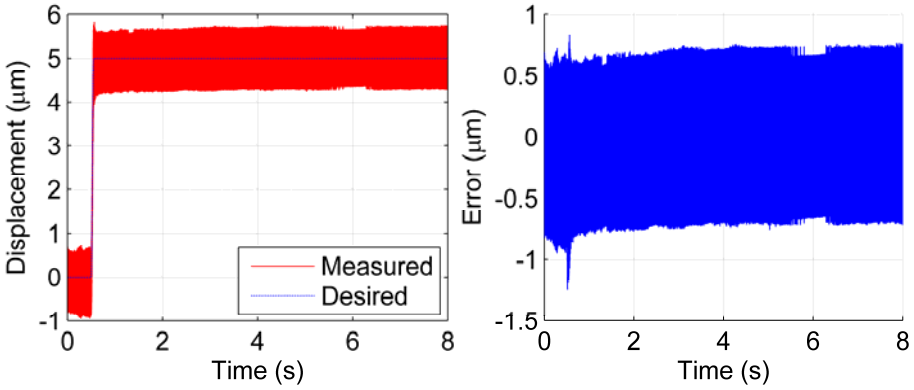

(a) (b)

Fig. 13 Results of the SM + α-β filter scheme quasi-step tracking experiment: (a) the desired and measured displacements and (b) the tracking error.

In the SMCBL + α-β filter scheme, the control action u_3 was generated by

$$u_3 = -\eta \frac{q}{|q| + \delta} \tag{45}$$

where η was tuned to be 122 and δ was tuned to be 60000 to ensure the tracking RMS error being as small as possible. The results of the SMCBL tracking a sine wave with $f_w = 10\,\text{Hz}$ and a quasi-step are

shown in Figs. 14 and 15, respectively, with the RMS error and the maximum error also listed in Table I for comparison. It can be seen that in both experiments, chattering was largely suppressed but still perceptible in the rising sections of the measured displacements. Increasing η or reducing δ could reduce the steady state error, but as a cost of reducing the capacity of chattering suppression. Since the chattering may cause damage to the PEA, no tracking experiments of higher frequencies were performed with the SMCBL + α-β filter scheme. Also, a steady state error of about -0.036 μm is observed in Fig. 15. As such, it can be concluded that the SMCBL + α-β filter scheme is inferior to the PIDSM + α-β filter control scheme in terms of steady state error elimination, and the RMS error and the maximum errors as well.

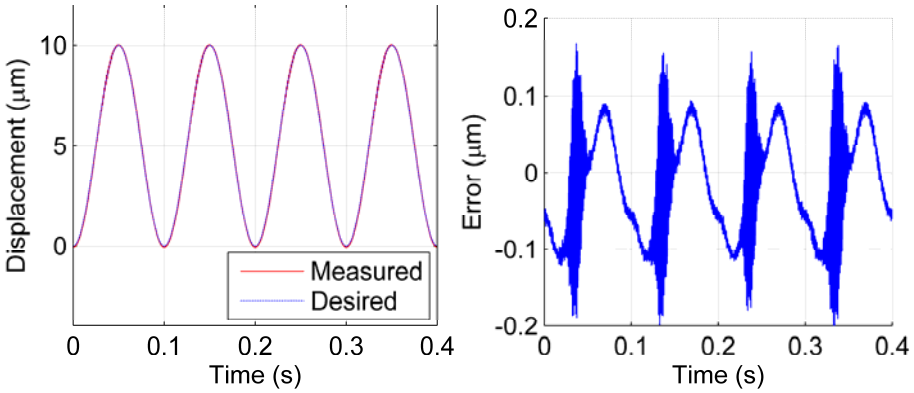

(a) (b)

Fig. 14 Results of the SMCBL + α-β filter tracking experiment with $f_w = 10\,\text{Hz}$: (a) the desired and measured displacements and (b) the tracking error.

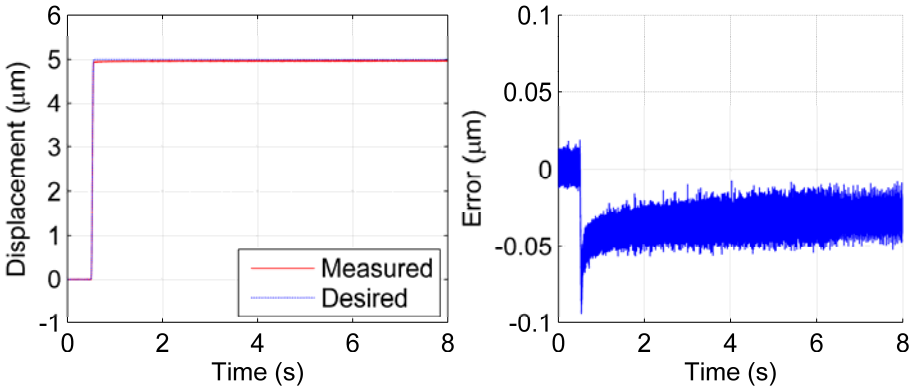

(a) (b)

Fig. 15 Results of SMCBL + α-β filter quasi-step tracking experiment: (a) the desired and measured displacements and (b) the tracking error.

5. Conclusions

Tracking control of PEAs has been proven to be a challenging task, mainly due to the involvement of the PEA nonlinear properties such as hysteresis. Although the existing SM-based control methods shows promising for use in the PEA tracking control due to their capability of rejecting matched nonlinearities and uncertainties, the problems of chattering and steady state error associated with these methods occurs, thus

degrading the tracking performances. To alleviate these problems, a PIDSM controller for the PEA tracking control was developed in the present study. Combined with a continuous-time α-β filter, a novel control scheme of PIDSM + α-β filter is resulted for use in PEA tracking control. The effectiveness of the developed control scheme was illustrated by the experiments performed on a commercially-available PEA and its performance was also compared with that of PID control, SM + α-β filter, and SMCBL + α-β filter by experiments. It is concluded that the PIDSM + α-β filter scheme as applied to the PEA can achieve a better performances in terms of the RMS and maximum tracking errors, chattering suppression, and steady state error reduction, in comparison with the other examined control schemes.

Table I Tracking errors corresponding to different control schemes

Desired displacement	PIDSM +α-β filter		PID		SM +α-β filter		SMCBL +α-β filter	
	RMS error (μm)	Max. error (μm)	RMS error (μm)	Max. error (μm)	RMS error (μm)	Max. error (μm)	RMS error (μm)	Max. error (μm)
10 Hz sine	0.024	0.057	0.023	0.061	0.442	1.398	0.073	0.252
50 Hz sine	0.105	0.196	0.117	0.206	n/a	n/a	n/a	n/a
100 Hz sine	0.181	0.339	0.241	0.411	n/a	n/a	n/a	n/a
150 Hz sine	0.262	0.375	0.374	0.643	n/a	n/a	n/a	n/a
quasi-step	0.007	0.023	0.007	0.030	0.517	0.890	0.034	0.058

Acknowledgement

The support from the Natural Sciences and Engineering Research Council (NSERC) of Canada to the present study is acknowledged.

References

[1] D. Croft, G. Shed, and S. Devasia, Creep, hysteresis, and vibration compensation for piezoactuators: Atomic force microscopy application, J. Dyn. Syst. Meas. Contr., 123(2001) 35-43.

[2] H. Song, G. Vdovin, R. Fraanje, G. Schitter, and M. Verhaegen, Extracting hysteresis from nonlinear measurement of wavefront-sensorless adaptive optics system, Opt. Lett., 34(2009) 61-63.

[3] J.-J. Wei, Z.-C. Qiu, J.-D. Han, and Y.-C. Wang, Experimental comparison research on active vibration control for flexible piezoelectric manipulator using fuzzy controller, J. Intell. Rob. Syst., 59(2010) 31-56.

[4] S. Devasia, E. Eleftheriou, and S. O. R. Moheimani, A survey of control issues in nanopositioning, IEEE Trans. Control Syst. Technol., 15(2007) 802-823.

[5] H. J. M. T. S. Adriaens, W. L. De Koning, and R. Banning, Modeling piezoelectric actuators, IEEE/ASME Trans. Mechatron., 5(2000) 331-341.

[6] D. Song and C. J. Li, Modeling of piezo actuator's nonlinear and frequency dependent dynamics, Mechatronics, 9(1999) 391-410.

[7] Y. Yu, Z. Xiaob, N. G. Naganathan, and R. V. Dukkipati, Dynamic Preisach modeling of hysteresis for the piezoceramic actuator system, Mech. Mach. Theory, 37(2002) 75-89.

[8] R. Ben Mrad and H. Hu, A model for voltage-to-displacement dynamics in piezoceramic actuators subject to dynamic-voltage excitations, IEEE/ASME Trans. Mechatron., 7(2002) 479-489.

[9] K. Kuhnen and F. Previdi, Modeling, identification and compensation of complex hysteretic nonlinearities: A modified Prandtl-Ishlinskii approach, Eur. J. Control, 9(2003) 407-421.

[10] W. T. Ang, P. K. Khosla, and C. N. Riviere, Feedforward controller with inverse rate-dependent model for piezoelectric actuators in trajectory-tracking applications, IEEE/ASME Trans. Mechatron., 12(2007) 134-142.

[11] J. Y. Peng and X. B. Chen, H_2-optimal digital control of piezoelectric actuators, in: Proceedings of the 8th World Congress on Intelligent Control and Automation, WCICA-2010, Jinan, China, July 2010, 3684-3690.

[12] J. Y. Peng and X. B. Chen, Modeling of piezoelectric-driven stick-slip actuators, IEEE/ASME Trans. Mechatron., 16(2011) 394-399.

[13] G. M. Clayton, S. Tien, A. J. Fleming, S. O. R. Moheimani, and S. Devasia, Inverse-feedforward of charge-controlled piezopositioners, Mechatronics, 18(2008) 273-281.

[14]Y. Cao and X. B. Chen, A novel discrete ARMA-based model for piezoelectric actuator hysteresis, IEEE/ASME Trans. Mechatron., 17(2012), pp. 737-744.

[15] K. Kuhnen, H. Janocha, D. Thull, and A. Kugi, A new drive concept for high-speed positioning of piezoelectric actuators, in: Proceedings of the 10th International Conference on New Actuators, Bremen, Germany, June 2006, pp. 82-85.

[16] K. K. Leang and S. Devasia, Feedback-linearized inverse feedforward for creep, hysteresis, and vibration compensation in AFM piezoactuators, IEEE Trans. Control Syst. Technol., 15(2007) 927-935.

[17] K. Kuhnen, Modeling, Identification and Compensation of complex hysteretic Nonlinearities and Log(t)-type Creep Dynamics, Contr. Intell. Syst., 33(2005) 134-147.

[18] S. Bashash and N. Jalili, A polynomial-based linear mapping strategy for feedforward compensation of hysteresis in piezoelectric actuators, J. Dyn. Syst. Meas. Contr., 130(2008) 031008.

[19] A. Badel, J. Qiu, T. Nakano, A new simple asymmetric hysteresis operator and its application to inverse control of piezoelectric actuators, IEEE Trans. Ultrason., Ferroelectr., Freq. Control, 55(2008) 1086-1094.

[20] C. Ru, L. Chen, B. Shao, W. Rong, and L. Sun, A hysteresis compensation method of piezoelectric actuator: Model, identification and control, Control Eng. Pract., 17(2009) 1107-1114.

[21] L. Sun, C. Ru, W. Rong, L. Chen, and M. Kong, Tracking control of piezoelectric actuator based on a new mathematical model, J. Micromech. Microeng., 14(2004) 1439-1444.

[22] C. Ru and L. Sun, Hysteresis and creep compensation for piezoelectric actuator in open-loop operation, Sensor Actuat. A: Phys., 122(2005) 124-130.

[23] L. Deng and Y. Tan, Modeling rate-dependent hysteresis in piezoelectric actuator, in: IEEE International Conference on Control Applications, 2008. CCA 2008. San Antonio, USA, September 2008, 978-982.

[24] H. Hu, H.M.S. Georgiou, and R. Ben-Mrad, Enhancement of tracking ability in piezoceramic actuators subject to dynamic excitation conditions, IEEE/ASME Trans. Mechatron., 10(2005) 230-239.

[25] U-X. Tan, W. T. Latt, C. Y. Shee, C.N. Riviere, and W. T. Ang, Feedforward controller of ill-conditioned hysteresis using singularity-free Prandtl–Ishlinskii model, IEEE/ASME Trans. Mechatron., (2009) 598-605.

[26] R. Merry, M. Uyanik, R. van de Molengraft, R. Koops, M. van Veghel, and M. Steinbuch, Identification, control and hysteresis compensation of a 3 DOF metrological AFM, Asian J. Control, 11(2009) 130-143.

[27] J. A. Main and E. Garcia, Piezoelectric stack actuators and control system design: Strategies and pitfalls, J. Guid., Control Dyn., 20(1997), 479-485.

[28] Physik Instrumente, The World of Nanopositioning and Micropositioning 2005 / 2006, (2005).

[29] X. Tan and J. S. Baras, Adaptive identification and control of hysteresis in smart materials, IEEE Trans. Autom. Control, 50(2005) 827-839.

[30] K. K. Leang and S. Devasia, Design of hysteresis-compensating iterative learning control: Application to atomic force microscopes, Mechatron., 16(2006) 141-158.

[31] J.-H. Xu, Neural network control of a piezo tool positioner, In: Canadian Conference on Electrical and Computer Engineering, 1993. Vancouver, Canada, September 1993. 1(1993) 333-336.

[32] S. Chang, J. Yi, and Y. Shen, Disturbance-observer-based hysteresis compensation for piezoelectric actuators, in: American Control Conference, 2009. ACC '09. St. Louis, USA, June 2009, 4196-4201.

[33] S. Salapaka, A. Sebastian, J. P. Cleveland, and M. V. Salapaka, High bandwidth nano-positioner: A robust control approach, Rev. Sci. Instrum., 73(2002) 3232-3241.

[34] C. Edwards and S. K. Spurgeon, Sliding mode control: theory and applications, Taylor & Francis, Abingdon, UK, 1998.

[35] P.-K. Huang, P.-H. Shieh, F.-J. Lin, and H.-J. Shieh, Sliding-mode control for a two-dimensional piezo-positioning stage, IET Control Theory Appl., 1(2007) 1104-1113.

[36] J.-C. Shen, W.-Y. Jywe1, C.-H. Liu, Y.-T. Jian, and J. Yang, Sliding-mode control of a three-degrees-of-freedom nanopositioner, Asian J. Control, 10(2008) 267-276.

[37] J.-C. Shen, H.-K. Chiang, and Y.-L. Shu, Precision tracking control of a piezoelectric-actuated system, Precis. Eng., 32(2008) 71-78.

[38] Q. Xu and Y. Li, Dynamics modeling and sliding mode control of an XY micropositioning stage, In: the 9th International Symposium on Robot Control (SYROCO'09), The International Federation of Automatic Control, Gifu, Japan, Sept. 2009, pp. 781-786.

[39] H. C. Liaw, B. Shirinzadeh, and J. Smith, Enhanced sliding mode motion tracking control of piezoelectric actuators, Sensor Actuat. A: Phys., 138(2007) 194-202.

[40] Y. Li, Q. Xu, Adaptive Sliding Mode Control With Perturbation Estimation and PID Sliding Surface for Motion Tracking of a Piezo-Driven Micromanipulator, IEEE Trans. Control Syst. Technol., 18(2010) 798-810.

[41] H. C. Liaw, B. Shirinzadeh, and J. Smith, Sliding-Mode Enhanced Adaptive Motion Tracking Control of Piezoelectric Actuation Systems for Micro/Nano Manipulation, IEEE Trans. Control Syst. Technol., 16(2008) 826-833.

[42] X. Chen and T. Hisayama, Adaptive Sliding-Mode Position Control for Piezo-Actuated Stage, IEEE Trans. Ind. Electron., 55(2008) 3927-3934.

[43] F. Gouaisbaut, M. Dambrine, and J. P. Richard, Robust Control of Delay Systems: A Sliding Mode Control Design via LMI, Syst. Contr. Lett., 46(2002) 219-230.

[44] E. Fridman, F. Gouaisbaut, M. Dambrine, and J. P. Richard, Sliding mode control of systems with time-varying delays via descriptor approach, Int. J. Syst. Sci., 34(2003) 553-559.

[45] M. Li, F. Wang, and F. Gao, PID-Based Sliding Mode Controller for Nonlinear Processes, Ind. Eng. Chem. Res., 40(2001) 2660-2667.

[46] S.-T. Peng, Sliding Mode Control System Design for Chemical Processes, Doctoral Dissertation, Feng Chia University, Taichung, Taiwan, 2004.

[47] C.-T. Chen and S.-T. Peng, A nonlinear control scheme for imprecisely known processes using the sliding mode and neural fuzzy techniques, J. Process Control, 14(2004) 501-515.

[48] J. W. Li, X. B. Chen, and W. J. Zhang, A new approach to modeling system dynamics - in the case of a piezoelectric actuator with a host system, IEEE/ASME Trans. Mechatron., 15(2010) 371-380.

[49] X. B. Chen, Q. Zhang, D. Kang, and W. Zhang, On the dynamics of piezoactuated positioning systems, Rev. Sci. Instrum., 79(2008) 116101-1-16101-3.

[50] M. Goldfarb and N. Celanovic, Modeling piezoelectric stack actuators for control of micromanipulation, IEEE Contr. Syst. Mag., 17(1997) 69-79.

[51] S. Huang, K. K. Tan, and T. H. Lee, Adaptive sliding-mode control of piezoelectric actuators, IEEE Trans. Ind. Electron., 56(2009) 3514-3522.

[52] J.H. Painter, D. Kerstetter, and S. Jowers, Reconciling steady-state Kalman and alpha-beta filter design, IEEE Trans. Aerosp. Electron. Syst., 26(1990) 986-991.

7 Integrated PID-Based Sliding Mode State Estimation and Control for Piezoelectric Actuators

Submitted to *IEEE/ASME Transactions on Mechatronics* for possible publication as:
J. Y. Peng and X. B. Chen, "Integrated PID-Based Sliding Mode State Estimation and Control for Piezoelectric Actuators," *IEEE/ASME Transactions on Mechatronics*, 2012, under review, manuscript ID: TMECH-09-2011-1873.R2.

7.1 Introduction and Objectives

Suppose that the vibration dynamics sub-model in the comprehensive PEA model developed in Chapter 5 is used as the nominal model of the PEA and there is a matched unknown input to the nominal model accounting for hysteresis, creep, and the external loading force. To estimate the states of this system, the Non-model-based observers, such as the continuous α-β filter used for state estimation in Chapter 6, may generate large phase lags if the desired level of noise suppression is enforced. There are existing model-based observers specifically developed for estimating the states of such systems with unknown inputs, referred to as the unknown input observers (UIOs). However, applications of these UIOs require that the so called observer matching condition be satisfied, which states that the rank of the product of the output matrix and the unknown input matrix in the state space model of the system must be equal to that of the unknown input matrix. Unfortunately, the aforementioned PEA model does not meet this condition. Attempts to relax the observer matching condition resulted in over complicated observers for the used in PEA tracking control.

Based on the above discussion, the objectives of this paper are (a) to develop a model-based UIO by employing the idea of the PID-based sliding mode, referred to as the PID-based sliding mode observer (PIDSMO), for state estimation of PEAs, which does not require the satisfaction of observer matching condition, and (b) to combine the PIDSMO with the PIDSMC developed in Chapter 6 to form a novel control scheme for PEAs, referred to as the PID-based sliding mode observer-controller (PIDSMOC).

7.2 Methods

(1) Following the same procedure described in Section 6.2 (1) to (3), a model of PEA with the vibration dynamics sub-model as its nominal model and with the effects of hysteresis, creep, and external load forces accounted for by a matched unknown input was obtained. The states of this model were taken as the states of the PEA. The output of this model represents the measurable output displacement of the PEA. The voltage applied to the PEA corresponds to the known input of the model. The problem is to estimate the immeasurable states in such a PEA model with the matched unknown input.

(2) Use the vibration dynamics sub-model as an ideal system.

(3) Use the PIDSM method to generate an input to the ideal system given by step (2) such that the states of the ideal system follows those of the actual PEA, as such the states of the ideal system are the estimates of the states of the PEA model mentioned in (1). The PIDSM method used only the input voltage and the output displacement of the PEA as inputs.

(4) The sliding mode behavior of the PIDSM observer is investigated. The sliding motion is a

first order system. The sliding surface parameter was actually implicitly determined by the PID parameters and the estimation errors in the PIDSM scheme. Their relationships and the stability condition of the sliding mode were investigated. The reachability conditions of the sliding surface was found

(5) The necessary and sufficient condition for the PIDSM observer to be stable is given.

(6) The frequency domain performance of the PIDSM observer which is related to the noise suppression capability is then investigated.

(7) The PIDSM observer is then combined with the PIDSM controller developed in Chapter 6 to form a PIDSMOC, with the stability condition analyzed.

(8) The PIDSM observer and the PIDSMO controller developed are implemented on a PEA with their effectiveness validated experimentally.

(9) A comparative study between the tracking control performances of the PIDSMOC and those of the PIDSM controller with α-β filter scheme when applied to PEA tracking control was performed experimentally.

(10) The robustness of the PIDSMO and the robustness of the PIDSMOC were examined through simulations.

7.3 Results

Experimental results showed that the PIDSMO developed is capable of estimating the PEA states accurately with small phase lag and strong noise suppression capability regardless of the presence of hysteresis, creep, and external loads. Also, it has been shown that the PIDSMOC

scheme can achieve a promising tracking performance, with the maximum error less than 3% of the PEA full displacement and RMS error around 1.5% of the PEA full displacement in the worst case scenario (150 Hz sine wave tracking). By comparison, the PIDSMOC scheme is generally better than the PIDSMC + α-β filter scheme in terms of the RMS and the maximum tracking errors in both no-load and loaded situations. Finally, through simulations, the performance PIDSMO and the PIDSMOC is found robust even with the presence unknown inputs, measurement noises, and modeling errors.

7.4 Contributions

The contribution of this work was the successful extension of the PIDSM method to observer design such that the observer matching condition for the conventional SM observer to exist was relaxed. Another contribution is the construction of the PIDSMOC and the successful implementation of PIDSMOC for tracking control of PEAs.

Integrated PID-Based Sliding Mode State Estimation and Control for Piezoelectric Actuators

J. Y. Peng and X. B. Chen, *Member, IEEE*

***Abstract*—Tracking control of piezoelectric actuators (PEAs) has stimulated the development of various advanced control schemes that utilizes the feedback of PEA system states for improved control performance. Among them, the one based on the concept of sliding mode has been shown promising due to its robustness to matched uncertainties, but leaving the required state estimation to be desired. Previous studies shows the PEA can be modeled as a linear dynamic system with matched uncertainties. On this basis, this paper presents the development of a novel observer based on the concept of proportional-integral-derivative-based (PID-based) sliding mode, in which the switching function is replaced by a PID regulator. The novel observer, referred to as the PID-based sliding mode observer (PIDSMO), relax the observer matching condition as required in the use of the unknown-input observers (UIOs). The PIDSMO is then integrated with the PID-based sliding mode controller (PIDSMC) to form a novel integrated PID-based sliding mode observer-controller (PIDSMOC) for PEA tracking control. Experiments performed on a PEA showed that the PIDSMO can accurately estimate the PEA states and that the integrated PIDSMOC can achieve better tracking control performances as compared to the PIDSMC with α-β filter control scheme.**

***Index Terms*—Control systems, Uncertain systems, Piezoelectric devices**

I. INTRODUCTION

PIEZOELECTRIC actuators (PEAs) have the advantages of high displacement resolution (sub nanometer) and large actuating force (typically a few hundreds of N) [1] and as such, they have found wide applications in the fields of micro- and nano-positioning [2]. However, the hysteresis, creep [1][2][3] (Fig. 1), and distributed vibration dynamics of PEAs [4] have proven to be able to significantly degrade their close-loop tracking control performances and even lead to system instability [1][3]. For improvement, the development of model-based closed-loop control schemes capable of suppressing such effects has been drawing considerable attention, e.g. [5][6].

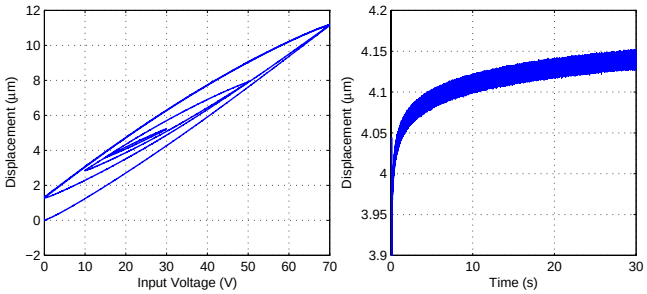

Fig. 1. (a) Hysteresis of a PEA and (b) Creep of a PEA subject to a 30 V

In all of the model-based closed-loop control schemes developed for PEAs, those based on sliding mode control are among the most widely used [6]-[15]. The merit of the sliding-mode-based techniques is due to the fact that they are insensitive to uncertainties in the input channels of the plant (referred to as matched uncertainties or matched unknown inputs), while a PEA can be modeled as a linear dynamic system with a matched unknown input to account for hysteresis, creep, and model error as well as the variation of external load [10][12]. Among various sliding-mode-based control schemes, the proportional-integral-derivative-based sliding mode controller (PIDSMC), in which the switching control term in the conventional sliding mode control is replaced with a PID regulator, has been shown to be promising for tracking control of PEAs. Compared to the commonly used PID control and other sliding-mode-based control schemes such as the sliding mode control with boundary layer, the PIDSMC show its superior capability to reduce tracking error, chattering, and to eliminate the steady-state error [12].

It is noticed that most of the sliding-mode-based schemes for the PEA control need the feedback of its states to close the system [9][12]. Unfortunately, not all of the system states are measurable, so state estimators or observers are essentially required. Several methods have been developed to estimate the

Manuscript received September 16, 2011. This work was supported by the Natural Sciences and Engineering Research Council (NSERC) of Canada.

J. Y. Peng is with the Department of Mechanical Engineering, University of Saskatchewan, Saskatoon, SK S7N5A9 Canada (corresponding author, phone: 306-241-5471; e-mail: jip747@mail.usask.ca).

X. B. Chen is with the Department of Mechanical Engineering, University of Saskatchewan, Saskatoon, SK S7N5A9 Canada (e-mail: xbc719@mail.usask.ca).

Manuscript received September 16, 2011. This work was supported by the Natural Sciences and Engineering Research Council (NSERC) of Canada.

J. Y. Peng is with the Department of Mechanical Engineering, University of Saskatchewan, Saskatoon, SK S7N5A9 Canada (corresponding author, phone: 306-241-5471; e-mail: jip747@mail.usask.ca).

X. B. Chen is with the Department of Mechanical Engineering, University of Saskatchewan, Saskatoon, SK S7N5A9 Canada (e-mail: xbc719@mail.usask.ca).

states and generally, they can be classified into two categories: non-model-based and model-based. Non-model-based filters/differentiators, such as the α-β filter [12], the high-gain differentiator [16], the integral-chain differentiator [16] and the sliding mode differentiator based on the super-twisting algorithm [17] can either generate large phase lags if the desired level of noise suppression is enforced (in the first four in the aforementioned methods) or generate excessive chattering in noisy systems (in the last method). Compared to non-model-based filters/differentiators, model-based observers, e.g., the Luenberger observer, can generate more accurate estimations if the model used is accurate enough. With the presence of uncertainties that would not be modeled, however, the performance of model-based observers degrades. For improvement, the system uncertainties can be treated as a lumped unknown input to the system model, and a kind of model-based observers referred to as unknown input observers (UIOs) can then be used to estimate the system states. Several UIOs have been reported in the past three decades, including the full-order UIO [18], the reduced-order UIO [19], the UIO designed based on projection operator [20], and the sliding-mode-based observers (SMOs) [9][21]-[24]. Applications of these UIOs require that the observer matching condition be satisfied [25][26], which states that the rank of the product of the output matrix and the unknown input matrix in the state space model of the system must be equal to that of the unknown input matrix [9]. Existing PEA models, such as those reported in [10] and [12], do not meet this condition. Attempt to relax the observer matching condition has been reported in [25][26], but the resultant UIOs were complicated.

This study was aimed to (a) develop a model-based UIO by employing the idea of the PID-based sliding mode [12][27], referred to as the PID-based sliding mode observer (PIDSMO), for state estimation of PEAs, which does not require the satisfaction of observer matching condition and also has a simpler structure than those reported in [25][26], and (b) combine the PIDSMO with the PIDSMC developed in our previous study [12] to form a novel control scheme for PEAs, referred to as the PID-based sliding mode observer-controller (PIDSMOC). This paper is arranged as follows. The experiment setup of a PEA-driven positioning system and its model are presented in Section II. The PIDSMO for PEA-driven system is developed in Section III, with an analysis on its sliding mode behavior, stability, and measurement noise suppression capability. The PIDSMO is then combined with the PIDSMC to form a novel PID-based sliding mode observer-controller (PIDSMOC) in Section IV, with the analysis on its stability. For experimental verification, in Section V the PIDSMO and the PIDSMOC developed are implemented on the PEA-driven system, which is followed by a comparative case study between the PIDSMOC and the PIDSMC + α-β filter scheme as applied to PEA tracking control. A robustness analysis of the PIDSMO and the PIDSMOC through simulation is also presented.

II. EXPERIMENT SETUP AND THE PEA MODEL

A. Experiment Setup

The experiment setup used in this study is a PEA-driven positioning system as shown in Fig. 2. The PEA used is P-753.1CD with power amplifier E-625.CR (Physik Instrumente), which has a traveling range of 12 μm and a resolution of 0.05 nm. The built-in capacitive displacement sensor with a resolution of 0.05 nm was used for displacement measurements. Both the PEA and the sensor were interfaced to a host computer via an I/O board (PCI-DAS1602/16, Measurement Computing) and MATLAB SIMULINK was used for implementing the state estimation and control algorithms on the setup. All measurements were taken with a sampling interval of $T_s = 0.00005\,\mathrm{s}$.

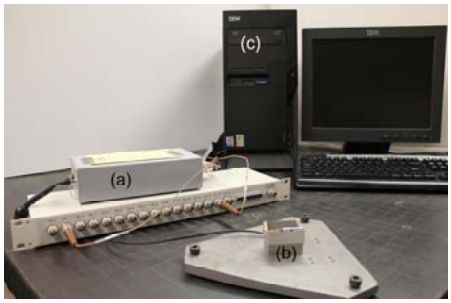

Fig. 2. Experiment setup including (a) a power amplifier E-625.CR, (b) the P-753 PEA, and (c) a computer with the PCI-DAS1602/16 I/O board.

B. PEA Model

Fig. 3(a) shows the schematic of the PEA used, in which the end-effector is connected to the base through flexure hinges and driven by a piezoelectric element under an input voltage of $u(t)$. $f_e(t)$ is the external load applied to the end-effector and $y(t)$ the displacement of the end-effector or the system output. To model this PEA, the nonlinear and linear characteristics of the PEA are decoupled by means of individual sub-models that are connected in cascade. The block diagram of the model is shown in Fig. 3(b), in which blocks of H, V, and F_c are the sub-models representing the PEA hysteresis, vibration dynamics, and creep, respectively; and $f(t)$ and $y_0(t)$ represent the internal actuation force and the output displacement of the end-effector without creep, respectively [2][28]-[31]. Based on such a cascading structure, a model representative of the PEA was reported in the authors' previous study [12]. Particularly, both V and F_c are treated as linear dynamic systems and the positions of V and F_c in the block diagram Fig. 3(b) are then swapped without affecting $y(t)$. Given that the mass of the end-effector is much larger than that of the piezoelectric element, V is approximated by using a second order system [32] with a natural frequency ω_n and a damping ratio ξ. The input to V is represented by $Ku(t)+K\varepsilon(t)$, where K is a known nominal gain and $\varepsilon(t)$ is an unknown input added to $u(t)$, i.e. a matched unknown input. The output induced by $\varepsilon(t)$ accounts for effects such as hysteresis, creep, the

external loads, the error induced by approximating V with a second order system, model parameter variations, and other interferences in the input channel. In practice $\|\varepsilon\| \le \varepsilon_{\max}$ and $\|\dot{\varepsilon}\| \le \dot{\varepsilon}_{\max}$. The resulting model of the PEA is

$$\begin{aligned}\begin{bmatrix}\dot{x}_1\\ \dot{x}_2\end{bmatrix} &= \begin{bmatrix}0 & 1\\ -\omega_n^2 & -2\xi\omega_n\end{bmatrix}\begin{bmatrix}x_1\\ x_2\end{bmatrix} + \begin{bmatrix}0\\ K\omega_n^2\end{bmatrix}(u+\varepsilon)\\ &= \dot{X} = AX + Bu + B\varepsilon \\ y &= \begin{bmatrix}1 & 0\end{bmatrix}\begin{bmatrix}x_1 & x_2\end{bmatrix}^T = CX\end{aligned} \tag{1}$$

where x_1 and x_2 are the states of the PEA model, denoting the displacement and the velocity of the end-effector, respectively. It can be seen that the both the input matrix for the unknown input $B = \begin{bmatrix}0 & K\omega_n^2\end{bmatrix}^T \in R^{2\times 1}$ and the output matrix $C = \begin{bmatrix}1 & 0\end{bmatrix} \in R^{1\times 2}$ are of full rank. But since $CB = 0$, one has $\text{rank}(CB) = 0 \neq \text{rank}(B) = 1$, so the observer matching condition is not satisfied.

In [12], the model parameters were identified and given by $\xi = 0.7876$, $\omega_n = 5352\,\text{rad}/s$, and $K = 0.1347\,\mu\text{m/V}$. It is noticed that the above model does not explicitly include the term representing the measurement noise. This is because only $y(t)$ is measurable, one cannot distinguish the effect of $\varepsilon(t)$ from the measurement noise added to $y(t)$. As a result, the measurement noise is treated as being resulting from $\varepsilon(t)$. In this study, the measurement noise is assumed to be of zero mean with a small variance compared to the PEA displacement.

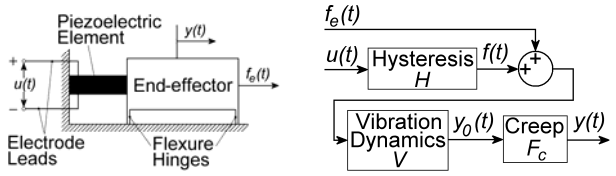

Fig. 3. (a) Schematic of a PEA and (b) its model.

III. PID-BASED SLIDING MODE OBSERVER

A. PIDSMO Development

In this section, a PID-based sliding mode observer (PIDSMO) is developed for the PEA presented in the previous section. The basic idea is to find the input r to a new linear system corresponding to the system given in (1) but without the unknown input, i.e.

$$\begin{aligned}\begin{bmatrix}\dot{\hat{x}}_1\\ \dot{\hat{x}}_2\end{bmatrix} &= \begin{bmatrix}0 & 1\\ -\omega_n^2 & -2\zeta\omega_n\end{bmatrix}\begin{bmatrix}\hat{x}_1\\ \hat{x}_2\end{bmatrix} + \begin{bmatrix}0\\ K\omega_n^2\end{bmatrix} r = \dot{\hat{X}} = A\hat{X} + Br \\ \hat{y} &= \begin{bmatrix}1 & 0\end{bmatrix}\begin{bmatrix}\hat{x}_1 & \hat{x}_2\end{bmatrix}^T = C\hat{X} = \hat{x}_1\end{aligned} \tag{2}$$

such that the states of the new system (2) converge to those of the system given in (1) and thus are used as estimates of the states of (1). The input r is found by using a PID-based sliding mode (PIDSM) scheme to regulate an error system (i.e. to bring the states of the error system to zero). The state vector of this error system is defined by

$$E_o = \begin{bmatrix}e_{o1} & e_{o2}\end{bmatrix}^T = \hat{X} - X = \begin{bmatrix}\hat{x}_1 - x_1 & \hat{x}_2 - x_2\end{bmatrix}^T \tag{3}$$

and the sliding surface is defined as

$$q_o = Q_o E_o = \begin{bmatrix}m_o & 1\end{bmatrix}\begin{bmatrix}e_{o1} & e_{o2}\end{bmatrix}^T = m_o e_{o1} + e_{o2} = 0 \tag{4}$$

where m_o is the sliding surface parameter, whose value is determined by the PID parameters in the PIDSM scheme as well as ε and e_{o1} (to be discussed in Section III B). The input to the PID regulator is the measurable state estimation error or the output estimation error

$$e_{o1} = \hat{x}_1 - x_1 = \hat{y} - y \tag{5}$$

For convenience, denote $A_{21} = -\omega_n^2$, $A_{22} = -2\xi\omega_n$, and $B_2 = K\omega_n^2$. By taking the first derivative of (3) and substituting (1) and (2) yields

$$\begin{aligned}\dot{E}_o &= \begin{bmatrix}\dot{e}_{o1} & \dot{e}_{o2}\end{bmatrix}^T = \begin{bmatrix}\dot{\hat{x}}_1 & \dot{\hat{x}}_2\end{bmatrix}^T - \begin{bmatrix}\dot{x}_1 & \dot{x}_2\end{bmatrix}^T \\ &= \begin{bmatrix}\hat{x}_2 - x_2 \\ A_{21}\hat{x}_1 + A_{22}\hat{x}_2 + B_2 r - A_{21}x_1 - A_{22}x_2 - B_2 u - B_2\varepsilon\end{bmatrix}\end{aligned} \tag{6}$$

The problem now becomes to find r to bring the states of system (6) to zero such that $\hat{X}$ will converge to X. Let r be

$$r = r_1 + r_{res1} = u + B_2^{-1}A_{21}y - B_2^{-1}A_{21}\hat{x}_1 + r_{res1} \tag{7}$$

Substituting (7) into (6) and using the relationships $x_1 = y$ and $\hat{x}_1 = \hat{y}$ yields

$$\begin{bmatrix}\dot{e}_{o1}\\ \dot{e}_{o2}\end{bmatrix} = \begin{bmatrix}e_{o2}\\ A_{22}e_{o2} + B_2 r_{res1} - B_2\varepsilon\end{bmatrix} \tag{8}$$

Notice that there are no measurable or calculable terms left in (8). The next step is to design a PIDSM regulator to generate r_{res1} and regulate the system (8). With a sliding surface defined by (4) (the value of m_o is not determined at the moment), during sliding motion one has

$$q_o = m_o e_{o1} + e_{o2} = \dot{q}_o = m_o\dot{e}_{o1} + \dot{e}_{o2} = 0 \tag{9}$$

Substituting (8) into (9) and using $e_{o1} = \hat{x}_1 - x_1 = \hat{y} - y$ yields

$$\dot{q}_o = -m_o^2(\hat{y} - y) - A_{22}m_o(\hat{y} - y) + B_2 r_{res1} - B_2\varepsilon = 0 \tag{10}$$

The equivalent control, r_{eq}, can be found by letting ε be zero and solving (10) for r_{res1} (i.e. $r_{res1} = r_{eq}$ if $\varepsilon = 0$), which gives

$$r_{eq} = B_2^{-1}\left(m_o^2\hat{y} - m_o^2 y + A_{22}m_o\hat{y} - A_{22}m_o y\right) \tag{11}$$

Because $\varepsilon \neq 0$, r_{res1} in (10) is consisted of r_{eq} and an additional term, r_3, to account for ε, or $r_{res1} = r_{eq} + r_3$. Using (11) and substituting r_{res1} into (10) without equating to 0 yields

$$\dot{q}_o = -B_2\varepsilon + B_2 r_3 \tag{12}$$

Since the term of ε in (12) is unknown, it is proposed that let r_3 being a PID regulator using the measurable value $(\hat{y} - y)$ as input such that $\dot{q}_o$ can be brought to zero, i.e.

$$r_3 = -\left[P_o(\hat{y} - y) + I_o\int_0^t(\hat{y} - y)\mathrm{d}t + D_o\,\mathrm{d}(\hat{y} - y)/\mathrm{d}t\right] \tag{13}$$

where P_o, I_o, and D_o are the PID parameters. It is noticed that r_{eq} is a proportional feedback of $(\hat{y}-y)$, so r_{eq} can be included into the term of $-P_o(\hat{y}-y)$ in r_3 such that $r_{res1}=r_3$. Then, the expression of r can be obtained by combining (7) and (13)

$$r = u + B_2^{-1}A_{21}y - B_2^{-1}A_{21}\hat{y} - \left[P_o(\hat{y}-y) + I_o\int_0^t(\hat{y}-y)\mathrm{d}t + D_o\,\mathrm{d}(\hat{y}-y)/\mathrm{d}t\right] \quad (14)$$

If the values of P_o, I_o, and D_o are properly chosen (to be discussed later), (14) will be able to regulate the error system (6), hence making the estimated states $\hat{X}$ in (2) converge to the actual states of the PEA X in (1) and achieving state observation. After the convergence of $\hat{X}$ to X, an estimation, $\hat{\varepsilon}$, of the unknown input ε can also be calculated by substituting (14) into (2) and comparing the resultant system with (1), which gives

$$\hat{\varepsilon} = r - u = B_2^{-1}A_{21}y - B_2^{-1}A_{21}\hat{y} - \left[P_o(\hat{y}-y) + I_o\int_0^t(\hat{y}-y)\mathrm{d}t + D_o\,\mathrm{d}(\hat{y}-y)/\mathrm{d}t\right] \quad (15)$$

A flowchart illustrating the above derivations of the PIDSMO is provided in Fig. 4 for better understanding.

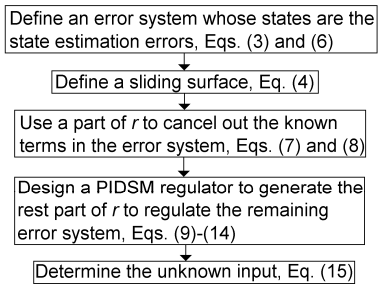

Fig. 4. Workflow of deriving the PIDSMO

B. Sliding Surface Parameter m_o

The sliding surface parameter m_o is affected by P_o, I_o, D_o, ε, and e_{o1}. Recall that r_{eq} is included in r_3 (i.e. $r_{res1}=r_3$) and $\hat{y}-y=\hat{x}_1-x_1=e_{o1}$, substituting (13) into (8) yields

$$\begin{bmatrix}\dot{e}_{o1}\\ \dot{e}_{o2}\end{bmatrix} = \begin{bmatrix} e_{o2} \\ A_{22}e_{o2} - B_2\left(P_o e_{o1} + I_o\int_0^t e_{o1}\mathrm{d}t + D_o\dot{e}_{o1}\right) - B_2\varepsilon\end{bmatrix} \quad (16)$$

During sliding motion, (9) is valid, so $e_{o2}=-m_o e_{o1}$. From (16), one has

$$(B_2D_o - A_{22} - m_o)\dot{e}_{o1} = -B_2P_oe_{o1} - B_2I_o\int_0^t e_{o1}\mathrm{d}t - B_2\varepsilon \quad (17)$$

Differentiating both sides of (17) and using the relationships $\dot{e}_{o1}=e_{o2}=-m_oe_{o1}$ and $\ddot{e}_{o1}=\dot{e}_{o2}=-m_o\dot{e}_{o1}$ obtained from (9) and (16), (17) becomes

$$e_{o1}m_o^3 + (A_{22}e_{o1} - B_2D_oe_{o1})m_o^2 + B_2P_oe_{o1}m_o + (-B_2I_oe_{o1} - B_2\dot{\varepsilon}) = 0 \quad (18)$$

Then during sliding motion, m_o can be found by solving (18) if P_o, I_o, D_o, ε, and e_{o1} are known. However, in practice ε is unknown. For this reason, one can only solve for the value of m_o under the conditions of $\varepsilon\equiv 0$, i.e. $m_o|_{\varepsilon\equiv 0}$. Setting $\dot{\varepsilon}=0$ in (18) and replacing m_o with $m_o|_{\varepsilon\equiv 0}$ yields the equation for solving for $m_o|_{\varepsilon\equiv 0}$

$$m_0^3\big|_{\varepsilon\equiv 0} + (A_{22}-B_2D_o)m_0^2\big|_{\varepsilon\equiv 0} + B_2P_om_o\big|_{\varepsilon\equiv 0} - B_2I_o = 0 \quad (19)$$

This is a third order polynomial having three roots. Since $m_o|_{\varepsilon\equiv 0}$ must be real and unique, it is convenient in practice to choose the P_o, I_o, and D_o values such that the discriminant

$$\Delta = 18(A_{22}-B_2D_o)B_2P_o(-B_2I_o) - 4(A_{22}-B_2D_o)^3(-B_2I_o) + (A_{22}-B_2D_o)^2(B_2P_o)^2 - 4(B_2P_o)^3 - 27(-B_2I_o)^2 \quad (20)$$

is negative and (19) will have only one real root.

Since the unknown input ε and $\dot{\varepsilon}$ are assumed to be bounded (Section II) and the output estimation error e_{o1} are also bounded in practice, the actual value of m_o will stay in a bounded range around $m_o|_{\varepsilon\equiv 0}$. On the other hand, m_o should be positive and real to ensure that the sliding motion (9) is stable. So it is desirable to locate m_0 at a point on the positive half real axis with a large distance from the origin such that the range of m_0 is also on the positive half real axis.

In practice, the bounds of m_0 may be difficult to be found, hence one can use the value of $m_o|_{\varepsilon\equiv 0}$ as one of the guidelines for determining the values of P_o, I_o, and D_o such that the stability of the sliding motion (9) is ensured.

C. Sliding Surface Reachability

For the sliding motion (9) to happen, the sliding surface (4) must be reachable, or the state estimation error vector (3) should be driven towards the sliding surface (4). The reachability of the sliding surface (4) is determined by the P_o, I_o, and D_o parameters and m_0 according to the following theorem.

Theorem:

For the error system defined by (6) with the sliding surface defined by (4), if the input r to the error system is given by (14) and the initial values of e_{o1} and q_o, and the values of ε are all bounded, then the sliding surface (4) is asymptotically reachable, i.e. $q_o\to 0$ as $t\to\infty$, if and only if the roots of

$$s^3 + (B_2D_o + m_o)s^2 + B_2P_os + B_2I_o = 0 \quad (21)$$

have negative real parts, where s is the Laplace transform operator.

Proof: the proof is given in the Appendix.

It can be seen form the above theorem and (19) that the existence of the integrator in the PIDSMO, i.e. $I_o\neq 0$, is a necessary condition for the sliding motion being stable and the sliding surface (4) being asymptotically reachable.

D. Stability of the PIDSMO

A sufficient condition for the PIDSMO to be stable can be obtained from the analysis on its sliding mode behavior (the system states reaching the SM first and then slide along it) in the previous two sub-sections. This sufficient condition states that if (a) the sliding surface is asymptotically reachable, i.e. the roots of (21) have negative real parts; and (b) the sliding motion is stable, i.e. $m_o > 0$, then the PIDSMO is stable.

In practice the above stability condition is difficult to check due to the effects of ε on m_o. Alternatively, a necessary and sufficient condition for the PIDSMO to be stable can be found by examining its transfer functions as follows.

For the PEA-PIDSMO system, which consists of the PEA (system (1)) and the PIDSMO ((2) and (14)), y can be decomposed into two components as

$$y = y_{o1} + y_{o2} \tag{22}$$

where y_{o1} is induced by u and y_{o2} is induced by ε. Then, $\hat{x}_1$ and $\hat{x}_2$ can be decomposed as

$$\hat{x}_1 = \hat{x}_{11} + \hat{x}_{12} \tag{23}$$

$$\hat{x}_2 = \hat{x}_{21} + \hat{x}_{22} \tag{24}$$

where $\hat{x}_{11}$ and $\hat{x}_{21}$ are estimated states based on y_{o1} and u, and $\hat{x}_{12}$ and $\hat{x}_{22}$ are estimated states based on y_{o2}. By setting $\varepsilon \equiv 0$, it can be derived from (1), (2), and (14) that

$$G_1(s) = \hat{X}_{11}(s)/Y_{o1}(s) = 1, \quad G_2(s) = \hat{X}_{21}(s)/[sY_{o1}(s)] = 1 \tag{25}$$

where $\hat{X}_{11}(s)$, $\hat{X}_{21}(s)$, and $Y_{o1}(s)$ are the Laplace transform of $\hat{x}_{11}$, $\hat{x}_{21}$, and y_{o1}, respectively. Equation (25) indicates that, if $\varepsilon \equiv 0$ (so that $\hat{x}_{11} = \hat{x}_1$ and $\hat{x}_{21} = \hat{x}_2$), $\hat{x}_1$ and $\hat{x}_2$ track y_{o1} and $\dot{y}_{o1}$, or x_1 and x_2 exactly. On the other hand, by setting $u \equiv 0$, it can be derived from (1), (2), and (14) that

$$G_3(s) = \hat{X}_{12}(s)/Y_{o2}(s) = G_4(s) = \hat{X}_{22}(s)/[sY_{o2}(s)] = \frac{B_2 D_o s^2 + (A_{21} + B_2 P_o)s + B_2 I_o}{s^3 + (B_2 D_o - A_{22})s^2 + B_2 P_o s + B_2 I_o} \tag{26}$$

where $\hat{X}_{12}(s)$, $\hat{X}_{22}(s)$, and $Y_{o2}(s)$ are the Laplace transform of $\hat{x}_{12}$, $\hat{x}_{22}$, and y_{o2}, respectively. $G_1(s)$, $G_2(s)$, $G_3(s)$, and $G_4(s)$ constitute the transfer functions of the PIDSMO. Among them, $G_1(s)$ and $G_2(s)$ in (25) are always stable, so the stability of the PIDSMO is determined by the stability of $G_3(s)$ and $G_4(s)$ in (26). Hence, the necessary and sufficient condition for the PIDSMO to be stable can be stated as: the PIDSMO is stable if and only if the poles of (26) are on the left half s-plane.

E. Measurement Noise Suppression of the PIDSMO

As mentioned previously, the measurement noise of y can be treated as being induced by ε. Given that the measurement noise is usually of high frequency, it can be considered as resulting from the high frequency components of ε. It is desirable for the PIDSMO to suppress the effects of such noise on $\hat{x}_1$ and $\hat{x}_2$. For this, the PIDSMO should have the low-pass frequency response, i.e. insensitive to the high frequency components of ε. To check this, the frequency response of the PIDSMO is examined in the following.

The frequency response of the PIDSMO is represented by the frequency responses of $G_1(s)$, $G_2(s)$, $G_3(s)$, and $G_4(s)$ presented in the last sub-section. The Bode plots of $G_3(s)$ and $G_4(s)$ in (26) are shown in Fig. 5, in which the model parameters given in Section II are used. The P_o, I_o, and D_o values used for plotting the Bode plots are also shown in the figures. It is noticed that $G_3(s)$ and $G_4(s)$ indeed possess the low-pass characteristic, which is highly desirable for measurement noise suppression. It is also observed from Fig. 5 that the cutoff frequency increases with P_o, that increasing I_o generates a resonant peak and may also lead to instability due to the increase in phase lag around the resonant peak, and that the attenuation and phase lag of the high frequency components deceases as D_o increases. Such observations will also be of great help in the tuning of the PIDSMO.

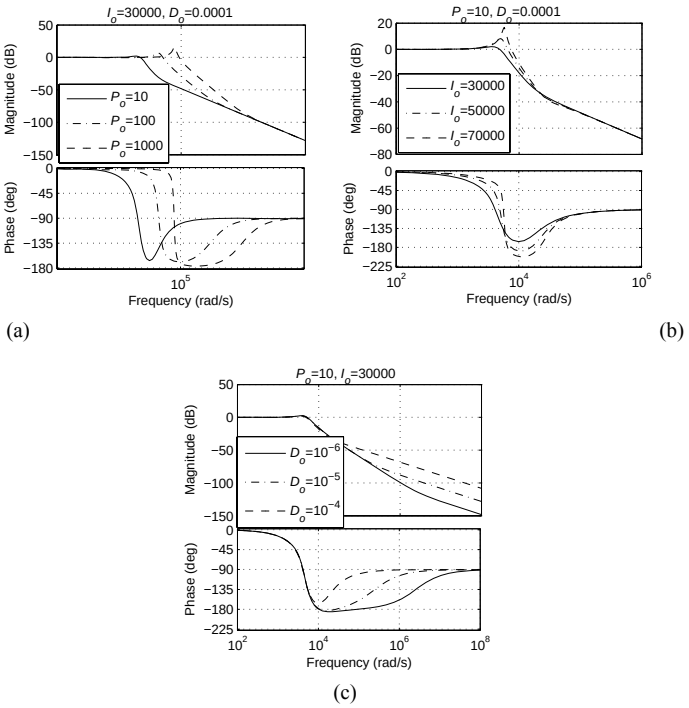

Fig. 5. Frequency responses of the transfer function (26) of the PIDSMO with different parameters.

IV. INTEGRATED PID-BASED SLIDING MODE OBSERVER-CONTROLLER

A. Integration of the PID-Based Sliding Mode Observer and Controller

A PIDSMC for tracking control of PEAs was developed in the authors' previous study [12]. The PIDSMC generates a control signal u by using the same idea for the development of the PIDSMO in the last section, i.e., replacing the switching

term in the sliding mode algorithm with a PID regulator. In the PIDSMC, u is generated such that the states of the PEA follow the desired or reference states, which is denoted by $X_d = [x_{d1} \quad x_{d2}]^T = [x_d \quad \dot{x}_d]^T$ where $x_d = y_d$ is the desired displacement of the PEA. Specifically, u is given by

$$\begin{aligned} u &= \left(B^T B\right)^{-1} B^T \left(\dot{X}_d - AX_d\right) \\ &\quad - B_2^{-1}\left(m_c e_{c2} + A_{21} e_{c1} + A_{22} e_{c2}\right) \\ &\quad - \left(P_c q_c + I_c \int_0^t q_c \,\mathrm{d}t + D_c \dot{q}_c\right) \end{aligned} \tag{27}$$

where P_c, I_c, and D_c are the PID parameters of the PIDSMC; and e_{c1} and e_{c2} are the state tracking errors, forming the following tracking control error vector

$$E_c = [e_{c1} \quad e_{c2}]^T = [x_1 - x_{d1} \quad x_2 - x_{d2}]^T \tag{28}$$

And m_c is the sliding surface parameter of the PIDSMC with the sliding surface defined by

$$q_c = m_c e_{c1} + e_{c2} = 0 \tag{29}$$

It has been shown that the PIDSMC is stable if and only if the roots of the following equation have negative real parts and $m_c > 0$ [12].

$$(B_2 D_c + 1)s^2 + B_2 P_c s + B_2 I_c = 0 \tag{30}$$

In this study, the PIDSMC (27) is combined with the PIDSMO developed in Section III ((2) and (14)) to form an integrated state estimation-control scheme for PEAs. This is established by replacing x_1 and x_2 in (28) with the PIDSMO estimated $\hat{x}_1$ and $\hat{x}_2$, i.e.,

$$E_c = [e_{c1} \quad e_{c2}]^T = [\hat{x}_1 - x_{d1} \quad \hat{x}_2 - x_{d2}]^T \tag{31}$$

In the following, this integrated state estimation-control scheme is referred to as the PID-based sliding mode observer-controller (PIDSMOC). Fig. 6 show the block diagram of the PIDSMOC as applied to a PEA.

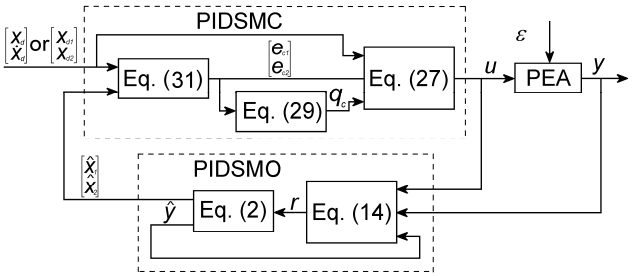

Fig. 6. Block diagram of the application of PIDSMOC to a PEA. In simulations, the PEA block is replaced with Equation (1).

B. Stability of the PIDSMOC

It is seen from Fig. 6 that the PIDSMOC applied to the PEA system is a two-input-one-output system with the desired state, x_d, and the unknown input, ε, as inputs and the measured displacement of the PEA, y, as output. Due to the linearity of closed loop system, y can be decomposed as

$$y = y_1 + y_2 \tag{32}$$

where y_1 is induced by x_d and y_2 is induced by ε. Then the stability of the PIDSMOC as applied to the PEA system can be examined through the transfer functions from x_d to y_1 and from ε to y_2. From (1), (2), (14), (27), (29), and (31), the following can be derived if $\varepsilon = 0$,

$$G_5(s) = Y_1(s)/X_d(s) = 1 \tag{33}$$

where $X_d(s)$ and $Y_1(s)$ are the Laplace transform of x_d and y_1, respectively. Equation (33) describes the dynamic relationship between x_d and y_1. It indicates that, if there is no unknown input, the output displacement of the PEA would follow the desired displacement x_d. Similarly if $x_d = 0$, one has (34) (at the bottom) where $Y_2(s)$ is the Laplace transform of y_2. Equation (34) describes the dynamic relationship between ε and y_2 or the effect of the unknown input ε on the output of the closed-loop system in Fig. 6. For y_2 to be stable, all the poles in (34) must be located in the left-half s-plane, which leads to $m_c > 0$ and the roots of both $(B_2 D + 1)s^2 + B_2 P s + B_2 I = 0$ and $s^3 + (B_2 D_o - A_{22})s^2 + B_2 P_o s + B_2 I_o = 0$ have negative real parts. Whilst the first two requirements are the same as the stability condition of the PIDSMC (SECTION IV A), the third requirement is identical to the stability condition of the PIDSMO (SECTION III D). Therefore, as long as the PIDSMO and the PIDSMC are stable individually, the PIDSMOC as applied to the PEA system is stable.

V. EXPERIMENTS AND SIMULATIONS

Experiments were performed on the experiment setup described in Section II A. Their objectives were (a) to validate the sliding mode behavior and effectiveness of the PIDSMO, (b) to validate the effectiveness of the PIDSMOC; and (c) to compare the performances of the PIDSMOC to that of the PIDSMC + α-β filter scheme. Simulations were also performed to examine the robustness of the PIDSMO and the PIDSMOC.

A. Experiments to validate the PIDSMO

Two experiments were performed to validate the PIDSMO. The first experiment was to validate the relationship between P_o, I_o, D_o, and $m_o|_{\varepsilon \equiv 0}$ (19) (m_o was not examined because it is affected by ε) and the reachability condition of the sliding surface, as discussed in Section III. This was performed by examining the measured phase portrait of the error system (6) to see if a sliding motion occurred and was stable and if yes, comparing the sliding surface shown in the measured phase portrait with that determined by $m_o|_{\varepsilon \equiv 0}$ (the theoretically predicted sliding surface). ε must be kept as small as possible in this experiment as indicated by the notion

$$G_6(s) = \frac{Y_2(s)}{\Sigma(s)} = \frac{sB_2\left[(1 + B_2 D_c)s^3 + (m_c + B_2 P_c + B_2 D_c m_c + B_2 D_o)s^2 + (A_{21} + B_2 P_c m_c + B_2 I_c + B_2 P_o)s + B_2 I_c m_c + B_2 I_o\right]}{(s + m_c)\left[(B_2 D + 1)s^2 + B_2 P s + B_2 I\right]\left[s^3 + (B_2 D_o - A_{22})s^2 + B_2 P_o s + B_2 I_o\right]} \tag{34}$$

of $m_o|_{\varepsilon\equiv 0}$. With this consideration, a constant input $u \equiv 0$ V was fed to the PEA without loads. In such conditions, only the part of ε that accounts for the measurement noise was in place. Since the noise is of zero mean with a small variance (as assumed in Section II), it is reasonable to assume $\varepsilon \approx 0$. The initial estimation errors or the initial states of the error system (6) were set to $e_{o1}(0) = -5.25\mu$m and $e_{o2}(0) = 625\mu$m/s) so that the process of these states being driven to the sliding surface and then slide along it before they converge to the origin could be observed in the phase portrait given that the reachability condition and the stability condition of the sliding surface were met. To produce this phase portrait, the states of (6) need to be measured. While $e_{o1} = \hat{x}_1 - y$ is measurable, $e_{o2} = \hat{x}_2 - x_2$ is not because x_2 is immeasurable. However, given that $u \equiv 0$ V and $\varepsilon \approx 0$, it was reasonable to assume $x_2 \equiv 0$. The PIDSMO parameters used in this experiment were chosen as $P_o = 7$, $I_o = 3000$, $D_o = 10^{-6}$ so that $m_o|_{\varepsilon\equiv 0} = 503 > 0$ according to (19), i.e. the sliding motion was stable in theory as m_o varies in the neighborhood of $m_o|_{\varepsilon\equiv 0}$, and the roots of (21) being $-38.8 \pm 5.20\times 10^3 i$ and -429,.i.e. the sliding surface was asymptotically reachable in theory. The measured phase portrait of the error system (6) is shown in Fig. 7, in which the sliding surface determined by $m_o|_{\varepsilon\equiv 0}$ (the theoretically predicted sliding surface) is also shown. It can be seen that the theoretically predicted sliding surface matches the sliding surface that appears in the measured phase portrait, hence validating the relationship between P_o, I_o, D_o, and $m_o|_{\varepsilon\equiv 0}$. And it can be observed that the states of the error system (6) were driven towards the sliding surface and then stayed on it. In other words, the sliding surface appeared in the measured phase portrait was reachable, which also agree with the theoretical prediction. Also shown in Fig. 7 is that both e_{o1} and e_{o2} eventually converge to the origin, indicating that the sliding motion (9) is stable and that the estimated states follow the PEA ones well afterward.

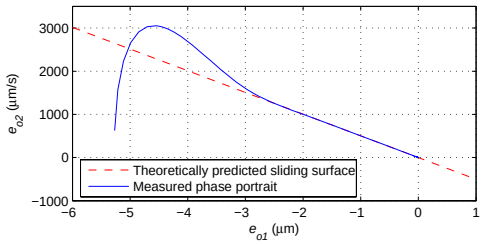

Fig. 7. Comparing the measured phase portrait of (6) and the theoretically predicted sliding surface.

The second PIDSMO experiment was to validate the state estimation capability of the PIDSMO in both no-load and loaded situations. In this experiment, the parameters of the PIDSMO (P_o, I_o, and D_o) were chosen such that the PIDSMO or (25) and (26) was stable and the frequency responses of (26) met certain performance requirements (e.g. cutoff frequency, peaking, etc.) for the sake of noise suppression. While the stability of the PIDSMO can be readily checked out, the frequency responses of the PIDSMO are tuned by adjusting P_o to achieve a desired cutoff frequency, adjusting D_o to achieve desired attenuations of the high frequency components, and adjusting I_o such that the resonant peak or peaking phenomenon occurs around the cutoff frequency can be modified (refer to Fig. 5). Particularly, the tuning process was carried out as follows. Firstly, the frequency range on which the cutoff frequency of the system G_3 in (26) should fall was determined. It was assumed that the frequency components below 200 Hz in y_{o2} should pass the system G_3. This served as a lower bound of the frequency band. To find an upper bound, the frequency composition of the measurement noise was examined. Fig. 8 shows the power spectrum density (PSD) of the measurement noise of the experiment setup described in Section II. It was observed that the first three peaks were around 455 Hz, 910 Hz, and 1370 Hz, respectively, with the 455 Hz peak lower than most of other peaks, especially the 1370 Hz peak. Based on this observation, the upper bound of the cutoff frequency of system G_3 was chosen as 910 Hz. With the so-determined range of the cutoff frequency, P_o, I_o, and D_o were then tuned to have values of 10, 20000, and 0.000006, respectively such that a cutoff frequency of about 710 Hz which is within the above-determined frequency range was obtained and that there was no peaking in the magnitude frequency response of G_3. The PIDSMO with these parameters is stable. The PSD of the measurement noise after passing through the PIDSMO, which is represented by the noise in $\hat{x}_1$, is also shown in Fig. 8. It can be seen that the PSD of the noise in $\hat{x}_1$ is almost zero, showing that the measurement noise has been significantly suppressed by the PIDSMO.

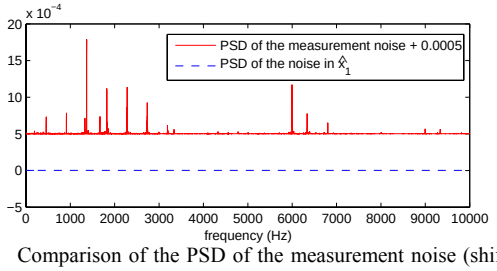

Fig. 8. Comparison of the PSD of the measurement noise (shifted up for clarity) to the PSD of the noise in $\hat{x}_1$ estimated by a PIDSMO with $P_o = 10$, $I_o = 20000$, and $D_o = 0.000006$.

This PIDSMO with the parameters determined above was then applied to estimate the states of the PEA in both no-load and loaded situations. In no-load situation, there was no external force applied to the PEA end-effector; and ε accounts for the unknown/difficult-to-model effects except the external loads. In the loaded situation, a mass of 142.1 g was attached to the PEA end-effector such that the resultant mass of the end-effector was approximately doubled (the original

mass of the end-effector is 150 g), causing a change in ε. In this experiment, the input voltage to the PEA was designed to be a piecewise function, which is described by

$$\begin{aligned} u(t) &= 0 \quad \text{for} \quad t \le 0.02\,\text{s} \\ u(t) &= 6.29\times10^{11}(t-0.02)^5 - 2.30\times10^{10}(t-0.02)^4 \\ &\quad + 2.17\times10^{8}(t-0.02)^3 \\ &\quad \text{for} \quad 0.02\,\text{s} < t \le 0.03\text{s} \\ u(t) &= (75/7)\sin[2\pi\cdot10(t-0.03)+\pi] \\ &\quad + (125/14)\sin[2\pi\cdot40(t-0.03)+0.5\pi] \\ &\quad + (25/7)\sin[2\pi\cdot100(t-0.03)+0.2\pi] \\ &\quad + (15/14)\sin[2\pi\cdot200(t-0.03)]+25 \end{aligned} \quad \text{for} \quad t > 0.03\,\text{s} \tag{35}$$

It is seen that the highest frequency of this input is 200 Hz. To examine the state estimation performance of the PIDSMO, $\hat{x}_1$ in both no-load and loaded situations were compared to the measured y or x_1. Ideally, $\hat{x}_2$ should also be compared to x_2. Since x_2 was immeasurable in the present experimental settings, an approximation of x_2, denoted as $\widetilde{x}_2$, was used instead, which was obtained by firstly passing the measurement of y through an eighth-order Butterworth low-pass filter with a cutoff frequency of 8000 Hz and then differentiating the Butterworth filter output signal. The comparisons between y and $\hat{x}_1$ and between $\widetilde{x}_2$ and $\hat{x}_2$ are shown in Fig. 9.

It was observed that in both no-load and loaded situations $\hat{x}_1$ tracked y or x_1 closely. The root mean square (RMS) estimation errors are 0.0217 μm and 0.0220 μm, respectively, which are very small. $\hat{x}_2$ also tracked $\widetilde{x}_2$ well in both situations. Meanwhile, it was also noticed that $\widetilde{x}_2$ had a small phase lag behind $\hat{x}_2$ despite a high cutoff frequency was chosen for the Butterworth filter and that $\widetilde{x}_2$ is more heavily contaminated by noise than $\hat{x}_2$. Estimations of the unknown input, $\hat{\varepsilon}$, to the system given in (1) in both no-load and loaded situations were calculated by using (15) with the results illustrated in Fig. 9 (e), in which the changes in $\hat{\varepsilon}$, hence ε, due to the attached mass in the loaded situation is clearly noticeable. Based on the above discussion, it can be concluded that the PIDSMO can estimate the PEA states accurately despite the existence of the unknown input ε, and that the PIDSMP has small phase lag and strong noise suppression capability.

B. Experiments to validate the PIDSMOC

In this section, the PIDSMOC developed was used for tracking control of the PEA with/without the presence of load to demonstrate its effectiveness. The parameters of the PIDSMOC were tuned based on the stability condition and the frequency responses of the closed-loop system. The stability condition of the PIDSMOC as applied to the PEA is described in Section IV whilst the effects of the PIDSMOC parameters on the frequency responses of the closed-loop system, which are represented by G_5 in (33) and G_6 in (34), are described as follows. The frequency response of G_5 is trivial (0 dB gain and 0° phase lag at all frequencies) whilst the frequency response of G_6 is more complicated. Generally speaking, the effects of the low and high frequency components of ε on y_2 are largely attenuated by G_6 whist the effects of the medium frequency components of ε on y_2 are less attenuated. Furthermore, the attenuation of the medium frequency components of ε increase as m_c, P_c, and P_o increase. I_c increases the attenuation of the low frequency components of ε whist D_c and D_o increase the attenuation of the high frequency components of ε. And I_o decreases the minimum attenuation of ε. Based on the above analysis, the PIDSMOC parameters were chosen as $m_c = 22000$, $P_c = 0.005$, $I_c = 1$, $D_c = 10^{-8}$, $P_o = 12$, $I_o = 50000$, $D_o = 10^{-4}$ for the no-load situation such that the RMS error when tracking $x_d = [5\sin(300\pi t)+5]$ μm was as small as possible.

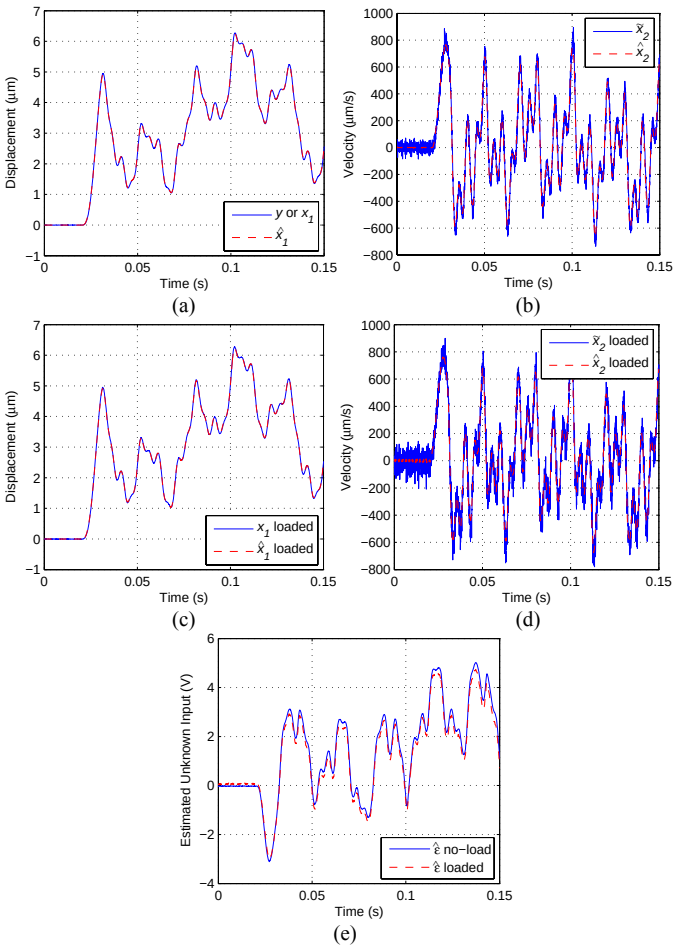

Fig. 9. PIDSMO state estimation experiment results: (a) comparison of x_1 to $\hat{x}_1$ without load; (b) comparison of $\widetilde{x}_2$ to $\hat{x}_2$ without load; (c) comparison of x_1 to $\hat{x}_1$ with a load; (d) comparison $\widetilde{x}_2$ to $\hat{x}_2$ with a load; and (e) estimated unknown inputs $\hat{\varepsilon}$ for both no-load and loaded situations.

The desired displacements, x_d, employed in the PIDSMOC tracking control experiments were $x_d = [5\sin(f_d 2\pi t) + 5]$ μm with a frequency f_d of 1 Hz, 5 Hz, 10 Hz, 50 Hz, 100 Hz, and 150 Hz, respectively. The RMS and maximum errors of the measured displacement in both no-load and loaded situations are listed in Table I; and x_d, y, and the tracking errors e_{c1} in the 100 Hz experiment are shown in Fig. 10. It can be observed from Fig. 10 (a) and (c) that the measured displacement of the PEA, y, tracked x_d closely in both no-load and loaded situations; and from Fig. 10 (b) and (d) that high frequency vibrations, though of small magnitudes, became noticeable in the loaded situation, thus increasing the tracking errors (see Table I). Such high frequency vibrations might be caused by the excitation of the reduced resonant frequency (by attaching the mass to the end-effector of the PEA) of the PEA. From Table I, it is also noticed that the tracking errors increased with the application of an external load and the variation of input frequency from 1 Hz to 150 Hz and that, overall, they remained relatively small and less than 3% of the maximum desired displacement (10 μm). Therefore, it can be concluded that good tracking performance, in terms of small tracking error, large bandwidth, and good unknown input suppression, can be achieved by the use of the PIDSMOC as applied to a PEA.

C. Comparative Experimental Study between the PIDSMOC Scheme and the PIDSMC + α-β Filter Scheme

In this section, the tracking control performance of the PIDSMOC scheme is compared to that of the PIDSMC + α-β filter scheme reported in [12] as applied to control the PEA with/without the presence of load The same PIDSMC parameters as those chosen in Section V B were used in these comparative experiments. In the PIDSMC + α-β filter scheme, the PIDSMC is the same as the one described by (27), (29), and (31), and the α-β filter is a non-model-based discrete-time state estimator that employs two parameters, i.e., α and β, to adjust its behavior. The α-β filter is particularly formulated as follows, for the PEA state estimation

$$\hat{x}_1(kT_s) = \hat{x}_1(kT_s - T_s) + T_s\hat{x}_2(kT_s - T_s) + \alpha[y(kT_s) - \hat{x}_1(kT_s)] \quad (36)$$

$$\hat{x}_2(kT_s) = \hat{x}_2(kT_s - T_s) + \beta[y(kT_s) - \hat{x}_1(kT_s)]/T_s \quad (37)$$

where $k = 0,1,2,\cdots$. In this study, however, a continuous-time version of the α-β filter [33], which was obtain by taking the inverse impulse invariant transform of (36) and (37), was employed due to the fact that both the PIDSMO developed and the PIDSMC used are in the continuous-time domain. The transfer functions of the continuous-time α-β filter are

$$G_7(s) = \frac{\hat{X}_1(s)}{Y(s)} = \frac{\omega_{fn}^2 + \omega_{fn}(2\xi_f - \omega_{fn}T_s)s}{s^2 + 2\xi_f\omega_{fn}s + \omega_{fn}^2} \quad (38)$$

$$G_8(s) = \frac{\hat{X}_2(s)}{sY(s)} = \frac{\omega_{fn}^2}{s^2 + 2\xi_f\omega_{fn}s + \omega_{fn}^2} \quad (39)$$

where $\hat{X}_1(s)$, $\hat{X}_2(s)$, and [illegible] are the Laplace transform of $\hat{x}_1$, $\hat{x}_2$, and y, respectively; and ξ_f and ω_{fn} are the damping ratio and the natural frequency of the continuous-time α-β filter, respectively. ξ_f, ω_{fn}, and T_s are related to α and β by

$$\alpha = \omega_{fn}T_s(2\xi_f - \omega_{fn}T_s/2) \quad (40)$$

$$\beta = (\omega_{fn}T_s)^2 \quad (41)$$

The PIDSMC + α-β filter scheme as applied to the PEA was then obtained by replacing the PIDSMO in Fig. 6 with the continuous-time α-β filter (38) and (39).

The parameters of the continuous-time α-β filter were tuned, leading to $\xi_f = 1/\sqrt{2}$ and $\omega_{fn} = 1200\pi$ rad/s for that there was no peaking in the magnitude frequency response of (39). In the tuning process, the cutoff frequency was set as 600 Hz, which is higher than the highest frequency component in x_d (i.e., 150 Hz) and lower than the frequency of the second peak in the PSD of the measurement noise (910 Hz). The parameters of the PIDSMC were then tuned for the no-load situation such that the RMS error when tracking $x_d = [5\sin(300\pi t) + 5]$ μm was as small as possible, which gives $m_c = 22000$, $P_c = 0.0004$, $I_c = 2$, and $D_c = 10^{-8}$.

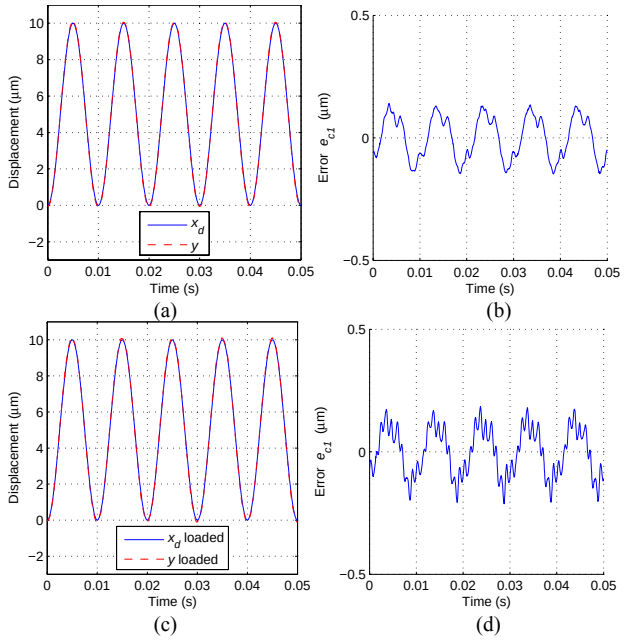

Fig. 10. PIDSMOC tracking control results: the comparison of the desired displacements x_d to the measured displacements y (left) and their difference or the error (right) at $f_d = 100$ Hz. (a) and (b): no-load situation; and (c) and (d): loaded situation.

PEA tracking control experiments using the PIDSMC + α-β filter scheme were then performed on the experiment setup with/without the presence of load. The desired displacements, x_d, used were the same as those in Section V B. The RMS and maximum errors of these experiments are also listed in Table I, while x_d, y, and the tracking errors e_{c1} in the 100 Hz experiments are shown in Fig. 11.

TABLE I
RMS E_{RMS} AND MAXIMUM ERRORS E_{MAX} OF THE MEASURED DISPLACEMENT IN PEA TRACKING EXPERIMENTS WITH THE PIDSMOC AND THE THE PIDSMC + α-β FILTER SCHEMES (CALCULATED USING 5 s OF DATA)

f_d and loading condition	PIDSMOC		PIDSMC + α- β filter	
	E_{RMS} (μm)	E_{max} (μm)	E_{RMS}(μm)	E_{max} (μm)
1 Hz, no-load	0.008	0.028	0.007	0.028
5 Hz, no-load	0.012	0.039	0.012	0.039
10 Hz, no-load	0.018	0.039	0.020	0.040
50 Hz, no-load	0.051	0.097	0.094	0.161
100 Hz, no-load	0.086	0.159	0.196	0.316
150 Hz, no-load	0.138	0.258	0.329	0.518
1 Hz, loaded	0.008	0.024	0.007	0.025
5 Hz, loaded	0.012	0.038	0.013	0.042
10 Hz, loaded	0.019	0.054	0.022	0.067
50 Hz, loaded	0.054	0.128	0.148	0.380
100 Hz, loaded	0.101	0.274	0.250	0.561
150 Hz, loaded	0.150	0.286	0.342	0.675

Comparing Fig. 10 and Fig. 11, it can be observed that the PIDSMC + α-β filter has larger tracking errors than the PIDSMOC in either no-load or loaded situation. From the errors listed in Table I, it is also seen that the PIDSMOC performs better than the PIDSMC + α-β filter except at 1 Hz. Particularly, if f_d is high (e.g. >50 Hz), the reduction of both RMS and maximum tracking errors by over 50% can be achieved by the use of the PIDSMOC instead of the PIDSMC + α-β filter. Also, it is noticed from Table I that the tracking errors in the PIDSMC + α-β filter experiments increases faster than those in the PIDSMOC experiments as f_d increases. Moreover, as can be seen in Fig. 11 (c) and (d), the high frequency vibration problem in the loaded PIDSMC + α-β filter experiments was more serious than in the PIDSMOC experiments.

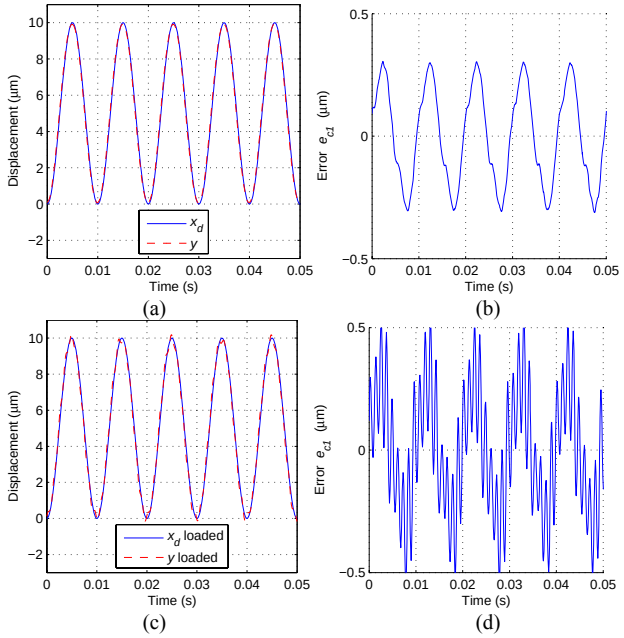

Fig. 11. PIDSMC + α-β filter tracking control results: the comparison of the desired displacements x_d to the measured displacements y (left) and their difference or the error (right) at $f_d = 100$ Hz. (a) and (b): no-load situation; and (c) and (d): loaded situation.

D. Robustness Analysis through Simulations

The robustness of the PIDSMO and the PIDSMOC were examined by simulations based on the block diagram Fig. 6, with the PEA block replaced by the PEA model (1). The PIDSMO and the PIDSMC in Section V B were used. The desired displacements was set as $x_d = [5\sin(200\pi t)+5]$ μm. An unknown input $\varepsilon = [10\sin(150t+1)+10]$V was added to the input u generated by the PIDSMC. Also, the output of the PEA model was subject to an additive noise with an RMS value of 0.05 μm. A simulation was carried out with the presence of modeling error, which was exemplified by +50% changes in all parameters (ξ, ω_n, and K) of the PEA model, for illustrating the robustness of the PIDSMO and the PIDSMOC. The results are shown in Fig. 12 and the state estimation errors and the tracking control errors remained below 5%. This suggests the strong robustness of the PIDSMO and the PIDSMOC despite the presence of large unknown inputs, measurement noises, and modeling error. It is noted that in the development of PIDSMO and PIDSMOC, there are no specific conditions imposed on the matched uncertainty as long as it and its first order derivative are bounded (Section II B). This indicates that theoretically, both PIDSMO and PIDSMOC can tolerate any bounded and differentiable matched uncertainty. In reality, however, this would be limited by the hardware performance or specifications, e.g. the control signal required to compensate for a large matched uncertainly may become so large that it saturates the power amplifier that drives the PEA.

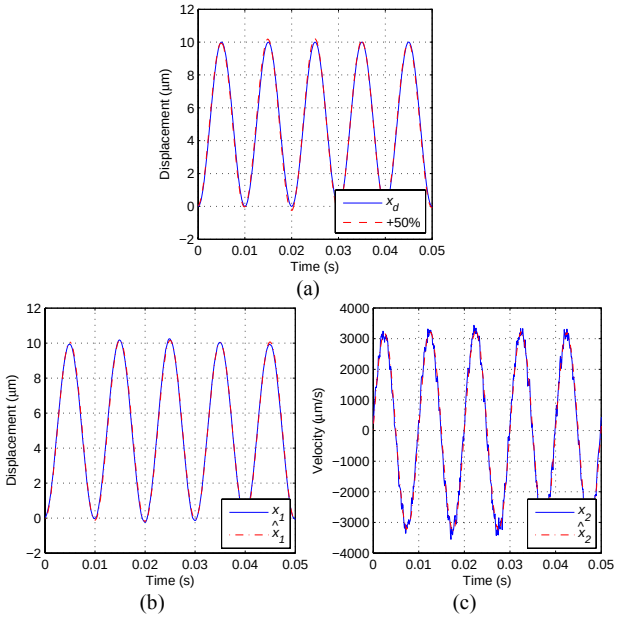

Fig. 12. Robustness analysis of the PIDSMOC and the PIDSMO. (a) Simulated performances of the PIDSMOC, comparing x_d to the simulated y corresponding to +50% model parameter variation. (b) and (c): Simulated performances of the PIDSMO as the model parameters are increased by 50%.

VI. CONCLUSIONS

Tracking control of PEAs has been drawing considerable

attention and a number of control schemes based on the state feedback have been developed for improved performance. However, the means by which the PEA states are obtained have not been well addressed in the literature. This paper presents the development of a novel so-called PIDSMO and its integration with PIDSMC for the PEA tracking control.

A PEA was represented by a second-order system with the matched unknown inputs to account for the influence of hysteresis, creep, external load, and other unknown effects. On this basis, a novel observer, i.e. PIDSMO, was developed based on the concept of PID-based sliding mode. Different from other UIOs, the PIDSMO does not require the observer matching condition to be satisfied. The developed PIDSMO was then combined with the PIDSMC to form a PIDSMOC for PEA tracking control. The stability condition of the PIDSMOC was examined. Experimental validation of the PIDSMO and PIDSMOC was then performed on a PEA, along with a comparison to the PIDSMC + α-β filter scheme. The robustness of the PIDSMO and the PIDSMOC were also examined through simulations.

It is concluded that the PIDSMO developed is capable of estimating the PEA states accurately with small phase lag and strong noise suppression capability regardless of the presence of hysteresis, creep, and/or external loads. Also, it has been shown that the novel scheme of PIDSMOC can achieve a promising tracking performance, with the maximum error less than 3% of the PEA full displacement examined. By comparison, the PIDSMOC scheme is generally better than the PIDSMC + α-β filter scheme in terms of the RMS and the maximum tracking errors in both no-load and loaded situations. Finally, the performance PIDSMO and the PIDSMOC is found robust even with the presence unknown inputs, measurement noises, and modeling errors.

APPENDIX

Proof of the Theorem in Section III C:

Substituting (13) into (12) and applying the relationship $e_{o1}=(\hat{y}-y)$ yields

$$\dot{q}_o=-B_2\varepsilon-B_2\left[P_o e_{o1}+I_o\int_0^t e_{o1}\mathrm{d}t+D_o\dot{e}_{o1}\right] \tag{42}$$

From (4) and (8), one has

$$q_o=me_{o1}+e_{o2}=me_{o1}+\dot{e}_{o1} \tag{43}$$

Decomposing e_{o1}, q_o, and ε as

$$\varepsilon=\varepsilon_0+\varepsilon_1,\quad e_{o1}=e_{o10}+e_{o11},\quad q_o=q_{o0}+q_{o1} \tag{44}$$

where $\varepsilon_0\equiv\varepsilon(0)$, $e_{o10}\equiv e_{o1}(0)$, and $q_{o0}\equiv q_o(0)$ are the initial value of ε, e_{o1}, and q_o, respectively. ε_1 has zero initial value with $|\varepsilon_1|\le\varepsilon_{1\max}$. e_{o11} and q_{o1} also have zero initial values.

Substituting (44) into (42) and (43) yields

$$\begin{aligned}\dot{q}_{o1}=&-B_2\varepsilon_0-B_2\varepsilon_1-B_2P_oe_{o10}-B_2P_oe_{o11}\\&-B_2I_o\int_0^t e_{o10}\mathrm{d}t-B_2I_o\int_0^t e_{o11}\mathrm{d}t-B_2D_o\dot{e}_{o11}\end{aligned} \tag{45}$$

$$q_{o0}+q_{o1}=m_oe_{o10}+m_oe_{o11}+\dot{e}_{o11} \tag{46}$$

The system defined by (45) and (46) can be treated as a linear dynamic system with four inputs, i.e. ε_0, ε_1, e_{o10}, and q_{o0}, and one output, i.e. q_{o1}, where e_{o11} is an intermediate variable. So, this linear dynamic system can be decomposed into four single-input-single-output (SISO) subsystems and each takes one of the four inputs as its input while its outputs being q_{o1n}, $n=1,2,\cdots4$ with $\sum_{n=1}^4 q_{o1n}=q_{o1}$. For the sliding surface to be reachable or $q_o\to0$ as $t\to\infty$, the system (45) and (46) must be stable. The corresponding stability condition is the combination of all stability conditions of the four subsystems, and the value of q_o as $t\to\infty$ is the sum of the values of q_{o1n} as $t\to\infty$ and q_{o0}. Following this idea, each subsystem is examined as follows.

The first subsystem takes ε_0 as input and q_{o11} as output. By setting other inputs in (45) and (46) to zero and then take the Laplace transform, one has

$$sQ_{o11}(s)=-B_2\Sigma_0(s)-B_2P_oE_{o11}(s)-\frac{B_2I_oE_{o11}(s)}{s}-B_2D_osE_{o11}(s) \tag{47}$$

$$Q_{o11}(s)=m_oE_{o11}(s)+sE_{o11}(s) \tag{48}$$

Solving (48) for $E_{o11}(s)$ and then substituting it to (47) yields the transfer function of the first subsystem,

$$\frac{Q_{o11}(s)}{\Sigma_0(s)}=\frac{-B_2s^2-B_2m_os}{s^3+(B_2D_o+m_o)s^2+B_2P_os+B_2I_o} \tag{49}$$

It can be seen that the first system (49) is asymptotically stable if and only if the roots of (21) have negative real parts. Also notice that there must be $I_o\neq0$.

Recall that $\varepsilon_0(t)\equiv\varepsilon(0)$, so $\Sigma_0(s)=\varepsilon(0)/s$. Applying the final value theorem of the Laplace transform to $Q_{o11}(s)$ yields

$$q_{o11}(\infty)=\lim_{s\to0}\frac{s\left(-B_2s^2-B_2m_os\right)\varepsilon(0)/s}{s^3+(B_2D_o+m_o)s^2+B_2P_os+B_2I_o}=0 \tag{50}$$

The second subsystem takes ε_1 as input and q_{o12} as output. Following the same procedure as applied to the first subsystem, the transfer function of the second subsystem can be found as

$$\frac{Q_{o12}(s)}{\Sigma_1(s)}=\frac{-B_2s^2-B_2m_os}{s^3+(B_2D_o+m_o)s^2+B_2P_os+B_2I_o} \tag{51}$$

So the second subsystem has the same stability condition as the first subsystem. Applying the final value theorem of the Laplace transform to $Q_{o12}(s)$ yields

$$q_{o12}(\infty)=\lim_{s\to0}\frac{s\left(-B_2s^2-B_2m_os\right)\Sigma_1(s)}{s^3+(B_2D_o+m_o)s^2+B_2P_os+B_2I_o} \tag{52}$$

Let $\mathrm{Re}(s)=s_r$ and $\mathrm{Im}(s)=s_i$. Notice that $|\varepsilon_1|\le\varepsilon_{1\max}<\infty$, so the Laplace transform of $\varepsilon_1(t)$, i.e. $\Sigma_1(s)$, satisfies

$$\begin{aligned}|\Sigma_1(s)|&=\left|\int_0^{+\infty}e^{-st}\varepsilon_1(t)\mathrm{d}t\right|\le\int_0^{+\infty}\left|e^{-st}\varepsilon_1(t)\right|\mathrm{d}t\le\varepsilon_{1\max}\int_0^{+\infty}\left|e^{-st}\right|\mathrm{d}t\\&=\varepsilon_{1\max}\int_0^{+\infty}\left|e^{-(s_r+is_i)t}\right|\mathrm{d}t\le\varepsilon_{1\max}\int_0^{+\infty}\left|e^{-s_rt}\right|\left|e^{-is_it}\right|\mathrm{d}t\\&=\varepsilon_{1\max}\int_0^{+\infty}\left|e^{-s_rt}\right|\left|\cos(-s_it)+i\sin(-s_it)\right|\mathrm{d}t=\frac{\varepsilon_{1\max}}{s_r}\end{aligned} \tag{53}$$

The region of convergence of $\Sigma_1(s)$ in the worst case

scenario is the region of $\mathrm{Re}(s)=s_r>0$ on the s-plane. So

$$\begin{aligned}
&\lim_{s\to 0}\left\|s\left(-B_2s^2-B_2m_os\right)\Sigma_1(s)\right\| \\
&=\lim_{s_r\to 0^+,\,s_i\to 0}\left\|\left(s_r+is_i\right)^2B_2\left(s_r+is_i+m_o\right)\Sigma_1\left(s_r+is_i\right)\right\| \\
&\le\lim_{s_r\to 0^+,\,s_i\to 0}\left(\left|\left(s_r+is_i\right)^2\right\|B_2\|s_r+is_i+m_o|\frac{\varepsilon_{1\max}}{s_r}\right) \\
&=\lim_{s_r\to 0^+}\left(s_r^2|B_2|\left(s_r+m_o\right)\frac{\varepsilon_{1\max}}{s_r}\right)=0
\end{aligned} \tag{54}$$

In other cases than the worst case scenario, $\Sigma_1(s)$ still converges on $\mathrm{Re}(s)=s_r>0$ since $|\varepsilon_1(t)|$ is still exponentially bounded by $e^{-0t}\varepsilon_{1\max}$, so (54) also applies. Also, there must be

$$\left|s\left(-B_2s^2-B_2m_os\right)\Sigma_1(s)\right|\ge 0 \tag{55}$$

Then it can be concluded from (54) and (55) that

$$\lim_{s\to 0}s\left(-B_2s^2-B_2m_os\right)\Sigma_1(s)=0 \tag{56}$$

Hence

$$q_{o12}(\infty)=\lim_{s\to 0}\frac{s\left(-B_2s^2-B_2m_os\right)\Sigma_1(s)}{s^3+\left(B_2D_o+m_o\right)s^2+B_2P_os+B_2I_o}=0 \tag{57}$$

The rest two subsystems takes e_{10} and q_{o0} as input, respectively, and q_{o13} and q_{o14} as output, respectively. Similar to the first subsystem, it is found that they have the same stability condition as the first subsystem and

$$q_{o13}(\infty)=0\,,\quad q_{o14}(\infty)=-q(0) \tag{58}$$

So the system given by (42) and (43) or (45) and (46) is asymptotically stable if and only if the P_o, I_o, D_o, and m_o values are such that the roots of (21) have negative real parts. Given that this stability condition is met, according to (44), (50), (57), and (58), it can be found that

$$q_o(\infty)=q_o(0)+q_{o11}(\infty)+q_{o12}(\infty)+q_{o13}(\infty)+q_{o14}(\infty)=0 \tag{59}$$

So the sliding surface (4) is asymptotically reachable, or $q_o\to 0$ as $t\to\infty$.

REFERENCES

[1] H. Song, G. Vdovin, R. Fraanje, G. Schitter, and M. Verhaegen, "Extracting hysteresis from nonlinear measurement of wavefront-sensorless adaptive optics system," *Optics Letters*, vol. 34, no. 1, pp. 61-63, Jan. 2009.

[2] J.-J. Wei, Z.-C. Qiu, J.-D. Han, and Y.-C. Wang, "Experimental comparison research on active vibration control for flexible piezoelectric manipulator using fuzzy controller," *Journal of Intelligent and Robotic Systems*, vol. 59, no. 1, pp. 31-56, July 2010.

[3] H. J. M. T. S. Adriaens, W. L. De Koning, and R. Banning, "Modeling piezoelectric actuators," *IEEE/ASME Transactions on Mechatronics*, vol. 5, no. 4, pp. 331-341, Dec. 2000.

[4] Physik Instrumente, *The World of Nanopositioning and Micropositioning 2005 / 2006*, 2005.

[5] Y. Li and Q. Xu, "Design and robust repetitive control of a new parallel-kinematic XY piezostage for micro/nanomanipulation", *IEEE/ASME Transactions on Mechatronics*, in press, 2011.

[6] P.-K. Huang, P.-H. Shieh, F.-J. Lin, and H.-J. Shieh, "Sliding-mode control for a two-dimensional piezo-positioning stage," *Control Theory & Applications, IET*, vol. 1, no. 4, pp. 1104-1113, July 2007.

[7] J.-C. Shen, W.-Y. Jywe1, C.-H. Liu, Y.-T. Jian, and J. Yang, "Sliding-mode control of a three-degrees-of-freedom nanopositioner," *Asian Journal of Control*, vol. 10, no. 3, pp. 267-276, May 2008.

[8] J.-C. Shen, H.-K. Chiang, and Y.-L. Shu, "Precision tracking control of a piezoelectric-actuated system," *Precision Engineering*, vol. 32, no. 2, pp. 71-78, Apr. 2008.

[9] C. Edwards and S. K. Spurgeon, *Sliding mode control: theory and applications*, Taylor & Francis, Abingdon, UK, 1998.

[10] H. C. Liaw, B. Shirinzadeh, and J. Smith, "Enhanced sliding mode motion tracking control of piezoelectric actuators," *Sensors and Actuators A: Physical*, vol. 138, no. 1, pp. 194-202, July 2007.

[11] Y. Li, Q. Xu, "Adaptive Sliding Mode Control With Perturbation Estimation and PID Sliding Surface for Motion Tracking of a Piezo-Driven Micromanipulator," *IEEE Transactions on Control Systems Technology*, vol. 18, no. 4, pp. 798-810, July 2010.

[12] J. Y. Peng and X. B. Chen, "PID-based sliding mode control for piezoelectric actuators", submitted to *Mechatronics* for possible publication, July 2011.

[13] H. C. Liaw, B. Shirinzadeh, and J. Smith, "Sliding-Mode Enhanced Adaptive Motion Tracking Control of Piezoelectric Actuation Systems for Micro/Nano Manipulation," *IEEE Transactions on Control Systems Technology*, vol. 16, no. 4, pp. 826-833, July 2008.

[14] X. Chen and T. Hisayama, "Adaptive Sliding-Mode Position Control for Piezo-Actuated Stage," *IEEE Transactions on Industrial Electronics*, vol. 55, no. 11, pp. 3927-3934, Nov. 2008.

[15] H. C. Liaw, B. Shirinzadeh, "Enhanced sliding-mode constrained motion tracking control of piezo-actuated flexure-based mechanisms," In: *IEEE/ASME International Conference on Advanced Intelligent Mechatronics, 2009*. AIM 2009, Singapore. pp. 1879-1884, July 2009.

[16] X. Wang, "High-order integral-chain differentiator and application to acceleration feedback," submitted to *Computer Science* for possible publication, 2011.

[17] A. Levant, "Robust Exact Differentiation via Sliding Mode Technique," *Automatica*, vol. 34, no. 3, pp. 379-384, 1998.

[18] F. Yang and R. W. Wilde, "Observers for linear systems with unknown inputs," *IEEE Transactions on Automatic Control*, vol. 33, pp. 667-681, July 1988.

[19] M. Hou and P. C. Muller, "Design of observers for linear systems with unknown inputs," *IEEE Transactions on Automatic Contro*l, vol. 37, pp. 871-875, June 1992.

[20] S. Hui and S. Żak, "Observer design for systems with unknown inputs," *International Journal of Applied Mathematics and Computer Science*, vol. 15, pp. 431-546, 2005.

[21] S. H. Zak and S. Hui, S. "Output feedback variable structure controllers and state estimators for uncertain/nonlinear dynamic systems," *IEE Proceedings D: Control Theory and Applications*, vol. 140, pp. 41-50, Jan. 1993.

[22] C. M. Kwan, "On variable structure output feedback controllers," *IEEE Transactions on Automatic Control*, vol. 41, pp. 1691-1693, Nov. 1996.

[23] F. Castanos and L. Fridman, "Analysis and design of integral sliding manifolds for systems with unmatched perturbations," *IEEE Transactions on Automatic Control*, vol. 51, pp. 853-858, May 2006.

[24] J.-L. Chang and T.-C. Wu, "Robust disturbance attenuation with unknown input observer and sliding mode controller," *Electrical Engineering*, vol. 90, pp. 493-502, 2008.

[25] T. Floquet, C. Edwards, and S. K. Spurgeon, "On sliding mode observers for systems with unknown inputs," *International Journal of Adaptive Control and Signal Processing*, vol. 21, no. 8-9, pp. 638–656, Oct.-Nov. 2007.

[26] K. Kalsi, J. Lian, S. Hui, and S. H. Zak, "Sliding-mode observers for systems with unknown inputs: A high-gain approach," *Automatica*, vol. 46, no. 2, pp. 347-353, Feb. 2010.

[27] M. Li, F. Wang, and F. Gao, "PID-Based Sliding Mode Controller for Nonlinear Processes," *Industrial and Engineering Chemistry Research*, vol. 40, pp. 2660-2667, June 2001.

[28] J. Y. Peng and X. B. Chen, "H2-optimal digital control of piezoelectric actuators," in: *Proceedings of the 8th World Congress on Intelligent Control and Automation*, WCICA-2010, Jinan, China, pp. 3684-3690, July 2010.

[29] J. Y. Peng and X. B. Chen, "Modeling of piezoelectric-driven stick-slip actuators," *IEEE/ASME Transactions on Mechatronics*, vol. 16, no. 2, pp. 394-399, Apr. 2011.

[30] G. M. Clayton, S. Tien, A. J. Fleming, S. O. R. Moheimani, and S. Devasia, "Inverse-feedforward of charge-controlled piezopositioners," *Mechatronics*, vol. 18, no. 5-6, pp. 273-281, June 2008.

[31] Y. Cao and X. B. Chen, "A novel discrete ARMA-based model for piezoelectric actuator hysteresis," *IEEE/ASME Tansactions on Mechatronics*, accepted for publication, 2011.
[32] X. B. Chen, Q. Zhang, D. Kang, and W. Zhang, "On the dynamics of piezoactuated positioning systems" *Review of Scientific Instruments*, vol. 79, pp. 116101-1 to 116101-3, 2008.
[33] J.H. Painter, D. Kerstetter, and S. Jowers, "Reconciling steady-state Kalman and alpha-beta filter design", *IEEE Transactions on Aerospace and Electronic Systems*, vol. 26, no. 6, pp. 986-991, Nov. 1990.

8 Conclusions and Future Work

8.1 Conclusions

PEAs are widely used in micro- and nano-positioning applications. The aim of this research work is to develop models and control schemes for PEAs in micro- and nano-positioning applications. The main conclusions of this research are summarized as follows.

1. The displacement and average speed of the end-effector of a PDSS actuator can be effected by the frequency and magnitude of the input saw-tooth voltage and the mass of the end-effector. From the voltage input and an end-effector mass, the displacement and average speed of the end-effector of a PDSS actuator can be predicted by means of the developed model.

2. The one-sided hysteresis behavior of PEAs, including the initial ascending curve and the hysteresis loops, can be modeled as the combined effect of an infinite number of the novel hysteresis operators proposed. Such novel hysteresis operators are modified from the Preisach hysteresis operator by introducing a second lower saturation value to account for both the initial ascending curve and the hysteresis loops. Both rate-independent and rate-dependent hysteresis of a PEA can be modeled by this method. Given the input waveform, the displacement of the PEA can be predicted by means of the developed hysteresis models.

3. The relationship between the displacement and the PEA input voltage can be modeled by a cascade of the rate-independent hysteresis model discussed previously, a second order linear system representing the vibration dynamics, and a higher order linear dynamic system representing the creep effect. The comparison between the experimental and simulation results indicate that the model can accurately predict the output displacement of a PEA subject to input voltage waveforms of broad bandwidth (up to 400 Hz).

4. Experimental results indicate that the PIDSM controller developed for tracking control of PEAs, which replaces the switching term in ideal SM controllers with a PID regulator, is capable of tracking control of a PEA with no steady state error, low chattering, and low tracking error. The experimental comparative study showed that the PIDSM control scheme was superior to PID control (in high frequency operations), ideal SM control, and SMBL control in the aforementioned terms.

5. The method of PIDSM can be extended to observer design by replacing the switching term in conventional SM observers with a PID regulator. The PIDSM observer developed by such method is capable of estimating both measurable and immeasurable states of the model of the PEA accurately with small phase lag and strong noise suppression capability despite the existence of hysteresis, creep, and external loads. Also, the observer matching condition is not needed for the PIDSM observer. The PIDSM observer and the PIDSM observer can be combined to form an integrated control scheme for PEAs, referred to as the PIDSMOC. Promising PEA tracking control performance up

to 150 Hz in both no-load and loaded situations, with the maximum error less than 3% of the maximum displacement of the PEA in the worst case scenario (150 Hz, 10 μm, loaded), can be achieve by the use of PIDSMOC. And the PIDSMOC scheme performs generally better than those of the PIDSM controller with α-β filter scheme in PEA tracking control applications. Both the PIDSM observer and the PIDSMOC are showed to be very robust against large model uncertainties.

8.2 Future Work

Based upon the work presented in this dissertation, a number of projects can be taken up to extend the current research.

1. Development of control schemes for PDSS actuators based on the model developed in Chapter 3. As the input voltage to a PDSS actuator must be (periodic) voltage waveforms that are asymmetric in each period, and the output displacement of the end-effector of a PDSS actuator is fluctuating when the end-effector is on the move, the key issue in such a project will be to define a suitable set of parameters to characterize the desired control performances, e.g. tracking errors. Based on which, the control schemes can then be developed.

2. Extending the hysteresis models developed in Chapter 4 to account for hysteresis behaviors of PEAs when the PEAs are subject to bipolar inputs.

3. Extending the PIDSM controller and observer to multi-input-multi-output systems. This will allow the control of multi-degree-of-freedom PEA-driven positioning systems,

especially those based on parallel mechanisms.

It is worth explicitly stating the limitations of the methods used in the present study so that future work based upon this research moves forward successfully. The model of PDSS actuator developed in Chapter 3 uses the Preisach hysteresis model to represent hysteresis in the PEA. This can introduce error in the predicted displacement of the end-effector since the Preisach hysteresis model can not represent the one sided hysteresis behavior of the PEA, as discussed in Chapter 4. More over, the modified elastoplastic friction model can only handle the situation that the end-effector moves horizontally since the model predicted friction is dependent on the mass of the end-effector instead of the normal force between the frictional surfaces. The model of PEAs developed in Chapter 5 does not account for the effect of external load. As such, in Chapter 6 and Chapter 7 the external load is treated as an additional input to the sub-model representing the vibration dynamics. Such a treatment is reasonable based on the fact that in PEAs the hysteresis only exists between the input voltage and the internal actuating force whist the vibration dynamics is linear.